

Exploration of novel triboelectric nanogenerator systems for coastal region applications

By

Yunzhong Wang

Doctorate in Electrical Engineering

Thesis
Submitted to Flinders University
for the degree of Doctor of Philosophy

Doctor of Philosophy

Collage of Science and Engineering 05/11/2025

TABLE OF CONTENTS

TABLE OF CONTENTS	I	
ABSTRACT	IV	
ECLARATIONCKNOWLEDGEMENTS		
LIST OF FIGURES	XI	
LIST OF TABLES		
CHAPTER 1 INTRODUCTION	1	
1.1 Introduction.		
1.2 Thesis structure	5	
1.3 Reference	9	
CHAPTER 2 LITERATURE REVIEW	13	
2.1 Milestones of development of ocean wave energy driven TENG	13	
2.2 Ocean wave energy harvesting as a renewable energy generator and self-powered sel	nsor.	
2.2.1 Solid – solid TENG		
2.2.2 Solid – liquid TENG		
2.2.3 Hybrid mode TENG		
2.2.4 Self-powered system for ocean application		
2.2.5 Energy storage system for ocean wave energy driven TENGs		
2.3 Discussion		
2.4 Future perspectives		
2.4.1 Utilisation of TENG based self-powered sensors to realise location evaluation		
2.4.2 Robustness testing of ocean wave driven TENGs under controlled water waves		
2.4.3 TENG technology-based ocean wave energy generator.		
2.5 Conclusion.		
2.6 Reference	40	
CHAPTER 3 DESIGN AND EVALUATE THE WAVE DRIVEN-TRIBOELECTRIC NANOGENERATOR UNDER EXTERNAL WAVE PARAMETERS: EXPERIMENT AND		
SIMULATION (WD-TENG)	47	
3.1 Introduction	47	
3.2 Experimental section	49	
3.2.1 Device fabrication and assembling	49	
3.2.2 Triboelectric material selection	49	
3.2.3 Simulated wave amplitude and frequency	49	
3.2.4 Hydrodynamic performance under computational fluid dynamic simulation		
3.2.5 WD-TENG charge performance evaluation	50	
3.3 Results and discussion	51	
3.4 Conclusion	60	

3.5 Reference	60
CHAPTER 4 AN AFFORDABLE MINIATURE 3D-PRINTING WAVE-GENERATION DEVICE WAVE ENERGY HARVESTING APPLICATION	
4.1 Introduction	66
4.2 Results	67
4.2.1 Concept of design and functionality of wave generation device	67
4.2.2 The working mechanism of the wave generation device	70
4.2.3 Analysis of generated wave under variation of water depth	72
4.2.4 Analysis of the wavelength of the generated wave under variations in pendulum ang	jle.74
4.3 Demonstration	76
4.4 Experimental procedures	77
4.4.1 Fabricate and functionality of the component consists of wave generation device	77
4.4.2 Material and components used for building modular concept wave generation device	∍80
4.4.3 Wave energy harvester evaluation	80
4.5 Discussion	81
4.6 Conclusion	81
4.7 Reference	82
CHAPTER 5 A HYBRID SELF-POWERED WAVE SENSING DEVICE ENABLES LOW-	
AMPLITUDE WAVE SENSING	
5.1 Introduction	
5.2 Results and discussion	
5.2.1 Working principle of the testing platform	
5.2.2 Design and working mechanism for CS-EMH and F-TENG in HSP-WS	
5.2.3 Performance evaluation and demonstration of the CS-EMH	
5.2.4 Explanation of the two operations modes of the CS-EMH	
5.2.5 Performance evaluation and analysis for the F-TENG	
5.2.6 Durability analysis of CS-EMH and F-TENG in HSP-WS	
5.2.7 Evaluation and analysis of HSP-WS under a wave generating system	
5.2.8 Signal analysis and potential applications	
5.3 Conclusion and outlook	
5.4 Experimental procedures	
5.4.1 Materials	
5.4.2 Fabrication of rGO/PVA hydrogel	
5.4.3 Fabrication of F-TENG	
5.4.4 Fabrication of CS-EMH	
5.4.5 Performance evaluation	
5.5 Reference	
CHAPTER 6 AN ACTIVE IMPACT DETECTION SYSTEM FOR OFFSHORE WIND TURBINE BASED ON TRIBOELECTRIC NANOGENERATOR	
6.1 introduction	
6.2 Experimental result	
6.2.1 Impact test	

6.2.2 Water droplet test	112
6.2.3 Wireless data transmission system	115
6.3 Demonstration	117
6.4 Conclusion	118
6.5 Reference	119
CHAPTER 7 CONCLUSIONS AND FUTURE PERSPECTIVES	123
7.1 Conclusions	123
7.2 Future perspectives and discussion	125
7.3 Reference	129
APPENDICES	130
Supporting information for Chapter 3	130
Supporting information for Chapter 4	142
Supporting information for Chapter 5	146

ABSTRACT

The demand for electricity is rapidly increasing today. At the same time, the need for non-carbon-emission energy sources is growing due to increasingly stringent environmental regulations and global carbon-neutral strategies. Ocean energy has increasingly gained attention, as it shows strong potential to serve as a sustainable energy source that is less affected by environmental fluctuations. However, ocean wave energy in coastal regions has long been overlooked due to the lack of efficient harvesters capable of capturing low-frequency and low-amplitude wave motion. Notably, wave energy near coastlines has the potential to provide approximately 2–3 TWh, making it a resource worth exploring. In 2012, Zhong Lin Wang introduced a groundbreaking technology known as the triboelectric nanogenerator (TENG). Thanks to its unique energy generation mechanism, TENG demonstrates exceptional performance in harvesting low-frequency and low-amplitude energy, making it particularly well-suited to capturing energy from ocean waves.

Since their introduction in 2012, TENGs have made significant progress in harvesting electrical energy from ocean wave motion. However, several challenges remain. The effects of external factors, such as wave frequency and amplitude, still require in-depth study, and the lack of suitable water wave testing platforms limits understanding of device dynamics under realistic ocean conditions. These limitations also restrict the further development and practical application of ocean wave driven TENGs. A major limitation of TENGs is their low output current at milli- or micro-levels, which restricts TENG been widely used. Hybrid-mode TENG combining TENGs and electromagnetic harvesters (EMH) shows potential to overcome low current output at low frequencies and amplitudes. Current radar-based sensors also struggle to monitor wave variations in coastal conditions which is the primary environment for TENG operation. Since TENGs can function as self-powered sensors for subtle environmental motions, they offer a promising alternative. Additionally, with the rise of offshore wind farms, TENGs are increasingly explored for structural health monitoring and damage detection in wind turbines.

In this study, several TENG-based systems and devices have been successfully developed to address the limitations. A contact and separation mode TENG was used to investigate the effects of

wave parameters, such as wave amplitude and wave frequency, on its output performance. An affordable wave generation system has been proposed to evaluate TENG performance in a cost-effective manner. A hybrid-mode TENG has been developed to enable monitoring of ocean wave parameter variations in coastal environments. An active impact detection system has been established to enable real-time monitoring of impacts on offshore wind turbines. In summary, this thesis has extensively explored TENG-based devices for coastal region applications, including both ocean wave energy generators and self-powered sensors for monitoring ocean wave parameters and environmental operating conditions. The results of this study make a significant contribution to the field of ocean wave energy harvesting.

DECLARATION

I certify that this thesis:

- 1. does not incorporate without acknowledgment any material previously submitted for a degree or diploma in any university
- 2. and the research within will not be submitted for any other future degree or diploma without the permission of Flinders University; and
- 3. to the best of my knowledge and belief, does not contain any material previously published or written by another person except where due reference is made in the text; and
- 4. has been completed without the use of generative artificial intelligence tools.

Signed	Wang
Date	24/08/2025

ACKNOWLEDGEMENTS

I am deeply honoured to have the opportunity to express my sincere gratitude to all those who have contributed to and supported the completion of my doctoral thesis.

First of all, I am deeply indebted to my primary supervisor, Professor Youhong Tang. I cannot express enough appreciation for the tremendous support, guidance, and encouragement you have provided to me, from my Bachelor thesis through to the completion of my Ph.D. degree.

I would like to express my sincere gratitude to my co-supervisor, Associate Professor Paulo Santos, for his invaluable feedback and advice on my research proposal and throughout my Ph.D. candidature. His support and guidance have greatly enhanced the quality of my writing skills, strengthened my critical thinking ability, and deepened my understanding of the research process.

Moreover, I would like to express my sincere gratitude to my adjunct-supervisor Associate Professor. Xiangxi Han, for his supporting on my CFD simulation studying. His support and guidance on CFD simulation have greatly enhanced the understanding of hydrodynamic of my researching candidature.

I would like to acknowledge the Australian Government Research Training Program Scholarship, which fully supported my living expenses, and Flinders University for providing tuition fee waivers throughout the 3.5 years of my doctoral research. In addition, I am grateful for the HDR conference support, the professional advice and assistance from the CSE Engineering Service, the opportunities provided through the Industrial Mentoring Network in STEM, and the support that enabled me to access the necessary research resources.

I extend my gratitude to Dr. Anh Tram Tan Pham for his support in 3D design, manufacturing, and experimentation. I have learned many valuable skills from Dr. Pham. Moreover, I sincerely appreciate his emotional support as a friend throughout the entire period of my Ph.D. candidature. In additional, thanks for Dr Pham's fired Tofu and fired peanuts as Friday work leaving sneaks.

I would like to express my sincere appreciation to Dr. Damian Richard Tohl for his support with MATLAB, programming, experimental assistance, and proofreading of my manuscripts. I have greatly benefited from his critical thinking, meticulous research notetaking, and expertise in MATLAB programming. I am truly grateful for his dedicated support. Moreover, I sincerely appreciate his ginger beer as Friday work leaving drinks.

I also wish to express my sincere appreciation to my friends Dr. Wenjin Xing, Dr. Huixin Zhu, Dr. Qi Hu, Dr. Zhi Cao, and Dr. Ling Chen for their professional advice and support throughout my research. In particular, I am grateful to Mr. Yupu Dai for his assistance during my research exchange between Australia and Germany.

I would like to sincerely thank my parents for their love and unwavering support throughout my studies. I am grateful for the time they spent traveling to Australia to be with me, and especially for their financial support during my academic journey.

PUBLICATIONS

- Yunzhong Wang, Anh Tran Tam Pham, Xiangxi Han, Dongsheng Du, Youhong Tang, Design and evaluate the wave driven- triboelectric nanogenerator under external wave parameters: Experiment and simulation, Nano Energy, Volume 93, 2022, 106844, ISSN 2211-2855, https://doi.org/10.1016/j.nanoen.2021.106844.
 This publication has been used as Chapter 3 in this thesis.
- Yunzhong Wang, Damian Tohl, Anh Tran Tam Pham, Youhong Tang. Developing an Affordable Miniature 3D-Printed Wave Generator for Wave Energy Harvesting Application. Micromachines. 2024; 15(12):1500. https://doi.org/10.3390/mi15121500.
 This publication has been used as Chapter 4 in this thesis.
- Yunzhong Wang, Huixin Zhu, Wenjin Xing, Damian Tohl, Youhong Tang. (2024). A hybrid self-powered wave sensing device enables low-amplitude wave sensing. Device. https://doi.org/10.1016/j.device.2024.100575.
 This publication has been used as Chapter 5 in this thesis.
- 4. Yunzhong Wang, Youhong Tang. Ocean Wave Energy Generators and Self-Powered Wave Sensors Based on Triboelectric Nanogenerators. This work has been accepted for publication in *Advanced Energy and Sustainability Research* on 13 August 2025. DOI: 10.1002/aesr.202500232.

This publication has been used as Chapter 1 introduction, Chapter 2 literature review and few content in conclusion and future perspective.

Other publications during candidature as co-author

- Jiang, Zongyi, Yunzhong Wang, Damian Tohl, Liming Fang, and Youhong Tang. 2024.
 "Utilizing Multiple Triboelectric Nanogenerator Sensors and Signal Processing Technology for Monitoring Periodic Leg Movements of Sleep" *Biosensors* 14, no. 11: 532. https://doi.org/10.3390/bios14110532.
- 2. Jiang, Zongyi, Yee Sum Lee, Yunzhong Wang, Honey John, Liming Fang, and Youhong Tang. 2024. "Advancements in Flexible Sensors for Monitoring Body Movements during Sleep: A Review" *Sensors* 24, no. 16: 5091. https://doi.org/10.3390/s24165091.

Conference during Ph.D. candidature

- 1. Invited talk in the 6th International Conference on Nanogenerators and Piezotronics, 2022, Sweden.
- 2. Oral presentation in The Chinese Materials Conference 2024 & The 2nd World Materials Conference, 2024, China.
- 3. Oral presentation in The International Conference on ocean Energy, 2024, Australia.

Award during Ph.D. Candidature

• Best HDR Student Publication Award, Flinders University, Australia, 2022

Applied patent during Ph.D. candidature

 Australia Patent (provisional - 2023902299): "A Commercial Water Channel-Based Wave Simulator with Active Control of Wafe frequency and amplitude for Research on Ocean Wave Energy Converters."

LIST OF FIGURES

Figure 1.1 Prototypes of wave energy converters (WECs): (A) Unveiling of the Ceto buoy by Carnegie Wave Energy, Australia [8]; (B) 1/4-scale model of the wave bob operating in Galway Bay, Ireland [8]; (C) 1/4-scale model of the OE buoy developed by Ocean Energy Ltd., Ireland [8]; and (D) WD prototype developed by SPOK [9].
Figure 1.2 The logic flowchart for this thesis and relationship between each chapter8
Figure 2.1 The key milestones of ocean wave energy driven TENGs from 2015 to 2024. The development of ocean wave energy-driven TENGs has undergone multiple stages of evolution, particularly in the design of their outer structures, with the goal of more efficiently utilizing ocean wave motion. Various types of TENGs have also been developed such as solid–liquid TENGs, which aim to harvest more available energy from the natural environment, and hybrid-mode TENGs, which combine electromagnetic harvesters (EMHs) to compensate for the low current output of TENGs. In the future, integrating TENG devices with wireless data transmission systems will be a key direction, unlocking greater potential for real-world applications [7], [14], [17], [29], [38], and [55]
Figure 2.2 Schematic structure of the spherical ocean wave-driven TENG (A) Spherical TENG [7], (B) Spherical TENG with silicone base material [8], (C) Soft-contact spherical triboelectric nanogenerator (SS-TENG) [9], (D) Self-assembly TENG network, and (E) Liquid/silicone core shell structure of SS-TENG [10].
Figure 2.3 Schematic structure of the cubic ocean wave-driven TENG (A) Integrated four contact and separation wavy-structured TENGs inside a cube shape exterior [12], (B) Air-driven membrane structures TENG [13], (C) Spring-assisted TENG based on the contact and separation mode [14], and (D) Spring-assisted TENG with enhanced output performance by applied ordinary material [15]
Figure 2.4 Schematic structure of the cylindrical ocean wave-driven TENG (A) Tandem disk triboelectric nanogenerator based on the rotational mode (TD-TENG) [16], (B) Multilayered rotational mode TENG for ocean wave energy harvesting [17], (C) Tower-like TENG based on the freestanding mode (T-TENG) [18], and (D) Anaconda-shaped spiral multi-layered triboelectric nanogenerators (ASM-TENG) [19]
Figure 2.5 Schematic structure of the water wave solid-liquid TENG (A) Networked integrated triboelectric nanogenerator (NI-TENG) [28], (B) Droplet-based (DB)-TENG [29], and (C) Solid-liquid contact-based saline water TENG [30]25
Figure 2.6 Schematic structure of the water wave hybrid generator combines with TENG and EMH (A) Teeterboard-like hybrid nanogenerator (THNG) [36], (B) Tube-shaped triboelectric–electromagnetic hybrid nanogenerator (TTEHG) [37], (C) Triboelectric-electromagnetic hybrid nanogenerator (TEH-NG) [38], and (D) Guided-liquid-based isotropic triboelectric-electromagnetic hybrid nanogenerator (I-TEHG) [39]
Figure 2.7 Schematic structure of the self-powered ocean wave sensors, (A) Highly sensitive wave sensors based on liquid-solid interfacing triboelectric nanogenerator (WS-TENG) [51], (B) Self-powered and high-performance triboelectric ocean-wave spectrum sensor (TOSS) [52], (C) Graded energy harvesting triboelectric nanogenerator (GEH-TENG) [53], and (D) Self-powered wide-range ocean-wave sensor [54]
Figure 2.8 Comparison of output power density (W/m³) for published ocean wave energy driven TENGs
Figure 3.1 (a) Geometric model and (b) hydrodynamic model of the WD-TENG. The length of the WD-TENG is in the X direction and the radius direction of the WD-TENG is in the Y direction in the simulation
Figure 3.2 (a) The initiate condition of the WD-TENG, where h is the maximum distance between two triboelectric materials. (b) The energy generation cycle of the WD-TENG (c) The exploded

view drawing of the WD-TENG with the components. Two generators have the same functions, structures, and performances. There is a I-shape internal sliding module inside the acrylic tube, used to place Aluminum (AI) films (grey colour). The acrylic tube is sealed by two 3D-printed caps. Each cap is equipped with a PTFE film (blue colour) and a small piece of copper (orange colour). The copper piece acted as the transmission layer to transfer the electrical energy from the AI films to the outside collector.
Figure 3.3 (a) Typical waveform of the output voltage, (b) typical waveform of the output current, (c) change of current cross resistor and voltage cross resistor under different load resistances, and (d) change of power density under different load resistances. The electrical output of the WD-TENG under the maximum speed of 0.582 m·s ⁻¹ and acceleration of 4.07 m·s ⁻² . The maximum displacement of the WD-TENG is 8.3 cm and the maximum displacement between PTFE and Al films is 8 mm.
Figure 3.4 Response amplitude operators (RAOs) of the WD-TENG in (a) pitch and (b) surge under CFD simulation
Figure 3.5 WD-TENG (a) and (b) time-history curves of position and (c) and (d) structural response frequency spectra in (a) and (c) surge (the X direction) and (b) and (d) pitch (the RY direction) 56
Figure 3.6 Effect of (a) external amplitude and (b) frequency on the output voltage and the power density of the WD-TENG. The frequency in (a) is 2.2 Hz, and the amplitude in (b) is fixed as 0. The load resistance is $5~\text{M}\Omega$
Figure 3.7 (a) The output voltage of the WD-TENG after 2-, 4-, 6-, and 8-hours operation under 2.2 Hz frequency and 11.6 cm amplitude, and (b) the WD-TENG as an electrical generator to charge an empty capacitor. The charging curves of three different capacitors, i.e., 47 μ F, 100 μ F, and 470 μ F. The testing condition is 5 Hz frequency and 0 amplitude.
Figure 4.1 Workflow diagram of the wave generation device in this study
Figure 4.2 A) Overview of the wave generation device, which involves two wave dampers and the commercial water channel, B) View of the six components that make up the wave generation device, (I) Motor driving unit, (II) Transmission belt, (III) Wave creation board, (IV) Driving shaft, (V) T-track, and (VI) Conveyor system balancer, and C) Photo of the actual wave generation device mounted in the water channel.
Figure 4.3 Schematic of the wave generating process, fx and fy represents the force component on x and y axes, respectively. d is the depth of water, and θ is the pendulum. $x(t)$ represents the displacement of the wave creation board on the y -axes direction. Waves are generated when the wave creation board applies pressure to the contact area of the water
Figure 4.4 Detailed cylinder charts of generated wave amplitudes with error bars under (A) 10 cm depth, (B) 15 cm depth, and (C) 20 cm depth respectively73
Figure 4.5 (A) Colormaps of the relationship among frequency, pendulum and amplitude under 10 cm, 15 cm, and 20 cm water depths. Detailed cylinder chart of generated wave amplitude under (B) 10 cm depth, (C) 15 cm depth, and (D) 20 cm depth74
Figure 4.6 (A) The block diagram for the image processing steps to determine the mean value of the wave amplitude and the wavelength. Generated waves under 20 cm depth water, 40 cm wavelength under 2.0 Hz (B) 18.18 $^{\circ}$, and (C) 21.51 $^{\circ}$. 60 cm wavelength under 1.5 Hz (D) 18.18 $^{\circ}$, (E) 21.51 $^{\circ}$, (F) 27.72 $^{\circ}$, and (G) 30.59 $^{\circ}$
Figure 4.7 (A) Output performance of the WD-TENG under various generated wave amplitude. The blue, green, and orange waveforms represent the generated waves with amplitudes of 4.6 cm, 5.1 cm, and 7.1 cm under a frequency of 1.5 Hz, respectively, and (B) The maximum output performance under generated wave from current study comparing with the previous publication [12]
Figure 4.8 The detailed view of the motor driving unit. (A) Base, (B) Locker, and (C) Motor driving pulley are fabricated from polylactic acid (PLA) using 3D-printing technology, as shown in green.

transparent acrylic board using a laser cutting machine. The stepper motor is shown in red; the microcontroller is shown in green, the Bluetooth module is shown in bright blue, and the 9V power supply is shown in pink.
Figure 4.9 The close view of the conveyor system balancer, with a sub insertion which involves (1) 3D printing pully, (2) Steel ball bearing, and (3) Transmission belt limiter. The 3D printing components as shown in green
Figure 4.10 The detailed view of the wave creation board, (A) Base board, (B) Rubber connection piece, (C) Wave generation board, (D) Ball bearing, (E) Shaft holder, and (F) Wave creator shaft. The 3D printing components as shown in green, and the white transparent pieces are acrylic components.
Figure 4.11 The detailed view of the driving shaft, (A) Transmission belt connector, (B) Metal shaft, (C) Roller, (D) Upper holder, (E) Lower holder, and (F) Ball bearing. The close view of the conjunction points (I) between upper and lower holders; and the position of the four ball bearings on the T-track (II).
Figure 5.1 Structural design and working principle of the testing platform. (A) Schematic drawing of the testing platform. (B) Schematic drawing of the operation cycle: (i) origin status, (ii) the disk rotates 90 degrees, (iii) the disk rotates 180 degrees, and (iv) the disk rotates 270 degrees. This testing platform is used to mimic wave motion, including wave frequency and wave amplitude. The five red dots represent adjustable wave amplitudes ranging from 6.6 cm to 8.1 cm, increasing by 0.5 cm at each stage. The blue dot represents the rotation point used to simulate wave motion on the left side of the testing platform.
Figure 5.2 (A) Overview of the HSP-WS, involving a contact and separate electromagnetic generator (CS-EMH) and a flexible triboelectric nanogenerator (F-TENG), (B) An exploded view of the HSP-WS. (The green parts are fabricated using PLA, and the transparent grey part is the acrylic tube), (C) Geometric dimensions of the HSP-WS, (D) An exploded view of the F-TENG, and (E) (i-iv) The energy generation cycle of the F-TENG.
Figure 5.3 (A) The output performance of CS-EMH at various frequencies (ranging from 1.5 Hz to 4.0 Hz) and amplitudes (ranging from 6.6 cm to 8.6 cm), (B) typical waveform of the output voltage of the CS-EMH operated under 3 Hz frequency and 8.6 cm amplitude, and (C) the power management system used for CS-EMH in this study.
Figure 5.4 Different operation modes of CS-EMH under various frequency ranges, utilising a 6.6 cm amplitude as an example. The green parenthesis involves four frequencies from 1.5 Hz to 3.0 Hz, working under Mode 1 as shown in (i). The blue parenthesis involves two frequencies of 3.5 Hz and 4.0 Hz, working under Mode 2 as shown in (ii). The solid line represents the calculated frequency of Mode 1 to Mode 2 transition, and the dashed line represents the actual experimental frequency of transition. The gap, as represented by the orange arrow, represents the difference between the experimental frequency and the calculated frequency
Figure 5.5 (A) The output performance of F-TENG is depicted at various frequencies with an amplitude of 8.6 cm. When the amplitude is set to 8.6 cm, the spherical magnet can generate maximum acceleration, leading to the highest input kinetic energy for F-TENG, (B) Typical waveform of the output voltage of F-TENG with 3 Hz frequency and 8.6 cm amplitude, (C) Explanation of two signals generated by F-TENG: Signal 1 is produced by electron transfer between the silicon rubber and the copper winding. The rGO hydrogel is used as conductive material to transfer the generated current to the copper electrode and then to the load circuit. Signal 2 is induced by electron transfer between rGO and the silicon rubber, which is then transferred to the load through the copper electrode.
Figure 5.6 The durability test results for (A) CS-EMH and (B) F-TENG. The output voltage of both the CS-EMH and F-TENG was tested under the operating condition of a 3.0 Hz frequency and an 8.6 cm amplitude
Figure 5.7 (A) Output waveform under different generated waves, and (B) comparison of output performance under the water channel and the testing platform

Figure 5.8 (A) Working principle of the HSP-WS, (B) workflow diagram of the HSP-WS with potential applications and module section definitions, and (C) the application potential of HSP-WS in IoT99
Figure 6.1 (A) Schematic of the self-powered single-electrode sensor. (B) Working mechanism of the sensor when operating as an impact detection device. (C) Working mechanism of the sensor when functioning as a water droplet detector.
Figure 6.2 (A) Impact testing platform (Instron 9440 Drop Tower, USA) and experimental setup. (B) Relationship of trend curve between output signal strength and input impact energy, and (C) Waveform of output electrical signal strength under different impact energy levels
Figure 6.3 (A) Experimental setup for water droplet testing using an oscilloscope (Keysight DSOX1204A, USA) and a dual-syringe pump (Ade-lab, Australia); (B) comparison of the output electrical signal strength between artificial seawater and tap water, (i) typical output waveform of the self-powered sensor under tap water, (ii) typical output waveform of the self-powered sensor under artificial seawater. The waveform of the generated electrical signal was recorded at a water droplet rate of 5 mL/min.
Figure 6.4 Schematic illustration: (A) Circuit diagram of the proposed active impact detection and wireless data transmission system; (B) Experimental setup for wireless data transmission during impact detection; (C) Experimental setup for wireless data transmission during the water rainfall test; (D) Waveform obtained from Arduino during impact test at 1.5 J; and (E) Waveform obtained from Arduino during the water rainfall test at a flow rate of 3 mL/min
Figure 6.5 Demonstration on vertical wind turbine (A) Experimental setup demonstrating the active impact detection system and (B) Screen capture showing the sensor's generated electrical signal output
LIST OF TABLES
Table 2.1 Summary of previously published solid-solid type triboelectric nanogenerators
Table 2.2 Summary of previously published solid-liquid type triboelectric nanogenerators25
$ {\it Table 2.3 \ Summary \ of \ previously \ published \ hybrid \ mode \ type \ triboelectric \ nanogenerators30 } $
Table 2.4 Summary of previously published self-powered sensors
Table 2.5 Summary of previously published energy storage system
Table 3.1 Size information for various WD-TENGs
Table 3.2 Vibration response characteristics of WD-TENGs with various geometries57
Table 6.1 Convert the measured water droplet rate into an equivalent daily rainfall value 113

CHAPTER 1 INTRODUCTION

This chapter includes content published in the fourth publication listed in the publication list above. **Yunzhong Wang**: Writing – original draft, reference collection, and figure plotting.

1.1 Introduction

In recent years, electronic devices have developed rapidly, and an increasing number of conventional mechanical devices now have electronic version [1,2], which significantly improving the convenience of daily life and enhancing work efficiency. However, the growing production and sales of electronic devices have led to a high demand for electricity. In 1974, total global electricity consumption was 5,268 TWh, and it has risen to 22,847 TWh in 2019, representing an increase of 433% [3]. However, the compulsory environmental policies, including the Net Zero strategy [4], are forcing our society toward the target of achieving net zero greenhouse gas emissions by 2050 [5]. Under these current stringent environmental policies, countries around the world urgently need to find alternative approaches to meet the growing demand for electricity. Also, that must ensure the electricity is generated from green, sustainable sources.

Ocean wave energy is one of the most reliable renewable energy sources, as it is less affected by day-night cycles and seasonal variations compared to wind and solar energy. Apart from it, the 71% surface area of the earth is occupied by ocean, which means that ocean can provides an abundant energy source for electrical energy harvesting. Additionally, the annual global ocean wave power potential is estimated to reach nearly 93,000 TWh which is approximately 4 times of the electricity consumption in 2019 [6], and the wave energy around the coastline also can provide approximately 2-3 TWh [7]. Wave energy converters (WECs) harness the periodic up-and-down motion of ocean waves to generate electrical energy. However, current WEC designs are often limited by their large size and high fabrication costs as shown in Figure 1.1 [8,9]. Take the WD prototype developed by SPOK from Denmark as an example as shown in Figure 1.1(D). This wave generator requires a minimum wave height of 4 meters and must be installed in ocean regions with a depth of 20 to 50 meters. Its rated output power is 3 MW per unit, with a maximum output of 4 MW. As a result, they require a substantial amount of energy to be activated. The abundant smaller waves around coastline have often been overlooked. However, these smaller waves can still provide a decent amount of electrical energy, as previously mentioned. The main challenge is the lack of a suitable generator capable of effectively utilizing this coastline wave energy.

In 2012, Wang and his team introduced a novel concept called the triboelectric nanogenerator (TENG) [10]. In recent years, TENGs have rapidly become a research hotspot in the field of renewable energy harvesting. Their unique characteristics including lightweight design, compact size, zero carbon emissions during operation, use of inexpensive and recyclable raw materials, and

the ability to function under low-frequency and low-amplitude conditions, make them highly attractive for low frequency and low amplitude renewable energy harvesting [11-15]. Wang's groundbreaking research successfully opened a new frontier in renewable energy harvesting under low-frequency and low-amplitude environments. TENGs operate through a combination of contact electrification and electrostatic induction, where electrons cyclically transfer between two materials with different electron affinities, known as triboelectric materials, to generate electrical energy. In essence, the repeated contact and separation of these materials produces an electrical energy output. Notably, a wide range of triboelectric materials can be used in TENG fabrication, including recyclable materials such as polymers and metals [16-18]. Apart from energy harvesting, triboelectric nanogenerators (TENGs) also demonstrate the capability to function as self-powered sensors. They can be used to detect the magnitude and frequency of motion. Unlike commercially available electronic sensors, TENG-based sensors do not require an external power source due to their self-generating ability. This significantly enhances the robustness and independence of the sensing system and reduces the risk of failure caused by power outages [19,20]. Therefore, TENG-driven self-powered sensors are well-suited for offshore applications, such as wave spectrum data capture. Additionally, when integrated with a wireless data transmission module, TENGs can enable remote data transmission, greatly contributing to the advancement of oceanic development and energy utilization [21,22].

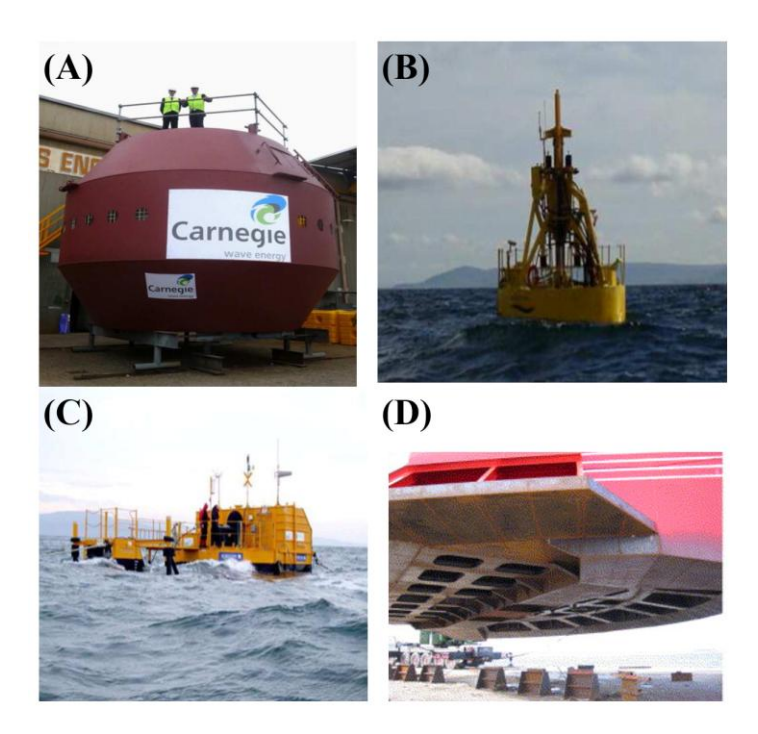


Figure 1.1 Prototypes of wave energy converters (WECs): (A) Unveiling of the Ceto buoy by Carnegie Wave Energy, Australia [8]; (B) 1/4-scale model of the wave bob operating in Galway Bay, Ireland [8]; (C) 1/4-scale model of the OE buoy developed by Ocean Energy Ltd., Ireland [8]; and (D) WD prototype developed by SPOK [9].

However, there are still some gaps and limitations existed in the ocean wave energy driven TENG area. Current research primarily focuses on increasing the surface charge density and enhancing the contact area of triboelectric materials, as these are the most direct factors influencing the output performance of TENGs [23-26]. However, these approaches may negatively impact the efficiency of ocean energy converters. Increasing the contact area often leads to a significant rise in the overall weight of the TENG device, which in turn raises the minimum wave frequency and amplitude required to produce a response. As a result, the overall utilization rate of ocean wave energy may decrease. In addition, enhancing the surface charge density through external treatments, additives, or surface Nano-structuring can significantly improve output performance. However, as previously emphasized, TENGs rely on repeated contact—separation motion to generate electricity. Over extended periods of operation, these surface treatments or nanostructures are easily to degradation due to friction between the materials. Given the demanding conditions of ocean environments, ensuring the long-term durability of triboelectric materials is crucial.

The active strategies mentioned above play an important role in enhancing the output performance of TENGs. However, passive factors such as wave parameters also significantly influence their energy convert efficiency. As is commonly known, TENGs operate based on contact and separation movements, which closely mimic the vertical (up-and-down) motion of ocean waves. While the impact of wave frequency on TENG performance has been widely investigated, the effect of wave amplitude remains largely underexplored. Therefore, studying the influence of wave parameters that particularly wave amplitude which is crucial for optimizing the output performance of TENGs. A successful investigation into the effect of wave amplitude on TENG output performance will not only contribute to optimizing overall energy conversion efficiency but also help researchers identify the most suitable operational regions within the diverse ocean wave environment.

Currently, researchers often rely on simplified methods to generate water waves for demonstrating the energy harvesting capability of ocean wave driven TENGs. For example, Shi et al. used a water tank that was manually shaken up and down to produce waves. However, this method lacks control and is unsuitable for scientific evaluation [27]. Wang et al. introduced a more controlled approach by using a water pump to generate waves. While this method offers improved consistency, it still does not allow independent adjustment of both wave frequency and wave amplitude, which significantly limits the evaluation range and accuracy [28]. Shen et al. modified a motor-driven double-axis platform by mounting a water tank on top to create a water wave generation system. This design successfully enabled the generation of repeatable and stable water waves and allowed for the adjustment of both wave frequency and wave amplitude though within a limited range [29]. Therefore, a modular water wave generation system with active control over wave frequency and amplitude is crucial for advancing the study of how wave parameters influence the output performance of ocean wave-driven TENGs.

To maximize energy conversion efficiency, studying and monitoring the wave amplitude range in the proposed specific ocean region is essential. However, current radar-based wave monitoring technologies lack the capability to accurately detect wave amplitude variations below 1 m [30,31]. These systems rely on antennas to transmit captured wave data to onshore stations for analysis. Unfortunately, irregular ocean winds can cause unintended antenna vibrations, resulting in inaccurate signals during data processing. This compromises the precision of wave amplitude analysis and significantly impacts the effective utilization of ocean wave energy. Due to the specific characteristics of TENG, it also can be used as a self-powered sensor [32,33]. Triboelectric nanogenerators (TENGs), with their unique characteristics such as high sensitivity to low-frequency and low-amplitude mechanical motion which presents a promising alternative. However, if a selfpowered sensor relies on wired data transmission, it significantly reduces the convenience and practicality of data collection. Moreover, TENGs are limited by their microampere-level current output. To support Bluetooth or Wi-Fi-based wireless data transmission, a TENG must first charge a supercapacitor for several minutes before it can activate the wireless module. Therefore, combining the self-powered sensor with a high current output generator is essential to reliably power wireless data transmission functions in order to realize high date transmission frequency. Conventional electromagnetic generators (EMG), based on the electromagnetic induction phenomenon, have been developed nearly two centuries since their discovery in 1831. However, conventional EMGs are limited by their bulky size, making them difficult to operate under low-input kinetic energy conditions. To overcome this issue, researchers have developed a new type of EMG. known as the electromagnetic harvester (EMH) [34,35]. EMH is preferred due to its simple structure, notable durability, and ability to operate under low-frequency and low-amplitude conditions compared to conventional electromagnetic generators. Therefore, combining EMH with TENG holds great potential for ocean wave parameter monitoring and detection applications. Detailed measurements of wave amplitude in specific regions using such systems can significantly aid in optimizing the placement and design of ocean wave energy driven TENGs, thereby maximizing their energy conversion efficiency.

Moreover, with the rapid expansion of offshore wind turbine farms and the harsh conditions typical of offshore environments, TENGs offer promising potential as self-powered sensors for detecting impacts from animals such as birds and bats. Their self-powered nature is particularly advantageous in marine settings, where traditional sensors typically rely on external batteries and numerous electronic components. A higher number of electronic components increases the risk of system failure due to corrosion caused by high humidity and salty air. The success of apply TENGs as self-powered sensor in ocean condition for monitoring and detecting demonstrate a valuable future.

In summary, this thesis focuses on analysing how wave amplitude affects the output performance of ocean wave-driven TENGs. An affordable, self-developed, remotely controlled water wave generation system will be proposed to evaluate the performance of TENGs under controlled water

wave conditions. A hybrid-mode self-powered sensor for detecting ocean wave amplitude changes will be designed, fabricated, and tested using the generated waves. Additionally, an active alert system that employing a TENG-based self-powered sensor integrated with a wireless data transmission system will be developed. Finally, the thesis will present a discussion of the experimental results, key findings, and future perspectives.

1.2 Thesis structure

This thesis focuses on the exploration of novel triboelectric nanogenerator (TENG) systems for coastal region applications. Using a self-developed motor-driven testing platform, we investigated the relationship between ocean wave parameters (such as wave amplitude and frequency) and the output performance of the wave-driven TENG (WD-TENG). Additionally, we approve that the commercially simulation software, such as ANSYS AQWA, can be used to predict the dynamics of the TENG system under varying ocean wave conditions, including different wave frequencies and amplitudes. Moreover, a wireless, remotely controllable water wave generation system was developed, capable of producing wave amplitudes ranging from 1.5 cm to 7.1 cm at frequencies between 1 Hz and 2 Hz. The previously proposed WD-TENG was tested under these generated water waves, and the results revealed that its dynamic behaviours differ significantly from that observed on the motor-driven testing platform. This highlights the importance of testing ocean wavedriven TENG systems under realistic wave conditions. Additionally, we proposed a hybrid-mode TENG system, which combines a triboelectric nanogenerator (TENG) and an electromagnetic harvester (EMH), to function as a self-powered sensor for detecting variations in wave amplitude. A specifically designed power management system was developed, which not only enhances the output performance of both the TENG and EMH but also minimizes system failure caused by malfunctioning electronic components. Following that, we proposed another self-powered sensor system, referred to as the Active Impact Alert System (AIAS), designed for offshore wind turbine blades in response to the rapid development of offshore wind farms. This TENG-based system is capable of detecting various types of impacts, such as collisions from birds or bats, which may damage turbine blades and reduce the overall lifespan of the wind turbine. The Active Alert System can identify these impacts and generate electrical signals, accordingly, enabling organized maintenance and service scheduling to ensure the continued normal operation of the wind turbines. This work not only helps to deepen the understanding of the effects of water wave motion and parameters but also provides practical solutions for effectively utilizing the generated power for both wave energy harvesting and self-powered sensing applications. This thesis consists of 7 chapters: Introduction, Literature Review, Wave-Driven Triboelectric Nanogenerator (WD-TENG), Water Wave Generation System, Hybrid Mode Self-Powered Sensor and Active Impact Alert System for Wind Turbine Blades, and Conclusion & Prospects. Figure 1.2 used to explain the logic flowchart for this thesis and relationship between each chapter.

Chapter 2 presents a literature review on the development milestones of ocean wave energy-driven TENGs, focusing on their applications as blue energy harvesters and self-powered sensors. It also provides detailed analyses of several representative TENG designs. It emphasizes key aspects such as outer structure design, the selection of working modes (vertical contact-separation, single-electrode, lateral-sliding, and freestanding triboelectric-layer), and TENG types (solid-solid and solid-liquid). Furthermore, the hybrid-mode TENG, aimed at harvesting ocean wave energy, is also examined. The chapter highlights the significance of designing TENGs suitable for high-humidity and high-salinity marine environments. A well-designed outer structure can significantly enhance the overall lifespan of the system, while selecting the optimal working mode and TENG type can improve system responsiveness to low-frequency and low-amplitude wave conditions. Additionally, an analysis of the most widely used triboelectric material pairs is presented. Finally, the review identifies existing gaps and limitations in the development of ocean wave energy-driven TENGs and discusses potential solutions to address these challenges. This chapter has been accepted by *Advanced Energy and Sustainability Research* on 13 August 2025 and is currently awaiting online release. DOI: 10.1002/aesr.202500232.

Chapter 3 introduces a water wave generation system titled An Affordable Miniature 3D-Printed Wave Generator for Wave Energy Harvesting Applications. This system enables remote control of wave frequency and amplitude, making it a valuable test platform for evaluating the output performance of TENG systems. Which has had been published on Micromachines [36], Wang, Yunzhong, Damian Tohl, Anh Tran Tam Pham, and Youhong Tang. 2024. "Developing an Affordable Miniature 3D-Printed Wave Generator for Wave Energy Harvesting Application" *Micromachines* 15, no. 12: 1500. https://doi.org/10.3390/mi15121500.

Chapter 4 presents the wave-driven triboelectric nanogenerator (TENG) and its performance tested under various wave frequencies and amplitudes. The experimental results confirm that changes in wave amplitude significantly affect the output performance of ocean wave-driven TENGs. Additionally, the commercially available simulation software ANSYS AQWA was used and validated to predict the dynamics of wave-driven TENGs in ocean environments, offering valuable guidance for optimal device placement. Which has been published on Nano Energy [37]: Yunzhong Wang, Anh Tran Tam Pham, Xiangxi Han, Dongsheng Du, Youhong Tang, Design and evaluate the wave driven triboelectric nanogenerator under external wave parameters: Experiment and simulation, Nano Energy, Volume 93, 2022, 106844. https://doi.org/10.1016/j.nanoen.2021.106844.

Chapter 5 introduces a hybrid-mode self-powered wave sensing device capable of detecting low-amplitude waves. The sensor integrates an electromagnetic harvester (EMH) and a single-electrode TENG. The EMH serves as an auxiliary power source for both a self-powered indicator and potentially for wireless data transmission systems. Meanwhile, the single-electrode TENG functions as a self-powered sensor to monitor changes in wave amplitude. Experimental results demonstrate

that the sensor can detect wave amplitude variations as small as 0.5 cm. Which has been published on Device [38]: Yunzhong Wang, Huixin Zhu, Wenjin Xing, Damian Tohl, Youhong Tang, A hybrid self-powered wave sensing device enables low-amplitude wave sensing, Device, Volume 3, 2025, https://doi.org/10.1016/j.device.2024.100575

Chapter 6 presents an active alert system designed to detect impacts on offshore wind turbine blades. A single-electrode TENG is employed as a self-powered sensor to identify collisions caused by unexpected animals such as birds and bats. A wireless data transmission system is proposed to enable remote communication, allowing the electrical signals generated by the self-powered sensor to be transmitted to a remote endpoint (e.g., a laptop) for further processing and analysis. This application demonstrates significant potential for offshore wind turbine farms. Successful analysis of the generated electrical signals can support maintenance and repair planning, helping to ensure the reliable operation of the wind turbine systems.

Finally, **Chapter 7** include the conclusion and analysis of the research results collected during my Ph.D. period. Additionally, the problems encountered during the experimental stage will be discuss and outlines plans to solve these issues in the future. This structure provides a comprehensive overview of my Ph.D. thesis.

Chapter 1: WD-TENG Background and introduction The study successfully investigated the effect of both wave amplitude and wave frequency Introduce the background of the current electrical variations on the output performance. energy crisis, which is driven by strict environmental policies and increased demand due Provide a potential approach for employing to the entry into the electrification century. commercially available simulation software to Introduce the concept of ocean energy and its predict the dynamics of a TENG under ocean wave conditions. merits, as well as the limitations of current ocean energy harvesters, such as being bulky, heavier, and expensive to build. Introduce the triboelectric nanogenerator (TENG), Chapter 2: Wave generation system which shows great potential as a solution for The study successfully achieved wave generation harvesting ocean wave energy due to its unique with frequency variations from 1 Hz to 2 Hz and characteristics, such as being compact, wave amplitudes ranging from 1.5 cm to 7.1 cm. lightweight, and generating no carbon emissions during operation. The system successfully enabled remote control of wave frequency and amplitude adjustments via a Bluetooth module. Literature review Chapter 3: Hybrid mode wave sensor The study successfully achieved wave amplitude Analyses the advantages and disadvantages of variation detection with 0.5 cm scale. previously published ocean wave-driven TENGs, including solid-solid type, solid-liquid type, Owing to the hybrid mode concept, the EMH hybrid-mode TENGs, and self-powered sensors integrated into the wave sensor demonstrates the used in ocean conditions. capability to act as a self-indicator and has the potential to power additional electronic devices in Four assumptions are proposed regarding the the future. future development of ocean wave-driven TENGs: 1. Investigate whether variations in wave amplitude affect the output performance of ocean wave-driven TENGs. Chapter 4: Active impact detection 2. There is a lack of a scientific method to sensor accurately mimic water waves under The study successfully achieved the detection of laboratory conditions. impact from 1.5 J to 3.5 J. 3. Self-powered sensors can be used to monitor Owing to the unique working mechanism of TENG, wave parameters and vibrations around the this sensor can also be employed as rainfall coastline, as these parameters are essential sensor. for optimizing the placement of ocean wavedriven TENGs to maximize energy harvesting. Realise the measure data wireless transfer. 4. Self-powered sensors also can be used to detect bird impacts on offshore wind turbine blades, especially as offshore wind farms have become increasingly prominent in recent Conclusion and perspective Summaries achievements during this thesis. 5. Combining self-powered sensors with wireless List perspective of utilising TENG technology in data transfer is the future. ocean application.

Figure 1.2 The logic flowchart for this thesis and relationship between each chapter.

1.3 Reference

- [1] Atradius, Electronics/ICT Industry Trends June 2024, Atradius (2024).
- [2] Anna Fleck, Overconsumption: The Growing Desire for Ever More Devices, Statista (2024).
- [3] IEA.ORG, World electricity final consumption by sector, 1974-2019, (2021).
- [4] Australian Government, Climate Active, Climate Active Carbon Neutral Standard (2023). https://www.dcceew.gov.au/climate-change/climate-active (accessed December 2, 2023).
- [5] Australia Government, Net Zero, Department of Climate Change, Energy, the Environment and Water (2025).
- [6] M. Melikoglu, Current status and future of ocean energy sources: a global review, Ocean Engineering 148 (2018) 563–573. https://doi.org/10.1016/j.oceaneng.2017.11.045.
- [7] A. Khaligh, O.C. Onar, Energy harvesting, CRC Press, 2017.https://doi.org/10.1201/9781439815090.
- [8] A. Babarit, J. Hals, M.J. Muliawan, A. Kurniawan, T. Moan, J. Krokstad, Numerical benchmarking study of a selection of wave energy converters, Renew Energy 41 (2012) 44–63. https://doi.org/10.1016/j.renene.2011.10.002.
- [9] J.P. Kofoed, P. Frigaard, E. Friis-Madsen, H.Chr. Sørensen, Prototype testing of the wave energy converter wave dragon, Renew Energy 31 (2006) 181–189.

https://doi.org/10.1016/j.renene.2005.09.005.

- [10] F.-R. Fan, Z.-Q. Tian, Z. Lin Wang, Flexible triboelectric generator, Nano Energy 1 (2012) 328–334. https://doi.org/10.1016/j.nanoen.2012.01.004.
- [11] Z.L. Wang, T. Jiang, L. Xu, Toward the blue energy dream by triboelectric nanogenerator networks, Nano Energy 39 (2017) 9–23. https://doi.org/10.1016/j.nanoen.2017.06.035.
- [12] G. Zhu, B. Peng, J. Chen, Q. Jing, Z. Lin Wang, Triboelectric nanogenerators as a new energy technology: from fundamentals, devices, to applications, Nano Energy 14 (2015) 126–138. https://doi.org/10.1016/j.nanoen.2014.11.050.
- [13] S. Wang, L. Lin, Z.L. Wang, Triboelectric nanogenerators as self-powered active sensors, Nano Energy 11 (2015) 436–462. https://doi.org/10.1016/j.nanoen.2014.10.034.
- [14] L. Liu, Q. Shi, J.S. Ho, C. Lee, Study of thin film blue energy harvester based on triboelectric nanogenerator and seashore IoT applications, Nano Energy 66 (2019) 104167. https://doi.org/10.1016/j.nanoen.2019.104167.
- [15] Z. Wen, H. Guo, Y. Zi, M.-H. Yeh, X. Wang, J. Deng, J. Wang, S. Li, C. Hu, L. Zhu, Z.L. Wang, Harvesting broad frequency band blue energy by a triboelectric–electromagnetic hybrid nanogenerator, ACS Nano 10 (2016) 6526–6534. https://doi.org/10.1021/acsnano.6b03293.

[16] J. Shen, Z. Yang, Y. Yang, B. Yang, Y. Song, X. Cheng, Z. Lai, H. Zhao, L. Ji, Z. Zhu, J. Cheng, A remote monitoring system for wind speed and direction based on non-contact triboelectric nanogenerator, Nano Energy 133 (2025) 110453.

https://doi.org/10.1016/j.nanoen.2024.110453.

- [17] X. Wu, T. Cai, Q. Wu, J. Meng, W. Wang, W. Li, C. Hu, X. Zhang, D. Wang, Droplet-based triboelectric nanogenerators with needle electrodes for efficient water energy harvesting, ACS Appl Mater Interfaces 17 (2025) 13762–13772. https://doi.org/10.1021/acsami.4c17442.
- [18] N. Kumar Das, S. Badhulika, Recyclable waste derived green triboelectric nanogenerator for self-powered synthesis of defect-free graphene via mechano-electrochemical exfoliation, Chemical Engineering Journal 480 (2024) 147897. https://doi.org/10.1016/j.cej.2023.147897.
- [19] X. Pu, C. Zhang, Z.L. Wang, Triboelectric nanogenerators as wearable power sources and self-powered sensors, Natl Sci Rev 10 (2023) nwac170. https://doi.org/10.1093/nsr/nwac170.
- [20] Y. Zhou, M. Shen, X. Cui, Y. Shao, L. Li, Y. Zhang, Triboelectric nanogenerator based self-powered sensor for artificial intelligence, Nano Energy 84 (2021) 105887.

https://doi.org/10.1016/j.nanoen.2021.105887.

- [21] H. Wang, J. Wang, K. Yao, J. Fu, X. Xia, R. Zhang, J. Li, G. Xu, L. Wang, J. Yang, J. Lai, Y. Dai, Z. Zhang, A. Li, Y. Zhu, X. Yu, Z.L. Wang, Y. Zi, A paradigm shift fully self-powered long-distance wireless sensing solution enabled by discharge-induced displacement current, Sci Adv 7 (2025) eabi6751. https://doi.org/10.1126/sciadv.abi6751.
- [22] Z. Xi, H. Yu, H. Du, H. Yang, Y. Wang, M. Guan, Z. Wang, H. Wang, T. Du, M. Xu, High performance magnetic mass-enhanced triboelectric-electromagnetic hybrid vibration energy harvester enabling totally self-powered long-distance wireless sensing, Adv Mater Technol 9 (2024) 2400451. https://doi.org/10.1002/admt.202400451.
- [23] X. Yang, L. Xu, P. Lin, W. Zhong, Y. Bai, J. Luo, J. Chen, Z.L. Wang, Macroscopic self-assembly network of encapsulated high-performance triboelectric nanogenerators for water wave energy harvesting, Nano Energy 60 (2019) 404–412. https://doi.org/10.1016/j.nanoen.2019.03.054.
- [24] P. Cheng, H. Guo, Z. Wen, C. Zhang, X. Yin, X. Li, D. Liu, W. Song, X. Sun, J. Wang, Z.L. Wang, Largely enhanced triboelectric nanogenerator for efficient harvesting of water wave energy by soft contacted structure, Nano Energy 57 (2019) 432–439.

https://doi.org/10.1016/j.nanoen.2018.12.054.

[25] B.B. Zhang, Y. Chen, F. Wang, R.Y. Hong, Surface modification of carbon black for the reinforcement of polycarbonate/acrylonitrile—butadiene—styrene blends, Appl Surf Sci 351 (2015) 280–288. https://doi.org/10.1016/j.apsusc.2015.05.106.

- [26] K. Xia, J. Fu, Z. Xu, Multiple-frequency high-output triboelectric nanogenerator based on a water balloon for all-weather water wave energy harvesting, Adv Energy Mater 10 (2020) 2000426. https://doi.org/10.1002/aenm.202000426.
- [27] Q. Shi, H. Wang, H. Wu, C. Lee, Self-powered triboelectric nanogenerator buoy ball for applications ranging from environment monitoring to water wave energy farm, Nano Energy 40 (2017) 203–213. https://doi.org/10.1016/j.nanoen.2017.08.018.
- [28] X. Wang, S. Niu, Y. Yin, F. Yi, Z. You, Z.L. Wang, Triboelectric nanogenerator based on fully enclosed rolling spherical structure for harvesting low-frequency water wave energy, Adv Energy Mater 5 (2015) 1501467. https://doi.org/10.1002/aenm.201501467.
- [29] F. Shen, D. Zhang, Q. Zhang, Z. Li, H. Guo, Y. Gong, Y. Peng, Influence of temperature difference on performance of solid-liquid triboelectric nanogenerators, Nano Energy 99 (2022) 107431. https://doi.org/10.1016/j.nanoen.2022.107431.
- [30] S. Chen, E.W. Gill, W. Huang, A first-order HF radar cross-section model for mixed-path ionosphere—ocean propagation with an FMCW source, IEEE Journal of Oceanic Engineering 41 (2016) 982–992. https://doi.org/10.1109/JOE.2015.2505778.
- [31] J. Walsh, W. Huang, E. Gill, The first-order high frequency radar ocean surface cross section for an antenna on a floating platform, IEEE Trans Antennas Propag 58 (2010) 2994–3003. https://doi.org/10.1109/TAP.2010.2052559.
- [32] M. Xu, S. Wang, S.L. Zhang, W. Ding, P.T. Kien, C. Wang, Z. Li, X. Pan, Z.L. Wang, A highly-sensitive wave sensor based on liquid-solid interfacing triboelectric nanogenerator for smart marine equipment, Nano Energy 57 (2019) 574–580. https://doi.org/10.1016/j.nanoen.2018.12.041.
- [33] C. Zhang, L. Liu, L. Zhou, X. Yin, X. Wei, Y. Hu, Y. Liu, S. Chen, J. Wang, Z.L. Wang, Self-powered sensor for quantifying ocean surface water waves based on triboelectric nanogenerator, ACS Nano 14 (2020) 7092–7100. https://doi.org/10.1021/acsnano.0c01827.
- [34] S.P. Beeby, R.N. Torah, M.J. Tudor, P. Glynne-Jones, T. O'Donnell, C.R. Saha, S. Roy, A micro electromagnetic generator for vibration energy harvesting, Journal of Micromechanics and Microengineering 17 (2007) 1257–1265. https://doi.org/10.1088/0960-1317/17/7/007.
- [35] Ö. Zorlu, H. Külah, A MEMS-based energy harvester for generating energy from non-resonant environmental vibrations, Sens Actuators A Phys 202 (2013) 124–134.
- https://doi.org/10.1016/j.sna.2013.01.032.
- [36] Y. Wang, A.T.T. Pham, X. Han, D. Du, Y. Tang, Design and evaluate the wave driven-triboelectric nanogenerator under external wave parameters: experiment and simulation, Nano Energy 93 (2022) 106844. https://doi.org/10.1016/j.nanoen.2021.106844.

[37] Y. Wang, D. Tohl, A. T. T. Pham, & Y. Tang, Developing an affordable miniature 3D-printed wave generator for wave energy harvesting application. Micromachines *15*(12) (2024). https://doi.org/10.3390/mi15121500

[38] Y. Wang, H. Zhu, W. Xing, D. Tohl, Y. Tang, A hybrid self-powered wave sensing device enables low-amplitude wave sensing, Device 3 (2025).

https://doi.org/10.1016/j.device.2024.100575.

CHAPTER 2 LITERATURE REVIEW

This chapter has been accepted and published by *Advanced Energy and Sustainability Research* with DOI: 10.1002/aesr.202500232. **Yunzhong Wang**: Reference collection, Figure plotting, First draft.

2.1 Milestones of development of ocean wave energy driven TENG

Since TENGs were first introduced to the public in 2012, 13 years of development have demonstrated their ability to serve as auxiliary power sources for extending battery life and as self-powered sensors, highlighting their rapid advancement and significant potential for ocean applications. As a new form of renewable energy generation, TENGs hold great promise for harvesting ocean energy as renewable energy generators or functioning as self-powered sensors to monitor and collect oceanic spectrum data. Notably, when considering deployment in ocean environments, key factors such as waterproof capability, internal volume, and responsiveness to low wave frequencies and amplitudes become critically important. Some of the previously published, unique, and distinctive ocean wave energy-driven TENG designs are highlighted as milestones in the timeline, shown in Figure 2.1.

According to Figure 2.1, solid-solid type ocean wave driven TENGs have undergone ten years of development with various outer shape designs. In 2015, the spherical-shaped TENG was proposed, demonstrating an exceptional ability to respond to minimal wave frequencies, meaning it can be activated even at relatively low frequencies. However, the internal volume is limited to the spherical shape led to less triboelectric material placement inside the spherical shape TENGs. Therefore, a cubic-shaped TENG was proposed in 2017. Its internal volume is considerably more spacious than that of the spherical design. However, for the same external volume, the cubic geometry provides less contact with water, so a larger input wave is required to activate it. Consequently, the cubic-shaped TENG is less effective at harvesting low-frequency, low-amplitude wave energy than the spherical design. In 2019, the cylindrical-shaped TENG was proposed. This design offers a more spacious internal volume than the spherical TENG while also providing better responsiveness to low-frequency and low-amplitude waves compared to cubic-shaped TENGs. Therefore, the cylindrical design strikes a balance between internal space and sensitivity to wave frequency and amplitude. Apart from these, several uniquely designed TENG shapes have also been reported, such as the seesaw structure [1,2] and gyroscope structure [3]. Those unique shape TENGs have their own advantages and disadvantages. Various outer geometries listed above aiming to achieve low response frequencies and providing large internal areas for triboelectric material placement.

Additionally, solid-liquid type TENGs have been developed in recent years, utilizing a single solid triboelectric material in conjunction with water droplets, such as rain or seawater, to generate

electricity. Typically, solid–liquid TENGs operate directly with water droplets. However, some designs use an additional energy source, such as gas flow, as an auxiliary input to accelerate the contact and separation process between the solid triboelectric material and the water droplets in order to enhance the output performance [4,5]. Furthermore, hybrid concept TENG that combine TENG with electromagnetic harvesters (EMHs) have been proposed to overcome the limitation of TENGs' micro-ampere-level output current. Hybrid mode TENGs demonstrate significant capability by successfully combining the advantages of both EMH and TENGs, while also minimising their respective limitations. Moreover, the hybrid mode demonstrates promising potential for practical applications, where the EMH can serve as a power source for wireless data transmission systems, while the TENG functions as a self-powered sensor for detecting wave motion.

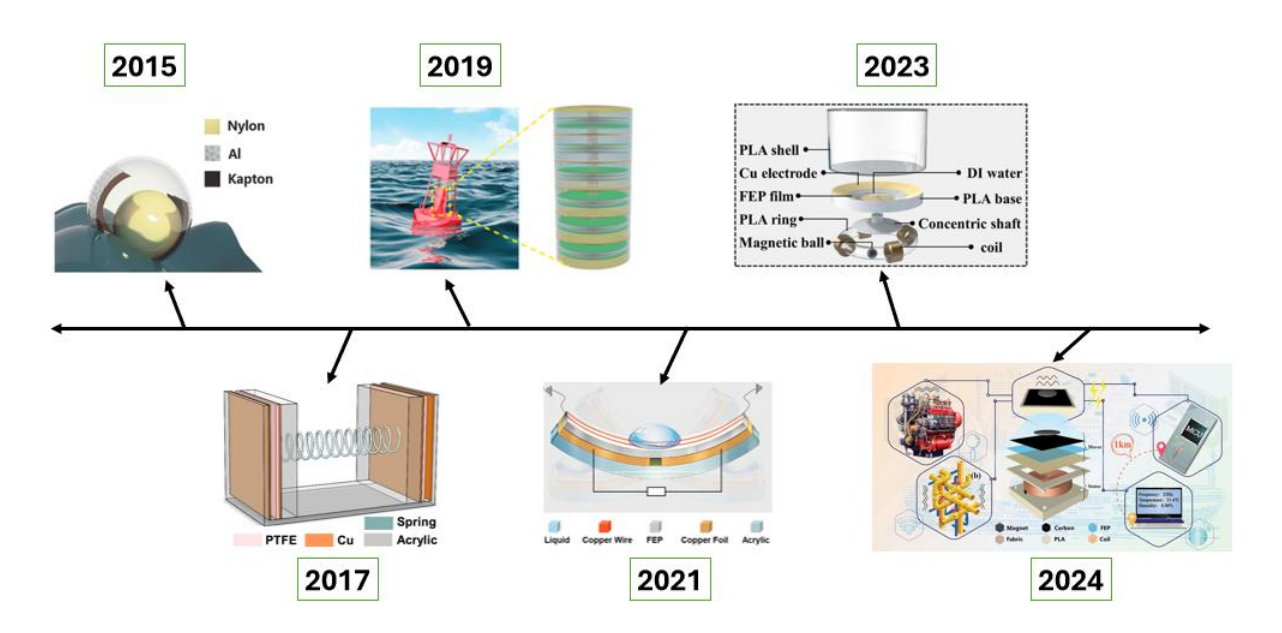


Figure 2.1 The key milestones of ocean wave energy driven TENGs from 2015 to 2024. The development of ocean wave energy-driven TENGs has undergone multiple stages of evolution, particularly in the design of their outer structures, with the goal of more efficiently utilizing ocean wave motion. Various types of TENGs have also been developed such as solid–liquid TENGs, which aim to harvest more available energy from the natural environment, and hybrid-mode TENGs, which combine electromagnetic harvesters (EMHs) to compensate for the low current output of TENGs. In the future, integrating TENG devices with wireless data transmission systems will be a key direction, unlocking greater potential for real-world applications [7], [14], [17], [29], [38], and [55].

2.2 Ocean wave energy harvesting as a renewable energy generator and self-powered sensor.

In 2014, Tollefson introduced the concept of "blue energy," which refers to the energy harnessed from the ocean. This includes two main sources of energy: shifting tides and the motion of ocean waves [6]. For ocean wave energy harvesting, this section will review key research on ocean wave energy generator based on TENGs. The advantages and disadvantages of these approaches will be summarised, highlighting key areas for future research and development.

2.2.1 Solid - solid TENG

The solid-solid structure TENG is the most traditional outer design for ocean wave driven TENGs. This configuration typically features a rigid outer shell, primarily designed to meet waterproofing requirements for operation in ocean environments. In this section, several typical solid-solid TENG structures and shapes will be introduced, including spherical, cubic, and cylindrical designs.

In 2015, Wang et al. designed and fabricated a spherical-shaped TENG to harvest ocean wave energy. It features a spherical outer shell with an aluminium (AI) film placed on the inner surface and a nylon ball inside the shell, as depicted in Figure 2.2(A). When driven by ocean waves, the nylon ball contacts the AI film, generating electrical energy. This TENG operates efficiently within a frequency range of 1.23 Hz to 1.55 Hz, producing a stable and repeatable waveform. Additionally, it can generate a maximum instantaneous short-circuit current of 1.2 µA and achieve an instantaneous output power density of 10 mW. However, the limited contact area between the AI film and the nylon ball reduces the efficiency of energy conversion and the material utilisation rate (UR) in order lead to low output performance [7].

In 2018, Xu et al. introduced an innovative approach to enhance the output performance of the spherical TENG by replacing the previously relatively hard nylon ball with a soft silicone rubber ball to increase the contact area between triboelectric materials lead to high output performance, as depicted in Figure 2.2(B). As a result, the maximum instantaneous short-circuit current reached 3.25 µA, which is approximately three times higher than Wang's research results in 2015 [7]. This modification aimed to improve contact area between two triboelectric materials and enhanced the surface charge density of triboelectric material to increase the overall energy conversion performance [8].

In 2019, Cheng et al. introduced a more flexible silicon rubber ball. Compared to Wang's design and Xu's design, this design exhibited exceptional flexibility, allowing for a greater contact area, as shown in Figure 2.2(C) and (E). As a result, this prototype achieved a maximum charge transfer of 500 nC, significantly surpassing the previous works of Wang's and Xu's design, which demonstrated maximum charge transfers of 20 nC and 100 nC, respectively [9]. The robustness of the silicone rubber is a major concern for this design. It is uncertain whether the liquid inside the silicone rubber

ball will leak after prolonged operation. If leakage occurs and the liquid comes into contact with the copper electrode, it could lead to device failure. Additionally, the spherical design makes the device difficult to repair.

In 2019, Yang et al. introduced a spherical-shaped TENG composed of multiple small sections, each containing a small ball that functions as an individual TENG unit as shown in Figure 2.2(D). Due to its unique and innovative structure, this prototype maximises energy conversion efficiency since all TENGs will generate electrical energy once the device has been activated by external force. As the result, it can generate a maximum short-circuit current of 10 μ A, which is approximately three times higher than Xu's prototype [10]. In addition, a spherical eccentric-structured TENG, which modified from the spherical-shaped TENG was introduced in 2022. This design features a complex internal structure, integrating 12 rotational TENG units within a polyhedral shell. Based on experimental results, this polyhedral TENG achieved a maximum output power density of 0.22 W/m², with a peak output voltage of 18.4 V and a maximum output current of 0.49 μ A under 2 Hz wave frequency [11]. However, the overly complex internal structure makes repair and maintenance challenging. There is also concern about whether the overall output performance remains stable if several TENG units fail.

TENGs with a spherical shape exhibit notable responsiveness to ocean wave motion and can significantly reduce the minimum activation frequency required for operation. However, they are limited by complex fabrication, challenging maintenance after prolonged operation, and a low material UR. The previous designs primarily focus on improving power output by optimising the flexibility of the internal ball, followed by enhancing the surface charge density of the triboelectric materials, which emphasises the important of high utilization rate of triboelectric materials. Additionally, Yang's design provides a unique design concept, which utilise magnet to realise matrix connection.

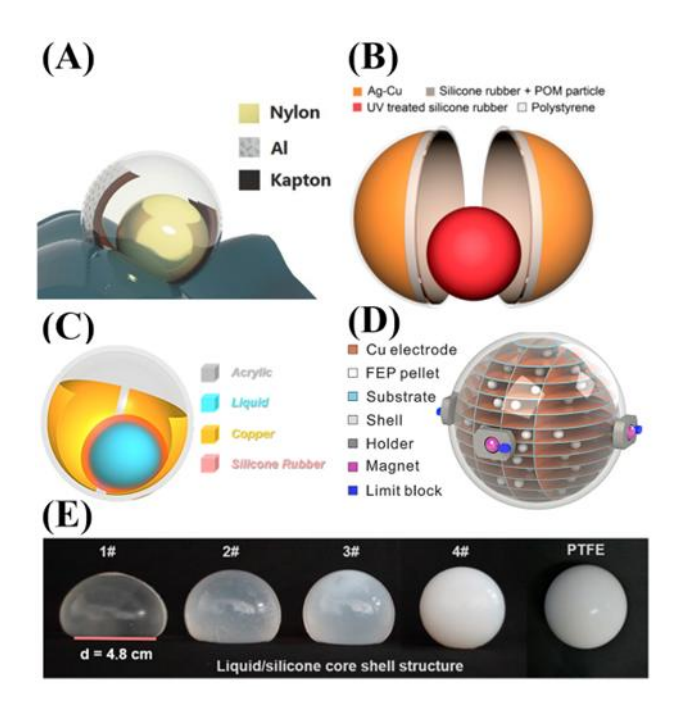


Figure 2.2 Schematic structure of the spherical ocean wave-driven TENG (A) Spherical TENG [7], (B) Spherical TENG with silicone base material [8], (C) Soft-contact spherical triboelectric nanogenerator (SS-TENG) [9], (D) Self-assembly TENG network, and (E) Liquid/silicone core shell structure of SS-TENG [10].

In 2015, Jiang et al. introduced a fully enclosed, well-sealed cube-shaped TENG as shown in Figure 2.3(A). This design involving four wavy-structured contact-separation TENGs inside, positioned on each inner walls of the cubic box. Fluorinated ethylene propylene (FEP) and Kapton were employed as the triboelectric materials in this prototype. A metal ball was placed at the centre of the box, serving as the input kinetic energy donor to convert ocean wave motion to kinetic energy. When the device actuated by incoming waves, the metal ball moved freely inside the box, periodically contacting with the wavy-structured TENGs. This impact caused the triboelectric materials to contact and separation, generating electrical energy. As a result, this prototype can deliver a maximum short-circuit current of approximately 100 μ A and a maximum power density of 3.4 mW at 2 Hz. The integrated wavy structure successfully enhanced energy transfer efficiency [12]. However, the durability of the triboelectric materials remains a concern, as the elasticity of FEP and Kapton tends to degrade after prolonged operation, reducing performance over time. Moreover, the energy generation is not easily controllable, as the metal balls move freely within the device.

In 2017, Xu et al. introduced an integrated TENG based on an air-driven structure as shown in Figure 2.3(B). This design utilises air pressure generated by ocean wave motion to drive the internal triboelectric material, inducing relative movement and generating electrical energy. Unlike most ocean wave-driven TENGs that directly utilises the kinetic energy from ocean wave motion, this prototype employs a unique internal spring-levitated oscillator structure, providing an innovative energy conversion mechanism. As the result, this TENG can deliver a maximum 187 µA short-circuit

current at 2.9 Hz [13]. Xu's design faces the same issue as Jiang's design, the elasticity of the triboelectric material degrades over long period operation, leading to an unexpected decline in output performance.

In 2017, Jiang et al. introduced a vertical contact-separation mode ocean wave-driven TENG with a cubic exterior as shown in Figure 2.3(C). Two TENG units were placed at both ends of the cube, utilising polytetrafluoroethylene (PTFE) and copper as triboelectric materials. Additionally, two rectangular modules were positioned in the middle of the cube, connected by a spring. When the cube activated by an incoming wave, the internal rectangular modules were triggered, additionally, the metal spring is starting to store mechanical energy. This stored energy was then released in the next cycle, effectively enhancing the overall output performance of the TENG. As a result, this prototype can provide a maximum power output of 5.38 mW at approximately 4.75 Hz. By employed the spring, the energy conversion efficiency has been enhanced by 150.3% [14]. This design successfully increased the input kinetic energy level by utilising a spring as an energy storage component. However, the elasticity of the spring will degrade over time, leading to mechanical fatigue. This deterioration can cause an unexpected instantaneous drop in the output performance of the TENG.

In 2018, Xiao et al. introduced an enhanced version of the spring-assisted TENG with improved output performance as shown in Figure 2.3(D). This version utilised a high-performance silicone-based artificial triboelectric material to replace the previous copper sheet. The benefit of using silicone as the triboelectric material is that its flexibility allows for increased contact area, which enhances charge transfer and improves the triboelectric charge density on the material surfaces. The enhanced TENG achieved a significant increase in output power density, rising from 0.7265 W/m³ to 2.40 W/m³, approximately tripling its energy harvesting capability [15]. Overall, the cube-shaped TENG is relatively easy to fabricate and effectively increases the UR of triboelectric materials. However, it remains bulky, requiring a high wave amplitude and a frequency range of 2.00 Hz to 4.75 Hz to be activated.

The cube-shaped TENG is not ideal for floating applications due to its flat side surfaces. This design requires long side lengths to provide sufficient contact area, ensuring the TENG remains afloat on the water surface. However, the cubic shape improves the UR of triboelectric materials compared to spherical designs. Additionally, incorporating elastic materials in the internal structure can enhance the ability to absorb and store kinetic energy. Nevertheless, the output performance may fluctuate unexpectedly if the elastic material fails.

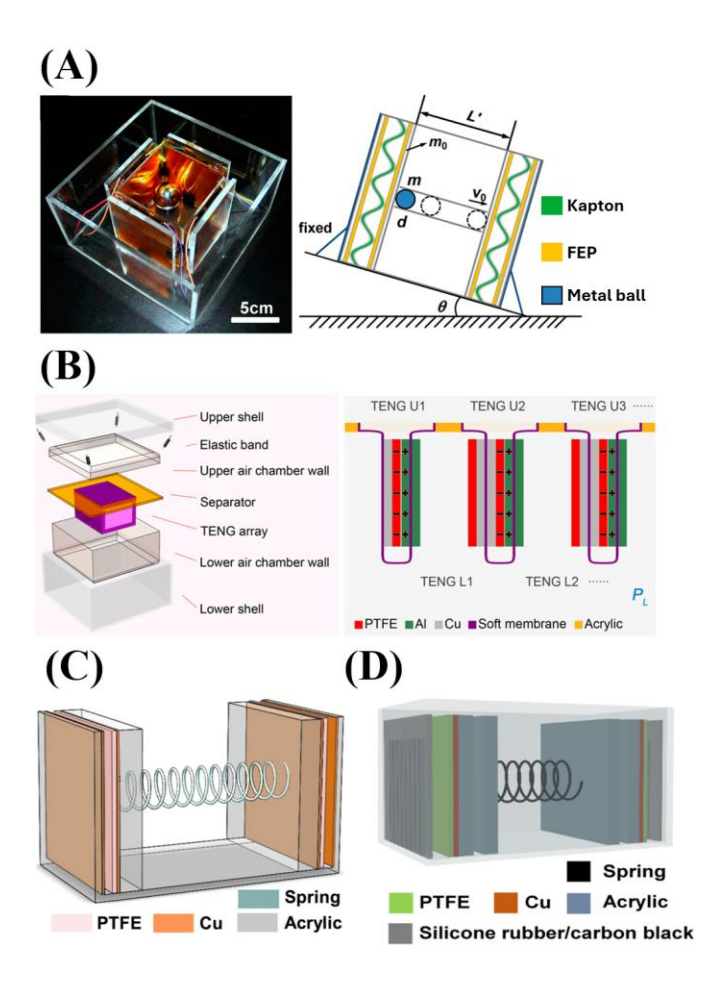


Figure 2.3 Schematic structure of the cubic ocean wave-driven TENG (A) Integrated four contact and separation wavy-structured TENGs inside a cube shape exterior [12], (B) Air-driven membrane structures TENG [13], (C) Spring-assisted TENG based on the contact and separation mode [14], and (D) Spring-assisted TENG with enhanced output performance by applied ordinary material [15].

In 2019, Bai et al. introduced a tandem disk triboelectric nanogenerator (TD-TENG) with a cylindrical exterior, based on the rotation mode. This design adopts a multi-unit structure, consisting of four TENGs within a single prototype as shown in Figure 2.4(A). It utilises PTFE and Cu as the triboelectric material pair. Bai's design is inspired by the automatic winding system of mechanical watches, optimising internal space utilization. This design delivers 299 µA at 1.5 Hz with a 60 mm wave amplitude. Additionally, the TD-TENG provides a maximum power density of 7.5 mW and can be activated at a minimum frequency of 0.75 Hz, which is significantly lower than that required for cube-shaped TENGs [16]. Bai's design successfully demonstrates the effective wave response capability of the cylindrical shape. It maximises internal space utilisation and can be triggered by a minimum wave amplitude of 10 mm.

In 2019, Xi et al. introduced a TENG with a cylindrical shape based on the contact and separation mode, as shown in Figure 2.4(B). However, this design incorporates multiple TENG units inside the cylinder. The up-and-down wave motion causes changes in the centre of gravity, facilitating the movement between the triboelectric materials. This prototype utilised FEP and Cu as triboelectric

materials. As a result, it achieved a maximum power density of 13.2 mW/m². However, its overall output power performance did not overcome that of Bai's TENG. It is worth noting that adding more TENG units inside the cylinder significantly increased the total weight of the device, requiring more input energy. Consequently, the response frequency increased to 2 Hz [17]. Therefore, finding the balance between the TENGs and the minimal response frequency of the device is crucial.

In 2019, Xu et al. introduced a capsule-shaped TENG based on the freestanding mode. This TENG is fixed in position by a mooring system at the bottom of the capsule, as shown in Figure 2.4(C). This design features a multilayer structure inside the capsule. The triboelectric materials used in this prototype are PTFE balls and a Nylon sheet. The energy generation mechanism relies on wave motion inducing the movement of PTFE balls, which then interact with the Nylon sheet to generate electrical energy. As a result, this TENG achieved an impressive maximum power density of 10.6 W/m³ at 2.4 Hz with 120 mm wave amplitude. Additionally, it can be activated at a minimum frequency of 0.8 Hz with a wave amplitude of 90 mm [18]. Mooring system effectively limited the unexpected moving of the TENG, maximise the UR of ocean wave motion.

In 2022, Yuan et al. introduced an anaconda-shaped multi-layered triboelectric nanogenerator (ASM-TENG) as shown in Figure 2.4(D). The triboelectric materials used are FEP and conductive fibre, with the conductive fibre also serving as the electrode. These two materials are placed on a helical TPU structure, which acts as the supporting framework. Due to the choice of materials, the entire TENG is flexible. There is a load in the middle; when the ASM-TENG faces incoming waves, the load slides to the other end due to gravitational force, enabling contact and separation between the triboelectric materials to induce electrical energy. Based on experimental results, the ASM-TENG can generate a maximum output voltage of 820 V and a current of 0.6 mA. Moreover, this generator can deliver a maximum peak power density of 80.6 W/m³ with a 1 G Ω load resistor. While this design provides notable output power density, the durability of the flexible components remains a major concern [19].

Compared to Xi's 2019 design, Yuan's design significantly improved the utilization rate of input kinetic energy by replacing the coil spring structure with fully flexible triboelectric materials. Moreover, several specialized cylindrical-shaped TENGs have been developed from the conventional cylindrical design to accommodate more TENG units and enhance overall energy conversion efficiency or enhance overall sensitivity to the input wave. For example, Tan et al. introduced an elliptical cylindrical shape TENG in 2022 which integrated two working mode TENG, one linear sliding mode and four contact and separate mode. Based on the experiment result, this elliptical cylindrical shape TENG can provide rated power at 1 Hz [20].

Through the analysis of cylindrical-shaped TENGs, we can conclude that they have a much lower activation frequency compared to cubic shaped TENGs and are comparable to spherical-shaped TENGs. Additionally, cylindrical TENGs are easier to fabricate than spherical TENGs, while also

provide ample internal space for placing triboelectric materials or incorporating more complex structures to increase the UR of triboelectric materials. In summary, the current development of solid-solid type ocean wave-driven TENGs focuses on enhancing output performance by selecting high charge density triboelectric materials, integrating multiple TENGs into a single energy harvesting system, and optimising the external structure's shape for improved efficiency.

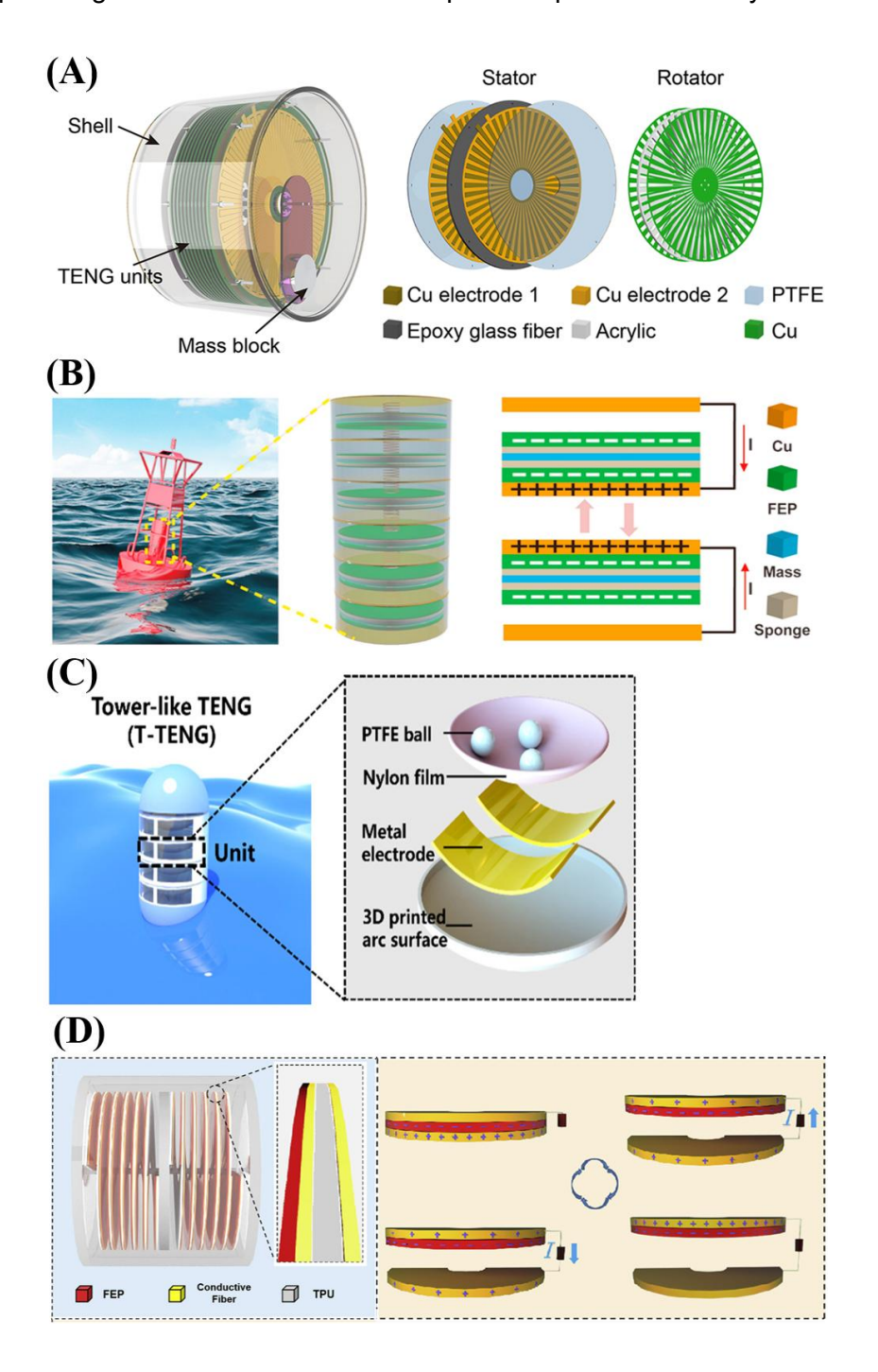


Figure 2.4 Schematic structure of the cylindrical ocean wave-driven TENG (A) Tandem disk triboelectric nanogenerator based on the rotational mode (TD-TENG) [16], (B) Multilayered rotational mode TENG for ocean wave energy harvesting [17], (C) Tower-like TENG based on the freestanding mode (T-TENG) [18], and (D) Anaconda-shaped spiral multi-layered triboelectric nanogenerators (ASM-TENG) [19].

Table 2.1 Summary of previously published solid-solid type triboelectric nanogenerators

Ref	Structure	Tribo-material	Electrode	Open- circuit voltage	Short- circuit current	Power density /power
[7]	Freestanding	Nylon	Kapton	12000 V	1.2 µA	≈ 10 mW
		PTFE	Al		≈ 0.6 µA	≈ 1 mW
[8]	Freestanding	Silicon rubber + POM particle / UV treated silicone rubber	Ag - Cu	1020 V	34.5 μA	0.71 W m ³
[9]	Freestanding	Silicon rubber	Cu	1.6 kV	5 μΑ	1.2 mW
[10]	Freestanding	FEP/ Cu	Cu	5 kV	5 μΑ	2.05 W m
[11]	Rotational	FEP/ Al	Al	18.4 V	0.49 μΑ	0.22 mW/m²
[12]	Contact and separation	FEP / Kapton	Cu	≈ 6 kV	100 μΑ	3.4 mW
[13]	Contact and separation	PTFE / Al	Cu	610 V	187 μΑ	13.23 W m ³
[14]	Contact and separation	PTFE / Cu	Cu	458.3 V	45.8 µA	726.48 m W/m³
[15]	Contact and separation	PTFE / Cu	Cu	630.7 V	22.3 µA	2.4 W m ³
[16]	Linear sliding	PTFE / Cu	Cu	365 V	8 μΑ	7.3 W m ³
[17]	Contact and separation	FEP / Cu	Cu	250 V	3 μΑ	13.2 mW /m ²
[18]	Contact and separation	PTFE / Nylon	Cu	105 V	1.3 µA	10.6 W/m³
[19]	Contact and separation	FEP/Conductive fibre	Conductive fibre	820V	0.6 mA	80.6 W/m³
[20]	Contact and separation / linear sliding	PTFE & Nylon film / PTFE & Al	AI / Conductive ink	460 V	22 μΑ	8.3 mW
[21]	Contact and separation	PTFE / Cu particle	Cu	124 V	0.97 μΑ	0.91 W m
[22]	Contact and separation	FEP / AI	Cu	420 V	80 μΑ	6.79 mW
[23]	Linear sliding	FEP / Al	Al	1.2 kV	16 µA	6.6 W m ³

[24]	Freestanding	PPCF (PTFE, PDMS, PVDF) / Nylon	Cu	~220 V	~1.1 µA	4 W/m ³
[25]	Freestanding	FEP	Cu	440 V	70 μA	45.18 m W kg ⁻¹
[26]	Linear sliding	PTFE / Nylon	Au	126.63 V	5.77 μA	0.481 W/m ²
[27]	Contact and separation	PTFE / Al	Au	333.67 V	25.07 μΑ	1.21 W/ m ²

2.2.2 Solid - liquid TENG

A solid-liquid TENG uses water as one of the triboelectric materials, operating with a conventional material from the triboelectric material series. Typically, solid-liquid TENGs function based on the contact and separation mode. This design offers significant advantages, particularly by eliminating the need for additional triboelectric materials. Furthermore, water is an abundant natural resource, easily sourced from the environment, including saline water, raindrops, and steam. Therefore, utilising a solid-liquid design can reduce material waste during the fabrication of TENGs and allow for a TENG with double the volume at the same material cost compared to solid-solid type TENGs.

In 2018, Zhao et al. introduced a networked integrated TENG (NI-TENG) with a size of 70 mm². This device can provide a stable output current of 13.5 µA and a power density of 1.03 mW under 120 mm wave amplitude, while generating a maximum output voltage of 300 V. The TENG utilizes PTFE as the triboelectric material and employs Kapton as the substrate instead of glass due to its excellent chemical stability and elasticity, as shown in Figure 2.5(A) [28]. The P-N type rectifier serves as the connection bridge between each TENG's output and the generator's overall output pin. Additionally, these P-N type rectifiers function as AC-to-DC converters. As a result, the generator produces a DC output voltage instead of the AC voltage typically generated by TENGs. This enables the output voltage to directly power external electronic devices. The integrated design TENG introduces a novel concept by combining multi-layer connections with rectification.

Water has a significant impact on the lifespan and output performance of all ocean wave energy generators. Seawater can corrode the triboelectric materials and cause short circuits in the internal circuitry of the TENG due to the entry of water vapor into the metal electrodes. To address this challenge, in 2021, Wei et al. introduced an all-weather droplet-based TENG (DB-TENG) as shown in Figure 2.5(B). The non-packaged DB-TENG demonstrates the ability to operate under harsh environmental conditions, such as high humidity and high concentrations of salt, acid, or alkaline solutions. This design offers improved reliability and reduced maintenance costs in such challenging environments. FEP and Al are employed as triboelectric material and electrode, respectively. The

authors emphasised that waterproofing is a major challenge for solid-liquid TENGs. In Wei's design, a curved substrate was introduced to ensure that water droplets slide along the curved FEP surface, enabling all-weather energy harvesting. As a result, this TENG can achieve a maximum rated power of 23.3 µW [29]. However, the authors did not provide evidence of robustness testing.

In 2024, Zheng et al. introduced an ocean water droplet energy generator utilising FEP as the triboelectric material as shown in Figure 2.5(C). As a result, this TENG can deliver a maximum output voltage of 700 V and a transferred charge of 5 μ C under a 1 Hz frequency with deionised (DI) water. Additionally, the authors tested the TENG using saline water, achieving a maximum charge transfer of 2.5 μ A and an instantaneous current of 2 mA, making it more suitable for ocean operation conditions. This design also demonstrates the capability to function as a self-powered sensor for detecting changes in wave amplitude. Apart from it, this TENG can also function as a seawater purification system, with experimental results demonstrating its ability to purify saline water continuously for 6 hours [30].

In summary, solid-liquid type TENGs are more suitable for use as self-powered sensors rather than renewable energy generators due to their relevant low output performance and the uncertain lifespan of triboelectric materials. Seawater can corrode these materials, affecting long-term output performance. Moreover, the issue of biofouling, such as the accumulation of algae and barnacles on solid-liquid TENGs, also needs to be considered. Increased biofouling on the contact surface of the triboelectric material leads to reduced output performance due to a decrease in effective contact area and the non-conductive nature of the fouling organisms. Therefore, improving the waterproofing of triboelectric materials is crucial for enhancing the durability and reliability of solid-liquid type TENGs.

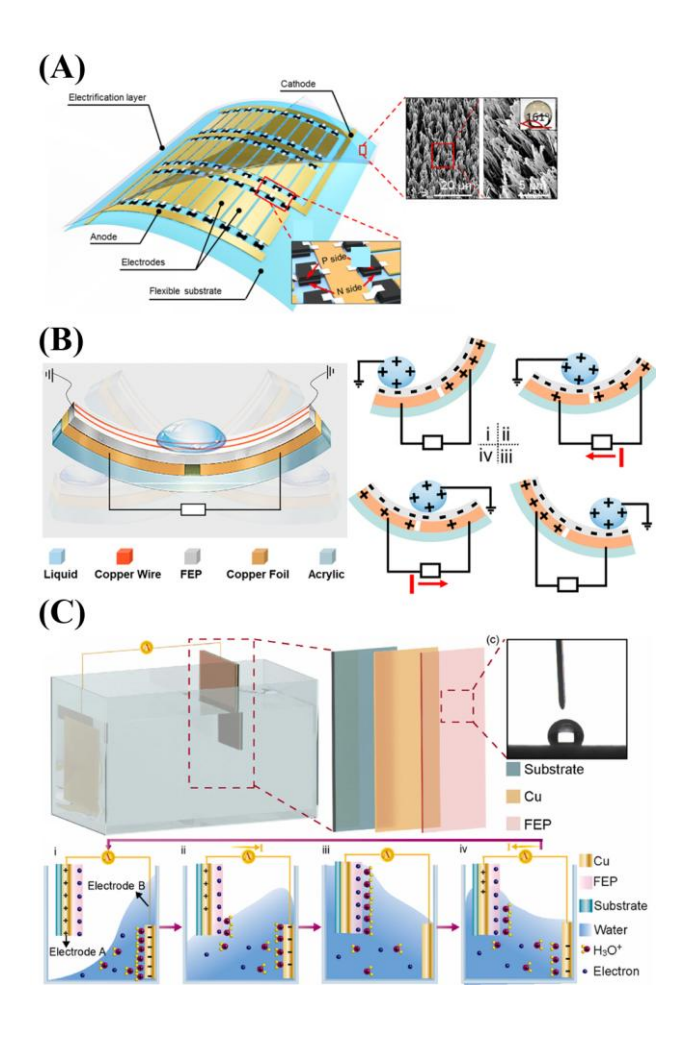


Figure 2.5 Schematic structure of the water wave solid-liquid TENG (A) Networked integrated triboelectric nanogenerator (NI-TENG) [28], (B) Droplet-based (DB)-TENG [29], and (C) Solid-liquid contact-based saline water TENG [30].

Table 2.2 Summary of previously published solid-liquid type triboelectric nanogenerators

Ref	Structure	Tribo- material	Electrode	Open- circuit voltage	Short-circuit current	Power density /power
[28]	Contact and separation	PTFE / Kapton	Conductive textile	300 V	13.5 µA	1.03 mW
[29]	Contact and separation	FEP	Cu	58.0 V	40.0 nA	23.3 μW
[30]	Contact and separation	FEP	Cu	700 V	2 mA	65 mW m ²
[31]	Contact and separation	PTFE	Steel	52 V	40.0 nA	N/A
[32]	Contact and separation	FEP	Al	283.1 V	10.8 μΑ	1.51 mW
[33]	Contact and separation	PTFE	Cu	563 V	4.76 mA	N/A

2.2.3 Hybrid mode TENG

Researchers have faced a significant challenge, i.e., the microampere-level output current of TENGs. This low current output is insufficient for real-time activation of electronic devices, requiring a TENG to charge a supercapacitor for several minutes before triggering an electronic device. To address this limitation, research groups worldwide have been working to enhance the output current level. For instance, surface modification approaches have been applied to increase surface charge density and contact area. As a result, the output of TENGs has improved from a few microamps to hundreds of microamps. However, this is still insufficient to directly power electronic devices. In comparison, conventional electromagnetic generators (EMGs), based on the electromagnetic induction phenomenon, have been developed nearly two centuries since their discovery in 1831. Conventional EMGs are limited by their bulky size, making them difficult to operate under low-input kinetic energy conditions. To overcome this issue, researchers have developed a new type of EMG, known as the electromagnetic harvester (EMH). EMHs typically operate in two modes: the magnet is fixed while the copper coil moves, and the coil remains stationary while the magnet moves [34,35]. This idea has inspired researchers focusing on TENGs. In recent years, they have combined EMHs with TENGs to harvest ocean energy more efficiently. By integrating these two mechanisms, hybrid energy generator can take advantage of TENGs' high voltage output at low frequency and milliampere level output current from EMHs. This combination enhances overall energy conversion efficiency and brings ocean wave energy harvesting close to practical applications.

In 2020, Wu et al. introduced a hybrid ocean wave energy generator inspired by a teeterboard mechanism. This system combines a free-standing rolling mode TENG and an EMH, each positioned at opposite ends of the teeterboard as shown in Figure 2.6(A). Al and PTFE employed as triboelectric materials in this design. When an incoming ocean wave impacts one side of the device, the TENG generates electrical energy by the input ocean wave kinetic energy, which caused Al tube rolling inside to realise relevant movement between triboelectric materials. While the EMH simultaneously induces electrical energy through piston-like motion between the copper coil and magnet. As the result, this hybrid generator achieves an output of 760 V on the TENG side and a maximum current of 10 mA on the EMH side. This prototype marks a significant improvement in the total current output, increasing from the microampere range to the milliampere range. However, a major disadvantage of this design is its bulky size and the lack of integration between the two generators, which function as separate components rather than a unified system [36].

In2022, Sun et al. introduced a tube-shaped hybrid-mode ocean wave energy generator that incorporated both a solid-liquid TENG and an EMH. FEP and DI water were used as the triboelectric materials as shown in Figure 2.6(B) [37]. The EMH consists of a cylindrical-shaped magnet and two copper windings, each with 6000 turns. A cylindrical magnet was placed inside the tube, floating on the DI water, which significantly reduced the friction force between the magnet and the FEP surface. However, the addition of DI water inside the tube increased the overall weight of the system, thereby

requiring high input energy for efficient operation. As a result, the TENG in this prototype produced a lower output voltage (approximately 300 V) compared to Wu's design [36]. The EMH side demonstrated a significant improvement, delivering an output current approximately three times higher than Wu's prototype in 2020, reaching about 30 mA due to the double EMH design. The most innovative aspect of this study was the integration of the EMH and TENG into a single unified system, rather than keeping them as separate components. However, the copper coil is placed on the exterior of the generator, exposure to water can lead to corrosion of the copper windings. This design cannot float on the ocean surface due to the externally placed copper coil windings.

In 2023, Xu et al. introduced a cylinder-shaped hybrid mode ocean wave energy generator. The TENG adopted a solid-liquid type, employing FEP and DI water as triboelectric materials as shown in Figure 2.6(C). On the EMH side, a spherical magnet was placed inside a polylactic acid (PLA) ring, with four sets of copper coils positioned around the outer surface of the PLA ring. A key concern was the electromagnetic permeability of PLA, which could impact the output performance of the EMH. As a result, the output voltage of the TENG in this prototype was similar to Sun's design, reaching approximately 300 V due to the use of the same coupling of triboelectric materials. Additionally, the output current of the EMH was lower than expected which is approximately maximum 10 mA [38]. Sun's prototype featured two copper coils, each with 6,000 turns, totalling 12,000 turns. In contrast, Xu's prototype employed four copper coils, each with 4,300 turns, for a total of 17,200 turns. Based on the Lenz's Law, as shown in Equation (2.1), increasing the number of coil turns should theoretically enhance the induced current. However, the use of PLA as the structural material may have impeded the efficiency of electromagnetic flux transfer between the magnet and the copper windings.

$$\epsilon = -N \frac{\Delta \varphi}{\Delta t} \tag{2.1}$$

where, ϵ represents induced voltage, also known as induced electromotive force (emf). N stands for number of loops in the copper winding, $\Delta \varphi$ represents change in magnetic flux, and Δt is change in time. Instead of counting number of loops in the copper winding, N is estimated based on the weight and size of copper winding. $\Delta \varphi$ represents the magnetic flux of spherical magnet.

In 2024, Zhang et al. introduced a hybrid ocean wave energy generator based on a commercially available floating buoy as shown in Figure 2.6(D) [39]. The key difference between Zhang's design and the previous three designs is that the ocean wave does not directly drive the generator. Instead, Zhang's design incorporates an air chamber at the bottom of the floating buoy similar like Xu's air chamber contact and separation TENG in 2017 [13]. The motion of the wave causes up and down movement in the water level within the air chamber, generating airflow that drives turbine blades to drive the generator. The EMH component of Zhang's design differs significantly from those of Sun's and Xu's prototypes. Zhang's EMH consists of six magnets and six copper coils rather than single

magnet in the previous designs, allowing it to generate electrical output up to 36 times per full rotation, significantly enhancing its energy harvesting capability. Additionally, there are no other materials between the magnets and copper coils, eliminating concerns about electromagnetic permeability that were presented in Xu's design. The TENG operates in rotational mode and employs FEP and Nylon as triboelectric materials. As a result, the TENG in Zhang's design achieves an output voltage of up to 545.4 V and a maximum output current of 202.5 mA which is approximately 20 times compared to Xu's design. Due to the high internal space requirements for accommodating the EMH component, hybrid-mode TENGs typically adopt a cylindrical shape or specialized variations developed from it, such as the water drop–form design [40].

A hybrid-mode TENG presents a promising solution to address the micro-level output current limitation of TENGs. However, an essential challenge remains how to efficiently utilise the generated electrical energy. If both EMH and TENG are used as renewable energy generators, the power management system must be carefully designed. This is because the voltage output characteristics of EMH and TENG differ significantly, and directly connecting their outputs could lead to a short circuit, potentially damaging the system. If use full bridge rectifiers to convert AC to DC voltage, there is a concern about the output of EMH side. Usually, there are four diodes in the full bridge and each diode will have a 0.4 V to 0.6 V voltage drop which means that 1.6 V to 2.4 V voltage loss on EMH side during rectifying. If a voltage regulator or step-down transformer is used, the TENG side may not be able to deliver enough current to power the electronic integrated chips. Therefore, the TENG needs to step down the voltage and increase the current before converting AC to DC to match the output voltage level of the EMH and then convert it to DC voltage.

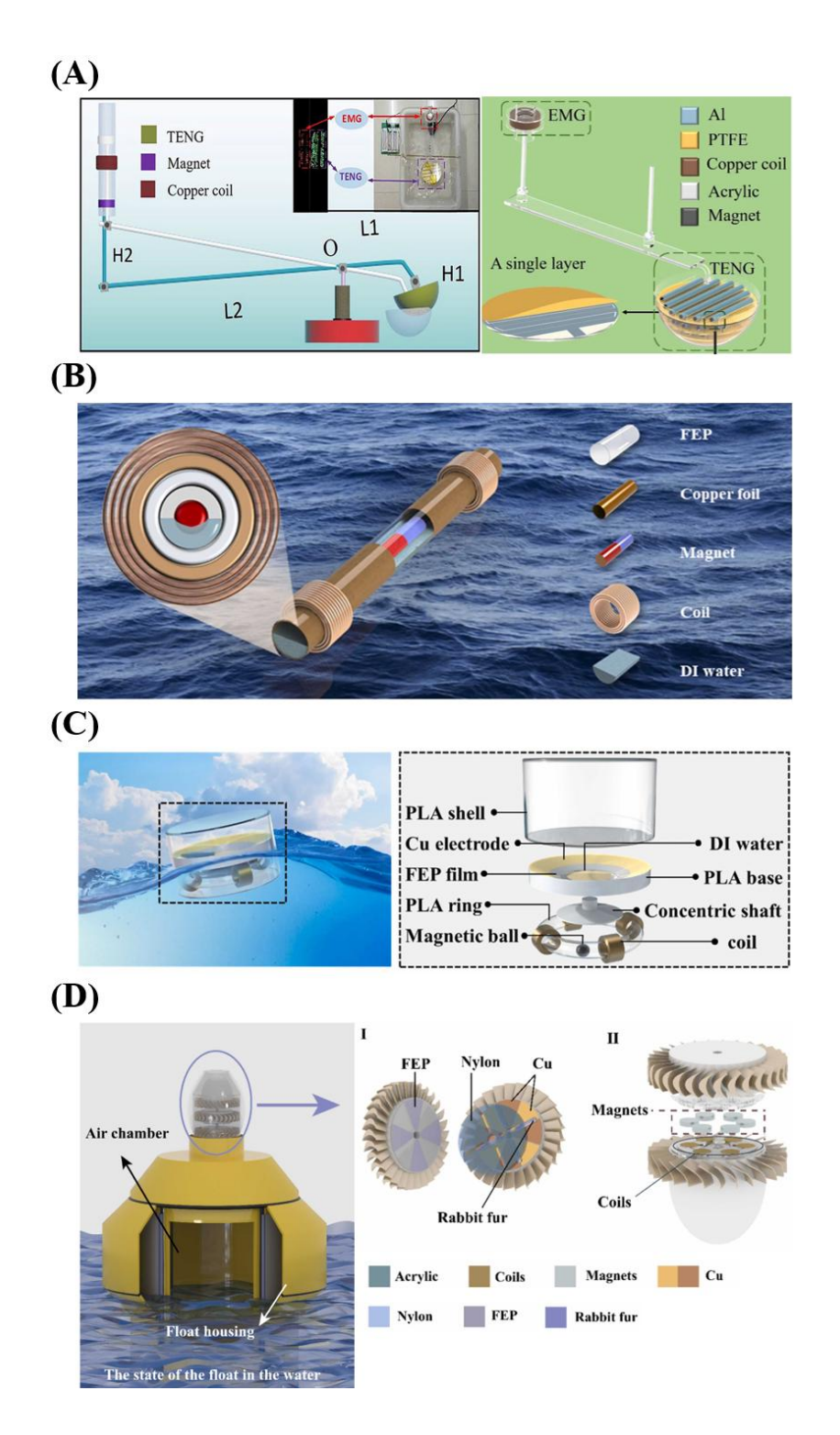


Figure 2.6 Schematic structure of the water wave hybrid generator combines with TENG and EMH (A) Teeterboard-like hybrid nanogenerator (THNG) [36], (B) Tube-shaped triboelectric–electromagnetic hybrid nanogenerator (TTEHG) [37], (C) Triboelectric-electromagnetic hybrid nanogenerator (TEH-NG) [38], and (D) Guided-liquid-based isotropic triboelectric-electromagnetic hybrid nanogenerator (I-TEHG) [39].

Table 2.3 Summary of previously published hybrid mode type triboelectric nanogenerators

Ref	Structure	Tribo-material	Electrode	Open- circuit voltage	Short- circuit current	Power density/ power
[36]	Freestanding	PTFE / Al	Al	760 V	4 μΑ	55 mW/m ²
	EMH	Magnet / Cu coil		2 V	10 mA	N/A
[37]	Contact and separation	FEP / DI water	Cu	≈ 300 V	1.832 µA	38 µW
	ЕМН	Magnet / Cu coil		≈ 45 V	30 mA	N/A
[38]	Contact and separation	FEP / DI water	Cu	168.08 V	2.03 μΑ	101.5 µW
	EMH	Magnet / Cu coil		≈ 30 V	≈ 6 mA	10.1 mW
[39]	Linear sliding	FEP / Nylon	Cu	545.4 V	23.4 μΑ	141.7 W m ³
	EMH	Magnet / Cu coil		13.6 V	202.5 mA	400.0 W m ³
[40]	Linear sliding	PTFE / Nylon	Cu	783 V	1.57 µA	N/A
	EMH	Magnet / Cu coil		1.45 V	1.5 mA	7.2 W/m ³
[41]	Contact and separation	PDMS / PVA Hydrogel	rGO	1.39 V	N/A	N/A
	ЕМН	Magnet / Cu coil		4.1 V	0.388 A	1.47 W

2.2.4 Self-powered system for ocean application

To more effectively utilise ocean wave energy sources, it is crucial to study ocean wave parameters such as wave frequency and wave amplitude, which are key components of the ocean wave spectrum in each sea region. Most sensors used for ocean spectrum data collection are currently based on radar technology, including real-aperture radar, high-frequency radar, and X-band radars [42-44], which means that these sensors require an additional power source to drive the radar antenna. Some of these sensors are combined with other renewable energy generators to reduce battery dependency, such as integrating solar PV systems or small-scale wind turbines [45-47]. The lithium batteries inside these sensors can have significant effects on marine life if the chemical contents leak into the sea. Regarding the negative effects of lithium on aquatic organisms, the studied taxonomic classes included fish and shellfish. Observed impacts included development inhibition, malformations, cellular and metabolic alterations, and behavioural changes [48]. Furthermore, the above radar technologies face limitations in collecting data on low-amplitude waves. For instance, real-aperture radar cannot detect wave conditions with amplitudes smaller than 2 m. In addition to this limitation, the vibration of the radar's antenna, caused by external

environmental factors such as irregular waves and wind, can significantly affect the accuracy of the ocean spectrum data [49,50]. These challenges highlight the need for more sensitive and accurate sensors that can capture the low wave amplitude condition without being impacted by environmental disturbances. Utilising other characteristics of TENG, such as employing them as self-powered sensors, demonstrates the potential to overcome the current limitations of ocean spectrum data collection sensors. TENGs can generate electrical signals independently, ensuring that the sensors do not rely on traditional batteries. This approach minimised negative effect of the ocean environment. Additionally, due to the wide selection of triboelectric materials, researchers can choose environmentally friendly triboelectric materials, further reducing the impact on marine ecosystems.

In 2019, Xu et al. introduced a self-powered wave sensor based on a solid-liquid type TENG as shown in Figure 2.7(A). PTFE and Cu were used as the triboelectric material and electrode, respectively. Due to its solid-liquid characteristics, this self-powered sensor demonstrates high sensitivity to variation of ocean wave amplitude, as the wave amplitude directly affects the contact area between PTFE and seawater. Additionally, it can accurately record wave frequency, as each voltage signal generated by the TENG corresponds to the contact and separation between the seawater wave and the PTFE. However, a concern has been raised regarding the sensor's lifespan, as PTFE is in direct contact with seawater. The corrosion of PTFE and Cu electrode could significantly degrade the sensor's output performance over time. Additionally, this design requires fixed installation on a static solid structure due to its wired data transmission setup, restricting its deployment to locations such as jetties, ports, or seawalls [51].

In 2020, Zhang et al. introduced a fully sealed solid-solid type ocean wave sensor based on the sliding mode, as shown in Figure 2.7(B). PTFE and Cu were employed as triboelectric materials in this design. The buoy moves with ocean waves, generating relative motion between the two triboelectric materials. Variations in wave amplitude result in different contact areas, producing electrical signals of varying strengths. As a result, this sensor demonstrates high sensitivity to wave amplitude, with a minimum detectable wave amplitude of 2 cm, which is a significant improvement compared to the radar-based sensors mentioned above. The major improvement over Xu's design is the adoption of a fully enclosed structure, effectively isolating the sensor from seawater to reduce the corrosion effects over long time operation. However, adopting the sliding mode may affect the linearity of the output signal if the surface of the PTFE becomes uneven after prolonged operation, potentially resulting in a non-linear output trend that could compromise accuracy during analysis [52].

In 2021, Xu et al. introduced a linear sliding mode solid-solid TENG for ocean wave amplitude and frequency detection as shown in Figure 2.7(C). Unlike Xu's 2019 design, this sensor does not operate directly with ocean waves but instead follows a similar approach to Zhang's 2020 design. The key distinction is that Zhang's design utilises wave amplitude changes to drive relative

movement between triboelectric materials, whereas Xu's 2021 design employs wave motion to drive a pendulum, inducing rotational movement in the TENG. As a result, this self-powered sensor can detect wave amplitudes as low as 50 mm and wave frequencies ranging from 0.5 Hz to 1.5 Hz. However, due to its more complex design, the minimum detectable wave amplitude and frequency are higher than those of Zhang's 2020 sensor [53]. However, the sliding mode may lead to increased material wear and tear over long-term operation, potentially resulting in inaccurate data analysis in the future.

In 2023, Chen et al. introduced a rotational mode solid-solid TENG-based self-powered sensor, employing Nylon and FEP as triboelectric materials as shown in Figure 2.7(D). The key difference from Xu's 2021 design is that Chen's sensor utilises a complex one-way overrunning clutches and brakes to efficiently convert up-and-down ocean wave motion into one direction kinetic energy to activated TENG. As a result, this self-powered sensor achieves a minimum wave amplitude response of 10 mm, representing a significant improvement over Xu's 2021 design [54]. Compared to Xu's design in 2021, Chen's design adopts a non-contact rotational mode, which can extend the lifespan of the triboelectric materials.

In summary, when employing TENG as a self-powered sensor to detect changes in wave amplitude and wave frequency, waterproof capability is a crucial factor. The corrosion caused by seawater can significantly affect the sensor's longevity. Solid-solid type TENGs usually demonstrate decent waterproof capabilities, making them more suitable for operation under seawater conditions. Considering the accuracy of the output signal strength, the linear sliding mode may not be the best choice compared with contact and separation mode. Additionally, since the wave motion is up-and-down, converting this motion to a rotational mode for the TENG requires cooperation with a complex transmission system. A more complex design increases the likelihood of risks of whole ocean wave energy harvesting device.

The above self-powered sensors demonstrate the feasibility of employing TENG-based systems to monitor and detect wave parameters such as amplitude and frequency variations. However, these sensors rely on wired connections to transmit collected data, which significantly limits their application. Hybrid mode may offer a viable solution to enable wireless functionality in self-powered sensors. TENG can be employed as a self-powered sensor, it can be used to detect ocean wave parameters, depending on its specific design and working mode. Meanwhile, the EMH can serve as a power source for wireless data transmission system for remote data transfer. To ensure continuous data transfer, EMH need to generate minimum 60 times per minutes. However, the nature of ocean wave conditions makes it challenging to meet this requirement. Fortunately, Zhang's 2024 design offers a potential solution to overcome the limitations of EMH generation frequency under low-frequency ocean wave conditions. The design incorporates multiple magnets and copper coils to achieve up to 60 generation cycles per second, thereby enabling real-time data transmission. The

successful realization of this real-time data transmission system could usher self-powered sensors into a new era.

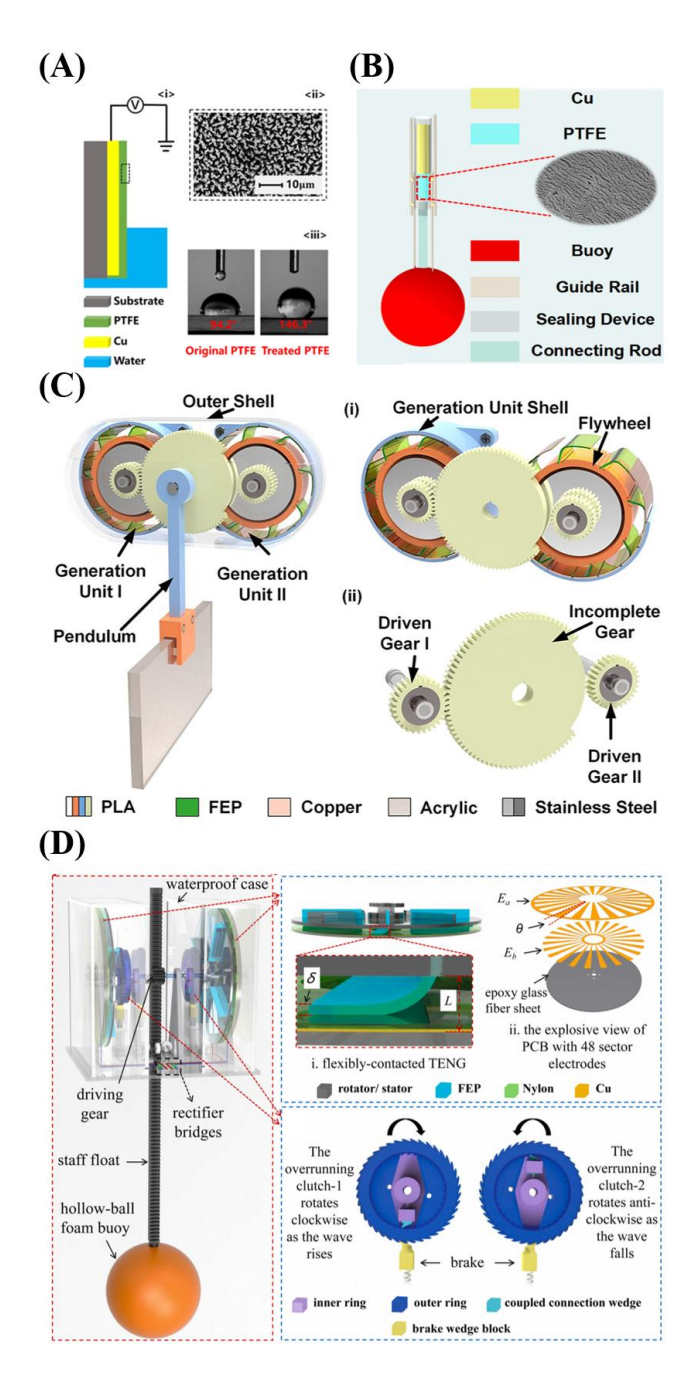


Figure 2.7 Schematic structure of the self-powered ocean wave sensors, (A) Highly sensitive wave sensors based on liquid-solid interfacing triboelectric nanogenerator (WS-TENG) [51], (B) Self-powered and high-performance triboelectric ocean-wave spectrum sensor (TOSS) [52], (C) Graded energy harvesting triboelectric nanogenerator (GEH-TENG) [53], and (D) Self-powered wide-range ocean-wave sensor [54].

Table 2.4 Summary of previously published self-powered sensors

Ref	Structure	Tribo-material	Electrode	Open- circuit voltage	Short- circuit current	Power density / power
[51]	Contact and separation	PTFE	Cu	≈ 3.5 V	N/A	N/A
[52]	Linear sliding	PTFE / Cu	Cu	280 V	N/A	0.089 mW
[53]	Contact and separation	PTFE / Water	Cu	≈ 2.2 V	N/A	4.63 mW
[54]	Linear sliding	FEP / Nylon	Cu	≈ 10 V	≈ 7.5 µA	0.09 mW

2.2.5 Energy storage system for ocean wave energy driven TENGs

TENGs offer an excellent solution for harvesting energy from low-frequency, low-amplitude waves. However, their development and widespread application have been limited by low output currents in the micro- to milliampere range and unstable voltage output. Therefore, an energy storage system is essential to accumulate the energy generated by TENGs for powering external devices. Moreover, considering the harsh ocean environment, minimizing the number of system components is crucial to improving robustness and reliability. According to the comparison results presented in Table 2.5, the combination of a full-bridge rectifier and capacitor is the most used energy storage configuration in ocean wave energy-driven TENGs. The full-bridge rectifier, typically composed of four diodes such as Schottky diodes, is employed to convert the AC output of the TENG into DC, which is more suitable for powering electronic devices or for storage. Additionally, the compact size of the full-bridge rectifier makes it ideal for applications with limited internal space and for systems utilizing a single TENG. However, the use of a full-bridge rectifier can lead to output voltage reduction due to energy losses during the AC-to-DC conversion process. This loss, known as voltage drop, typically ranges from 0.4 V to 0.6 V per diode.

To address this issue, voltage multipliers have been employed. A voltage multiplier is a specialized rectifier circuit that uses a combination of diodes and capacitors to form a voltage-boosting system. It not only converts the AC output of the TENG into DC, but also increases the output voltage level simultaneously, thereby improving the overall energy harvesting efficiency. Based on the experimental results of Wang's project in 2024 [41], the output voltage of the TENG was approximately 1.39 V, which is significantly lower than the minimum voltage required to power an LED which is 2.5 V. If a full-bridge rectifier and capacitor are used as the energy storage strategy, most or all the TENG's output voltage would be lost during the rectification stage. As mentioned above, each diode in the rectifier introduces a voltage drop of approximately 0.4 V to 0.6 V, resulting in a total drop of 1.6 V to 2.4 V across the full bridge rectifier. This energy loss makes the use of

conventional full-bridge rectifiers unsuitable for low-voltage TENG outputs. However, when the TENG output is combined with a voltage multiplier, the boosted voltage can successfully power external devices, with significant results observed even under daylight conditions. Therefore, employing a voltage multiplier for both rectification and voltage boosting before charging a capacitor or battery is the most effective approach, especially since batteries typically require a much higher amount of energy to charge compared to capacitors. Supercapacitors are a more suitable energy storage option for TENGs, as they offer larger energy storage capacity than conventional capacitors and enable faster charging and discharging compared to batteries.

In addition, Table 2.5 highlights the electronic devices that have been powered by the stored energy. According to the data, electronic thermometers are the most used devices, followed by electronic water sensors, calculators, and wireless transmitters. Combining a wireless transmitter with an electronic thermometer enables real time monitoring of ocean temperature, contributing to the protection of marine life. Alternatively, other sensors such as oxygen sensors can be integrated to monitor the oxygen content in ocean waters. However, analysing the charged voltage in the energy storage unit remains challenging due to the lack of standardized capacitance values, which presents a similar issue to the difficulty of comparing power density across different systems.

Table 2.5 Summary of previously published energy storage system

Ref	AC-DC rectifier	Energy storage	Powered devices
[7]	Full bridge rectifier	Supercapacitors	Electronic thermometer
[8]	Full bridge rectifier	Capacitor	Electronic thermometer
[9]	Full bridge rectifier	Capacitor	Electronic watch
[10]	Full bridge rectifier	Capacitor	Wireless transmitter
[11]	Full bridge rectifier	Capacitor	Electronic thermometer
[13]	Full bridge rectifier	Capacitor	N/A
[14]	Full bridge rectifier	Capacitor	N/A
[16]	Full bridge rectifier	Capacitor	Electronic thermometer
[17]	Full bridge rectifier	Capacitor	Electronic thermometer & etc
[18]	Full bridge rectifier	Capacitor	Electronic thermometer
[19]	N/A	Capacitor	Electronic thermometer
[20]	Full bridge rectifier	Capacitor	Electronic calculator
[21]	Full bridge rectifier	Capacitor	N/A
[22]	Full bridge rectifier	Capacitor	Electronic thermometer
[22]	Full bridge rectifier	Capacitor	Electronic thermometer

[23]	Full bridge rectifier	Capacitor	Temperature/Humidity meter & Electronic calculator & Electronic watch
[24]	Full bridge rectifier	Capacitor	Electronic thermometer
[25]	Full bridge rectifier	Capacitor	Electronic thermometer
[26]	Full bridge rectifier	Capacitor	N/A
[27]	Full bridge rectifier	Capacitor	N/A
[29]	N/A	Capacitor	N/A
[30]	N/A	Capacitor	Electrolytic cell
[32]	Full bridge rectifier	Capacitor	Electronic thermometer
[33]	Full bridge rectifier	Capacitor	N/A
[36]	Full bridge rectifier	Capacitor	N/A
[37]	Full bridge rectifier	Capacitor	Electronic thermometer
[38]	Full bridge rectifier	Capacitor	Electronic calculator & Electronic watch
[39]	Full bridge rectifier	Capacitor	Electronic thermometer & PH sensor
[40]	Full bridge rectifier	Capacitor	PH sensor
[41]	Voltage multiplier	Capacitor	N/A

2.3 Discussion

The data from Tables 2.1-2.4 present the common working modes for ocean wave energy driven TENGs and highlights the popular combinations of triboelectric materials used in both solid—solid and solid—liquid TENG. As blue energy generators, waterproof capability is crucial because water droplets or steam can cause the TENG to short-circuit and fail if they come to inside of the device and contact with the triboelectric material or metal electrodes. Therefore, the solid-solid type TENG is well-suited to meet this requirement due to the fully sealed outer shape. As is commonly known, the sliding and rotational modes typically exhibit high output performance. However, the material wear in the sliding mode is significant, leading to more frequent maintenance. Consider the offshore operation condition, guaranteed the lifespan of triboelectric materials is important. Additionally, ocean wave motion is primarily up-and-down, the contact and separation mode can effectively harness this motion without the need for the complex internal mechanical system which required in the rotational mode. However, on the other hand, Zhang et al. proposed a rotational hybrid-mode TENG in 2024. The most innovative aspect of this design is that the TENG is not directly activated by wave motion. Instead, it utilizes an air chamber that converts the vertical motion of waves into upward-directed wind energy through air compression caused by rising waves. This design

effectively overcomes the limitations associated with adopting the rotational mode for ocean wave energy harvesting, which often involves complex mechanical structures, as seen in the designs proposed by Xu in 2021 and Chen in 2023 [53,54]. However, Zhang's design is also limited by the bulky size of the overall ocean wave energy harvester. The external dimensions and weight still need to be optimized to minimize the response frequency and amplitude.

Analysing the power density of ocean wave-driven TENGs is crucial for identifying the most effective structural designs and material combinations based on previously works. As shown in Figure 2.8, Yuan's 2022 design demonstrates the highest power density which is 80.6 W/m³. In that study, FEP and conductive fibre were used as triboelectric materials, conductive fibre also serving as the electrode [19]. Notably, the most common material pairings for contact–separation mode TENGs involve PTFE or FEP as the electron donor, combined with metal materials such as Al or Cu as the electron acceptor as shown in Table 2.1. Since both Al and Cu are highly conductive, they can serve dual functions as both triboelectric materials and electrodes. This dual functionality helps reduce the structural complexity of generators, which is a critical factor for offshore applications.

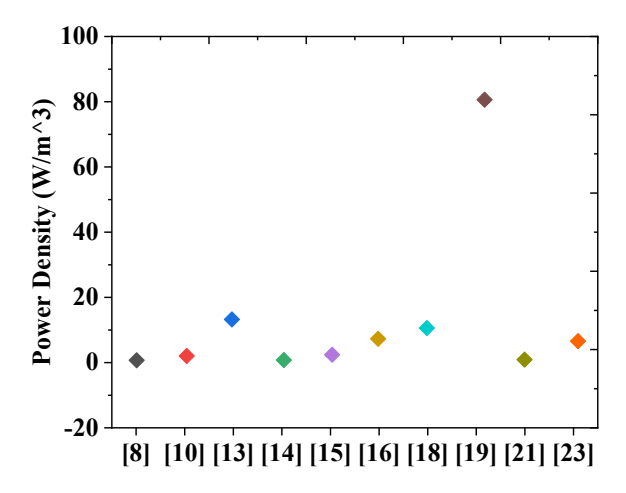


Figure 2.8 Comparison of output power density (W/m³) for published ocean wave energy driven TENGs.

When TENGs are used as self-powered sensors for ocean variation sensing, output performance is not the primary concern. Instead, the most critical factor is the linearity of the generated electrical signals. As previously mentioned, ocean wave motion is predominantly up-and-down, making the contact—separation mode is the most suitable working modes for such applications. On the one hand, even if the sensor adopts a solid-liquid structural design, FEP and PTFE remain the most used triboelectric materials due to their notable hydrophobic properties. Cu is also widely used as electrodes in solid-liquid structure TENGs or self-powered sensors as shown in Table 2.2 and 2.4, as they offer relatively low cost and decent electrical conductivity compared to materials like Au and Ag. Moreover, data analysis has revealed a problem: the unit of power density is not standardized, making result comparison difficult.

2.4 Future perspectives

2.4.1 Utilisation of TENG based self-powered sensors to realise location evaluation.

TENGs are well-suited for use as self-powered sensors in ocean environments, as they can generate electrical signals independently. Moreover, the TENG output is correlated with both wave frequency and amplitude. The output strength of TENG will change with variation of wave amplitude and frequency. However, current self-powered TENG sensors rely on wired data transmission, which significantly limits their operating environments. They lack an integrated wireless data transfer system. Fortunately, hybrid-mode ocean wave energy generators offer a promising solution. EMHs, which can generate milliampere-level output currents, are capable of powering wireless data transmission systems. In 2024, Xi et al. introduced a wireless data transfer system powered by a hybrid-mode TENG. In their design, the EMH powered a wireless data transmission system based on an Arduino platform integrated with a microcontroller unit (MCU). As a result, the system achieved a maximum communication distance of 1.06 km under urban conditions [55]. According to the Arduino website, there are two MCU versions capable of wireless signal transmission: one utilising low-energy Bluetooth, and the other based on Wi-Fi technology [56,57]. Xi's design provided a potential application for ocean monitoring applications without battery.

However, the generation frequency of EMH needs to match the signal transfer rate to achieve real-time data transmission. At the current research stage, a power management system and an energy storage system are required to boost the output performance of EMHs and store the harvested energy in a battery for later use. This approach ensures a stable power supply for wireless data transmission. However, it does not achieve real-time energy transfer and still cannot operate independently from a lithium battery. Apart from that, the choice of power management strategy needs to be carefully considered. For instance, what is the primary purpose of the device? Where will it be placed? Additionally, does it require frequent maintenance? These factors significantly impact the selection of an appropriate power management system, influencing overall efficiency, longevity, and practicality in real-world ocean conditions. Moreover, considering the ocean environment, humidity and seawater corrosion pose significant challenges for electronic circuits. A higher number of electronic components increases the risk of system failure, making durability and reliability key factors in power management system design. Therefore, a comprehensive review and test of the seawater corrosion resistance of the triboelectric material, which will be in direct contact with seawater, is necessary.

In addition, thanks to the rapid development of AI technology and advanced programming algorithms, the use of AI tools to assist in experimental data analysis has become increasingly feasible and reliable. Wave parameters detected by self-powered sensors can be wirelessly transmitted to an onshore endpoint, where analysts can apply AI or machine learning techniques to process the recorded wave data. This enables active prediction of future ocean conditions and

enhances real-time environmental monitoring capabilities. In summary, significant improvements in power management systems and EMH design are essential. The successful development of real-time data transfer would be a game changer for ocean spectrum mapping and would greatly enhance the overall utilization rate of ocean wave energy.

2.4.2 Robustness testing of ocean wave driven TENGs under controlled water waves.

Robustness is a critical factor for the future development of ocean wave-driven TENGs. The overall system lifespan under high humidity and high salt content region lack study. Evaluating the entire TENG system under controlled wave conditions is essential for understanding its long-term performance and lifespan of the design. However, conventional ground-based wave generation systems are costly to construct and maintain. Currently, testing TENG-based devices under actual water wave is challenging due to the lack of wave generation systems. Therefore, there is an urgent need for a compact, cost-effective wave generation system capable of producing continuous, repeatable, and stable waveforms to facilitate robustness testing of ocean wave-driven TENGs. This wave generation system should be portable and capable of being moved to different water channels or water tanks. Additionally, it should consist of easily obtained, commercially available components to enhance reproducibility. Moreover, utilising wireless control into this system can significantly improve operational efficiency and user experience. A successfully designed wave generation system will make a significant contribution to the lifetime cost analysis of ocean wave-driven TENGs.

2.4.3 TENG technology-based ocean wave energy generator.

In the case of ocean wave-driven TENGs, material selection and device shape optimisation are the primary research focuses. Evaluating the output performance of ocean wave-driven TENGs with different frequencies is a common testing practice. Ocean wave parameters include wave frequency and amplitude. However, the effect of wave amplitude on ocean wave-driven TENGs remains significantly underexplored. Understanding this relationship is crucial, as wave amplitude will affect the output performance of contact and separation mode TENGs under real ocean wave conditions. This assumption is based on the Equation $F = mgsin\theta$, where. F represents the gravitational force acting on an inclined plane, m is the mass of the sliding object on the inclined plane, which typically consists of sliding module and triboelectric materials, g is the gravitational acceleration due to Earth, and $sin\theta$ denotes the inclination angle of the plane, which corresponds to the wave amplitude in an ocean wave energy generator. Assume that the contact surface between m is flat and there is no friction force, an increase in the inclination angle will result in a greater gravitational force. Therefore, wave amplitude will cause the triboelectric materials to move more quickly, thereby influencing the operating frequency of the TENG. This highlights the importance of studying the effect of wave amplitude variations on the TENG's output performance. In addition, the low output current at the micro- to milliampere level remains a major challenge for ocean-wave-driven TENGs. The most common solution is to use a power management system to enhance and stabilize the output.

However, these systems typically consist of multiple electronic components that are prone to failure in ocean environments due to corrosion from salt and moisture during operation. Therefore, there is an urgent need to develop more effective approaches for utilizing ocean wave energy through TENGs.

2.5 Conclusion

This review summarises the key milestones in the development of ocean wave energy-driven TENGs, focusing on their applications as renewable energy generators and self-powered sensors. It introduces various external designs and structural configurations, including solid—solid, solid—liquid, hybrid modes, and self-powered sensors. The achievements and limitations of published representative designs are critically evaluated. The review also emphasises optimal triboelectric material pairings, working modes, and structural designs suited for ocean wave environments. In recent years, significant progress has been made in material enhancement and design optimisation. However, three major research gaps remain: (1) effects of wave amplitude on TENG output performance require further investigation; (2) development of a wireless data transmission system powered by a hybrid-mode TENG is urgently needed to enable the commercial application of self-powered sensors; and (3) lack of standardised evaluation methods under controlled wave conditions results in unclear performance mappings, limiting the optimisation of energy harvesting efficiency. By overcoming these limitations, TENGs will demonstrate great potential for ocean wave energy harvesting and the collection of ocean wave parameter data.

2.6 Reference

[1] H. Hong, X. Yang, H. Cui, D. Zheng, H. Wen, R. Huang, L. Liu, J. Duan, Q. Tang, Self-powered seesaw structured spherical buoys based on a hybrid triboelectric–electromagnetic nanogenerator for sea surface wireless positioning, Energy Environ Sci 15 (2022) 621–632. https://doi.org/10.1039/D1EE02549J.

- [2] J. Cheng, X. Zhang, T. Jia, Q. Wu, Y. Dong, D. Wang, Triboelectric nanogenerator with a seesaw structure for harvesting ocean energy, Nano Energy 102 (2022) 107622. https://doi.org/10.1016/j.nanoen.2022.107622.
- [3] S. Jia, X. Yang, W. Feng, L. Liu, L. Zhao, L. Wu, S. Li, W. Zuo, Q. Tang, T. Jiang, Z. Wang, Self-adaptive gyroscope-structured hybrid triboelectric-electromagnetic buoy system for real-time ocean currents monitoring, Small 21 (2025). https://doi.org/10.1002/smll.202501073.
- [4] Y. Dong, S. Xu, C. Zhang, L. Zhang, D. Wang, Y. Xie, N. Luo, Y. Feng, N. Wang, M. Feng, X. Zhang, F. Zhou, Z.L. Wang, Gas-liquid two-phase flow-based triboelectric nanogenerator with ultrahigh output power, Sci Adv 8 (2022). https://doi.org/10.1126/sciadv.add0464.

- [5] Q. Wu, L. Zhang, W. Wang, H. Xu, J. Cheng, X. Wu, Y. Liu, X. Zhang, D. Wang, High-performance pneumatic solid–liquid triboelectric nanogenerator, Nano Energy 123 (2024) 109391. https://doi.org/10.1016/j.nanoen.2024.109391.
- [6] J. Tollefson, Power from the oceans: blue energy, Nature 508 (2014) 302–304. https://doi.org/10.1038/508302a.
- [7] X. Wang, S. Niu, Y. Yin, F. Yi, Z. You, Z.L. Wang, Triboelectric nanogenerator based on fully enclosed rolling spherical structure for harvesting low-frequency water wave energy, Adv Energy Mater 5 (2015) 1501467. https://doi.org/10.1002/aenm.201501467.
- [8] L. Xu, T. Jiang, P. Lin, J.J. Shao, C. He, W. Zhong, X.Y. Chen, Z.L. Wang, Coupled triboelectric nanogenerator networks for efficient water wave energy harvesting, ACS Nano 12 (2018) 1849–1858. https://doi.org/10.1021/acsnano.7b08674.
- [9] P. Cheng, H. Guo, Z. Wen, C. Zhang, X. Yin, X. Li, D. Liu, W. Song, X. Sun, J. Wang, Z.L. Wang, Largely enhanced triboelectric nanogenerator for efficient harvesting of water wave energy by soft contacted structure, Nano Energy 57 (2019) 432–439.

https://doi.org/10.1016/j.nanoen.2018.12.054.

- [10] X. Yang, L. Xu, P. Lin, W. Zhong, Y. Bai, J. Luo, J. Chen, Z.L. Wang, Macroscopic self-assembly network of encapsulated high-performance triboelectric nanogenerators for water wave energy harvesting, Nano Energy 60 (2019) 404–412. https://doi.org/10.1016/j.nanoen.2019.03.054.
- [11] Z. Qu, M. Huang, C. Chen, Y. An, H. Liu, Q. Zhang, X. Wang, Y. Liu, W. Yin, X. Li, Spherical triboelectric nanogenerator based on eccentric structure for omnidirectional low frequency water wave energy harvesting, Adv Funct Mater 32 (2022). https://doi.org/10.1002/adfm.202202048.
- [12] T. Jiang, L.M. Zhang, X. Chen, C.B. Han, W. Tang, C. Zhang, L. Xu, Z.L. Wang, Structural optimization of triboelectric nanogenerator for harvesting water wave energy, ACS Nano 9 (2015) 12562–12572. https://doi.org/10.1021/acsnano.5b06372.
- [13] L. Xu, Y. Pang, C. Zhang, T. Jiang, X. Chen, J. Luo, W. Tang, X. Cao, Z.L. Wang, Integrated triboelectric nanogenerator array based on air-driven membrane structures for water wave energy harvesting, Nano Energy 31 (2017) 351–358. https://doi.org/10.1016/j.nanoen.2016.11.037.
- [14] T. Jiang, Y. Yao, L. Xu, L. Zhang, T. Xiao, Z.L. Wang, Spring-assisted triboelectric nanogenerator for efficiently harvesting water wave energy, Nano Energy 31 (2017) 560–567. https://doi.org/10.1016/j.nanoen.2016.12.004.

- [15] T.X. Xiao, T. Jiang, J.X. Zhu, X. Liang, L. Xu, J.J. Shao, C.L. Zhang, J. Wang, Z.L. Wang, Silicone-based triboelectric nanogenerator for water wave energy harvesting, ACS Appl Mater Interfaces 10 (2018) 3616–3623. https://doi.org/10.1021/acsami.7b17239.
- [16] Y. Bai, L. Xu, C. He, L. Zhu, X. Yang, T. Jiang, J. Nie, W. Zhong, Z.L. Wang, High-performance triboelectric nanogenerators for self-powered, in-situ and real-time water quality mapping, Nano Energy 66 (2019) 104117. https://doi.org/10.1016/j.nanoen.2019.104117.
- [17] F. Xi, Y. Pang, G. Liu, S. Wang, W. Li, C. Zhang, Z.L. Wang, Self-powered intelligent buoy system by water wave energy for sustainable and autonomous wireless sensing and data transmission, Nano Energy 61 (2019) 1–9. https://doi.org/10.1016/j.nanoen.2019.04.026.
- [18] M. Xu, T. Zhao, C. Wang, S.L. Zhang, Z. Li, X. Pan, Z.L. Wang, High power density tower-like triboelectric nanogenerator for harvesting arbitrary directional water wave energy, ACS Nano 13 (2019) 1932–1939. https://doi.org/10.1021/acsnano.8b08274.
- [19] W. Yuan, B. Zhang, C. Zhang, O. Yang, Y. Liu, L. He, L. Zhou, Z. Zhao, J. Wang, Z.L. Wang, Anaconda-shaped spiral multi-layered triboelectric nanogenerators with ultra-high space efficiency for wave energy harvesting, One Earth 5 (2022) 1055–1063.

https://doi.org/10.1016/j.oneear.2022.08.013.

[20] D. Tan, Q. Zeng, X. Wang, S. Yuan, Y. Luo, X. Zhang, L. Tan, C. Hu, G. Liu, Anti-overturning fully symmetrical triboelectric nanogenerator based on an elliptic cylindrical structure for all-weather blue energy harvesting, Nanomicro Lett 14 (2022) 124.

https://doi.org/10.1007/s40820-022-00866-w.

- [21] R. Ouyang, Y. Huang, H. Ye, Z. Zhang, H. Xue, Copper particles-PTFE tube based triboelectric nanogenerator for wave energy harvesting, Nano Energy 102 (2022) 107749. https://doi.org/10.1016/j.nanoen.2022.107749.
- [22] T.X. Xiao, X. Liang, T. Jiang, L. Xu, J.J. Shao, J.H. Nie, Y. Bai, W. Zhong, Z.L. Wang, Spherical triboelectric nanogenerators based on spring-assisted multilayered structure for efficient water wave energy harvesting, Adv Funct Mater 28 (2018) 1802634. https://doi.org/10.1002/adfm.201802634.
- [23] P. Rui, W. Zhang, Y. Zhong, X. Wei, Y. Guo, S. Shi, Y. Liao, J. Cheng, P. Wang, High-performance cylindrical pendulum shaped triboelectric nanogenerators driven by water wave energy for full-automatic and self-powered wireless hydrological monitoring system, Nano Energy 74 (2020) 104937. https://doi.org/10.1016/j.nanoen.2020.104937.

- [24] L. Liu, X. Yang, L. Zhao, H. Hong, H. Cui, J. Duan, Q. Yang, Q. Tang, Nodding duck structure multi-track directional freestanding triboelectric nanogenerator toward low-frequency ocean wave energy harvesting, ACS Nano 15 (2021) 9412–9421. https://doi.org/10.1021/acsnano.1c00345.
- [25] C. Zhang, W. Yuan, B. Zhang, J. Yang, Y. Hu, L. He, X. Zhao, X. Li, Z.L. Wang, J. Wang, A rotating triboelectric nanogenerator driven by bidirectional swing for water wave energy harvesting, Small 19 (2023) 2304412. https://doi.org/10.1002/smll.202304412.
- [26] Y. Wang, A. Pham, D. Tohl, Y. Tang, Simulation guided hand-driven portable triboelectric nanogenerator: design, optimisation, and evaluation, Micromachines (Basel) 12 (2021) 955. https://doi.org/10.3390/mi12080955.
- [27] Y. Wang, A.T.T. Pham, X. Han, D. Du, Y. Tang, Design and evaluate the wave driven-triboelectric nanogenerator under external wave parameters: experiment and simulation, Nano Energy 93 (2022) 106844. https://doi.org/10.1016/j.nanoen.2021.106844.
- [28] X.J. Zhao, S.Y. Kuang, Z.L. Wang, G. Zhu, Highly adaptive solid–liquid interfacing triboelectric nanogenerator for harvesting diverse water wave energy, ACS Nano 12 (2018) 4280–4285. https://doi.org/10.1021/acsnano.7b08716.
- [29] X. Wei, Z. Zhao, C. Zhang, W. Yuan, Z. Wu, J. Wang, Z.L. Wang, All-weather droplet-based triboelectric nanogenerator for wave energy harvesting, ACS Nano 15 (2021) 13200–13208. https://doi.org/10.1021/acsnano.1c02790.
- [30] Y. Zheng, Y. Ni, Y. Zi, H. Cui, X. Li, Enhanced triboelectric nanogenerators in saline environments and their applications in the ocean, Nano Energy 126 (2024) 109636. https://doi.org/10.1016/j.nanoen.2024.109636.
- [31] C. Zhang, B. Zhang, W. Yuan, O. Yang, Y. Liu, L. He, Z. Zhao, L. Zhou, J. Wang, Z.L. Wang, Seawater-based triboelectric nanogenerators for marine anticorrosion, ACS Appl Mater Interfaces 14 (2022) 8605–8612. https://doi.org/10.1021/acsami.1c23575.
- [32] L. Liu, Q. Shi, J.S. Ho, C. Lee, Study of thin film blue energy harvester based on triboelectric nanogenerator and seashore IoT applications, Nano Energy 66 (2019) 104167. https://doi.org/10.1016/j.nanoen.2019.104167.
- [33] X. Wu, T. Cai, Q. Wu, J. Meng, W. Wang, W. Li, C. Hu, X. Zhang, D. Wang, Droplet-based triboelectric nanogenerators with needle electrodes for efficient water energy harvesting, ACS Appl Mater Interfaces 17 (2025) 13762–13772. https://doi.org/10.1021/acsami.4c17442.

- [34] S.P. Beeby, R.N. Torah, M.J. Tudor, P. Glynne-Jones, T. O'Donnell, C.R. Saha, S. Roy, A micro electromagnetic generator for vibration energy harvesting, Journal of Micromechanics and Microengineering 17 (2007) 1257–1265. https://doi.org/10.1088/0960-1317/17/7/007.
- [35] Ö. Zorlu, H. Külah, A MEMS-based energy harvester for generating energy from non-resonant environmental vibrations, Sens Actuators A Phys 202 (2013) 124–134.

https://doi.org/10.1016/j.sna.2013.01.032.

[36] Y. Wu, Q. Zeng, Q. Tang, W. Liu, G. Liu, Y. Zhang, J. Wu, C. Hu, X. Wang, A teeterboard-like hybrid nanogenerator for efficient harvesting of low-frequency ocean wave energy, Nano Energy 67 (2020) 104205. https://doi.org/10.1016/j.nanoen.2019.104205.

[37] X. Sun, C. Shang, H. Ma, C. Li, L. Xue, Q. Xu, Z. Wei, W. Li, Y. Yalikun, Y.-C. Lai, Y. Yang, A tube-shaped solid–liquid-interfaced triboelectric–electromagnetic hybrid nanogenerator for efficient ocean wave energy harvesting, Nano Energy 100 (2022) 107540.

https://doi.org/10.1016/j.nanoen.2022.107540.

[38] Q. Xu, C. Shang, H. Ma, Q. Hong, C. Li, S. Ding, L. Xue, X. Sun, Y. Pan, T. Sugahara, Y. Yalikun, Y.-C. Lai, Y. Yang, A guided-liquid-based hybrid triboelectric nanogenerator for omnidirectional and high-performance ocean wave energy harvesting, Nano Energy 109 (2023) 108240. https://doi.org/10.1016/j.nanoen.2023.108240.

[39] C. Zhang, S. Yang, X. Dai, Y. Tu, Z. Du, X. Wu, Y. Huang, J. Fan, Z. Hong, T. Jiang, Z.L. Wang, Hybridized triboelectric-electromagnetic nanogenerators for efficient harvesting of wave energy for self-powered ocean buoy, Nano Energy 128 (2024) 109929.

https://doi.org/10.1016/j.nanoen.2024.109929.

[40] L. Liu, J. Li, Z. Guan, L. Zhao, Z. Tian, S. Jia, H. Hong, Z. He, H. Wen, R. Huang, H. Cui, W. Ou-Yang, X. Yang, Ultra-high output hybrid nanogenerator for self-powered smart mariculture monitoring and warning system, Chemical Engineering Journal 472 (2023) 145039. https://doi.org/10.1016/j.cej.2023.145039.

- [41] Y. Wang, H. Zhu, W. Xing, D. Tohl, Y. Tang, A hybrid self-powered wave sensing device enables low-amplitude wave sensing, Device (2024). https://doi.org/10.1016/j.device.2024.100575.
- [42] J.C.N. Borge, K. Reichert, J. Dittmer, Use of nautical radar as a wave monitoring instrument, Coastal Engineering 37 (1999) 331–342. https://doi.org/10.1016/S0378-3839(99)00032-0.
- [43] R. Howell, J. Walsh, Measurement of ocean wave spectra using narrow-beam HE radar, IEEE Journal of Oceanic Engineering 18 (1993) 296–305. https://doi.org/10.1109/JOE.1993.236368.

- [44] Z. Sun, J. Sun, C. Guan, S. Liu, X. Suo, Performance of ocean wave spectrometer in detecting ocean wave spectra, in: 2012 2nd International Conference on Remote Sensing, Environment and Transportation Engineering, IEEE, 2012: pp. 1–4. https://doi.org/10.1109/RSETE.2012.6260652.
- [45] HydroTerra, Stygo 3 Float Surface Water IoT Hub, Satellite, Solar Powered, HydroTerra (n.d.).
- [46] IMOS Integrated Marine Observing System, Wireless Sensor Network, IMOS Integrated Marine Observing System (n.d.).
- [47] Naval Technology, Saildrone Explorer Unmanned Surface Vessel, US, Naval Technology (2024).
- [48] H. Barbosa, A.M.V.M. Soares, E. Pereira, R. Freitas, Lithium: A review on concentrations and impacts in marine and coastal systems, Science of The Total Environment 857 (2023) 159374. https://doi.org/10.1016/j.scitotenv.2022.159374.
- [49] S. Chen, E.W. Gill, W. Huang, A first-order hf radar cross-section model for mixed-path ionosphere—ocean propagation with an FMCW source, IEEE Journal of Oceanic Engineering 41 (2016) 982–992. https://doi.org/10.1109/JOE.2015.2505778.
- [50] J. Walsh, W. Huang, E. Gill, The first-order high frequency radar ocean surface cross section for an antenna on a floating platform, IEEE Trans Antennas Propag 58 (2010) 2994–3003. https://doi.org/10.1109/TAP.2010.2052559.
- [51] M. Xu, S. Wang, S.L. Zhang, W. Ding, P.T. Kien, C. Wang, Z. Li, X. Pan, Z.L. Wang, A highly-sensitive wave sensor based on liquid-solid interfacing triboelectric nanogenerator for smart marine equipment, Nano Energy 57 (2019) 574–580.

https://doi.org/10.1016/j.nanoen.2018.12.041.

- [52] C. Zhang, L. Liu, L. Zhou, X. Yin, X. Wei, Y. Hu, Y. Liu, S. Chen, J. Wang, Z.L. Wang, Self-powered sensor for quantifying ocean surface water waves based on triboelectric nanogenerator, ACS Nano 14 (2020) 7092–7100. https://doi.org/10.1021/acsnano.0c01827.
- [53] Y. Xu, W. Yang, X. Lu, Y. Yang, J. Li, J. Wen, T. Cheng, Z.L. Wang, Triboelectric nanogenerator for ocean wave graded energy harvesting and condition monitoring, ACS Nano 15 (2021) 16368–16375. https://doi.org/10.1021/acsnano.1c05685.
- [54] X. Chen, G. Bao, S. Xie, X. Qin, J. Wang, A self-powered wide-range ocean-wave sensor enabled by triboelectric nanogenerators embedded with overrunning clutches, Nano Energy 115 (2023) 108685. https://doi.org/10.1016/j.nanoen.2023.108685.

[55] Z. Xi, H. Yu, H. Du, H. Yang, Y. Wang, M. Guan, Z. Wang, H. Wang, T. Du, M. Xu, High performance magnetic mass-enhanced triboelectric-electromagnetic hybrid vibration energy harvester enabling totally self-powered long-distance wireless sensing, Adv Mater Technol 9 (2024) 2400451. https://doi.org/10.1002/admt.202400451.

[56] Arduino, Arduino® Nano ESP32, Arduino Official Website (n.d.).

[57] Arduino, Arduino Nano 33 BLE, Arduino Official Website (n.d.).

CHAPTER 3 DESIGN AND EVALUATE THE WAVE DRIVEN-TRIBOELECTRIC NANOGENERATOR UNDER EXTERNAL WAVE PARAMETERS: EXPERIMENT AND SIMULATION (WD-TENG)

This chapter has been published on Nano Energy with DOI: 10.1016/j.nanoen.2021.106844. **Yunzhong Wang**: Conceptualization, Device design and fabrication, Experiment, Data analysis, Writing – original draft.

3.1 Introduction

Electrical energy is one of the most important requirement energies of society. The storage volume of non-renewable resources such as natural gas, coal, and fossil fuels becomes rare with the increasing of time, which results in the increasing of the price of the energy. Also, environmental regulations are becoming more and more stringent to limited greenhouse gas exhaust. Utilized renewable energy from the natural environment to ease the energy crisis becomes a top priority. The triboelectric nanogenerator (TENG) is the most popular method to harvest electrical energy from low-frequency conditions with low fabrication cost, lightweight, and no emission pollution [1-7]. The TENG utilized coupling of triboelectrification and electrostatic induction effect to convert mechanical and kinetic energy to electricity. The main working modes of TENG are the linear sliding mode and the contact and separation mode. The contact and separation mode TENG is a popular mode when harvesting energy under the low-frequency condition due to the low friction between triboelectric material [8-13]. The linear sliding mode has higher output compared with that of the contact and separation mode, but the roughness of the triboelectric material surface will be changed due to the increase of the test period which leads to unstable and uncontrollable output after a certain period [14-19].

The main renewable sources that TENG can harvest are wind energy and ocean energy. Most wind energy driven TENG uses the sliding mode principle to convert wind energy to electricity [20-28]. Ocean wave is relative stable compared with the wind speed. Also, the 71% surface area of the earth is the ocean, which provides a natural and abundant energy source for harvest electrical energy. The annual global ocean wave power potential is estimated to reach nearly 93,000 TWh [29], and the ocean wave energy around the coastlines is estimated to be 2–3 TW [30]. Wave power converts the periodic up-and-down movement of the oceans waves into electricity by placing equipment on the surface of the oceans that captures the energy produced by the wave movement and converts this mechanical energy into electrical power. Since 2014, over 40 research team applied the ocean wave energy to the TENG, these TENGs have different working strategies and shapes [31]. In 2015, Wang et al. designed and fabricated a spherical-shape ocean wave TENG. It has a spherical shape shell with an aluminium (Al) film been placed on the surface of the inner shell and a nylon ball been

placed into the spherical shell. The nylon ball contacts with the Al film to generate electricity when ocean wave was used to drive the TENG. It can efficiently work between 1.23 Hz and 1.55 Hz with a stable and repeatable waveform. But the contact area between the triboelectric material is small, which will reduce efficiency of energy transmission [32]. In 2018, Xu et al. provided a solution to improve the contact area between triboelectric material by replacing the harder nylon ball with a softer silicon rubber ball [33]. Some research groups also focus on the improvement of the TENG output by using high-performance polymers as triboelectric material or using soft liquids as triboelectric material to improve the contact area [34-38]. TENGs with spherical shapes are promising structures since this kind of design can transfer the ocean wave energy to electricity efficiently, but the fabrication of a spherical shape is not easy.

In 2014, Wang et al. firstly introduced a wavy structure TENG. It is consisted of two flat PTFE films and a wave shape Kapton. The wave shape Kapton is placed between two flat PTFE films. When a PTFE film is impacted by an external force, the vertical impact force will be changed to the horizontal force, which causes the horizontal sliding of the Kapton film. After impact, the wavy structure TENG will restore automatically [39]. The ability of integrated wavy structure TENG has been evidenced by Jiang et al. in 2015 [40]. The wavy structure can harvest kinetic energy of ocean, but the durability of the triboelectric material is a serious problem due to the elasticity decreasing of the wave shape material. In 2017, Jiang et al. introduced a vertical contact and separation mode ocean wave driven TENG. It consists of a rectangular acrylic shell with triboelectric material on both ends and an I-shape spring with triboelectric material placed on both ends. The spring can store the mechanical energy of the triggering process and release them on the next cycle [41]. Then, Jiang's group has utilized the high-performance polymer as the triboelectric material to improve the output of the spring assistance TENG in 2018 [42]. This type of spring assistance TENG has the problem on the durability and the elasticity decreasing of the spring will change the output of the TENG with increasing of the time.

In this study, a simple wave driven (WD)-TENG was designed, fabricated, and evaluated to convert the kinetic energy from wave energy to generate electricity. The hydrodynamic model of the designed and optimized TENGs with various geometries was built to calculate the hydrodynamic features and predict the performance of the TENGs under the simulated wave spectrum through computational fluid dynamics simulation. Meanwhile, effect of the WD-TENG output with the external factors from the ocean wave has been analyzed experimentally. The material used in the WD-TENG is recyclable to adopt increasingly stringent environmental regulations. This WD-TENG shows strong adaptability under different frequencies and amplitudes of ocean waves with excellent durability and also demonstrates the excellent capability for wave energy harvest.

3.2 Experimental section

3.2.1 Device fabrication and assembling

The body of the WD-TENG is made of an acrylic tube obtained from lampshade with a 150 mm length, and 3D-printing components are made from polylactic acid (PLA). The acrylic tube has inner and outer diameters of 64 mm and 70 mm, respectively. The caps are made by 3D printing (Monoprice Maker Ultimate 2 +, Rancho Cucamonga, USA). It has a 62.5 mm inner diameter with a 15 mm height, and the outer diameter is 73 mm with 1.4 mm thickness and 10 mm height. To reduce the weight of the device, the hollow-out processing is applied on both caps. A 34.91 mm^2 island is made at the edge of the inner circle of both caps to place the transmission layer, which will transmit the current yielded by the triboelectric material inside the tube to the outside collectors.

3.2.2 Triboelectric material selection

Firstly, a 290 μ m thick PTFE film was coated with a 50 nm thickness gold (Q300T-D, Quorum, UK) on one side as the electrode layer. The 280 μ m Al film does not need an electrode layer because itself is a conductor. These two PTFE films with a diameter of 62.5 mm were placed on the two 3D-printed caps. Then, the prepared two 250 μ m thickness Al films with 60 mm diameter were placed on the 3D-printed internal sliding module. A small size copper piece was fixed on both caps as the transmission layer to transfer the electrical power of the Al films to the outside.

3.2.3 Simulated wave amplitude and frequency

An experiment platform has been designed to simulate different external frequency and amplitude effects on the WD-TENG. The platform is fabricated by using the 3D printing machine (Monoprice Maker Ultimate 2 +, Rancho Cucamonga, USA). The platform is driven by a DC step motor, by changing the components and voltage input of the DC step motor to realized different frequencies and amplitudes.

3.2.4 Hydrodynamic performance under computational fluid dynamic simulation

The hydrodynamic model of the WD-TENG was built by ANSYS AQWA. The geometric model and hydrodynamic model are shown in Figure 3.1. The hydrodynamic coefficients were calculated by AQWA. AQWA can well solve the radiation/diffraction model and multi-body interaction in fluid. It is a general hydrodynamics software based on the potential flow theory and the three-dimensional second-order radiation/ diffraction slice theory. It can be used to solve the velocity potential and first-order second-order force acting on the floating body wet surface. The JONSWAP spectrum was used as a wave spectrum here to simulate the WD-TENG performance under an irregular wave. Various geometrical parameters of the WD-TENG have been used in the simulation to obtain the optimized geometrical parameters, which will be used for fabricating the physical WD-TENG for experimental evaluation. The detail information on main parameters of WD-TENG, hydrodynamic

simulation parameters and the wave spectrum is listed in supporting information of Tables S3.1-S3.3 and Figure S3.1.

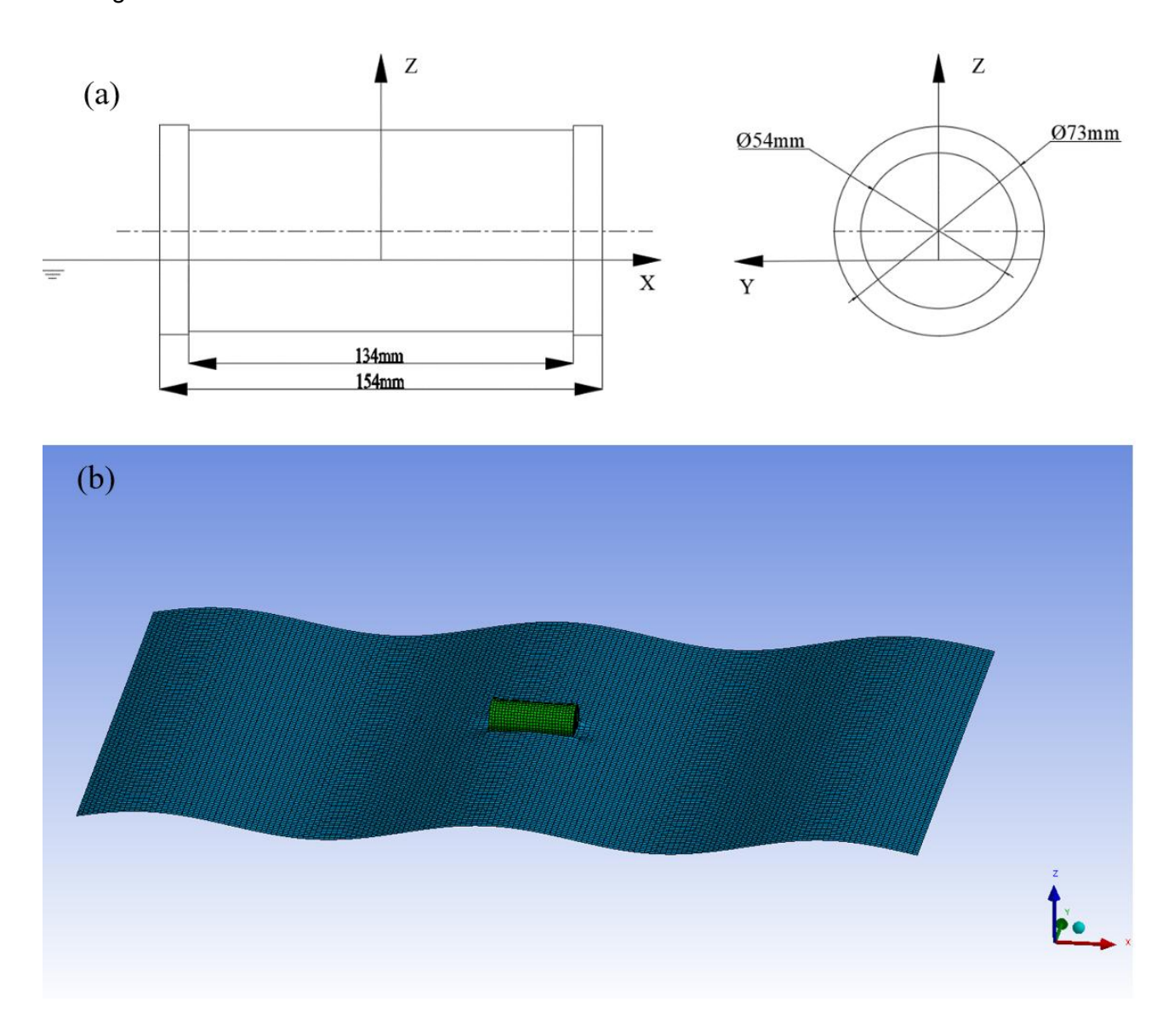


Figure 3.1 (a) Geometric model and (b) hydrodynamic model of the WD-TENG. The length of the WD-TENG is in the X direction and the radius direction of the WD-TENG is in the Y direction in the simulation.

3.2.5 WD-TENG charge performance evaluation

To demonstrate the WD-TENG application, a bridge full-wave rectifier was used to convert AC voltage to DC voltage for charging an empty capacitor. An oscilloscope (Keysight, infiniiVision MS0-X 2004A, USA) was connected to the capacitor to monitor the changing of the capacitor in a minute. Three commercial capacitors with the capacities of 47 μ F, 100 μ F, and 470 μ F were connected to the WD-TENG.

3.3 Results and discussion

As reported, when the maximum displacement between two triboelectric materials, i.e., h is chosen to be ~10 times of the thickness of the materials, the output voltage reaches the maximum value [43]. So, h was designed as 8 mm here to ensure the output voltage is on the maximum condition ranges, as shown in Figure 3.2(a). The mechanism of energy generation is shown in Figure 3.2 (b). When the Al film on the internal sliding module moves to the PTFE film until they are fully conducted, the positive charge and negative charge were generated on the surfaces of Al and PTFE films, respectively, as shown in Figure 3.2(b)(1). When the separation starts between the Al and PTFE films, the electron from the negative charge material, i.e., PTFE flows to the positive charge material, i.e., Al to keep the electric neutrality between two triboelectric materials, as shown in Figure 3.2 (b)(2). These two triboelectric materials need full separation to achieve the maximum charge transfer capacity, as shown in Figure 3.2(b)(3). Then, the electron flow from the positive charge material, i.e., Al to the positive charge material, i.e., PTFE to generate an opposite direction current, as shown in Figure 3.2(b)(4). An exploded view of the proposed WD-TENG, shown in Figure 3.2(c), consists of five components. The acrylic tube is the base of the WD-TENG, and other components were assembled into the tube. The two caps are used to place the PTFE films on the inside surfaces and seal the whole structure to avoid water penetration. The internal sliding module is used to facilitate the Al films. There are six hemispheres on each bottom of the module to reduce the friction and vibration between the module and the acrylic tube when WD-TENG is working. This design facilitates two generators into one device to increase the utilization ratio of the wave energy, as shown in Figure 3.2(c). The geometry of the fabricated WD-TENG has been optimized by the simulation which will be discussed below.

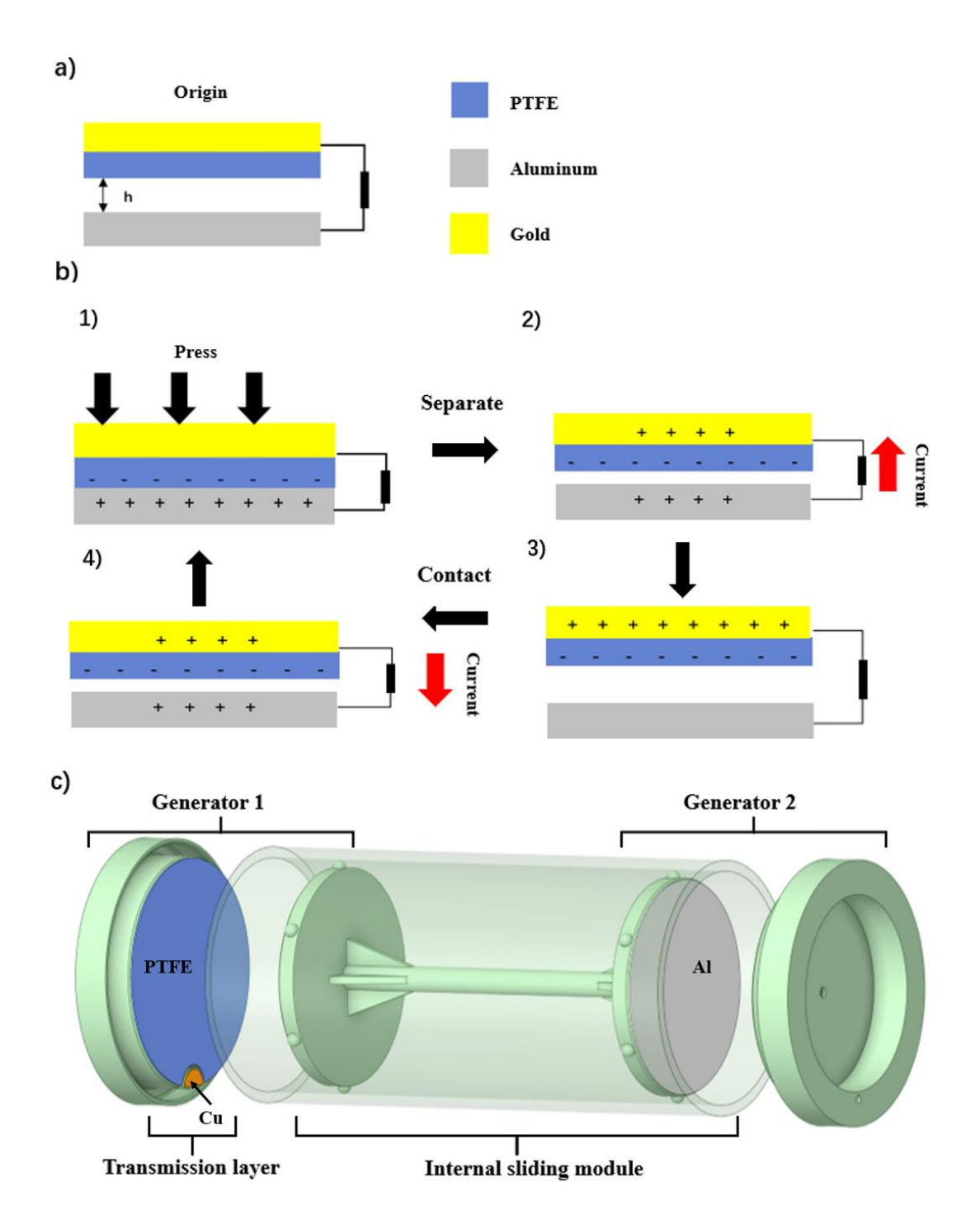


Figure 3.2 (a) The initiate condition of the WD-TENG, where h is the maximum distance between two triboelectric materials. (b) The energy generation cycle of the WD-TENG (c) The exploded view drawing of the WD-TENG with the components. Two generators have the same functions, structures, and performances. There is a I-shape internal sliding module inside the acrylic tube, used to place Aluminum (AI) films (grey colour). The acrylic tube is sealed by two 3D-printed caps. Each cap is equipped with a PTFE film (blue colour) and a small piece of copper (orange colour). The copper piece acted as the transmission layer to transfer the electrical energy from the AI films to the outside collector.

The optimal load resistance for the WD-TENG is firstly determined in this study. Since the triboelectric material has its impedance (Z), the output of the TENG is normally connected to a load resistance (R_L) to keep the output current, as shown in the inset of Figure 3.3(c). The output efficiency of the TENG is most relevant to the load resistance based on Equation (3.1), which is used to determine the voltage across the component in the circuit.

$$V_{Load} = V_o \times \frac{R_L}{R_L + Z} \times 100\% \tag{3.1}$$

where V_o and V_{Load} represents the output voltage of a TENG and the voltage across the load resistance, respectively, R_L and Z represent the load resistance and internal impedance of the triboelectric material, respectively. Based on Equation (3.1), the efficiency for the load circuit can be obtained in Equation (3.2).

$$Efficency(\%) = \frac{R_L}{R_L + Z} \times 100\% \tag{3.2}$$

Under the maximum speed of 0.582 m/s (based on the maximum rotation speed of the step motor chosen in this experiment), and the fixed displacement of 8.3 cm conditions (dependent on the driving disk which fixed on the step motor) in the 3D printed test platform, the mean open-circuit voltage and short-circuit current of the WD-TENG is 333.67 V and 25.07 μ A, respectively in a 1.5-seconds period with the stable and repeatable waveforms, as shown in Figure 3.3(a) and (b). The load voltage increases with the increase of the load resistance; however, the load current has a opposite trend, as shown in Figure 3.3(c). Figure 3.3(d) shows the power density of the WD-TENG as a function of load resistance. It shows that under the 5 M Ω resistance, the system achieved the highest power density, which demonstrated the optimized the load resistance for the current WD-TENG design where the WD-TENG can reach the maximum efficiency. This load resistance is used for evaluating the external effect factor in this study. The maximum transferred charge under this experiment condition is 19.81 nC with the detail calculation in Figure S3.2.

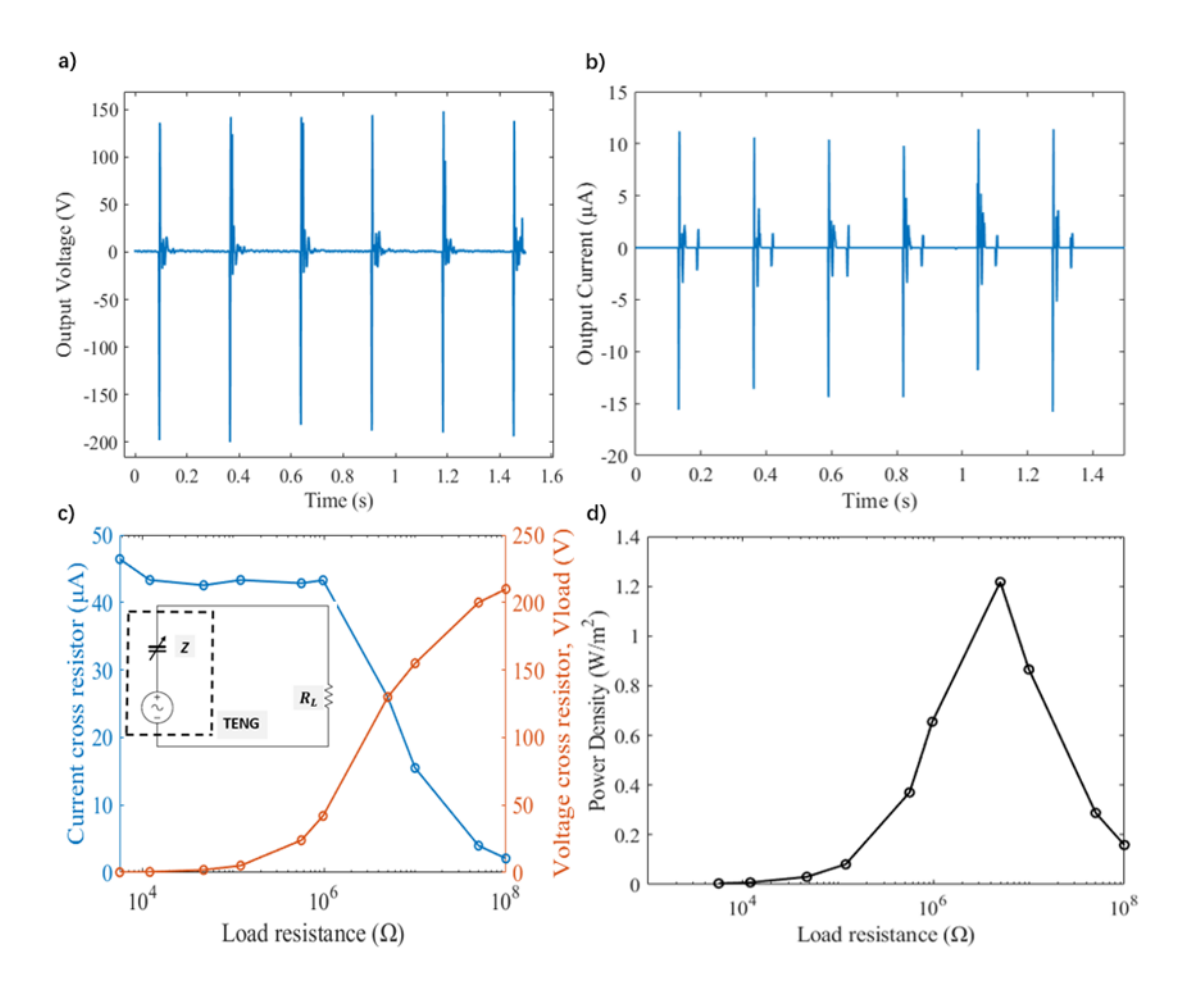
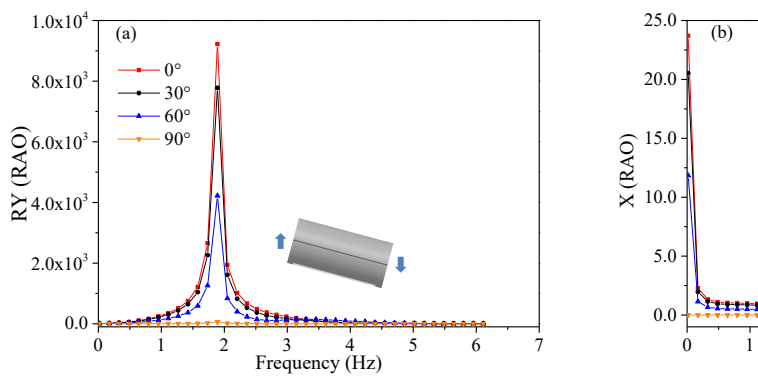


Figure 3.3 (a) Typical waveform of the output voltage, (b) typical waveform of the output current, (c) change of current cross resistor and voltage cross resistor under different load resistances, and (d) change of power density under different load resistances. The electrical output of the WD-TENG under the maximum speed of 0.582 m·s⁻¹ and acceleration of 4.07 m·s⁻². The maximum displacement of the WD-TENG is 8.3 cm and the maximum displacement between PTFE and Al films is 8 mm.

As analytical demonstration shown in supporting information with Figure S3.3 and Equations (S3.2-S3.7), increasing amplitude and frequency will increase the slide velocity of the internal sliding module, which affects the output result of the WD-TENG. The hydrodynamic performance of the WD-TENGs with various geometries and the performance of the WD-TENGs under a certain wave spectrum are simulated under computational fluid dynamics (CFD). The six degrees of freedom (6 DOF) motion of a WD-TENG is considered in the simulation, the most relevant motions of surge (the X direction) and pitch (the RY direction) are shown in Figure 3.4. The calculation results in other directions are shown in the support information of Figure S3.4. For the analysis of a WD-TENG, only the interval between 0° and 90° is calculated because of the symmetry of the structure. The wave direction angle defines the positive X-axis direction as 0°. In the field of ship design and design of other floating structures, a response amplitude operator (RAO) is an engineering statistic, or set of such statistics, that are used to determine the likely behaviour of a floating structure when operating

at sea [44]. RAOs are effectively transfer functions used to determine the effect that a sea state will have upon the motion of a float structure through the water. The pitch RAO (Figure 3.4(a)) and surge RAO (Figure 3.4(b)) of the WD-TENG in the wave directions of 0°, 30°, 60° and 90° are calculated respectively. As shown in Figure 3.4(a), the pitch RAO in the 90° wave direction of the WD-TENG is almost 0. The trend of RAO at 0°, 30° and 60° wave direction of the WD-TENG is roughly the same, and the peak appear at 1.891 Hz. In terms of surge shown in Figure 3.4(b), in the low-frequency phase, the surge RAO of the WD-TENG was large, while in the high-frequency phase, the surge RAO of the WD-TENG decreases suddenly toward zero. The corresponding wavelength is long, i.e., the wave frequency is low, the surge RAO of the WD-TENG without any constraints is larger under the action of a longer wavelength wave.



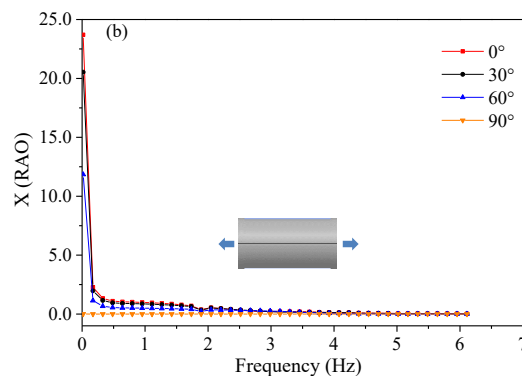


Figure 3.4 Response amplitude operators (RAOs) of the WD-TENG in (a) pitch and (b) surge under CFD simulation.

Ocean waves are produced by the wind. The faster the wind, the longer the wind blows, and the bigger the area over which the wind blows. Considering the working characteristics of WD-TENG, the Joint North Sea Wave Observation Project (JONSWAP) spectrum was used as the irregular wave spectrum with the spectrum parameters listed in supporting information of Table S3.3. Figure 3.5(a) and (b) show the time-history curves of displacement of the pitch and surge under the action of the wave in the 0° direction, respectively. The displacements are calculated with the centre of gravity of the WD-TENG as the reference point. The maximum and minimum displacement in the surge is -0.329 m and -0.457 m, respectively. While the maximum and minimum displacement in the pitch (the RY direction) is 2.280 ° and -2.784 °, respectively. Based on the displacement difference during pitch, it is easy to calculate the maximum amplitude of 13.6 cm can be achieved by WD-TENG under the current wave spectrum (See support information and Figure 3.6). The time-history curves of WD-TENG velocity of pitch and surge under the action of the wave are shown in Figure S3.5. The displacement frequency spectra in the pitch and surge directions of the WD-TENG with the vertical coordinate representing the amplitude of the vibration response after the Fourier transform are shown in Figure 3.5(c) and (d), respectively. In the surge direction of the WD-TENG, the frequency corresponding to the maximum amplitude is 1.953 and the characteristics of multifrequency vibration and broadband vibration are obvious, and the main vibration range is from 1 Hz to 3 Hz. In the pitch direction of the WD-TENG, the frequency corresponding to the maximum amplitude is 2.305. The characteristics of multi-frequency vibration and broadband vibration are more obvious, and the main vibration range is from 0.5 Hz to 3 Hz. Figure 3.5 shows that the designed WD-TENG has a broad structure response in surge and pitch directions with max response among 1.9-2.3 Hz.

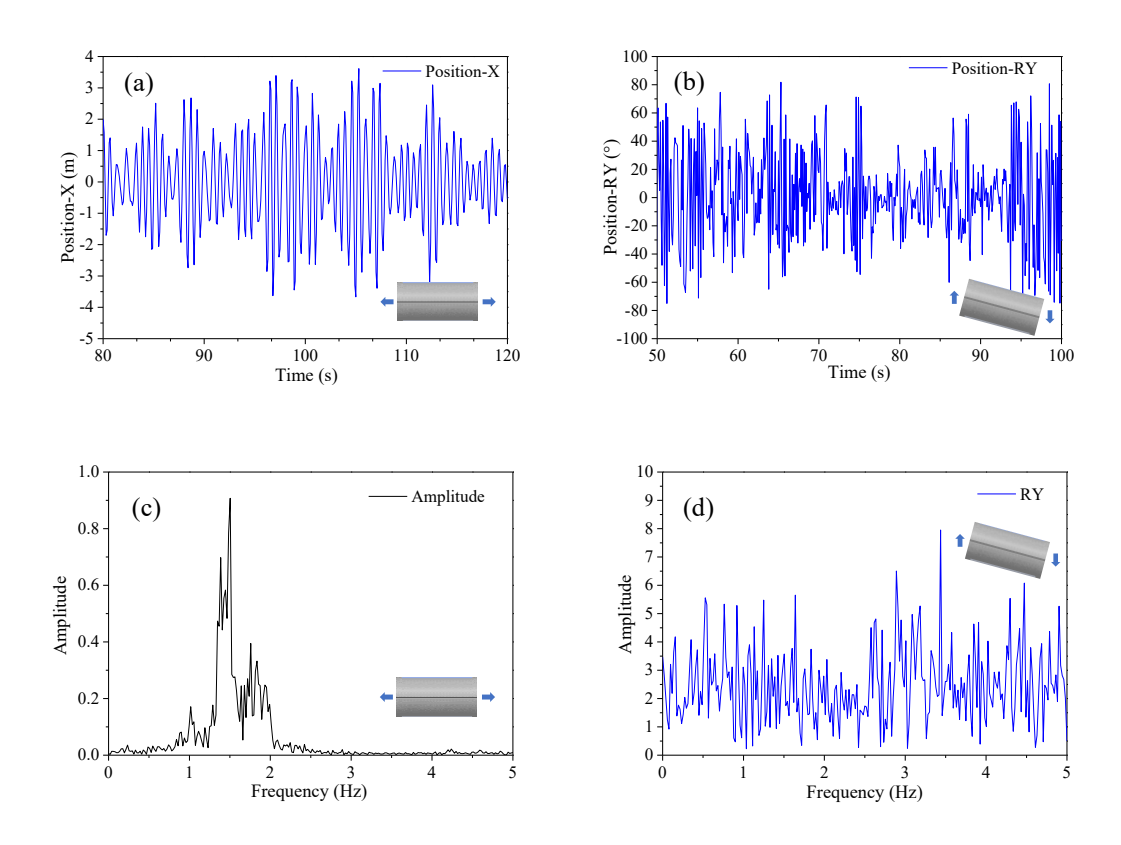


Figure 3.5 WD-TENG (a) and (b) time-history curves of position and (c) and (d) structural response frequency spectra in (a) and (c) surge (the X direction) and (b) and (d) pitch (the RY direction).

The hydrodynamic characteristics of WD-TENGs with different geometries are simulated to understand the TENG geometry effects on its performance and provide an optimized best-performance geometry parameter for experimental evaluation. Four cases are proposed, as listed in Table 3.1 with initial length L₀= 154 mm and initial diameter D₀=73 mm (Case 2 in this study, also the best performance geometry).

Table 3.1 Size information for various WD-TENGs

Case 1	Case 2 (Current)	Case 3	Case 4
Length: 0.5L ₀	Length: 1.0L ₀	Length: 2.0L ₀	Length: 2.0L ₀
Diameter: 1.0D ₀	Diameter: 1.0D ₀	Diameter: 1.0D ₀	Diameter 2.0D ₀
$L/D=1/2 (L_0/D_0)$	$L/D=L_0/D_0$	$L/D=2 (L_0/D_0)$	$L/D=L_0/D_0$

Figure S3.6-S3.9 shows RAOs of the pitch and surge of Cases 1-4, respectively. The larger the ratio of length to diameter (L/D), the higher the pitch frequency is. Also, a larger RAO will be generated in a broad frequency range. If the L/D is the same, the larger the diameter, the higher the frequency is. The L/D has no obvious effect on the RAO of the surge. Figure S3.10-S3.13 show the time-history curves of displacement and structural response frequency spectra of the pitch and surge of Cases 1-4 under the action of the wave in the 0° direction, respectively. In the surge direction of the WD-TENG, the characteristics of multi-frequency vibration and broadband vibration are obvious. The frequency responses to the maximum amplitude and the main vibration range of Cases 1-4 are shown in Table 3.2. It can be seen that the vibration amplitude of Case 2 is the largest and the frequency domain that produces a large vibration response is the widest. The maximum and minimum displacement in the surge is 3.61 m and -3.66 m, respectively. Based on the simulation, Case 2 can generate large vibration response amplitude over a wide range of frequency domains, so it has been chosen as the geometry for experimental evaluation.

Table 3.2 Vibration response characteristics of WD-TENGs with various geometries

	The frequency corresponding to the maximum amplitude	The main vibration range
Case 1	1.133 Hz	From 0.75 Hz to 1.50 Hz
Case 2	1.504 Hz	From 1.00 Hz to 2.00 Hz
Case 3	0.4883 Hz	from 0.25 Hz to 0.70 Hz
Case 4	0.6055 Hz	from 0.50 Hz to 0.75 Hz

Based on the above CFD simulation results, experimental setup has been conducted. The effects of external amplitude and frequency on the WD-TENG with optimized geometries have been evaluated. Figure 3.6(a) shows the output voltage of the WD-TENG with the changing of the external amplitude and according to the results shown in Figure 3.5, the constant frequency of 2.2 Hz has been selected in this experiment. When the amplitude is less than 10.25 cm, the open circuit voltage is almost constant with the magnitude around 100 V. However, when the amplitude is large than 10.25 cm, the open-circuit voltage increases to 133 V with the amplitude reaching 11.5 cm. The waveform of the power density has the almost same trend with that of the output voltage, and the maximum power density reaches 0.22 W/m² under 11.6 cm amplitude, as shown in Figure 3.6(a). The waveform of the WD-TENG under the different amplitudes is shown in Figure S3.14. The frequency range used to the current experiment is from 3 Hz to 7 Hz which are the common ocean wave frequency range in the offshore and covers the reported low frequency of 5 Hz in TENG studies [45]. The output voltage of the WD-TENG increases with the increase of the frequency, and the output voltage under

the testing frequency of 7 Hz is around 333.67 V, and the maximum power density reach 1.23 W/m² under 11.6 cm amplitude as shown in Figure 3.6(b). The power density reaches the saturation condition when the external frequency reaches 5 Hz. The waveform of the WD-TENG under the different frequencies is shown in Figure S3.15. The waveform of the output current is similar with the waveform of power density, and waveform of the output current for different frequencies and amplitudes are shown in Figure S3.16. At 7 Hz, the device achieved a maximum power density of approximately 3.36 W/m³ obtained from Equation (3.3).

Power density per
$$m^3 = \frac{1}{V_{(WD-TENG)}} \times \frac{output\ voltage_{(at\ 7\ Hz)}}{output\ current_{(at\ 7\ Hz)}}$$
 (3.3)

Where, output voltage at 7 Hz is 333.67 V as shown in Figure 3.6 and output current is 26 μ A which refers to the figure S3.16 (B).

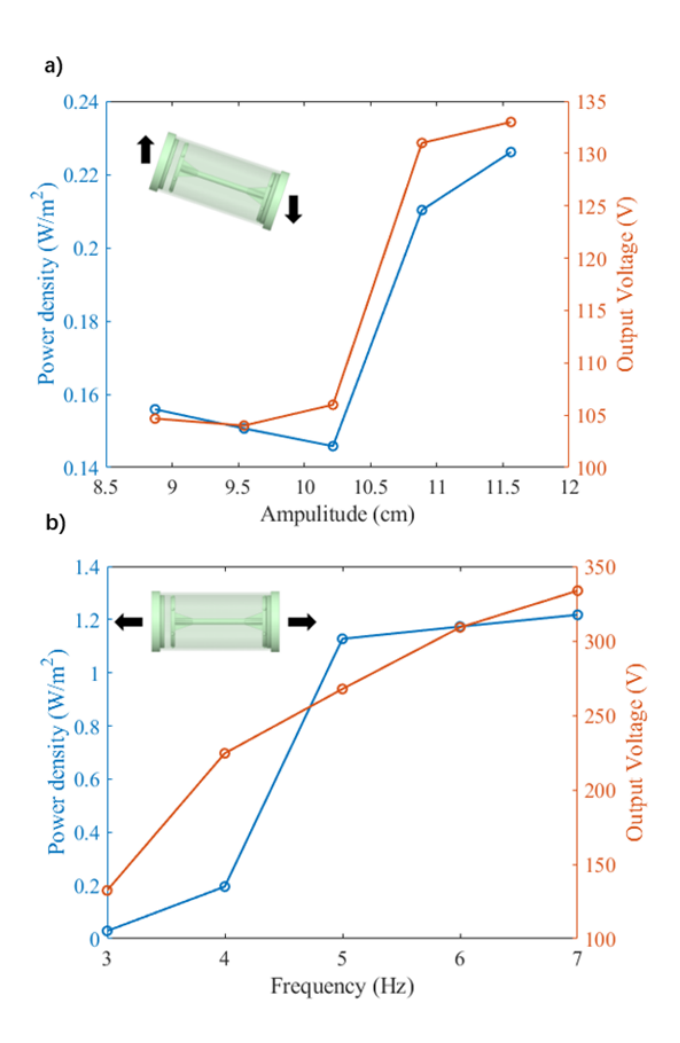


Figure 3.6 Effect of (a) external amplitude and (b) frequency on the output voltage and the power density of the WD-TENG. The frequency in (a) is 2.2 Hz, and the amplitude in (b) is fixed as 0. The load resistance is $5 \text{ M}\Omega$.

The robustness of the WD-TENG operated under the best conditions, i.e., frequency of 2.2 Hz and amplitude of 11.6 cm was evaluated. The output voltage of the WD-TENG within 8 hours has been monitored and 20-seconds output voltages at various time intervals are shown in Figure 3.7(a). At

the initial conditions and after the 2-hour operations, the output voltages are the same with the value of 131 V. After the 4-hours operation, the output voltage of the WD-TENG slightly reduces to 112 V, but the value becomes stable and repeatable until the experiment was finished at 8 hours. The result indicates that the WD-TENG has decent durability and robustness under continuous operation. The observed decrease in the output voltage of the WD-TENG can be caused by triboelectric material fatigue [46], which leads to the mechanical degradation of the triboelectric materials [47]. In addition, charge dissipation [48] may be another potential factor influencing the output performance of the TENG during generation. Meanwhile, the WD-TENG can charge the 47 μ F to 0.496V in a minute under 5 Hz frequency. When the capacitance increasing, the charging voltage is decreasing, as shown in Figure 3.7(b). The charging speed of the smaller capacitance is higher than that of the larger capacitances due to the impedance of the capacitor is inverse with the capacitance.

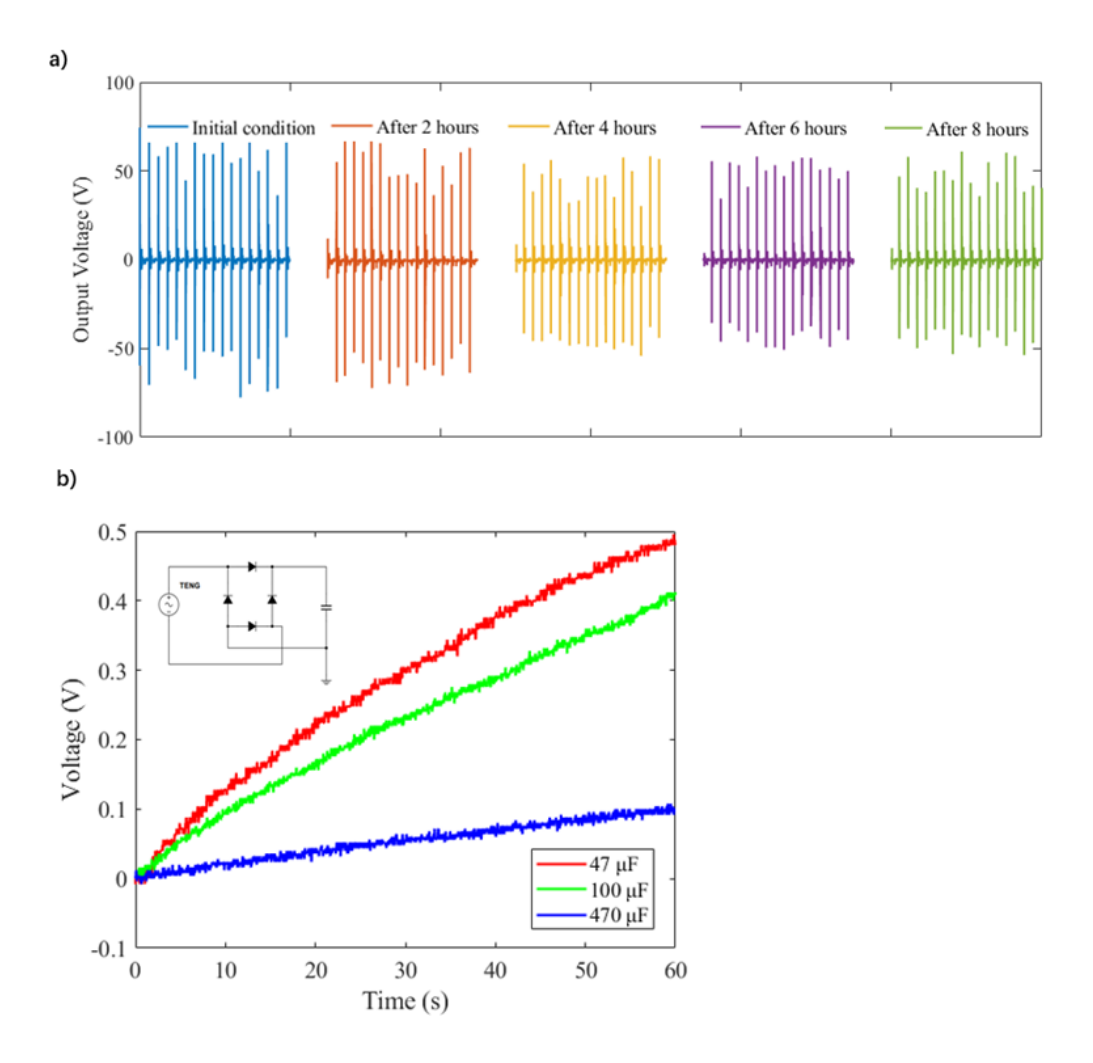


Figure 3.7 (a) The output voltage of the WD-TENG after 2-, 4-, 6-, and 8-hours operation under 2.2 Hz frequency and 11.6 cm amplitude, and (b) the WD-TENG as an electrical generator to charge an empty capacitor. The charging curves of three different capacitors, i.e., 47 μ F, 100 μ F, and 470 μ F. The testing condition is 5 Hz frequency and 0 amplitude.

3.4 Conclusion

In this study, a wave driven (WD)-TENG, i.e., two generators integrated into a recyclable tube has been designed and cost-effectively fabricated to convert the ocean wave energy to electricity. Based on CFD simulation results on the hydrodynamic behaviour of the WD-TENG and the structure performance under a regular wave spectrum, an experiment testing platform has been built to simulate wave frequency and amplitude to evaluate those external factors on voltage output of the WD-TENG experimentally. The testing result indicates the WD-TENG can almost reach the rated output at 5 Hz with 1.05 W/m² power density. The WD-TENG also demonstrated decent durability and strong adaptability under different frequencies and amplitudes of ocean waves. Meanwhile, the WD-TENG can sustainably charge a 47 µF capacitor to 0.496 V in a minute. The exchange charge density of the used triboelectric materials arising from the triboelectric charge exchange is 19.81 nC.

3.5 Reference

- [1] Z.L. Wang, T. Jiang, L. Xu, Toward the blue energy dream by triboelectric nanogenerator networks, Nano Energy 39 (2017), 9-23, https://doi.org/10.1016/j.nanoen.2017.06.035.
- [2] G. Zhu, B. Peng, J. Chen, Q. Jing, Z. Lin Wang, Triboelectric nanogenerators as a new energy technology: from fundamentals, devices, to applications, Nano Energy 14 (2015), 126-138, https://doi.org/10.1016/j.nanoen.2014.11.050.
- [3] F.-R. Fan, Z.-Q. Tian, Z. Lin Wang, Flexible triboelectric generator, Nano Energy 1 (2012), 328-334, https://doi.org/10.1016/j.nanoen.2012.01.004.
- [4] S. Wang, L. Lin, Z.L. Wang, Triboelectric nanogenerators as self-powered active sensors, Nano Energy 11 (2015), 436-462, https://doi.org/10.1016/j.nanoen.2014.10.034.
- [5] L. Liu, Q. Shi, J.S. Ho, C. Lee, Study of thin film blue energy harvester based on triboelectric nanogenerator and seashore IoT applications, Nano Energy 66 (2019), 104167,

https://doi.org/10.1016/j.nanoen.2019.104167.

[6] G. Liu, H. Guo, S. Xu, C. Hu, Z.L. Wang, Oblate spheroidal triboelectric nanogenerator for all-weather blue energy harvesting, Advanced Energy Materials 9 (2019), 1900801,

https://doi.org/10.1002/aenm.201900801.

[7] Z. Wen, H. Guo, Y. Zi, M.-H. Yeh, X. Wang, J. Deng, J. Wang, S. Li, C. Hu, L. Zhu, Z.L. Wang, Harvesting broad frequency band blue energy by a triboelectric-electromagnetic hybrid nanogenerator, ACS Nano 10 (2016), 6526-6534, http://doi.org/10.1021/acsnano.6b03293.

- [8] Z.L. Wang, L. Lin, J. Chen, S. Niu, Y. Zi, Triboelectric nanogenerator: vertical contact-separation mode. In Triboelectric Nanogenerators, Springer International Publishing: Cham, 2016; pp 23-47, https://doi.org/10.1007/978-3-319-40039-6 2.
- [9] X. Yin, D. Liu, L. Zhou, X. Li, C. Zhang, P. Cheng, H. Guo, W. Song, J. Wang, Z.L. Wang, Structure and dimension effects on the performance of layered triboelectric nanogenerators in contact-separation mode, ACS Nano 13 (2019), 698-705, http://doi.org/10.1021/acsnano.8b07935.
- [10] B. Yang, X.-m. Tao, Z.-h. Peng, Upper limits for output performance of contact-mode triboelectric nanogenerator systems, Nano Energy 57 (2019), 66-73,

https://doi.org/10.1016/j.nanoen.2018.12.013.

- [11] S. Niu, S. Wang, L. Lin, Y. Liu, Y.S. Zhou, Y. Hu, Z.L. Wang, Theoretical study of contact-mode triboelectric nanogenerators as an effective power source, Energy & Environmental Science 6 (2013), 3576-3583, http://doi.org/10.1039/C3EE42571A.
- [12] Z.L. Wang, Triboelectric nanogenerators as new energy technology and self-powered sensors principles, problems and perspectives, Faraday Discussions 176 (2014), 447-458,

http://doi.org/10.1039/C4FD00159A.

- [13] B. Yang, W. Zeng, Z.-H. Peng, S.-R. Liu, K. Chen, X.-M. Tao, A fully verified theoretical analysis of contact-mode triboelectric nanogenerators as a wearable power source, Advanced Energy Materials 6 (2016), 1600505, https://doi.org/10.1002/aenm.201600505.
- [14] S. Niu, Y. Liu, S. Wang, L. Lin, Y.S. Zhou, Y. Hu, Z.L. Wang, Theory of sliding-mode triboelectric nanogenerators, Advanced Materials 25 (2013), 6184-6193,

https://doi.org/10.1002/adma.201302808.

- [15] J. Shao, T. Jiang, W. Tang, L. Xu, T.W. Kim, C. Wu, X. Chen, B. Chen, T. Xiao, Y. Bai, Z.L. Wang, Studying about applied force and the output performance of sliding-mode triboelectric nanogenerators, Nano Energy 48 (2018), 292-300, https://doi.org/10.1016/j.nanoen.2018.03.067.
- [16] H. Zhang, C. Zhang, J. Zhang, L. Quan, H. Huang, J. Jiang, S. Dong, J. Luo, A theoretical approach for optimizing sliding-mode triboelectric nanogenerator based on multi-parameter analysis, Nano Energy 61 (2019), 442-453, https://doi.org/10.1016/j.nanoen.2019.04.057.
- [17] W. Zhang, D. Diao, K. Sun, X. Fan, P. Wang, Study on friction-electrification coupling in sliding-mode triboelectric nanogenerator, Nano Energy 48 (2018), 456-463,

https://doi.org/10.1016/j.nanoen.2018.04.007.

- [18] W.-Z. Song, H.-J. Qiu, J. Zhang, M. Yu, S. Ramakrishna, Z.L. Wang, Y.-Z. Long, Sliding mode direct current triboelectric nanogenerators, Nano Energy 90 (2021), 106531,
- https://doi.org/10.1016/j.nanoen.2021.106531.
- [19] Y. Hu, X. Wang, H. Li, Z. Li, N. Sun, Tribological properties and electrification performance of patterned surface for sliding-mode triboelectric nanogenerator, Langmuir 35 (2019), 9396-9401, http://doi.org/10.1021/acs.langmuir.9b01020.
- [20] Y. Xie, S. Wang, L. Lin, Q. Jing, Z.-H. Lin, S. Niu, Z. Wu, Z.L. Wang, Rotary triboelectric nanogenerator based on a hybridized mechanism for harvesting wind energy, ACS Nano 7 (2013), 7119-7125, http://doi.org/10.1021/nn402477h.
- [21] C. Zhang, Y. Liu, B. Zhang, O. Yang, W. Yuan, L. He, X. Wei, J. Wang, Z.L. Wang, Harvesting wind energy by a triboelectric nanogenerator for an intelligent high-speed train system, ACS Energy Letters 6 (2021), 1490-1499, http://doi.org/10.1021/acsenergylett.1c00368.
- [22] X. Fan, J. He, J. Mu, J. Qian, N. Zhang, C. Yang, X. Hou, W. Geng, X. Wang, X. Chou, Triboelectric-electromagnetic hybrid nanogenerator driven by wind for self-powered wireless transmission in internet of things and self-powered wind speed sensor, Nano Energy 68 (2020), 104319 https://doi.org/10.1016/j.nanoen.2019.104319.
- [23] J. Wang, W. Ding, L. Pan, C. Wu, H. Yu, L. Yang, R. Liao, Z.L. Wang, Self-powered wind sensor system for detecting wind speed and direction based on a triboelectric nanogenerator, ACS Nano 12 (2018), 3954-3963, http://doi.org/10.1021/acsnano.8b01532.
- [24] H. Zhang, J. Wang, Y. Xie, G. Yao, Z. Yan, L. Huang, S. Chen, T. Pan, L. Wang, Y. Su, W. Yang, Y. Lin, Self-powered, wireless, remote meteorologic monitoring based on triboelectric nanogenerator operated by scavenging wind energy, ACS Applied Materials & Interfaces 8 (2016), 32649-32654, http://doi.org/10.1021/acsami.6b12798.
- [25] L. Long, W. Liu, Z. Wang, W. He, G. Li, Q. Tang, H. Guo, X. Pu, Y. Liu, C. Hu, High performance floating self-excited sliding triboelectric nanogenerator for micro mechanical energy harvesting, Nature Communications 12 (2021), 4689, http://doi.org/10.1038/s41467-021-25047-y.
- [26] J. Qian, X. Jing, Wind-driven hybridized triboelectric-electromagnetic nanogenerator and solar cell as a sustainable power unit for self-powered natural disaster monitoring sensor networks, Nano Energy 52 (2018), 78-87, https://doi.org/10.1016/j.nanoen.2018.07.035.
- [27] S. Sriphan, N. Vittayakorn, Facile roughness fabrications and their roughness effects on electrical outputs of the triboelectric nanogenerator, Smart Materials and Structures 27 (2018), 105026, http://doi.org/10.1088/1361-665x/aadb65.

- [28] B. Chen, Y. Yang, Z.L. Wang, Scavenging wind energy by triboelectric nanogenerators, Advanced Energy Materials 8 (2018), 1702649, https://doi.org/10.1002/aenm.201702649.
- [29] M. Melikoglu, Current status and future of ocean energy sources: a global review, Ocean Engineering 148 (2018), 563-573, https://doi.org/10.1016/j.oceaneng.2017.11.045.
- [30] A. Khaligh, O.C. Onar, Energy harvesting: solar, wind, and ocean energy conversion systems. CRC press: Boca Raton, FL, 2017.
- [31] B. Huang, P. Wang, L. Wang, S. Yang, D. Wu, Recent advances in ocean wave energy harvesting by triboelectric nanogenerator: an overview, Nanotechnology Reviews 9 (2020), 716-735, http://doi.org/doi:10.1515/ntrev-2020-0055.
- [32] X. Wang, S. Niu, Y. Yin, F. Yi, Z. You, Z.L. Wang, Triboelectric nanogenerator based on fully enclosed rolling spherical structure for harvesting low-frequency water wave energy, Advanced Energy Materials 5 (2015), 1501467, https://doi.org/10.1002/aenm.201501467.
- [33] L. Xu, T. Jiang, P. Lin, J.J. Shao, C. He, W. Zhong, X.Y. Chen, Z.L. Wang, Coupled triboelectric nanogenerator networks for efficient water wave energy harvesting, ACS Nano 12 (2018), 1849-1858, http://doi.org/10.1021/acsnano.7b08674.
- [34] X. Zhang, Y. Zhang, B. Tian, K. Song, P. Liu, Y. Jia, X. Chen, J. An, Z. Zhao, Y. Liu, A.A. Volinsky, X. Li, T. Yin, Review of nano-phase effects in high strength and conductivity copper alloys, Nanotechnology Reviews 8 (2019), 383-395, http://doi.org/doi:10.1515/ntrev-2019-0034.
- [35] M. Gao, F. Zheng, J. Xu, S. Zhang, S.S. Bhosale, J. Gu, R. Hong, Surface modification of nano-sized carbon black for reinforcement of rubber, Nanotechnology Reviews 8 (2019), 405-414, http://doi.org/doi:10.1515/ntrev-2019-0036.
- [36] P. Cheng, H. Guo, Z. Wen, C. Zhang, X. Yin, X. Li, D. Liu, W. Song, X. Sun, J. Wang, Z.L. Wang, Largely enhanced triboelectric nanogenerator for efficient harvesting of water wave energy by soft contacted structure, Nano Energy 57 (2019), 432-439,

https://doi.org/10.1016/j.nanoen.2018.12.054.

- [37] K. Xia, J. Fu, Z. Xu, Multiple-frequency high-output triboelectric nanogenerator based on a water balloon for all-weather water wave energy harvesting, Advanced Energy Materials 10 (2020), 2000426, https://doi.org/10.1002/aenm.202000426.
- [38] X. Yang, L. Xu, P. Lin, W. Zhong, Y. Bai, J. Luo, J. Chen, Z.L. Wang, Macroscopic self-assembly network of encapsulated high-performance triboelectric nanogenerators for water wave

energy harvesting, Nano Energy 60 (2019), 404-412, https://doi.org/10.1016/j.nanoen.2019.03.054.

[39] X. Wen, W. Yang, Q. Jing, Z.L. Wang, Harvesting broadband kinetic impact energy from mechanical triggering/vibration and water waves, ACS Nano 8 (2014), 7405-7412,

http://doi.org/10.1021/nn502618f.

[40] T. Jiang, L.M. Zhang, X. Chen, C.B. Han, W. Tang, C. Zhang, L. Xu, Z.L. Wang, Structural optimization of triboelectric nanogenerator for harvesting water wave energy, ACS Nano 9 (2015), 12562-12572, http://doi.org/10.1021/acsnano.5b06372.

[41] T. Jiang, Y. Yao, L. Xu, L. Zhang, T. Xiao, Z.L. Wang, Spring-assisted triboelectric nanogenerator for efficiently harvesting water wave energy, Nano Energy 31 (2017), 560-567, https://doi.org/10.1016/j.nanoen.2016.12.004.

[42] T.X. Xiao, T. Jiang, J.X. Zhu, X. Liang, L. Xu, J.J. Shao, C.L. Zhang, J. Wang, Z.L. Wang, Silicone-based triboelectric nanogenerator for water wave energy harvesting, ACS Applied Materials & Interfaces 10 (2018), 3616-3623, http://doi.org/10.1021/acsami.7b17239.

[43] H. Zou, Y. Zhang, L. Guo, P. Wang, X. He, G. Dai, H. Zheng, C. Chen, A.C. Wang, C. Xu, Z.L. Wang, Quantifying the triboelectric series, Nature Communications 10 (2019), 1427,

http://doi.org/10.1038/s41467-019-09461-x.

[44] Q. Ding, C. Li, B. Li, W. Hao, Z. Ye, Research on the influence of helical strakes and its parameters on dynamic response of platform of floating wind turbine based on optimization method of orthogonal design, Journal of Solar Energy Engineering 139 (2017),

http://doi.org/10.1115/1.4037091.

[45] Y. Zi, H. Guo, Z. Wen, M.-H. Yeh, C. Hu, Z.L. Wang, Harvesting low-frequency (<5 Hz) irregular mechanical energy: a possible killer application of triboelectric nanogenerator, ACS Nano 10 (2016), 4797-4805, http://doi.org/10.1021/acsnano.6b01569.

[46] C. Ma, A. Matin Nazar, A.H. Moradi, H. Goharian, G. Mao, M. Yari, X. Ji, S. Dong, Advanced triboelectric nanogenerator sensing technologies for high-efficiency cardiovascular monitoring, Energy Technology 13 (2025), 2401863. https://doi.org/10.1002/ente.202401863.

[47] S.R. White, N.R. Sottos, P.H. Geubelle, J.S. Moore, M.R. Kessler, S.R. Sriram, E.N. Brown, S. Viswanathan, Autonomic healing of polymer composites, Nature 409 (2001) 794–797. https://doi.org/10.1038/35057232.

[48] Y. Li, Y. Luo, H. Deng, S. Shi, S. Tian, H. Wu, J. Tang, C. Zhang, X. Zhang, J.-W. Zha, S. Xiao, Advanced dielectric materials for triboelectric nanogenerators: principles, methods, and applications, Advanced Materials 36 (2024) 2314380. https://doi.org/10.1002/adma.202314380.

CHAPTER 4 AN AFFORDABLE MINIATURE 3D-PRINTING WAVE-GENERATION DEVICE FOR WAVE ENERGY HARVESTING APPLICATION

This chapter has been published on Micromachines with DOI: 10.3390/mi15121500. **Yunzhong Wang**: Conceptualization, methodology, software, validation, formal analysis, investigation, data curation.

4.1 Introduction

Energy crisis is a straight challenge in the 21st century, with deeply effect for human civilisation development, particularly concerning electrical energy. The urgent need for alternative energy sources, driven by carbon neutrality regulations worldwide, has encouraged governments and organisations to focus on investigating clean energy solutions that do not contribute to carbon emissions [1]. Ocean wave energy has emerged as a focal point of interesting due to the pressing challenges of the global energy crisis. With approximately 71% of the Earth's surface covered by oceans. Ocean wave energy holds substantial potential as a sustainable and renewable energy solutions without the significant environment effect and need for land [2,3]. Recently, researchers have focused on developing low-frequency and low-amplitude energy harvesters involving electromagnetic generators (EMG) and triboelectric nanogenerators (TENG) to harvest ocean wave energy [4–11]. However, the lack of an affordable evaluation platform has seriously limited the further development of ocean wave energy harvesters towards real applications because current groundbased water channels are oversized, requiring massive amounts of land and being expensive to construct, making them hard to afford. Studying dynamics of ocean wave energy harvester under realistic ocean wave conditions is seriously crucial for evaluating the output performance of ocean wave energy harvesters and is also contribute to device's designing optimisation. Previous researchers have used the commercial simulation software to find the best response frequency and amplitude to guide the design of ocean wave energy harvester [12]. Nonetheless, finite element simulation results often lack realism due to overfitting. As a result, researchers are attempting to modify existing devices to generate water waves for evaluating the performance of ocean wave energy harvesters. For instance, Wang et al. and Zhao et al. placed an electric water pump into a water tank to generate water waves. However, the generated waves were irregular and lacked variability in both frequency and amplitude because the waveform depended on the inlet and outlet water flow speed of the pump. This setup could only be used for demonstration rather than for scientifically evaluating the performance of the wave energy harvesters [13,14].

In 2022, Feng et al. and Wen et al. demonstrated a wave generation tank for wave energy harvester. It utilises electric fans located on the side or bottom of a water tank to generate waves. This setup demonstrated stable wave frequency control but lacked the ability to change the wave amplitude due

to the fixed contact area between the fan blades and water. Additionally, the generated waveform close to a swirl rather than a typical ocean wave, making it difficult to use for evaluating device performance [15,16]. In 2022, Shen et al. employed a motor-driven double-axle platform combined with a water tank positioned above this platform. Waves were generated through the back-and-forth motion of the platform. This setup allowed for simple amplitude and frequency control through the motor, but it faced limitations as the short water tank could not generate fully developed waves. Moreover, the motor-driven double-axle platform was also too expensive to afford [17]. In 2024, Zhou et al. used a self-developed wave generation device to demonstrate the performance of a wave energy harvester. However, due to the limited length of the wave tank, it could not fully develop lowfrequency waves with long wavelengths [18]. Previous solutions not only lack variability in generated wave frequency and amplitude but also cannot provide a fully developed wave due to the limited length of water tanks. A month later, Zhang et al. utilised a ground-based water channel system as an experimental platform to demonstrate a wave energy harvester. However, the large land requirements and high construction costs make ground-based water channels difficult to afford as mentioned before [19]. Longer water channels can generate more stable and repeatable waves, which are crucial for evaluating the performance of wave energy harvesters. Consequently, a laboratory-sized water channel attracted our attention due to its significantly lower cost compared to a conventional ground-based water channel system and it has a longer water tank compared to selfdeveloped systems. Taking HM 160 experimental flume from Gunt Hamburg (Germany) as an example [20], the entire system has a length of 5 meters, which provides a decent length of water tank for long wavelength wave development while also balances land requirements and costs.

In this study, a modular wave generator, facilitating a commercially available laboratory-sized water channel has been proposed to address this limitation. It was manufactured using 3D printing and laser cutting technologies with recyclable materials to satisfy sustainability requirements. This manufacturing approach can significantly reduce costs and minimize material waste when adjusting the water tank dimensions. The core driving unit of this device is based on a stepper motor and the Arduino programming platform, enhancing reproducibility. This research aims to overcome the limitations of current ground-based water channels and promote the development of low frequency ocean wave energy harvester. A comprehensive study of how motor parameters affect the generated waves in the water channel is presented here and verified by experimental results. Furthermore, a previously reported wave energy harvester (WD-TENG) is employed as a test device to demonstrate the capability of the developed wave generation device as an evaluation platform.

4.2 Results

4.2.1 Concept of design and functionality of wave generation device

The wave generation device utilises Bluetooth technology to enable remote wireless control of generated wave amplitude and frequency. These parameters are controlled by a stepper motor in

this design. The rotation speed of stepper motor determines the generated wave frequency, while the number of travelled steps of motor affects the generated wave amplitude, as shown in Figure 4.1.

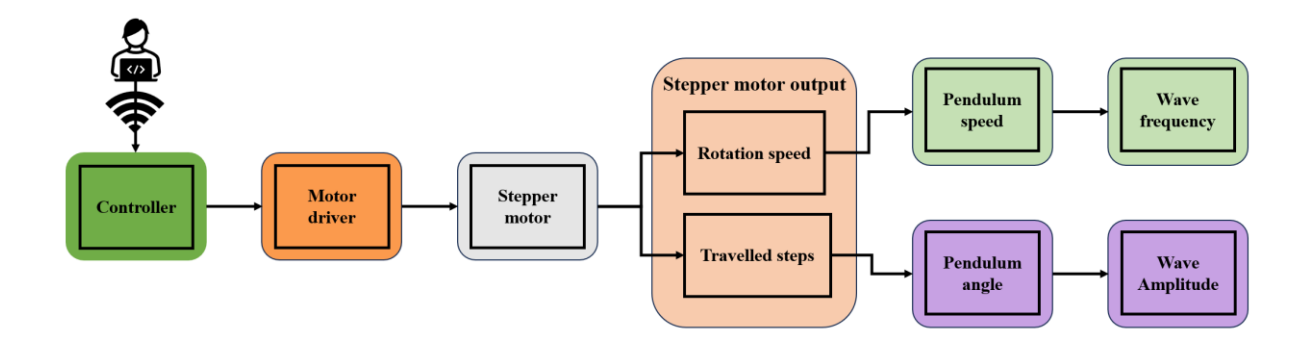


Figure 4.1 Workflow diagram of the wave generation device in this study.

In this study, a commercial water channel (HM 160 Experimental flume, Gunt Hamburg, Germany) with dimensions of water channel length 500 cm, width 8.6 cm, and height 30 cm is used. Two multi-ladder-shaped wave dampers are employed to minimise the impact of reflected waves on newly generated waves. Wave Damper 1 and Wave Damper 2 are placed at the outlet and inlet of the water channel tank, respectively, as shown in Figure 4.2(A). The inlet damper is designed with a gap between it and the bottom of the water channel to allow for free variations in water depth.

The wave generation device follows a modular design concept to minimize waste when the water channel dimensions are modified, correspond with sustainability goals. Based on the modular design, the wave generation device is composed of six core units: (I) motor driving unit, (II) transmission belt, (III) wave creation board, (IV) driving shaft, (V) T-track and (VI) conveyor system balancer as shown in Figure 4.2(B).

- (I) Motor driving unit: It is the core of the wave generation device and enabling signal transmission between an endpoint laptop and a microcontroller via a Bluetooth module for remote control. By controlling stepper motor parameters, such as rotation speed, rotation direction, and number of travelled steps in order to drive the timing belt and generate water waves through the wave creation board.
- (II) Transmission belt: A timing belt transfers kinetic energy from the stepper motor through a 3D-printed pulley to the (III) wave creation board via the (IV) driving shaft.
- (III) Wave creation board: It is driven by kinetic energy from the stepper motor via the (II) transmission belt and the (IV) driving shaft. The back-and-forth movement of the wave creation board generates waves. The board is placed inside the water channel tank and securely fixed to the bottom of the tank using screws from Gunt Hamburg.

- (IV) Driving shaft: It is employed as connector between the (II) transmission belt and (III) wave creation board, enabling the board to be driven by kinetic energy from the stepper motor. Secured in the groove of the (V) T-track, and four stainless ball bearings are employed to reduce friction between (IV) the driving shaft and (V) the T-track.
- (V) T-track: Two T-tracks are used to support the (I) motor driving unit and (VI) conveyor system balancer, forming the main body structure. This structure also provides support for the (IV) driving shaft when the device is mounted on the water channel tank. A 3D-printed lock is used to secure the positions of the (I) motor driving unit and (VI) conveyor system balancer on the T-track.
- (VI) Conveyor system balancer: The core component of the conveyor system balancer is a stainless-steel ball bearing aligned with a 3D-printed toothed gear, together forming a transmission pulley. The conveyor system balancer is used to maintain the height of the (II) transmission belt and is positioned at the other end of the (V) T-track, enabling the horizontal conveyor system. This unit also uses a 3D-printed lock to secure its position.

The wave generation system installed on the water channel tank is shown in Figure 4.2(C). Thanks to its modular design, the wave generation device offers versatile application possibilities, allowing it to integrate with laboratory-sized commercial water channels of varying dimensions with minimal modifications to the 3D-printed components.

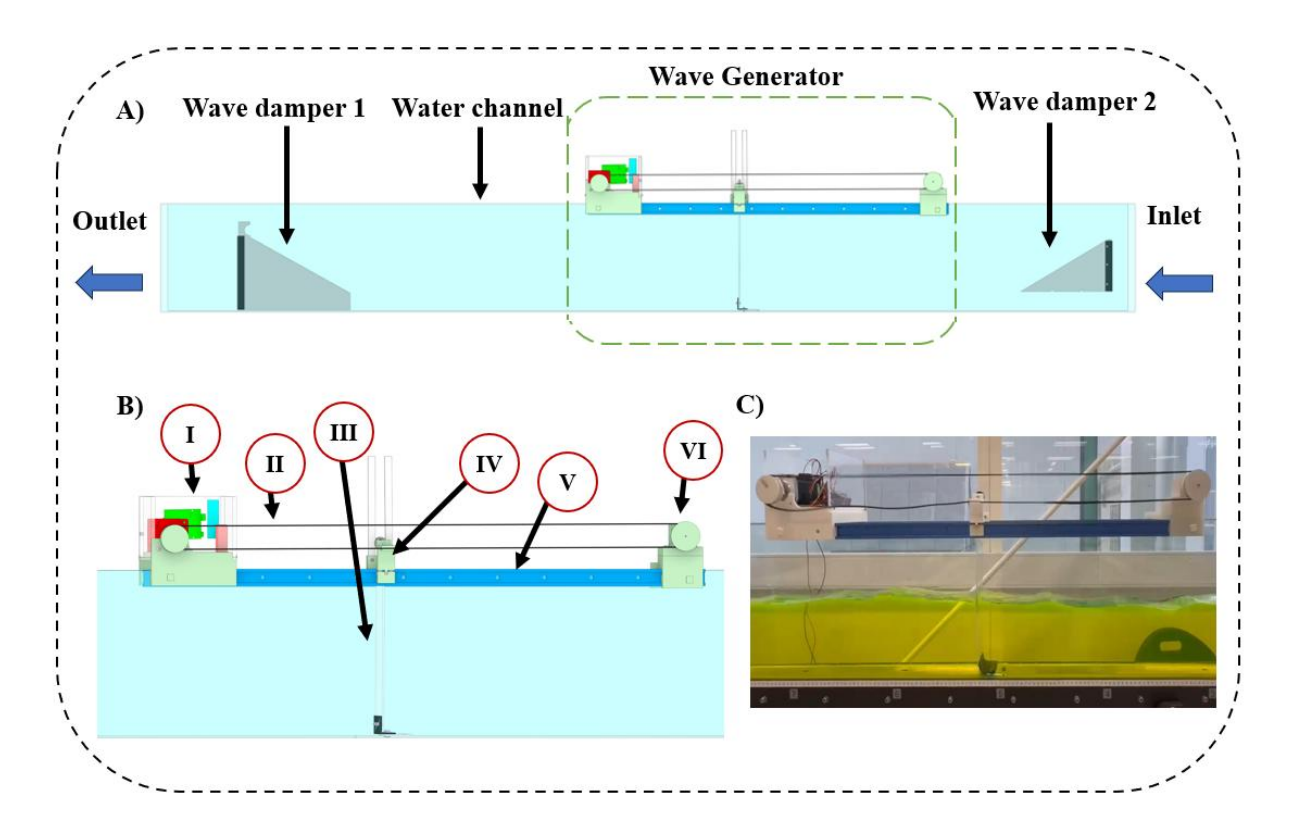


Figure 4.2 A) Overview of the wave generation device, which involves two wave dampers and the commercial water channel, B) View of the six components that make up the wave generation device, (I) Motor driving unit, (II) Transmission belt, (III) Wave creation board, (IV) Driving shaft, (V) T-track,

and (VI) Conveyor system balancer, and C) Photo of the actual wave generation device mounted in the water channel.

4.2.2 The working mechanism of the wave generation device

The generated waves are realised through the back-and-forth motion of the wave creation board driven by the stepper motor. Through adjust the rotation speed and the number of travelled steps of the motor taken in order to control the generated wave frequency and wave amplitude, respectively. Theoretically, the wave motion is represented as an approximate sinusoidal wave. The wave motion in the water channel system is described as follows:

$$y = a * \sin(bx - h) + k \tag{4.1}$$

where a, b, h, and k represent the wave amplitude, wavelength, horizontal phase shift, and vertical phase shift of the wave, respectively. Considering wave generation under static water conditions, where the water depth in the channel tank remains constant, the effect of vertical phase shift (k) can be ignored. Additionally, the use of two dampers effectively reduces the impact of horizontal phase shift (h), allowing it to be assumed as zero in this experimental setup.

To explain how the stepper motor is used to control the generated wave, two equations are employed to determine the force factors affecting the generated wave. The derivation of the force components along the X and Y axes is described as follows:

$$f_{v} = F * \cos(\theta) \tag{4.2}$$

$$f_{x} = F * \sin(\theta) \tag{4.3}$$

Equation (4.2) describe the force component of Y-axis of the wave creation board during wave generation, which is directly proportional to the water depth d as shown by the blue dashed line in Figure 4.3. While Equation (4.3) represents the force component on the X-axis of wave creation board corresponding to the pendulum θ as shown by the yellow dashed line in Figure 4.3. Water depth d and pendulum θ will be the most important factors which will affect the generated wave amplitude. Pendulum θ is depending on the number of travelled steps of the stepper motor or named as displacement of the wave creation board x(t). The water depth d will be adjusted by the HM 160 water channel system before wave generation. The period of one wave generating cycle can be considered as the frequency of generated wave frequency f, and the frequency of generated wave controlled by the motor rotation speed v. The back-and-forth movement of the wave creation board can be achieved by adjusting the rotation direction of the stepper motor, which applies pressure to the contact area of the water to generate waves.

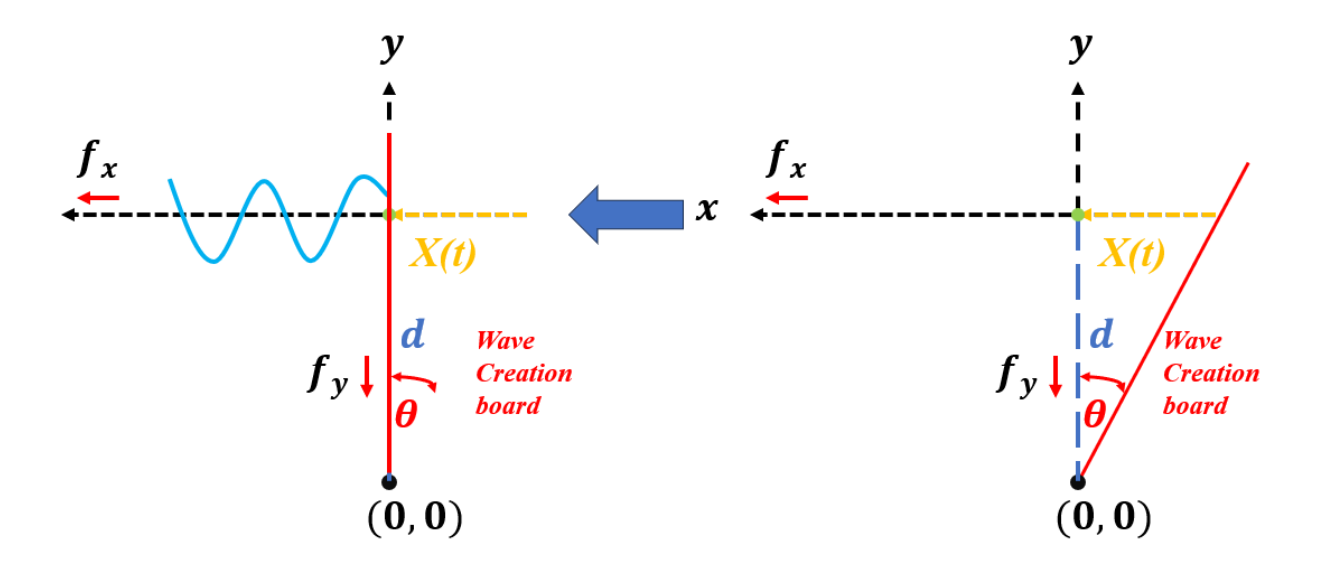


Figure 4.3 Schematic of the wave generating process, f_x and f_y represents the force component on x and y axes, respectively. d is the depth of water, and θ is the pendulum. x(t) represents the displacement of the wave creation board on the y-axes direction. Waves are generated when the wave creation board applies pressure to the contact area of the water.

$$a = \frac{2\pi d}{L}x(t) = \frac{2\pi d}{\frac{v}{f_{w}}}S\tag{4.4}$$

Equation (4.4) is used to define the motor parameters that will affect the generated wave amplitude, where d, L, and x(t) represents the water depth, wavelength, and displacement of the wave creation board, respectively [21]. Inserting the motor parameter into Equation (4.4), wavelength can be placed by $\frac{v}{f_w}$ where v and f_w represent the motor rotation speed and the frequency of one wave generation cycle, respectively.

Consequently, there are three factors that will affect the amplitude of generated wave which are frequency f_w which is dependent by motor rotation speed v; displacement of wave creation board x(t) which is dependent by pendulum θ ; and depth of water d.

$$f_{w} = \frac{1}{\frac{2 \cdot x(t)}{v}} = \frac{v}{2 \cdot x(t)} \tag{4.5}$$

Equation (4.5) is utilised to define the frequency of generated wave, where v represent the rotation speed, and x(t) represents the displacement of wave creation board or named as pendulum θ . Since the generated wave is caused by the back-and-forth movement of wave creation board, there are two displacements of wave creation board $2 \cdot x(t)$ within one generation cycle. When the displacement of wave creation board x(t) is fixed, adjusting the motor rotation speed can control the generated wave frequency, f.

4.2.3 Analysis of generated wave under variation of water depth

Figure 4.4 shows the mean amplitude of the generated wave with error bars for water depth 10 cm, 15 cm, and 20 cm, respectively. The tested pendulum angles are 18.18°, 21.51°, 24.69°, 27.72°, and 30.59°, corresponding to 2,500, 3,000, 3,500, 4,000, and 4,500 motor steps, respectively. The maximum generated wave amplitude, approximately 7.1 cm, is observed at a frequency of 1.5 Hz, with a pendulum of 30.59 ° and water depth of 20 cm. Additionally, the lowest amplitude of approximately 1.5 cm is recorded at a frequency of 1.5 Hz, with a pendulum of 18.18 ° and under the 10 cm water depth. However, the generated wave amplitude for all three frequencies, 1.0 Hz, 1.5 Hz, and 2.0 Hz with a pendulum of 18.18 ° and water depth of 10 cm were similar. When the pendulum increases from 18.18 ° to 30.59 °, the generated wave amplitude demonstrates a significant direct proportional increase with the pendulum at various water depths. Furthermore, the results indicate that the increase of frequency, especially from 1.0 Hz to 1.5 Hz, does not significantly increase the generated wave amplitude for a water depth of 10 cm compared with 15 cm and 20 cm water depth. The increase in frequency from 1.5 Hz to 2.0 Hz does not show a significant difference in amplitude for water depths of 15 cm and 20 cm. Therefore, the pendulum angle and the water depth are the most majority parameters which affect the generated wave amplitude. Moreover, the stability and repeatability of the wave generation device were verified under various water depths of 10 cm, 15 cm, and 20 cm. The maximum tolerance observed was 3.3% at a water depth of 20 cm, while the minimum tolerance was 2.0% at a water depth of 10 cm.

Figure 4.5(A) depicts a 3D colormap that effectively illustrates the capacity of the wave generation device, the three tiers, from top to bottom, represent water depths of 20 cm, 15 cm, and 10 cm, respectively. The detailed trend of the change in amplitude for each water depth is shown in Figure 4.5(B – D). Take the cylinder chart of 10 cm water depth, as shown in Figure 4.5(B) as an example, it demonstrates the trend of change in amplitude of generated wave with various pendulums. The change in pendulum has obviously affected on generated wave amplitude for each of the three water depths. Similar trend of change in amplitude has been observed on 15 cm and 20 cm water depths as shown in Figure 4.5(C) and (D). Notably, the water depth d has the most significant influence on the generated wave amplitude when compared to frequency and pendulum. The experimental results verify the derived mathematical model. Moreover, although frequency f is one of the factors that affects the generated wave amplitude, as shown in Equation (4.5), the experimental results demonstrated that the generated wave amplitude is not significantly affected by frequency. To achieve higher wave frequency and amplitude in the future, a faster stepper motor, also manufactured by Trinamic (Germany), can be used to replace the current motor setup without modifying the connection layout. A maximum wave frequency of 8 Hz and a wave amplitude of 50.78 cm can be achieved with the faster motor. Details of the motor selection are provided in Note S4.1, Table S4.1, and Table S4.2.

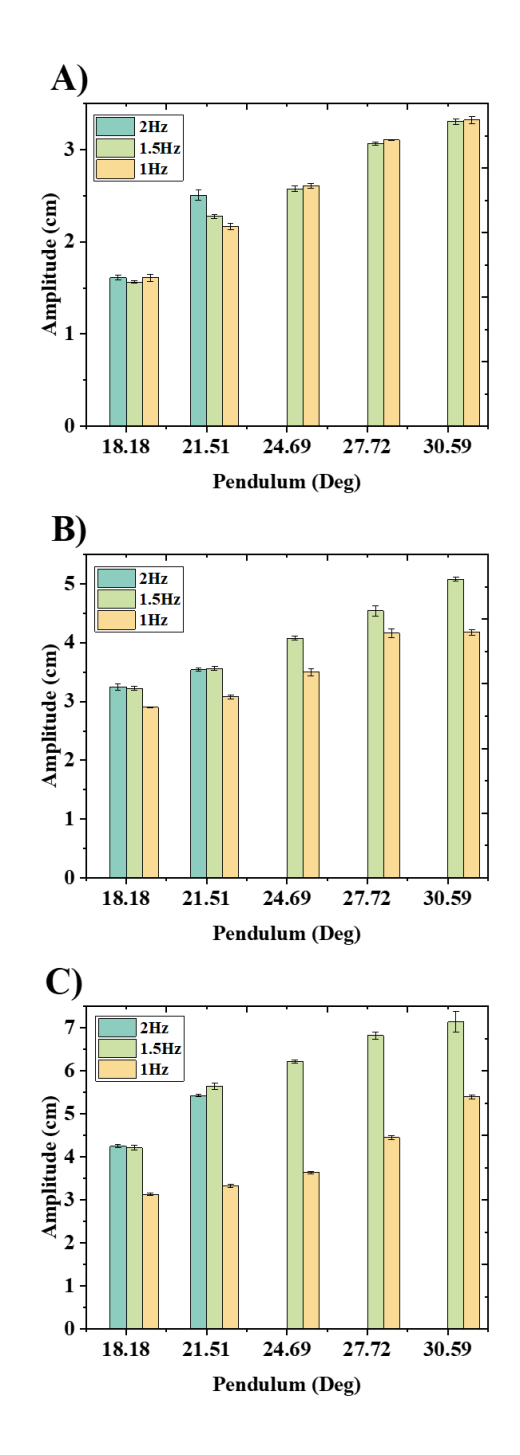


Figure 4.4 Detailed cylinder charts of generated wave amplitudes with error bars under (A) 10 cm depth, (B) 15 cm depth, and (C) 20 cm depth respectively.

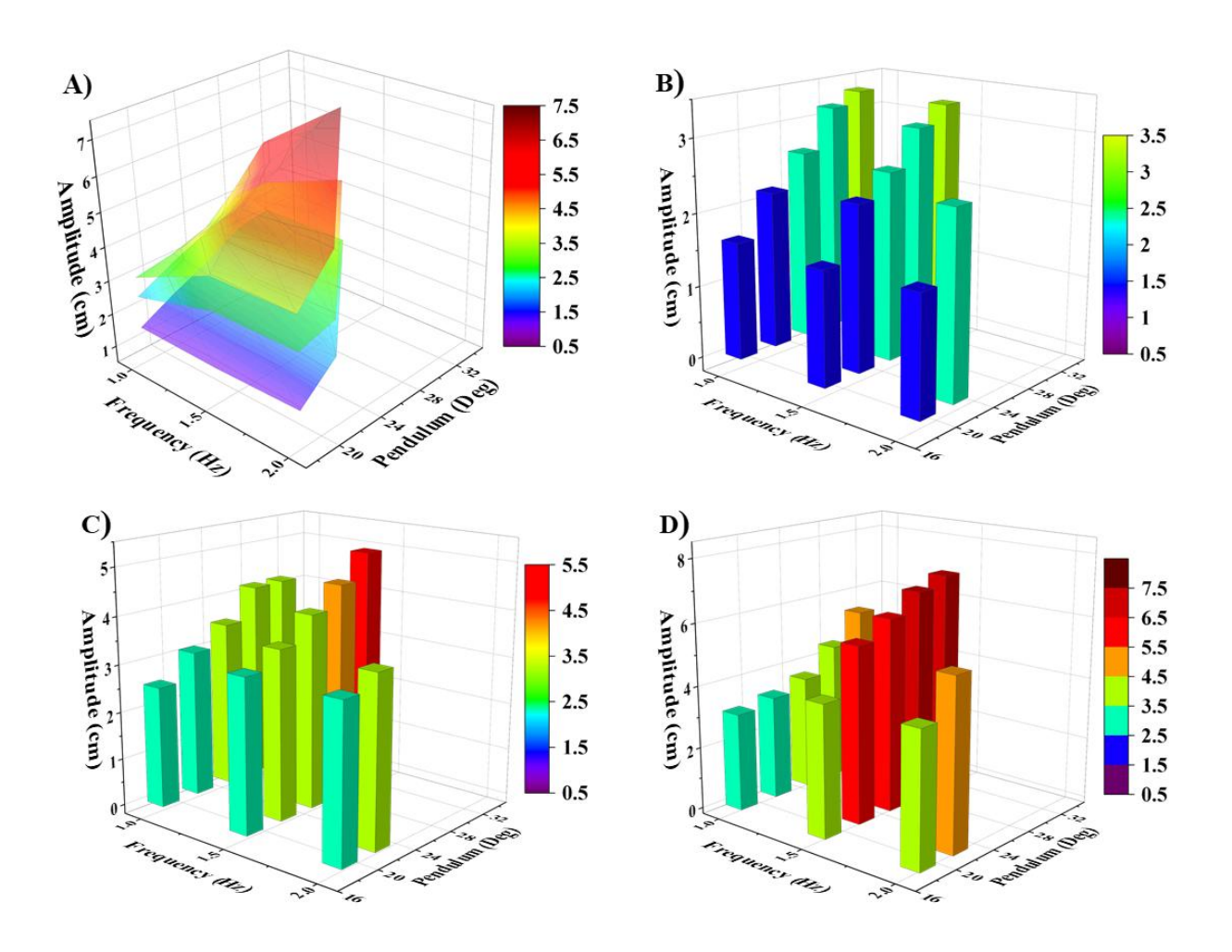


Figure 4.5 (A) Colormaps of the relationship among frequency, pendulum and amplitude under 10 cm, 15 cm, and 20 cm water depths. Detailed cylinder chart of generated wave amplitude under (B) 10 cm depth, (C) 15 cm depth, and (D) 20 cm depth.

4.2.4 Analysis of the wavelength of the generated wave under variations in pendulum angle.

A high-speed camera (FASTCAM NOVA S4.6, Photron, Tokyo, Japan) was employed to continuously record the motion of the generated waves in the water channel for 7.5 seconds, resulting in a 3-minute video. The video was then processed using a video editor to extract peak amplitude screenshots. Subsequently, an image processing method was applied to analyse the screenshots, as illustrated by the flowchart in Figure 4.6. Figure 4.6(A(I)) shows a captured image from the high-speed camera video, which was used to determine the peak-to-peak amplitude of the waveform in the next step. The number of pixels corresponding to the peak-to-peak amplitude was measured, as shown in Figure 4.6(A(II)). A 5 cm × 5 cm square grid backdrop was used to assist in the analysis of wave amplitude. First, count the number of pixels from the top to the bottom of the square grid. Then, calculate the pixel count of the peak-to-peak wave amplitude and convert it into metric units using the pixel count of the square grid, as shown in Figure 4.6(A(III)). Five generated waves were selected from the three-minute high-speed camera video to determine the mean value of the wave amplitude.

The wavelength of the generated wave for a water depth of 20 cm, under various frequencies and pendulums, is shown in Figure 4.6(B - G). Applied the same image processing method to determine the wavelength. Figure 4.6(B) and (C) illustrate the wavelength of generated wave at a frequency of 2.0 Hz and pendulum of 18.18 ° and 21.51 °, respectively, the results show that both waves have the same wavelength of approximately 40 cm. In addition, the wavelengths generated by a frequency of 1.5 Hz and pendulums under 18.18 $^{\circ}$, 21.51 $^{\circ}$, 27.72 $^{\circ}$, and 30.59 $^{\circ}$ are shown in Figure 4.6(D -G), respectively. The wavelength at a pendulum of 24.69 ° and a frequency of 1.5 Hz is shown in Figure S4.1(D). They are shown a similar trend with the constant wavelength of approximately 60 cm. Furthermore, a constant wavelength of approximately 120 cm was generated for a frequency of 1.0 Hz with different pendulums as shown in Figure S4.1(H-L). The wavelength of generated waves for a water depth of 15 cm and 10 cm are shown in Figure S4.2 and S4.3, respectively. Notably, the wave shows the same wavelength when observed under a water depth of 15 cm and 10 cm. The relationship between different pendulum, θ and rotation speeds, v, for different frequencies, f, are shown in Figure S4.4, which agrees with Equation (4.4) well since wavelength, L, is equal to $\frac{v}{f}$. Therefore, the wave generation device shows the ability to generate a repeatable wave with a fixed frequency.

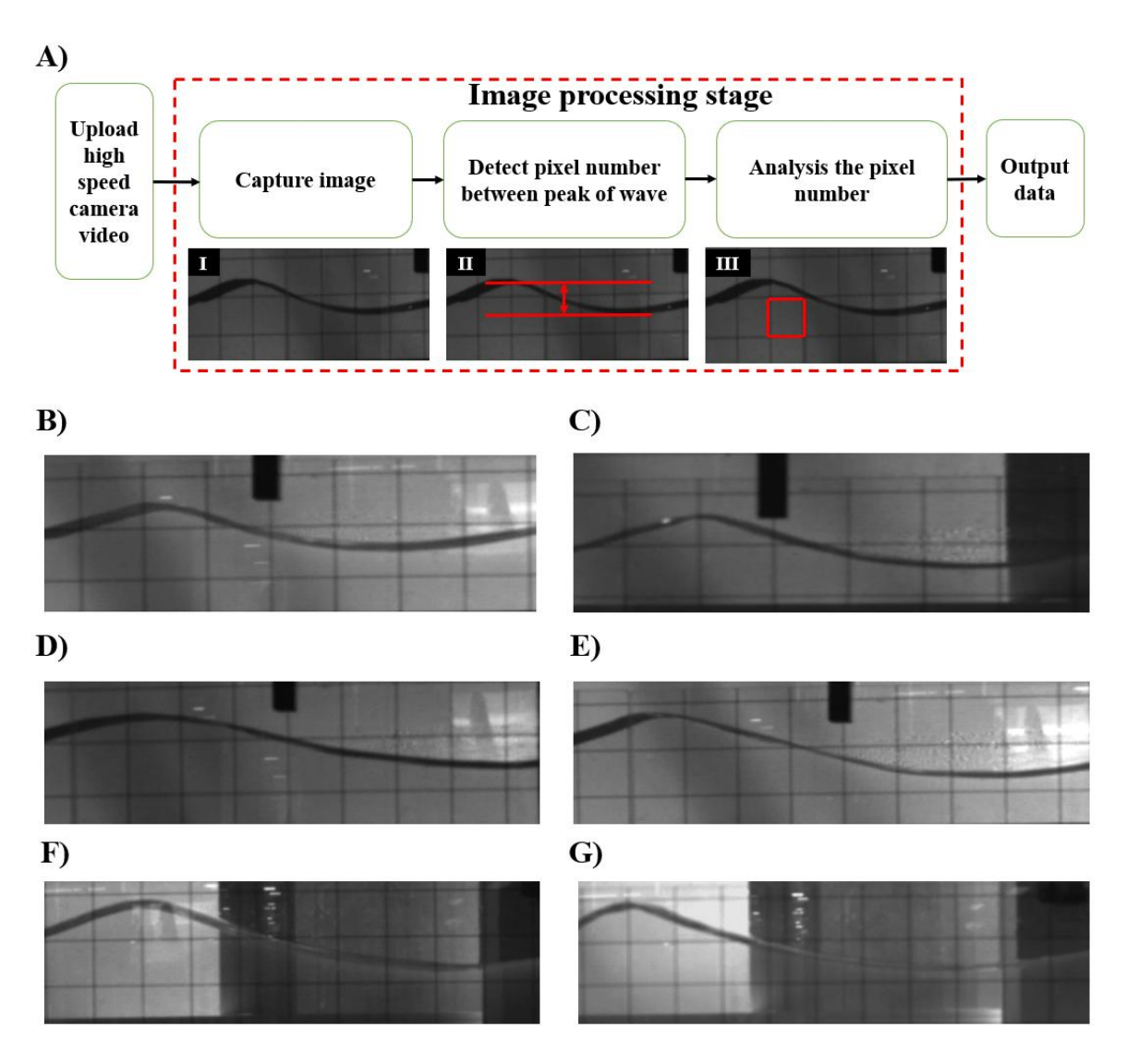


Figure 4.6 (A) The block diagram for the image processing steps to determine the mean value of the wave amplitude and the wavelength. Generated waves under 20 cm depth water, 40 cm wavelength under 2.0 Hz (B) 18.18 °, and (C) 21.51 °. 60 cm wavelength under 1.5 Hz (D) 18.18 °, (E) 21.51 °, (F) 27.72 °, and (G) 30.59 °.

4.3 Demonstration

Previous published device which named as wave-driven triboelectric nanogenerator (WD-TENG) and introduced in Chapter, was employed as a test device to verify the feasibility of modular design wave generation device as an evaluation platform for low-frequency and amplitude wave energy harvester. The triboelectric materials used in the WD-TENG and its working mechanism are shown in Figure 3.2.

The dynamic of the WD-TENG under a generated wave of 7.1 cm amplitude with a 1.5 Hz frequency. As shown in Figure 4.7(A), the WD-TENG responded four times to the generated wave with amplitudes of 4.6 cm and 5.1 cm. Once the amplitude was increased to 7.1 cm, the WD-TENG responded five times to the generated wave. Due to a higher amplitude, there is an increase in the gravitational force, allowing more kinetic energy to easily overcome the friction force between the internal sliding module and the acrylic tube. Figure 4.7(B) indicates that the output voltage of the WD-TENG increased with generated wave amplitude. These results indicate that when tested with real waves created by the proposed wave generation device, the WD-TENG performed similarly trend with the previously published results. The linear relationship between the strength of the electrical signals and the wave amplitude demonstrates the potential for using this setup as a wave sensor to detect changes in wave amplitude.

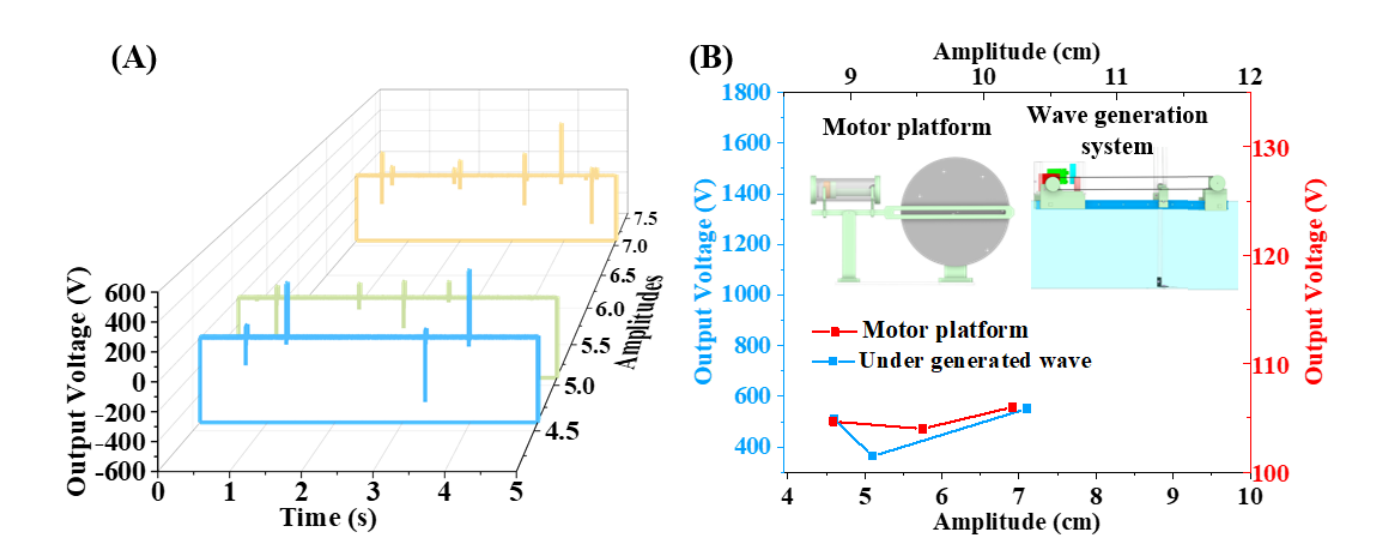


Figure 4.7 (A) Output performance of the WD-TENG under various generated wave amplitude. The blue, green, and orange waveforms represent the generated waves with amplitudes of 4.6 cm, 5.1

cm, and 7.1 cm under a frequency of 1.5 Hz, respectively, and (B) The maximum output performance under generated wave from current study comparing with the previous publication [12].

4.4 Experimental procedures

4.4.1 Fabricate and functionality of the component consists of wave generation device

4.4.1.1 Motor driving unit

The base of motor driving unit (A), locker (B) and motor driving pully (C) are fabricated through a 3D printer by using polylactic acid (PLA) as shown in green components in Figure 4.8(A, B, and C). The bottom of the base (A) features notches designed for insertion into the grooves of the T-track. Additionally, two 3D-printed lockers (B) are employed to firmly secure the motor driving unit's position on the T-tracks. The modular design allows the position of the motor driving unit to be adjusted as needed. The enclosure of motor driving unit, comprising three pieces designed to safeguard electronic components, is produced through a laser cutter machine with a 4.5 mm thickness transparent acrylic board, forming the white transparent part shown in Figure 4.8(D, E, and F).

The stepper motor (PD-1076, Trinamic, German), shown in red, was chosen as the kinetic energy source for the wave generation device. A microcontroller (Arduino UNO), shown in green, and a Bluetooth module (Dsd Tech Hc-05), shown in bright blue, are employed as the signal processor and signal receiver, respectively. The microcontroller converts Bluetooth signals from the endpoint laptop into digital signals for the motor driver, allowing remote adjustment of the stepper motor parameters to control the generated wave frequency and amplitude. A 9V power supply, shown in pink, is used to power the microcontroller. Thanks to the Bluetooth module, the wave generation device can be controlled wirelessly, eliminating the need for the operator to use a keypad or buttons.

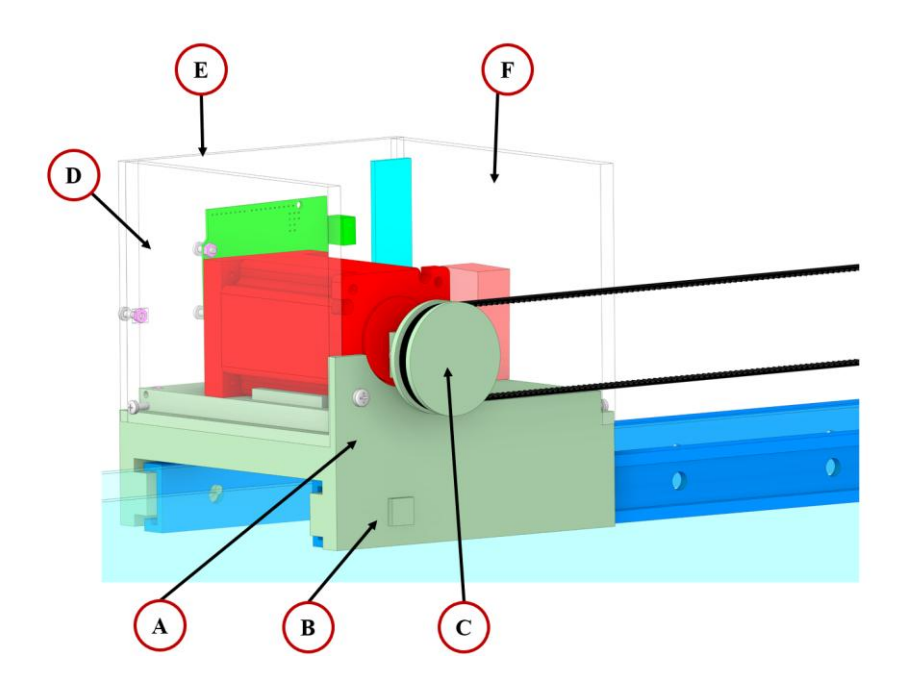


Figure 4.8 The detailed view of the motor driving unit. (A) Base, (B) Locker, and (C) Motor driving pulley are fabricated from polylactic acid (PLA) using 3D-printing technology, as shown in green. (D) Left enclosure, (E) Back enclosure, and (F) Right enclosure are made from 4.5 mm thick transparent acrylic board using a laser cutting machine. The stepper motor is shown in red; the microcontroller is shown in green, the Bluetooth module is shown in bright blue, and the 9V power supply is shown in pink.

4.4.1.2 Conveyor system balancer

The entire conveyor system balancer has been fabricated using 3D printing technology with polylactic acid (PLA) and assembled by M3 screws and nuts as shown in Figure 4.9. A ball bearing has been used to form a transmission pulley, as shown in the insertion Figures. The 3D-printed pulley (1) with 48 teeth gear is used to transfer the kinetic energy from the stepper motor, which is mounted on the ball bearing (2). A transmission belt limiter (3) is used to prevent system failure that could be caused by the timing belt slipping off the pulley (1). The conveyor system balancer also utilises a notched design concept similar to the motor driving unit. This notched design allows for easy repositioning of the conveyor system balancer on the T-track by use 3D-printed lockers.

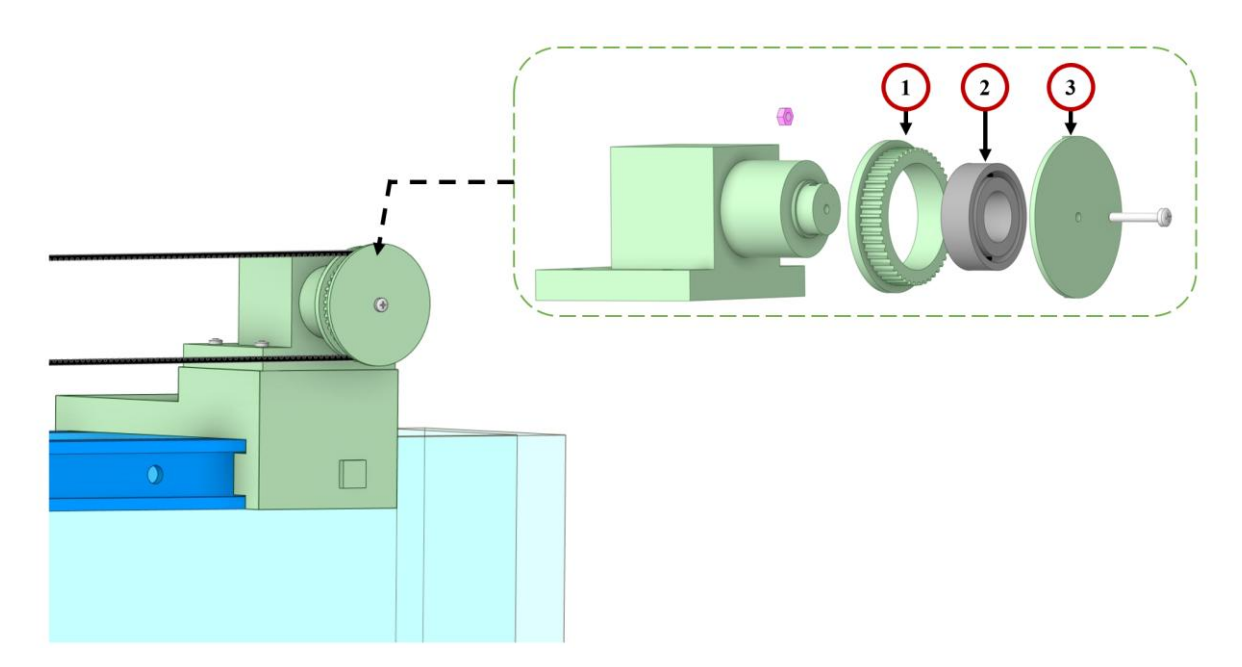


Figure 4.9 The close view of the conveyor system balancer, with a sub insertion which involves (1) 3D printing pully, (2) Steel ball bearing, and (3) Transmission belt limiter. The 3D printing components as shown in green.

4.4.1.3 Wave creation board

The components consist of wave creation board, excluding the rubber connection piece (B) and shaft holder (E), were fabricated from a white transparent acrylic board as shown in Figure 4.10. Shaft holder (E) fabricated 3D printing technology with polylactic acid (PLA). The base board (A) and wave generation board (C) are made from a 3 mm thick transparent acrylic board, and wave creator shaft (F) is made from a 10 mm thick transparent acrylic board, respectively. The base fix board (A) is

used to fix with the commercial water tank system through the screws from Gunt Hamburg. A rubber piece (B) is used to connect the base fix board (A) and the wave creation board (C) by M3 screws and nuts. Shaft holder (E) is used to connect between wave creation board (C) and two wave creator shafts (F). Four steel ball bearings (D) placed on each corner of the shaft holder (E) are used to reduce the friction between wave creation board and glass water channel tank. Wave creators (F) are used to co-operate with the driving shaft to realise back and forth movement of the wave creation board (C).

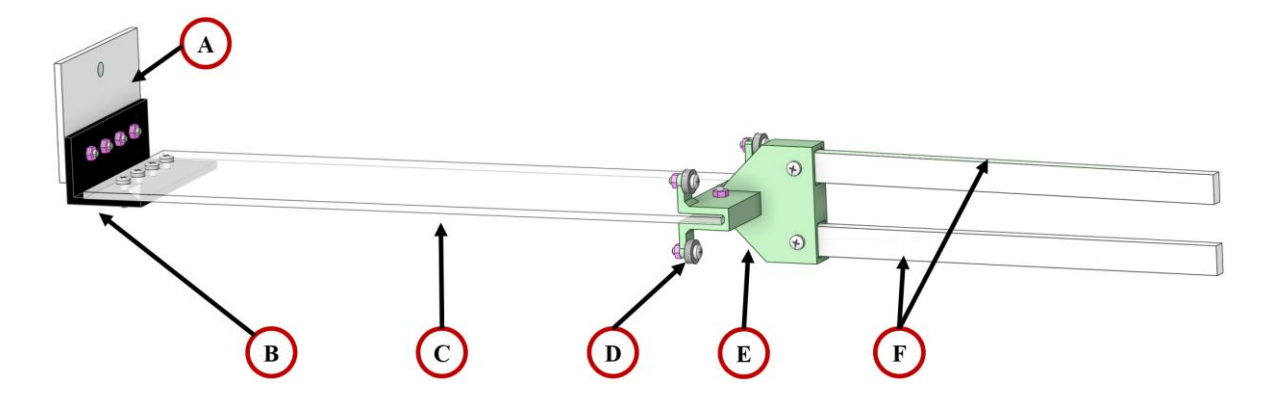


Figure 4.10 The detailed view of the wave creation board, (A) Base board, (B) Rubber connection piece, (C) Wave generation board, (D) Ball bearing, (E) Shaft holder, and (F) Wave creator shaft. The 3D printing components as shown in green, and the white transparent pieces are acrylic components.

4.4.1.4 Driving shaft

The transmission belt connector (A) is used to transfer kinetic energy from the stepper motor. Roller (C) is placed at the end of the metal shaft (B), secured with nuts, and inserted between the two wave creator shafts of wave creation board. The holder of the driving shaft has been separated into two parts, i.e., the upper holder (D) and the lower holder (E). Both fabricated 3D printing technology with polylactic acid (PLA). They are aligned together using a screw and nut, as shown in Figure 4.11(I). The designated positions for the four ball bearings (F) are illustrated in Figure 4.11(II), with two positioned in the groove of the T-track and the other two in contact with the surface of the T-track. The purpose of utilising the ball bearings is to reduce the friction between driving shaft and T-track.

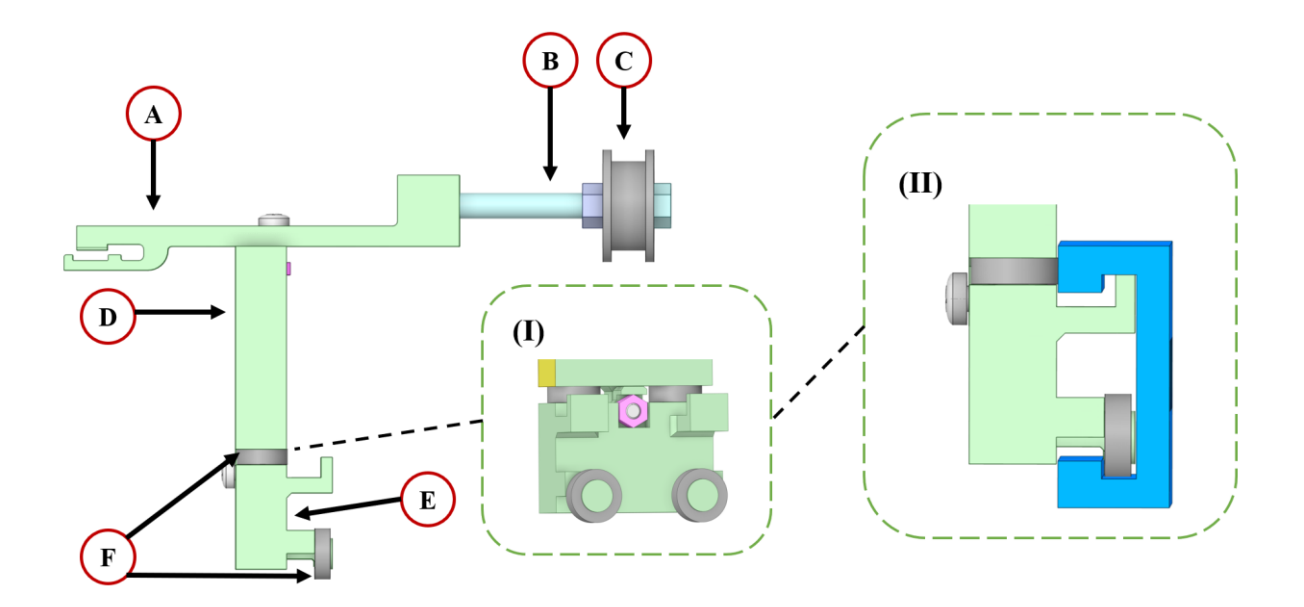


Figure 4.11 The detailed view of the driving shaft, (A) Transmission belt connector, (B) Metal shaft, (C) Roller, (D) Upper holder, (E) Lower holder, and (F) Ball bearing. The close view of the conjunction points (I) between upper and lower holders; and the position of the four ball bearings on the T-track (II).

4.4.2 Material and components used for building modular concept wave generation device

The parts of the wave generation device as shown in green colour and transparent colour were fabricated by utilising a 3D printer (Monoprice Maker Ultimate 2+, Rancho Cucamonga, USA) and a laser cutter (Rayjet 300EDU, Australia) to treat the transparent acrylic board and polylactic acid (PLA), respectively. The two T-tracks are used as the main body structure to set down units for the wave generation device. M3 Screws and nuts were used to assemble the laser cut pieces and 3D printing parts. The processor (Arduino UNO, Ivrea, Italy) used to control the stepper motor's driver (PD-1076, Trinamic, German). Bluetooth module (Dsd Tech Hc-05) used to transfer the digital signal to stepper motor's driver in order to generate water wave. A 9V battery dock (Jaycar, Australia) is used to power the Arduino. A ball-bearing E2.6003-2Z/C3 (SKF, Australia) is selected as the core component of the transmission pulley of the conveyor system balancer to balance the transmission belt position and transmit kinetic energy from the stepper motor. Eight stainless-steel ball bearings (SMR106ZZ, RS PRO, Australia) are used to reduce friction between the wave generation components and the glass water channel wall or the T-track, respectively.

4.4.3 Wave energy harvester evaluation

The previously published wave-driven triboelectric nanogenerator (WD-TENG) [12] was used to validate the capabilities of the wave-generation device and verify its ability to serve as an experimental platform for the low-frequency wave energy harvesters. An oscilloscope (Keysight, InfiniiVision MSO-X 2004A, USA) was connected to the TENG output to monitor the output electrical waveform to demonstrate the capacity of wave generation device.

4.5 Discussion

Moreover, whether the output performance of the wave driven TENG is influenced by the ratio between the device dimensions and the wavelength of the incident waves is a crucial factor for future scaling and optimization. The equation used to estimate the power of the incident wave is presented in Equation (4.6).

$$P_{incident \, wave} = \frac{1}{8} \rho g \alpha^2 c_g \tag{4.6}$$

Where, ρ represents the water density, g represents the gravitational force, a represents the wave amplitude of incident wave, and c_g represents the group velocity. By follow the linear wave theory, c_g can be expressed as shown in Equation (4.7).

$$c_g = \frac{\omega}{2k} \left(1 + \frac{2kd}{\sinh(2kd)} \right) \tag{4.7}$$

Where, ω represents the wave angular frequency, it can be expressed as $\omega=2\pi f=2\pi\frac{v}{\lambda}$. Here, λ represents the wavelength of incident wave and v represents speed of incident waves. Therefore, based on the previous derivation, the ratio between the device dimensions and the wavelength of the incident waves influences the output performance of the wave driven TENG. A larger wavelength corresponds to lower wave power, and vice versa. Consequently, higher wave power results in greater output performance of the wave-driven TENG.

4.6 Conclusion

In this study, a modular concept wave generation device was proposed. Thanks to 3D-printing technology and the modular design concept, the system requires only minor modifications to adapt to different water channel dimensions if needed in the future. This approach significantly saves costs and time while reducing material waste, enhancing material sustainability. In addition, the Arduino-based programming platform offers ample resources, making reproducibility more convenient. Moreover, the use of the Bluetooth module enables wireless remote control of the wave generation device, further enhancing its practicality. The relationship between motor parameters and generated wave parameters has been derived by mathematical modelling and verified with experiment results. Based on the analysis result of experiment, controllable and repeatable waves were successfully generated under various testing conditions from water depths from 10 cm to 20 cm. The frequency range of the generated waves was limited to 1.0 Hz to 2.0 Hz due to the maximum rotation speed of the currently selected stepper motor. However, a higher wave frequency and amplitude can be achieved by replacing the current stepper motor with a higher-speed one. The generated wave amplitude varies between 1.5 cm and 7.1 cm, demonstrating exceptional stability and repeatability with a maximum tolerance of 2.2%, 2.0%, and 3.3% for water depths of 10 cm, 15 cm, and 20 cm,

respectively. A previously published ocean wave energy harvester was employed as a test device and successfully generated electricity under the generated waves. The demonstration results of the test device showed similar increasing trends compared to previously published results. The result confirms that the modular wave generation device offers a valuable solution for evaluating low-frequency and low-amplitude ocean energy harvesters, while also providing easier reproducibility.

4.7 Reference

- [1] Australian Government, Climate Active, Climate Active Carbon Neutral Standard (2023). https://www.dcceew.gov.au/climate-change/climate-active (accessed December 2, 2023).
- [2] M. Melikoglu, Current status and future of ocean energy sources: A global review, Ocean Engineering 148 (2018) 563–573. https://doi.org/10.1016/j.oceaneng.2017.11.045.
- [3] A. Khaligh, O.C. Onar, Energy Harvesting, CRC Press, 2017. https://doi.org/10.1201/9781439815090.
- [4] Z.L. Wang, T. Jiang, L. Xu, Toward the blue energy dream by triboelectric nanogenerator networks, Nano Energy 39 (2017) 9–23. https://doi.org/10.1016/j.nanoen.2017.06.035.
- [5] L. Liu, Q. Shi, J.S. Ho, C. Lee, Study of thin film blue energy harvester based on triboelectric nanogenerator and seashore IoT applications, Nano Energy 66 (2019) 104167. https://doi.org/10.1016/j.nanoen.2019.104167.
- [6] X. Wen, W. Yang, Q. Jing, Z.L. Wang, Harvesting broadband kinetic impact energy from mechanical triggering/vibration and water waves, ACS Nano 8 (2014) 7405–7412. https://doi.org/10.1021/nn502618f.
- [7] W. Wang, J. Cao, N. Zhang, J. Lin, W.-H. Liao, Magnetic-spring based energy harvesting from human motions: design, modeling and experiments, Energy Convers Manag 132 (2017) 189–197. https://doi.org/10.1016/j.enconman.2016.11.026.
- [8] J. Chen, J. Yang, Z. Li, X. Fan, Y. Zi, Q. Jing, H. Guo, Z. Wen, K.C. Pradel, S. Niu, Z.L. Wang, Networks of triboelectric nanogenerators for harvesting water wave energy: a potential approach toward blue energy, ACS Nano 9 (2015) 3324–3331. https://doi.org/10.1021/acsnano.5b00534.
- [9] X. Li, J. Tao, X. Wang, J. Zhu, C. Pan, Z.L. Wang, Networks of high performance triboelectric nanogenerators based on liquid–solid interface contact electrification for harvesting low-frequency blue energy, Adv Energy Mater 8 (2018) 1800705. https://doi.org/10.1002/aenm.201800705.

- [10] W. Liu, Y. Li, H. Tang, Z. Zhang, X. Wu, J. Zhao, L. Zeng, M. Tang, D. Hao, The nexus of sustainable fisheries: a hybrid self-powered and self-sensing wave energy harvester, Ocean Engineering 295 (2024) 116996. https://doi.org/10.1016/j.oceaneng.2024.116996.
- [11] X. Zhang, H. Zhang, X. Zhou, Z. Sun, Recent advances in wave energy converters based on nonlinear stiffness mechanisms, Appl Math Mech 43 (2022) 1081–1108. https://doi.org/10.1007/s10483-022-2864-6.
- [12] Y. Wang, A.T.T. Pham, X. Han, D. Du, Y. Tang, Design and evaluate the wave driven-triboelectric nanogenerator under external wave parameters: experiment and simulation, Nano Energy 93 (2022) 106844. https://doi.org/10.1016/j.nanoen.2021.106844.
- [13] X. Wang, S. Niu, Y. Yin, F. Yi, Z. You, Z.L. Wang, Triboelectric nanogenerator based on fully enclosed rolling spherical structure for harvesting low-frequency water wave energy, Adv Energy Mater 5 (2015) 1501467. https://doi.org/10.1002/aenm.201501467.
- [14] X.J. Zhao, S.Y. Kuang, Z.L. Wang, G. Zhu, Highly adaptive solid–liquid interfacing triboelectric nanogenerator for harvesting diverse water wave energy, ACS Nano 12 (2018) 4280–4285. https://doi.org/10.1021/acsnano.7b08716.
- [15] H. Wen, P. Yang, G. Liu, S. Xu, H. Yao, W. Li, H. Qu, J. Ding, J. Li, L. Wan, Flower-like triboelectric nanogenerator for blue energy harvesting with six degrees of freedom, Nano Energy 93 (2022) 106796. https://doi.org/10.1016/j.nanoen.2021.106796.
- [16] J. Feng, H. Zhou, Z. Cao, E. Zhang, S. Xu, W. Li, H. Yao, L. Wan, G. Liu, 0.5 m triboelectric nanogenerator for efficient blue energy harvesting of all-sea areas, Advanced Science 9 (2022) 2204407. https://doi.org/10.1002/advs.202204407.
- [17] F. Shen, D. Zhang, Q. Zhang, Z. Li, H. Guo, Y. Gong, Y. Peng, Influence of temperature difference on performance of solid-liquid triboelectric nanogenerators, Nano Energy 99 (2022) 107431. https://doi.org/10.1016/j.nanoen.2022.107431.
- [18] J. Zhou, H. Tang, L. Zeng, Z. Zhang, J. Zhao, A. Li, L. Kong, M. Tang, Y. Hu, A self-powered and self-sensing wave energy harvesting system for the sea-crossing bridge, Mater Today Nano 27 (2024) 100500. https://doi.org/10.1016/j.mtnano.2024.100500.
- [19] C. Zhang, S. Yang, X. Dai, Y. Tu, Z. Du, X. Wu, Y. Huang, J. Fan, Z. Hong, T. Jiang, Z.L. Wang, Hybridized triboelectric-electromagnetic nanogenerators for efficient harvesting of wave energy for self-powered ocean buoy, Nano Energy 128 (2024) 109929. https://doi.org/10.1016/j.nanoen.2024.109929.

[20] Gunt Hamburg, HM 160 Experimental flume 86x300mm, (n.d.).

[21] Jr. Cyril J. Galvin, Wave-height prediction for wave generators in shallow water, 1964.

CHAPTER 5 A HYBRID SELF-POWERED WAVE SENSING DEVICE ENABLES LOW-AMPLITUDE WAVE SENSING

This chapter has been published on Device with DOI: 10.1016/j.device.2024.100575. **Yunzhong Wang**: Conceptualization, device design and fabrication, experiment, data analysis, figure plotting, writing – original draft.

5.1 Introduction

Ocean wave amplitude (vertical distance between highest or lowest point of a wave and a horizontal reference) is one of the major parameters characterising the ocean spectrum. It plays a key role in utilisation of ocean wave resources, such as the placement of wave energy harvester to obtain ocean renewable energy [1–3]. Most devices for ocean spectrum data collection are based on radars technology such as real-aperture radar, high-frequency radar, and X-band radars [4–6]. However, the aforementioned radar technology cannot collect low frequency and low amplitude wave data. Taking real-aperture radar as an example, it does not detect conditions with wave amplitudes less than 2 m. Apart from this, the vibration of antenna on the radar-based sensor, caused by external environmental factors such as irregular waves and wind, can affect the accuracy of ocean spectrum [7,8]. Therefore, a device that can monitor low frequency and low amplitude wave is required to refine wave data along coastlines, offshores, inner gulfs and lakes. The device will also contribute the emerging research area of low frequency and low amplitude wave energy harvesting [9]. A high-resolution wave spectrum can efficiency utilised wave energy and also assist in the placement of wave power energy harvester.

Conventional electromagnetic generator (EMG) requires high operation frequency and large input kinetic energy to activate its functions. To utilise low frequency and low amplitude energy, researchers have focused on developing electromagnetic energy harvesters (EMH) [10]. For EMEHs, there are two typical operation modes, one mode is that the magnet is fixed and the copper winding moves [11], and another mode is that the copper winding is fixed and the magnet moves [12]. The later design is preferred due to its low frequency operation characteristic and simple structure compared with the conventional EMGs.

In 2023, Hao et al. introduced an EMG to convert low-frequency and low-amplitude human motion energy into electrical energy [13]. Six different sets of coils make up the stator with the same winding specification, and the rotor consists of several magnets. An eccentric rotor, employed as a flywheel, is used to drive the rotor to measure the flux density change. This design achieves a stable output waveform at a frequency of 3 Hz, because the friction during generation has been eliminated. Changing wave amplitude and frequency will dramatically affect the output performance of ocean

wave energy harvester. Therefore, a refined wave spectrum can be used to provide useful feedback for improving the harvesting efficiency.

Triboelectric nanogenerator (TENG), based on the principles of triboelectrification and electrostatic induction, is a promising approach to convert low-frequency and low-amplitude kinetic energy to electrical energy [14,15]. Compared to conventional EMG and EMH, TENGs offer several advantages, including a low frequency operation range, compact dimensions, light weight, and no emissions or pollution during the generation stage [16–18]. TENG is comprised of four distinct operation modes, i.e., vertical contact-separation, contact-sliding, single-electrode, and freestanding triboelectric-layer modes [19]. These operation modes can be grouped into two main categories: contact-separation and linear sliding modes. The contact-separation mode harnesses the relative displacement between the contact surfaces of the triboelectric material to generate electrical energy. This mode is preferred for low-frequency operations due to a lower friction force between contact surfaces when compared to the linear sliding mode [20–24]. Considering the limitation of interior area, the single-electrode mode is the most suitable choice owing to its simple structure, but it is limited by relevant low output performance. However, the output performance was not the majority requirement for sensor application [25].

In 2021, Luo et al. introduced a concept of utilising flexible TENG as an energy harvester to converter low frequency and amplitude human kinetic energy to electricity [26]. It utilised polyvinyl alcohol (PVA) hydrogel and polydimethylsiloxane (PDMS) as electrode and triboelectric material, respectively. Flexible TENG shows the ability to detect human body motion, and their output performance increases with the magnitude of motion. The linear relationship between the output performance of TENGs and input kinetic energy demonstrates their feasibility as sensors for measuring changes in wave amplitudes. Moreover, additives such as reduced graphene oxide (rGO) or MXENE can be added to the triboelectric material to enhance its electrical properties and obtain a high electrical output.

In this study, a hybrid self-powered wave sensor (HSP-WS) for monitoring wave amplitude variations is designed and fabricated, combining a contact and separation mode electromagnetic generator (CS-EMH) and a single electrode mode flexible triboelectric nanogenerator (F-TENG). The effects of wave frequencies and wave amplitudes of movements were experimentally analysed through a custom-made testing platform for both generators. Moreover, the HSP-WS was evaluated on a water channel with our previously developed wave generating system to demonstrate the feasibility of the prototype as a sensor for detecting low frequence and low amplitude waves.

5.2 Results and discussion

5.2.1 Working principle of the testing platform

The movement of the HSP-WS under wave involves both variations in frequency and amplitude. Therefore, the testing platform as shown in Figure 5.1(A) was used to analyse the effect of these two variables on the output performance of F-TENG and CS-EMH. The grey disk, as shown in Figure 5.1, adjusts the amplitude by changing different positions of connection shaft (highlighted by the red circles), and it produces a variety of different amplitudes ranging from 6.6 cm to 8.6 cm. The disk is driven by a linear motor which is behind the motor shaft in Figure 5.1(A), the motor shaft has been connected to the central of the disk, and frequency adjustments (1.5 Hz to 4.0 Hz) are made by changing the input voltage of linear motor. The design of testing platform allows the independent testing of changes in amplitude and frequency on the HSP-WS. Figure 5.1(B) demonstrates how the testing platform mimics wave motion and the real-time operation of HSP-WS with the testing platform. At stage (i), the HSP-WS is kept in the initial condition at 0°. Once the disk starts to rotate 90°, as shown in stage (ii), the spherical magnet starts to roll down as the gravitational force component which acts on the spherical magnet exceeds the friction between the magnet and the sliding rail. The disk continues to rotate to 180°, at which point the spherical magnet reaches the end of sliding rail. The disk then continues to rotate to 270°, where the spherical magnet starts to roll back to the starting point. Once the disk completes one cycle, the spherical magnet is restored to its initial state. To mimic a larger wave amplitude, a more powerful motor can be used to drive larger disk.

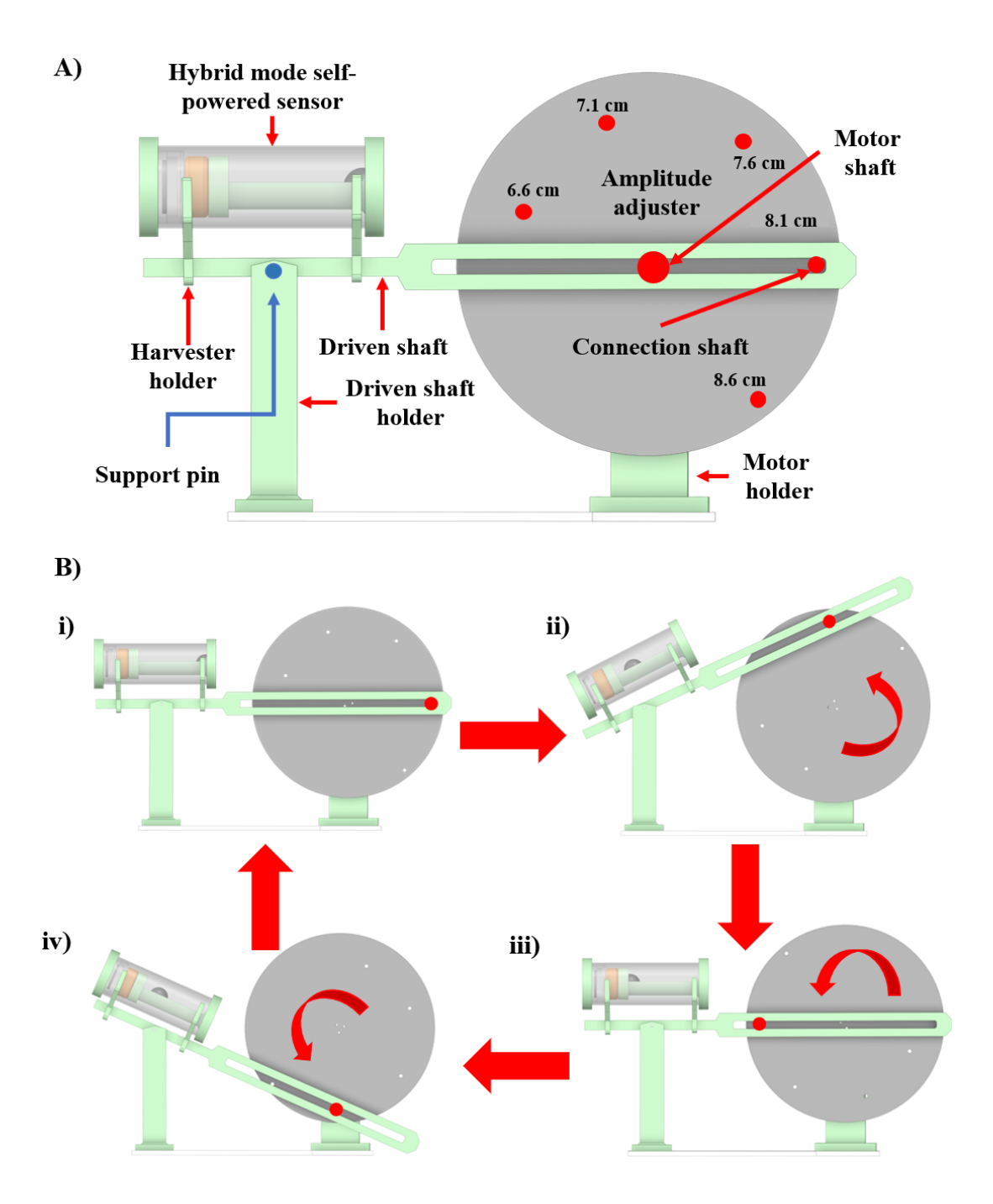


Figure 5.1 Structural design and working principle of the testing platform. (A) Schematic drawing of the testing platform. (B) Schematic drawing of the operation cycle: (i) origin status, (ii) the disk rotates 90 degrees, (iii) the disk rotates 180 degrees, and (iv) the disk rotates 270 degrees. This testing platform is used to mimic wave motion, including wave frequency and wave amplitude. The five red dots represent adjustable wave amplitudes ranging from 6.6 cm to 8.1 cm, increasing by 0.5 cm at each stage. The blue dot represents the rotation point used to simulate wave motion on the left side of the testing platform.

5.2.2 Design and working mechanism for CS-EMH and F-TENG in HSP-WS

HSP-WS is consisting of a CS-EMH and a F-TENG, as depicted in Figure 5.2(A). The CS-EMH consists of a spherical magnet and a copper winding. The electrical energy is induced by the relative movement between the copper winding and the spherical magnet, caused by movement of the spherical magnet related to the copper winding. The F-TENG is fabricated using flexible materials to ensure deformability in order to obtain maximum contact area, and thus it enables harvesting kinetic energy when the spherical magnet impacts the copper winding due to the pitching movement of acrylic tube. Additionally, the HSP-WS has compact dimensions as illustrated in Figure 5.2(C), with weight of only 300 g. A transparent acrylic tube serves as the primary structure for the exterior of HSP-WS. Two bottom cups, one of which integrates an open-ended rail to avoid unnecessary kinetic energy losses between magnet and rail, and the other one is used to seal the device. Both were fabricated using polylactic acid (PLA) through 3D printing technology. The copper winding has been positioned behind an O-shaped ring, which is employed to limit the position of copper winding. F-TENG is situated behind the copper winding, while the spherical magnet is positioned on the rail, as depicted in Figure 5.2(B). An expanded view of F-TENG is shown in Figure 5.2(D) where triboelectric materials for F-TENG include PVA-based hydrogel with reduced graphene oxide (rGO) and silicone rubber. Furthermore, copper pieces are employed as electrodes for the single-electrode mode F-TENG.

A typical one cycle of F-TENG generation is depicted in Figure 5.2(E(i) -E(iv)). When the spherical magnet contacts with the copper winding, the kinetic energy is transmitted to F-TENG. The kinetic energy creates pressure between the silicone rubber and the PVA-based hydrogel, as depicted in Figure 5.2(E(i)). When the spherical magnet moves away from the copper winding, the pressure between the copper winding and F-TENG dissipates. Consequently, the silicone rubber moves away from the PVA-based hydrogel as depicted in Figure 5.2(E(ii)). In the meantime, the positive charges present on the surface of PVA-based hydrogel induce charges on the electrodes, owing to electrostatic induction effect. The potential difference between the electrodes and the grounding wire induces electron flow, resulting in current generation. When the silicone rubber separates from the PVA-based hydrogel, the charge flow is driven by the potential difference, leading the device to reach an electrostatic equilibrium, as shown in Figure 5.2(E(iii)). At this stage, the electrons will flow to the PVA hydrogel from the silicon rubber. When the copper winding compresses the F-TENG once more, electrons flow back from the PVA hydrogel to the silicone rubber and an opposite direction current will be generated, as depicted in Figure 5.2(E(iiv)).

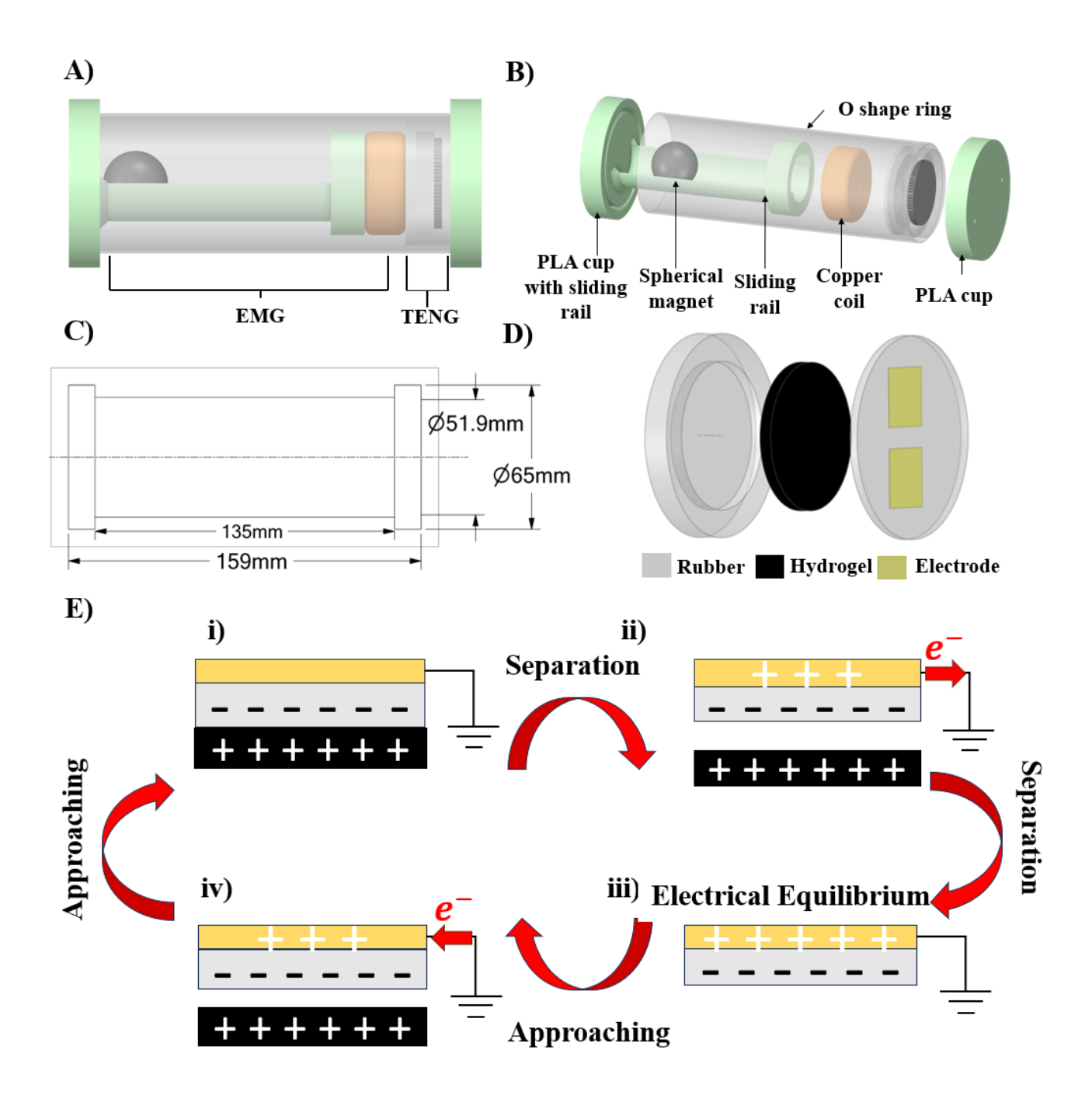


Figure 5.2 (A) Overview of the HSP-WS, involving a contact and separate electromagnetic generator (CS-EMH) and a flexible triboelectric nanogenerator (F-TENG), (B) An exploded view of the HSP-WS. (The green parts are fabricated using PLA, and the transparent grey part is the acrylic tube), (C) Geometric dimensions of the HSP-WS, (D) An exploded view of the F-TENG, and (E) (i-iv) The energy generation cycle of the F-TENG.

5.2.3 Performance evaluation and demonstration of the CS-EMH

The output performance of CS-EMH was examined first, based on Equation (5.1) known as the Lenz's law.

$$\epsilon = -N \frac{\Delta \varphi}{\Delta t} \tag{5.1}$$

where, ϵ represents induced voltage, also known as induced electromotive force (emf). N stands for number of loops in the copper winding, $\Delta \varphi$ represents change in magnetic flux, and Δt is change in time. Instead of counting number of loops in the copper winding, N is estimated based on the weight and size of copper winding. $\Delta \varphi$ represents the magnetic flux of spherical magnet.

Based on Equation (5.1), the main factor which will affect the output performance of CS-EMH is Δt , i. e., the reciprocal of frequency of wave motion. Under this mathematical derivation, the voltage output of CS-EMH should increase as frequency increases. As shown in Figure 5.3(A), the voltage output of CS-EMH at all five different amplitudes (6.6, 7.1, 7.6, 8.1 and 8.6 cm) continues to increase with increasing frequency up to 3.0 Hz. The output performance of CS-EMH under 3.5 Hz of all five amplitudes is slightly decreasing or remains the same. Furthermore, when the operating frequency is set as 4.0 Hz, the output performance of the CS-EMH becomes unstable.

Based on the analysis results, the amplitude also influences the CS-EMH output performance. The detailed waveforms for each amplitude at different frequencies are provided in Figure S5.3-S5.7. Moreover, Figure 5.3(B) illustrates the typical waveform of the open-circuit voltage of CS-EMH, with a peak-to-peak voltage of 4.1 V. The copper winding has a self-resistance of 9.8 Ω , resulting in an output current of 0.4 A as depicted in Figure S5.13(A). The CS-EMH demonstrates a noticeable low-frequency operation ability which can be activated by a frequency as low as 1.5 Hz. The experiment results in Figure 5.3(A) show that the best operation frequency range for CS-EMH is between 1.5 Hz to 3.0 Hz.

A mathematical model is described in the next section to assist the understanding of the working mode of CS-EMH above 3.0 Hz. A power management system for the CS-EMH which consists of four Schottky diodes and four 150 nF capacitors is shown in Figure 5.3(C). It can convert AC output to DC, and it can boost the voltage output. The capacitor is charged by the input voltage generated by CS-EMH. Those charges are then directed through a pathway which is dictated Schottky diode direction. A capacitor and a Schottky diode are considered as one pair. In theory, the output can be boosted multiple times, depending on the number of Schottky diode and capacitor pairs in the power management system. As shown in Figure 5.3(A), the maximum voltage of CS-EMH at 1.5 Hz is only 1.4 V which is not adequate to light an LED. However, by employing the power manage system, it can light an LED under 1.5 Hz generated wave in the water channel system.

The results show that CS-EMH functions as a self-powered flashing indicator. If the capacitors in the power management system are replaced by 100 μ F capacitors, the CS-EMH can continuously light up a LED at 3.0 Hz. This demonstrates that CS-EMH can power additional devices integrated within the HSP-WS, such as Bluetooth, enabling remote signal transmission such as frequency and amplitude of ocean wave measured by F-TENG.

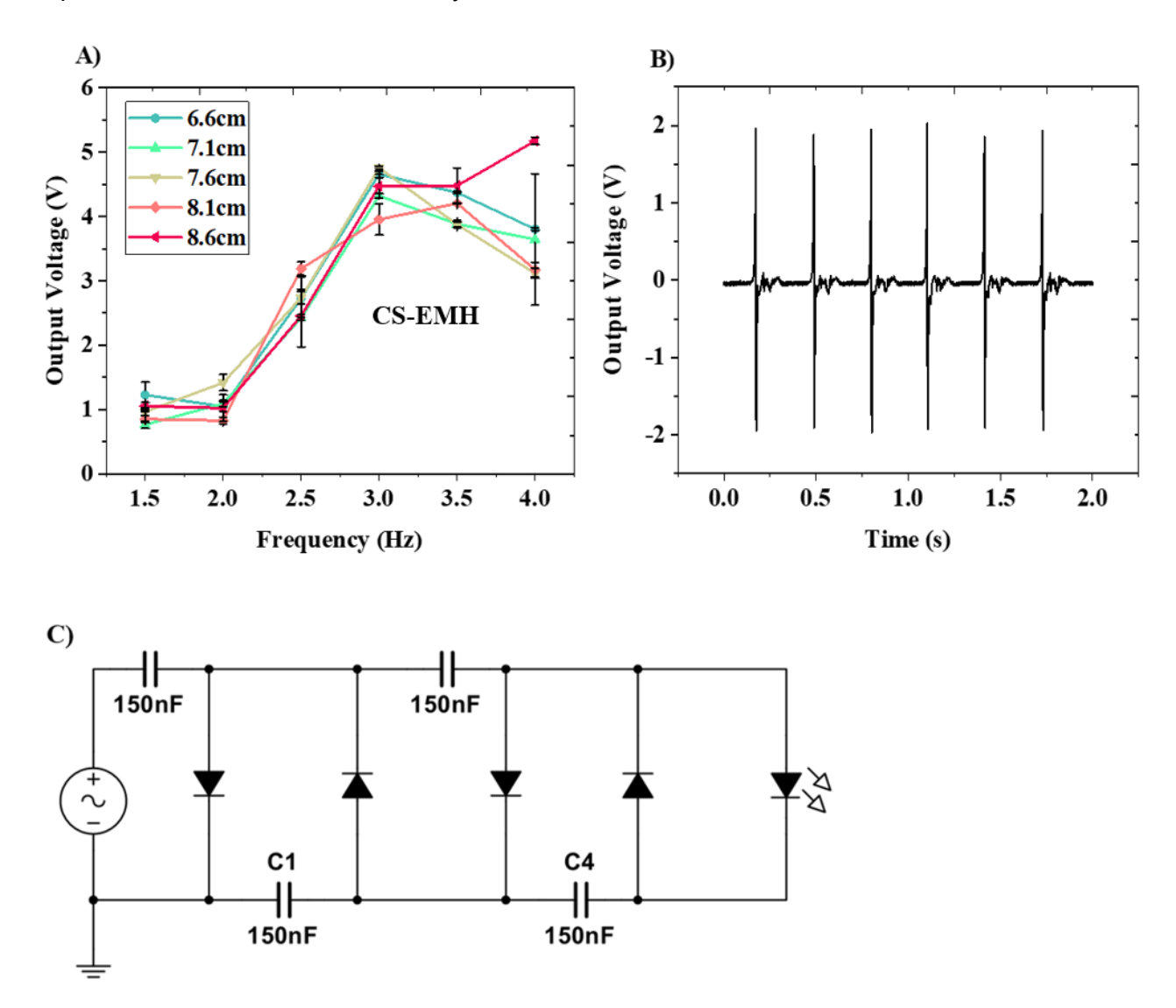


Figure 5.3 (A) The output performance of CS-EMH at various frequencies (ranging from 1.5 Hz to 4.0 Hz) and amplitudes (ranging from 6.6 cm to 8.6 cm), (B) typical waveform of the output voltage of the CS-EMH operated under 3 Hz frequency and 8.6 cm amplitude, and (C) the power management system used for CS-EMH in this study.

5.2.4 Explanation of the two operations modes of the CS-EMH

Assuming that the spherical magnet is a rigid body, and the rail contact surface is smooth and rigid, a single-point contact condition is expected between the spherical magnet and the rail. The spherical magnet is also expected to roll down without any slipping when the swing amplitude is set to be

moderate (≤ 25 °) [27], According to these conditions, the following basic linear and rotational motion equations of the spherical magnet can be used to describe the current kinematic state:

$$m\frac{dv}{dt} = mgsin\theta - F_f \tag{5.2}$$

$$I_c \frac{d\omega}{dt} = F_f R$$

(5.3)

where m stands for the mass of spherical magnet; g stands for acceleration due to gravity 9.81 N/m; I_c is the moment of inertia about the rotation axis through centre of mass; F_f is the friction force; and R is the radius of spherical magnet. Equation (5.2) corresponds to linear motion, representing the downward rolling acceleration of spherical magnet, while Equation (5.3) reflects force balance for the rotational degree of freedom. Based on Equation (5.2) and (5.3), Equation (5.4) can be obtained:

$$\frac{dv}{dt} = R \frac{d\omega}{dt}. ag{5.4}$$

A mathematical formula can be reached to calculate the approximate time for spherical magnet to reach from rest at one rail end to the other end:

$$t_{travel} = \sqrt{\frac{14*(L-d)}{5gsin\theta}} \tag{5.5}$$

where *L*, and *d* represents the length of the rail (102 mm) and diameter (25 mm) of the spherical magnet, respectively. To calculate the actual distance travelled by the centre of mass of the magnet, the magnet 2R is subtracted from the rail length. It should be noted that Equation (5.5) only works for the mode of rolling without slipping and provides the lower bound of travel time, which corresponds to the upper bound of operation frequency. However, it can be utilised to evaluate the effect of amplitude (tilt angle) change on the operation frequency of CS-EMH. Through the calculation results, larger amplitudes result in higher acceleration, generating short travelling time which corresponds to high operation frequency of CS-EMH. The complete derivation is provided by Figure S5.12, Table S5.2, and Equation (S5.1-S5.5).

Experimentally, it can be observed that the operation frequency of CS-EMH results in two different operation modes. In Mode 1, the spherical magnet slides along the rail. In Mode 2, the spherical magnet jumps between the bottom cup and the copper winding because the magnet travel time exceeds the rotation speed of a half cycle on the testing platform, as shown in Figure 5.4. When the frequency is less than 3.0 Hz, the spherical magnetic is rolling on the rail, i.e., the CS-EMH works in Mode 1. Once the operation frequency is over 3.0 Hz, the CS-EMH will operate in Mode 2. Based on Figure 5.4 and Equation (S5.1-S5.5), the calculated frequency is higher than the experimental response frequency because the spherical magnet only starts to slide once the rolling force overcomes the friction force during the rotation of the testing platform's circular disk. This difference

causes the small gap (shown in Figure 5.4) between calculated (3.4 Hz) and experimental (3.0 Hz) frequencies of the Mode 1 to Mode 2 transition.

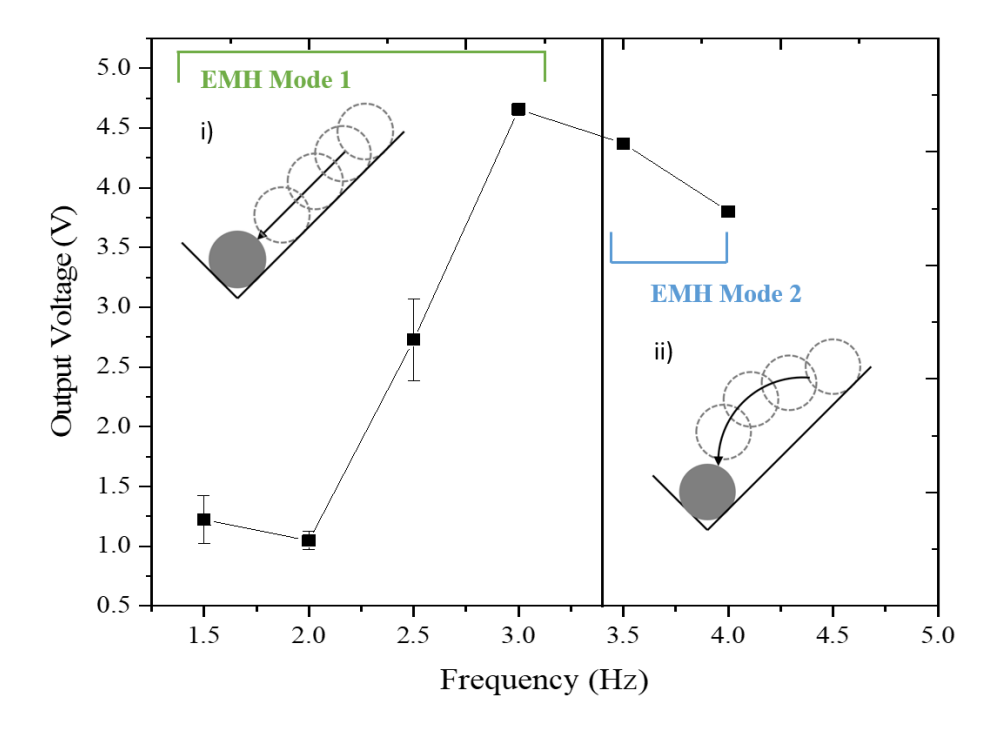


Figure 5.4 Different operation modes of CS-EMH under various frequency ranges, utilising a 6.6 cm amplitude as an example. The green parenthesis involves four frequencies from 1.5 Hz to 3.0 Hz, working under Mode 1 as shown in (i). The blue parenthesis involves two frequencies of 3.5 Hz and 4.0 Hz, working under Mode 2 as shown in (ii). The solid line represents the calculated frequency of Mode 1 to Mode 2 transition, and the dashed line represents the actual experimental frequency of transition. The gap, as represented by the orange arrow, represents the difference between the experimental frequency and the calculated frequency.

5.2.5 Performance evaluation and analysis for the F-TENG

The output performance of single-electrode mode F-TENG can be estimated by Equation (5.6) [28].

$$V_{oc} = \frac{\sigma w l C_2}{C_1 C_2 + C_2 C_3 + C_3 C_1} \tag{5.6}$$

where, σ is the surface charge density of triboelectric material, w and l represent the width and length of triboelectric material or named as contact area. C_1 , C_2 , and C_3 represent the equivalent capacitance of single-electrode mode TENG system which depends on the electrical property of triboelectric material as shown in Figure S5.14. Therefore, the contact area of triboelectric material is the major factor which will affect the output performance of single electrode mode F-TENG. The large contact area can be achieved by increasing the amplitude of testing platform, i.e., higher amplitude results in higher input kinetic energy, which creates a larger contact area between two triboelectric materials. So, the amplitude was set to 8.6 cm for further study.

It was found that the output performance of F-TENG is increased with the increase of frequency. At a frequency of 4.0 Hz and with 0% and 0.5 wt.% rGO weight content ratio, the F-TENG can generate 1.14 V and 1.19 V, respectively, whilst with 1.0 wt.% and 1.5 wt.% rGO weight content ratio, it can generate 1.39 V, as shown in Figure 5.5(A). Experiment results show that a higher rGO content in the hydrogel enhances the output performance, and the enhancement becomes more obvious with the increase of frequency. The observed result shows the linear relationship between the input kinetic energy and the output performance. The detailed waveforms for different rGO contents at different frequencies are provided in Figures S5.8-S5.11. Moreover, the typical waveform of output voltage of F-TENG under an amplitude of 8.6 cm and a frequency of 3 Hz generates a peak-to-peak voltage of 1.15 V, as depicted in Figure 5.5(B). It was noted that an additional relevant smaller peak signal appears between two operation cycles of F-TENG as shown in red brackets in Figure 5.5(B). The signal (Signal 1) is induced by electron transfer through the contact and separation between the copper winding and the silicon rubber as shown in Figure 5.5(C). The potential difference between the copper winding and the silicon rubber is less than that between the silicon rubber and the hydrogel. Due to this potential difference, an electrical signal (Signal 2) was generated, as shown in the blue box in Figure 5.5(B), caused by the electron transfer between the silicon rubber and the PVA-hydrogel. The detailed process of generating Signal 2 is illustrated in Figure 5.5(C).

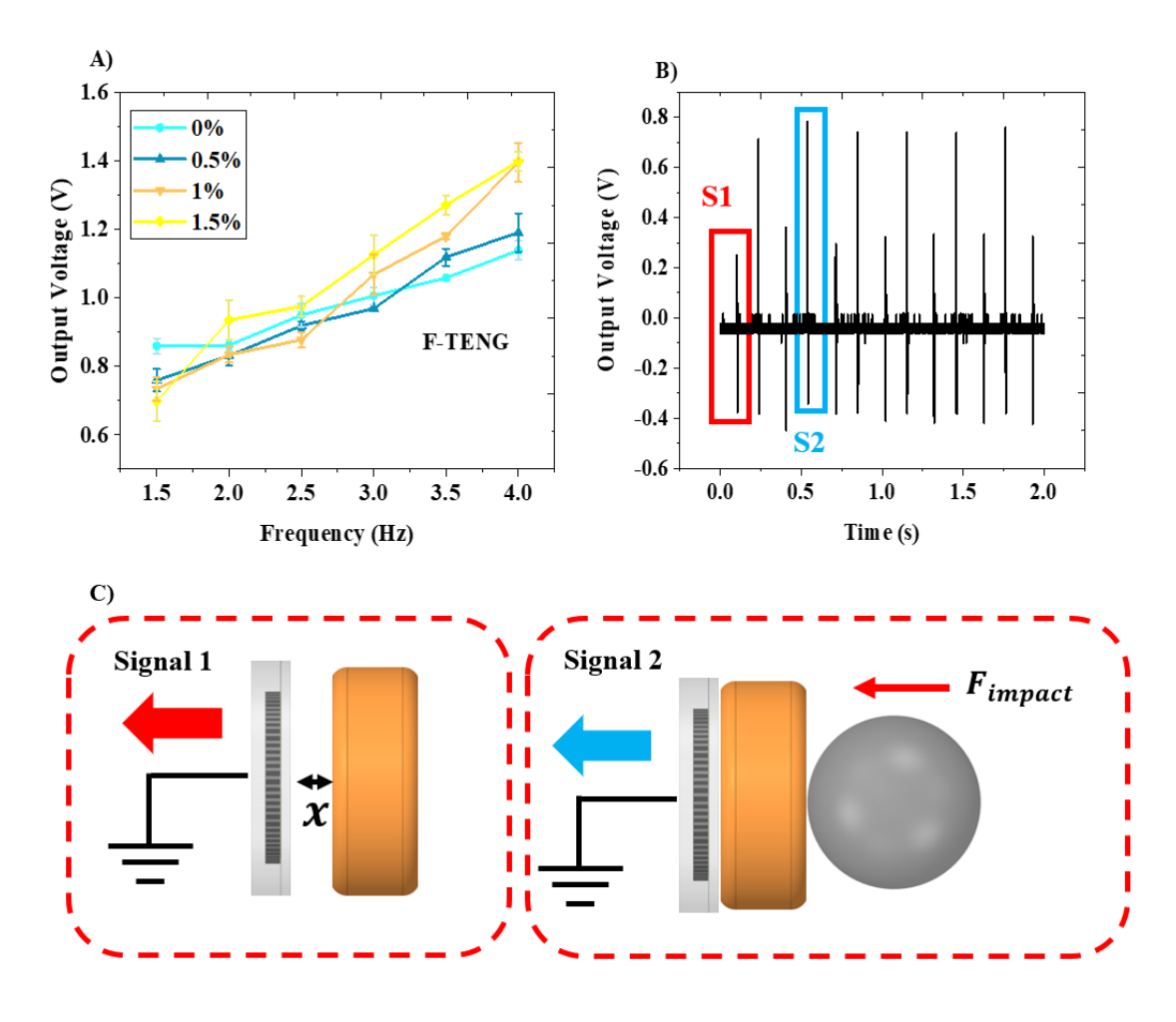


Figure 5.5 (A) The output performance of F-TENG is depicted at various frequencies with an amplitude of 8.6 cm. When the amplitude is set to 8.6 cm, the spherical magnet can generate maximum acceleration, leading to the highest input kinetic energy for F-TENG, (B) Typical waveform of the output voltage of F-TENG with 3 Hz frequency and 8.6 cm amplitude, (C) Explanation of two signals generated by F-TENG: Signal 1 is produced by electron transfer between the silicon rubber and the copper winding. The rGO hydrogel is used as conductive material to transfer the generated current to the copper electrode and then to the load circuit. Signal 2 is induced by electron transfer between rGO and the silicon rubber, which is then transferred to the load through the copper electrode.

5.2.6 Durability analysis of CS-EMH and F-TENG in HSP-WS

The durability of CS-EMH and F-TENG was evaluated under the optimised condition mentioned above, i. e., a frequency of 3.0 Hz and an amplitude of 8.6 cm. The output voltage of the CS-EMH was monitored over a 5-day testing period, where the device runs continuously for 8 h each day. The 50-second output voltage versus different days is illustrated in Figure 5.6(A) and (B). The output data was recorded while the device was placed on the testing platform, initially an output voltage of 4.30±0.40 V was recorded on the first day as shown day 0. After 8 h of continuous operation on day 1, the CS-EMH's output showed no significant change, with an output voltage of 4.20±0.40 V. Similarly, on day 2, after 8 h of continuous operation, the output voltage remained at 4.20±0.40 V. After two days of testing, the output of the CS-EMH stabilised and became repeatable, maintaining an output voltage of 4.10±0.40 V until the experiment was completed on day 5. The durability of F-TENG was evaluated in parallel as shown in Figure 5.6(B), recording an initial output voltage of 1.20±0.30 V (Day 0), which did not change during the first day. However, the output slightly increased on day 2 and day 3, with an output voltage of 1.28±0.30 V. Subsequently, the output of the F-TENG returned to the Day 0 value of 1.20±0.30 V and remained the same for the rest of the experiment. Based on these results, both the CS-EMH and F-TENG exhibited decent durability over the 5-day period, which indicates the potential for application.

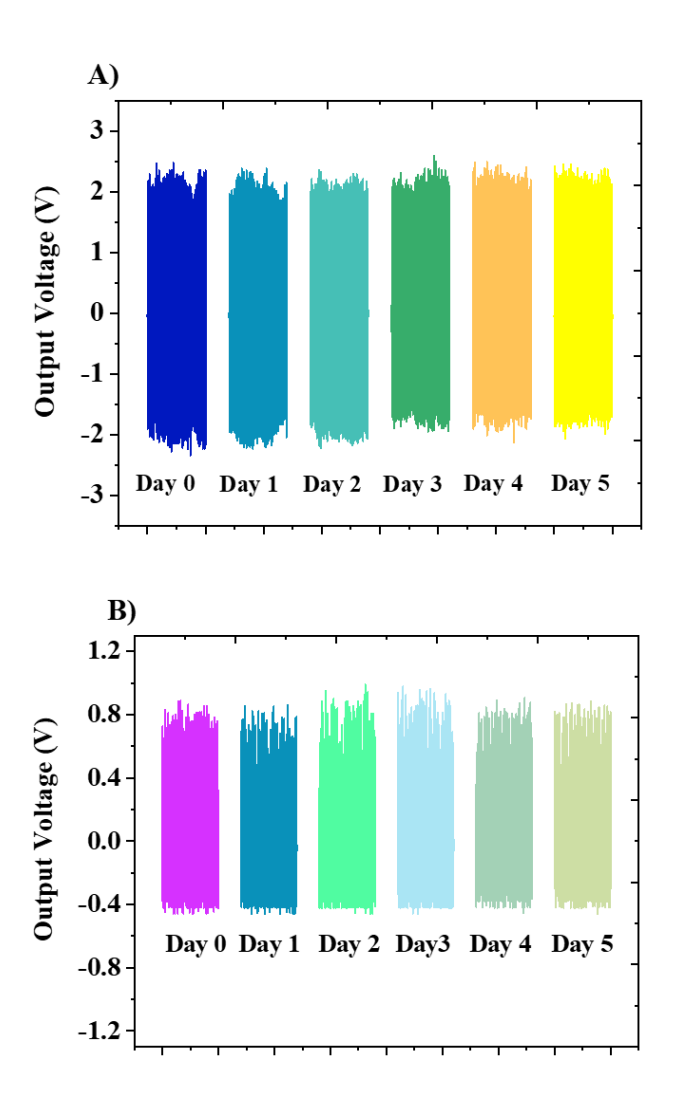


Figure 5.6 The durability test results for (A) CS-EMH and (B) F-TENG. The output voltage of both the CS-EMH and F-TENG was tested under the operating condition of a 3.0 Hz frequency and an 8.6 cm amplitude.

5.2.7 Evaluation and analysis of HSP-WS under a wave generating system

The output performance of the HSP-WS was tested under generated waves on a water channel with 1.5 Hz frequency and amplitudes with 5.6 cm, 6.2 cm, 6.8 cm, and 7.1 cm, respectively as shown in Figure 5.7(A). The response of HSP-WS increases with the increment of amplitude, and the output electrical signal is stable and repeatable once the wave amplitude exceeds 6.2 cm. The experimental results, based on the generated waves in the water channel, demonstrate that HSP-WS's ability to monitor wave amplitude changes for waves larger than 6.2 cm. The CS-EMH with the power management system lights the LED under 1.5 Hz and demonstrates the potential to be employed as a flashing indicator. The output comparison of the F-TENG under the wave channel and the testing platform is shown in Figure 5.7(B). These results show a similar increasing trend with the increment of wave amplitude, demonstrating the flexible TENG can be used to detect the wave amplitude changes.

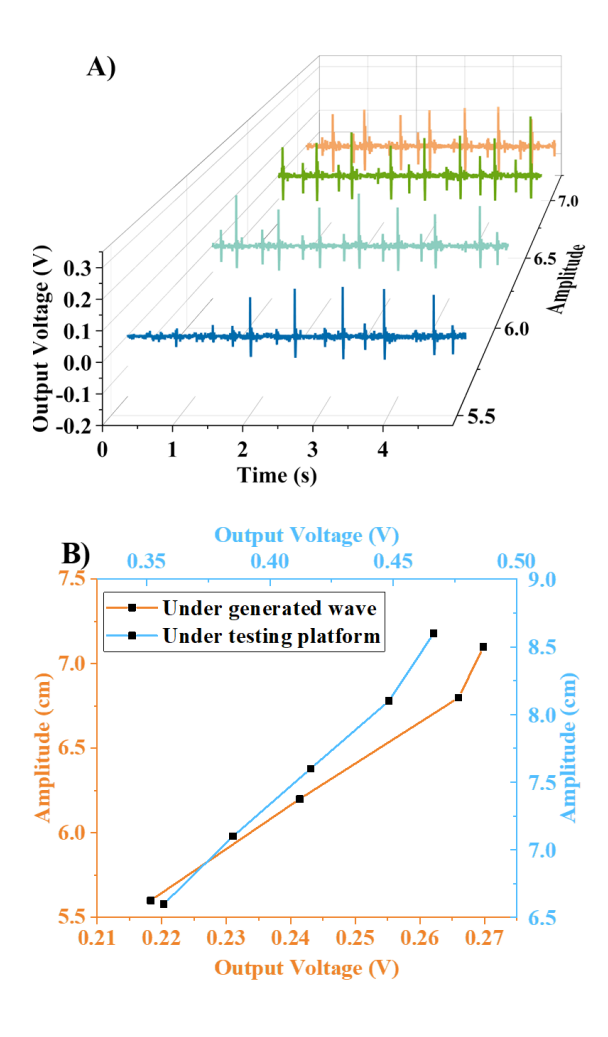


Figure 5.7 (A) Output waveform under different generated waves, and (B) comparison of output performance under the water channel and the testing platform.

5.2.8 Signal analysis and potential applications

Figure 5.8(A) illustrates how the electrical signal is generated with wave variations and how the device operates as a wave amplitude sensor. In stage 1 (the initial state), the device floats on water surface without motion due to the absence of applied kinetic energy. Once HSP-WS is triggered by the pitching motion of a wave, the spherical magnet rotates and impacts the copper winding, causing relative movement between the copper winding and the F-TENG, which generates Signal 1 as shown in stage 2. After that, Signal 2 is generated due to the time requirement on the force transferring. The magnitude change of Signal 2 represents the change in the wave amplitude, as shown in stage 3. Afterwards, the HSP-WS moves downward, and the spherical magnet returns to the initial condition, as shown in stage 4. In stage 5, the HSP-WS is back to the initial condition. The distance between two peak electrical signals represents the wave period, also known as the wave frequency. The HSP-WS includes an energy transfer module, a self-powered flashing indicator module, and a self-powered sensor module, as shown in Figure 5.8(B). A 0.388 A current and 1.47 W output power is generated under the output voltage of CS-EMH of 3.8 V and a self-resistance of 9.8 Ω , which demonstrates the potential application of powering electronic devices such as water temperature sensor, water oxygen sensor, and low energy Bluetooth. The energy requirement of those electronic

devices has been provided in Table S5.3. A low-energy Bluetooth module can enable the remote signal transfer to an onshore station for further processing by an operator. The detailed flowchart as shown in Figure 5.8(C) demonstrates the application potential of this device in Internet of Things (IoT).

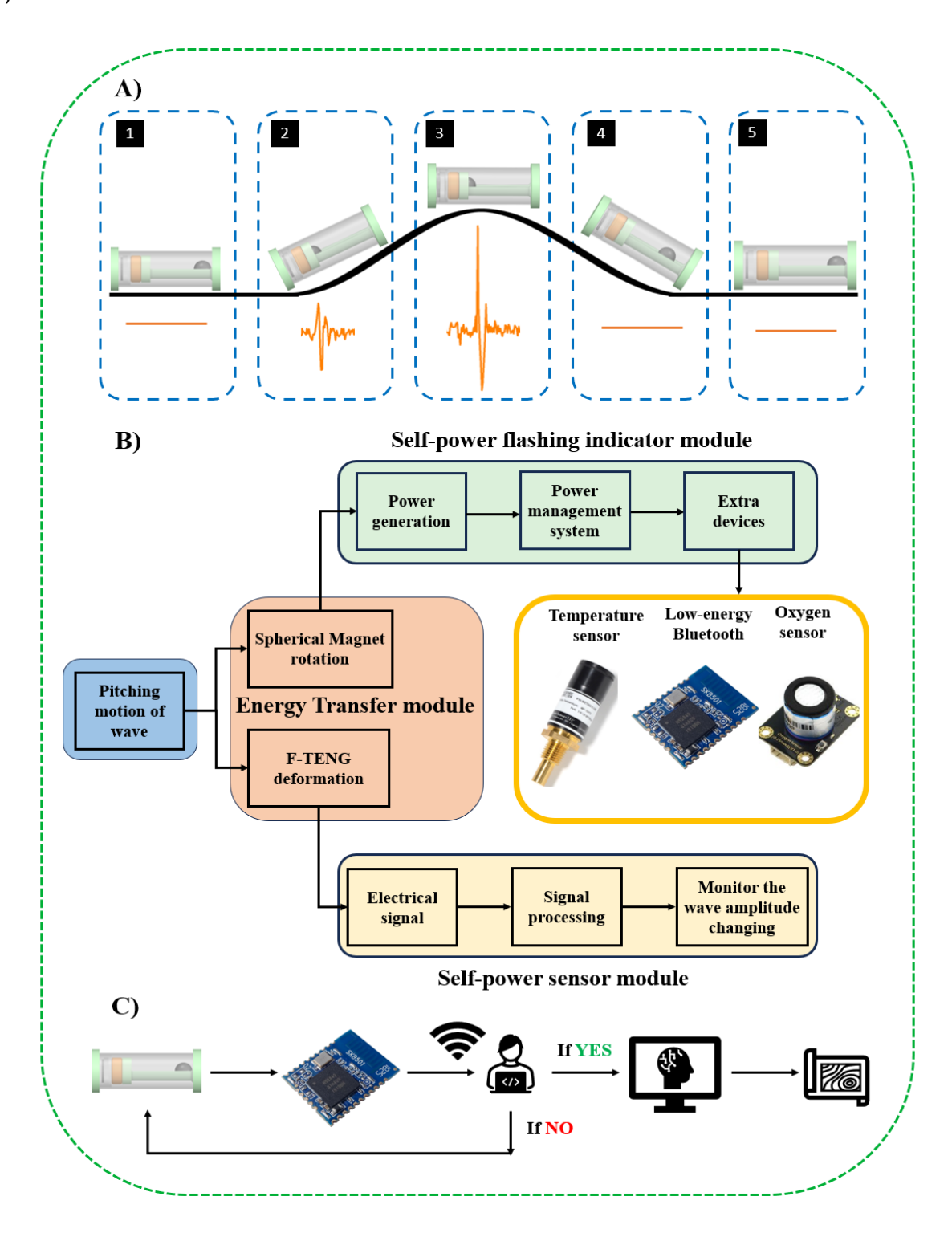


Figure 5.8 (A) Working principle of the HSP-WS, (B) workflow diagram of the HSP-WS with potential applications and module section definitions, and (C) the application potential of HSP-WS in IoT.

5.3 Conclusion and outlook

In this study, a hybrid self-powered wave sensing device has been proposed, which can utilise low-frequency and low-amplitude wave energy as a flashing indicator and a wave amplitude sensor. F-TENG employed as a wave amplitude sensor, providing a linear relationship between wave amplitude and strength of electrical signal. It demonstrates the extra low reactive wave amplitude of 6.2 cm which is significantly lower than that of a current radar-based ocean wave sensor.

The CS-EMH exhibits low-frequency operation ability. It can cooperate with a power management system and be employed as a power supplier for a flashing indicator or extra electronic devices, such as sensors or low-energy Bluetooth modules under 1.5 Hz and 3 Hz, respectively. Both the CS-EMH and F-TENG demonstrated excellent durability during a 5-day robustness test with 432,000 working cycles, and adaptability to different frequencies and amplitudes when tested under the generated waves. The device will be explored for omnidirectional capabilities in the future [29]. More importantly, this device shows potential as a self-powered sensor to refine and optimise the ocean spectrum along coastline, offshore and inner gulf which benefits from the utilisation of ocean resources in the future. The hybrid self-powered wave sensor can be used as a battery-free ocean wave sensor for remote wave amplitude monitoring.

5.4 Experimental procedures

5.4.1 Materials

PVA powder (Mw 89,000 - 98,000, degree of alcoholysis: 99 mol%) from Sigma Aldrich (Australia), high conductive reduced graphene oxide (rGO) from ACS material (USA) and Ecoflex 00-30 from smooth-on (USA) were used in this study without further treatment. 100 g copper wire with 0.5 mm diameter, a 25 mm diameter 50 g weight neodymium spherical magnet with a Nickel-Copper-Nickel (Ni-Cu-Ni) coating (Frenergy, Australia) provides 0.2938 T magnetic field intensity employed as a flux donator. An acrylic tube supplied by Acrylic Online (Australia) with a 55 mm outer diameter, 51 mm inner diameter, and 150 mm length was utilised as the main body of the HSP-WS.

5.4.2 Fabrication of rGO/PVA hydrogel

A highly conductive rGO/PVA hydrogel was synthesised using a freezing and thawing process. A 10 wt.% PVA solution was prepared by dissolving 4 g of PVA powder in 40 ml of deionized water at 95 0C. The PVA powder and deionised water were thoroughly mixed using a magnetic stirrer set at 1200 rpm for 1 h. Subsequently, rGO was added to the PVA solution and stirred for 10 min to ensure thorough dispersion of the rGO powder. The mixed solution was then subjected to ultrasonic treatment for 0.5 h to achieve a uniform distribution of rGO powder within the PVA solution. Finally, the mixed PVA solution was stored in a 35 mm inner diameter tube in a freezer at -20 0C for 12 h and then thawed for 4 h, completing one cycle. This freezing and thawing process was repeated six times to ensure a satisfactory mechanical integrity through a high degree of crystallization of PVA

chains, forming the rGO/PVA hydrogel. After this, the hydrogel is cut to a thickness of 2 mm and 72 h freeze-dried to remove the moisture inside as much as possible, thereby eliminating the effect of moisture evaporation. The comparison of electrical property of the hydrogel before and after freeze-dried is shown in Figure S5.1, S5.2 and Table S5.1.

5.4.3 Fabrication of F-TENG

Mixed silicone rubber was poured into a 3D printed mould to separately fabricate the bottom and top cover parts for F-TENG. Wait for 2 h until the silicon rubber fully solidified. After that, the PVA-based hydrogel was cut to a 2 mm thickness and placed on the top of the base silicon rubber part. Then, silicone rubber solution was poured around the PVA-based hydrogel until it slightly covered the top of the PVA-based hydrogel. Left solution for 2 h to cure, and then a few drops of adhesive were applied between the hydrogel and silicone rubber parts to enhance the interfacial adhesion. The silicone rubber solution was also applied between the top cover and the base part and then assembled them together until there were cured together.

5.4.4 Fabrication of CS-EMH

One end of the copper wire was fixed to a 3 mm diameter shaft of a winding device. The copper wire was wound by the device until 100 g copper wire had been used. The size of the copper winding was limited by the inner diameter of acrylic tube. Therefore, a position limiter was used to adjust the copper winding to a thickness of 20 mm.

5.4.5 Performance evaluation

An oscilloscope (Keysight, InfiniiVision MSO-X 2004A, USA) was used to record the output waveform for both F-TENG and CS-EMH. A digital multimeter (Fluke 8808a, USA) was used to record the resistivity of PVA-based hydrogels. For the hydrogel in F-TENG, a freeze dryer (Virtis Benchtop PRO Freeze Dryers, UK) was used to decrease moisture inside the PVA-based hydrogel to determine effect of moisture on the hydrogel's conductivity.

5.5 Reference

- [1] J. Tollefson, Ocean-wide sensor array provides new look at global ocean current, Nature 554 (2018) 413–414. https://doi.org/10.1038/d41586-018-02113-y.
- [2] T.S. Hristov, S.D. Miller, C.A. Friehe, Dynamical coupling of wind and ocean waves through wave-induced air flow, Nature 422 (2003) 55–58. https://doi.org/10.1038/nature01382.
- [3] Z.L. Wang, Catch wave power in floating nets, Nature 542 (2017) 159–160. https://doi.org/10.1038/542159a.
- [4] J.C.N. Borge, K. Reichert, J. Dittmer, Use of nautical radar as a wave monitoring instrument, Coastal Engineering 37 (1999) 331–342. https://doi.org/10.1016/S0378-3839(99)00032-0.

- [5] R. Howell, J. Walsh, Measurement of ocean wave spectra using narrow-beam HE radar, IEEE Journal of Oceanic Engineering 18 (1993) 296–305. https://doi.org/10.1109/JOE.1993.236368.
- [6] Z. Sun, J. Sun, C. Guan, S. Liu, X. Suo, Performance of ocean wave spectrometer in detecting ocean wave spectra, in: 2012 2nd International Conference on Remote Sensing, Environment and Transportation Engineering, IEEE, 2012: pp. 1–4. https://doi.org/10.1109/RSETE.2012.6260652.
- [7] S. Chen, E.W. Gill, W. Huang, A first-order HF radar cross-section model for mixed-path ionosphere—ocean propagation with an FMCW source, IEEE Journal of Oceanic Engineering 41 (2016) 982–992. https://doi.org/10.1109/JOE.2015.2505778.
- [8] J. Walsh, W. Huang, E. Gill, The first-order high frequency radar ocean surface cross section for an antenna on a floating platform, IEEE Trans Antennas Propag 58 (2010) 2994–3003. https://doi.org/10.1109/TAP.2010.2052559.
- [9] C. Song, X. Zhu, M. Wang, P. Yang, L. Chen, L. Hong, W. Cui, Recent advances in ocean energy harvesting based on triboelectric nanogenerators, Sustainable Energy Technologies and Assessments 53 (2022) 102767. https://doi.org/10.1016/j.seta.2022.102767.
- [10] K. Fan, M. Cai, H. Liu, Y. Zhang, Capturing energy from ultra-low frequency vibrations and human motion through a monostable electromagnetic energy harvester, Energy 169 (2019) 356–368. https://doi.org/10.1016/j.energy.2018.12.053.
- [11] Ö. Zorlu, H. Külah, A MEMS-based energy harvester for generating energy from non-resonant environmental vibrations, Sens Actuators A Phys 202 (2013) 124–134. https://doi.org/10.1016/j.sna.2013.01.032.
- [12] W. Wang, J. Cao, N. Zhang, J. Lin, W.-H. Liao, Magnetic-spring based energy harvesting from human motions: Design, modeling and experiments, Energy Convers Manag 132 (2017) 189–197. https://doi.org/10.1016/j.enconman.2016.11.026.
- [13] D. Hao, L. Kong, Z. Zhang, W. Kong, A.M. Tairab, X. Luo, A. Ahmed, Y. Yang, An electromagnetic energy harvester with a half-wave rectification mechanism for military personnel, Sustainable Energy Technologies and Assessments 57 (2023) 103184. https://doi.org/10.1016/j.seta.2023.103184.
- [14] F.-R. Fan, Z.-Q. Tian, Z. Lin Wang, Flexible triboelectric generator, Nano Energy 1 (2012) 328–334. https://doi.org/10.1016/j.nanoen.2012.01.004.
- [15] L. Long, W. Liu, Z. Wang, W. He, G. Li, Q. Tang, H. Guo, X. Pu, Y. Liu, C. Hu, High performance floating self-excited sliding triboelectric nanogenerator for micro mechanical energy harvesting, Nat Commun 12 (2021) 4689. https://doi.org/10.1038/s41467-021-25047-y.

- [16] L. Liu, Q. Shi, J.S. Ho, C. Lee, Study of thin film blue energy harvester based on triboelectric nanogenerator and seashore IoT applications, Nano Energy 66 (2019) 104167. https://doi.org/10.1016/j.nanoen.2019.104167.
- [17] X. Wang, S. Niu, Y. Yin, F. Yi, Z. You, Z.L. Wang, Triboelectric nanogenerator based on fully enclosed rolling spherical structure for harvesting low-frequency water wave energy, Adv Energy Mater 5 (2015) 1501467. https://doi.org/10.1002/aenm.201501467.
- [18] X. Wen, W. Yang, Q. Jing, Z.L. Wang, Harvesting broadband kinetic impact energy from mechanical triggering/vibration and water waves, ACS Nano 8 (2014) 7405–7412. https://doi.org/10.1021/nn502618f.
- [19] Z.L. Wang, Triboelectric nanogenerators as new energy technology for self-powered systems and as active mechanical and chemical sensors, ACS Nano 7 (2013) 9533–9557. https://doi.org/10.1021/nn404614z.
- [20] W. Xu, L.-B. Huang, M.-C. Wong, L. Chen, G. Bai, J. Hao, Environmentally friendly hydrogel-based triboelectric nanogenerators for versatile energy harvesting and self-powered sensors, Adv Energy Mater 7 (2017) 1601529. https://doi.org/10.1002/aenm.201601529.
- [21] L. Xu, T. Jiang, P. Lin, J.J. Shao, C. He, W. Zhong, X.Y. Chen, Z.L. Wang, Coupled triboelectric nanogenerator networks for efficient water wave energy harvesting, ACS Nano 12 (2018) 1849–1858. https://doi.org/10.1021/acsnano.7b08674.
- [22] T.X. Xiao, X. Liang, T. Jiang, L. Xu, J.J. Shao, J.H. Nie, Y. Bai, W. Zhong, Z.L. Wang, Spherical triboelectric nanogenerators based on spring-assisted multilayered structure for efficient water wave energy harvesting, Adv Funct Mater 28 (2018) 1802634. https://doi.org/10.1002/adfm.201802634.
- [23] T. Jiang, Y. Yao, L. Xu, L. Zhang, T. Xiao, Z.L. Wang, Spring-assisted triboelectric nanogenerator for efficiently harvesting water wave energy, Nano Energy 31 (2017) 560–567. https://doi.org/10.1016/j.nanoen.2016.12.004.
- [24] Y. Wang, A.T.T. Pham, X. Han, D. Du, Y. Tang, Design and evaluate the wave driven-triboelectric nanogenerator under external wave parameters: experiment and simulation, Nano Energy 93 (2022) 106844. https://doi.org/10.1016/j.nanoen.2021.106844.
- [25] M. Li, Y. Zhang, K. Li, Y. Zhang, K. Xu, X. Liu, S. Zhong, J. Cao, Self-powered wireless sensor system for water monitoring based on low-frequency electromagnetic-pendulum energy harvester, Energy 251 (2022) 123883. https://doi.org/10.1016/j.energy.2022.123883.

- [26] X. Luo, L. Zhu, Y.-C. Wang, J. Li, J. Nie, Z.L. Wang, A flexible multifunctional triboelectric nanogenerator based on mxene/pva hydrogel, Adv Funct Mater 31 (2021) 2104928. https://doi.org/10.1002/adfm.202104928.
- [27] R. Cross, Rolling and Sliding down an Inclined Plane, Phys Teach 61 (2023) 568–571. https://doi.org/10.1119/5.0112746.
- [28] S. Niu, Z.L. Wang, Theoretical systems of triboelectric nanogenerators, Nano Energy 14 (2015) 161–192. https://doi.org/10.1016/j.nanoen.2014.11.034.
- [29] H. Hong, T. Chen, J. Yang, Y. Hu, J. Hu, D. Li, F. Liu, L. Liu, H. Wu, Omnidirectional water wave energy harvesting by a spherical triboelectric nanogenerator with sliced-pizza-shaped electrodes, Cell Rep Phys Sci 5 (2024) 101933. https://doi.org/10.1016/j.xcrp.2024.101933.

CHAPTER 6 AN ACTIVE IMPACT DETECTION SYSTEM FOR OFFSHORE WIND TURBINES BASED ON TRIBOELECTRIC NANOGENERATOR

6.1 introduction

With the rapid electrification of traditional mechanical systems, there is an increasing demand for renewable energy sources to supply electricity to power modern society. Furthermore, more serious environmental regulations such as carbon neutrality strategies, which are accelerating the move toward sustainable energy solutions [1]. The Carbon Neutral strategy by 2050 emphasizes the largescale commercialization of sustainable energy sources, particularly solar photovoltaics (PV) and wind turbines [2]. Wind turbines have increasingly attracted the attention of both the market and researchers in recent years. Wind energy offers substantial potential as a naturally abundant resource, driving rapid development in both onshore and offshore wind power sectors [3-6]. The length of wind turbine blades continues to increase to meet the demand for greater power output. However, this trend introduces a new concern that the lifespan of the wind turbine. Current blade design follows the safe-life concept, which assumes that blades must consider the worst-case conditions throughout their service life, including potential impacts and overload scenarios [7]. In 2023, the Australian government introduced the Southern Ocean Region Offshore Wind Farm project off the coast of Victoria. This initiative aims to reduce carbon dioxide emissions generated by coalfired power stations, supporting the nation's goal of achieving carbon neutrality by 2050 [8]. The wind turbine used in this project is based on the United States National Renewable Energy Laboratory's 15 MW model, also known as the IEA 15 MW Offshore Reference Wind Turbine. This turbine features 117-meter-long blades. Maintenance and inspection of wind turbines of this scale are labour-intensive and require costly equipment [9].

Wind turbine blades are susceptible to various external impact loads, including those caused by animals and environmental conditions. Among weather-related factors, rain and hail can be significant sources of impact damage. Large hailstones can directly damage wind turbine blades, while rainwater, especially in offshore environments with high saline content, can cause corrosion on the blade's outer surface [10,11]. Fortunately, these weather factors can typically be predicted and monitored in advance using data from meteorological stations, allowing for a proactive preventive safety inspection and reducing the risk of potential failures. Unfortunately, with current technology, it is not possible to accurately predict bird movements. As a result, animal activity, particularly bird strikes, remains one of the most critical and unpredictable external factors that can cause damage to wind turbine blades [12]. Moreover, those external impacts can severely reduce the aerodynamic performance of wind turbine blades, leading to significant losses in power generation. In the worst-case scenario, structural failures such as bending or blade fracture could

occur during operation, resulting in substantial financial losses and large-scale power outages. Therefore, a suitable impact detection system is essential for wind turbine farms.

The current damage detection methods used in the wind turbine field mainly include visual inspection, acoustic emission, and strain monitoring [13]. Visual inspection is the most basic non-destructive testing (NDT) method used for large-scale wind turbines. Its primary advantages include low equipment cost, rapid assessment, and the ability to cover large surface areas. However, this method is only suitable for detecting damage that is clearly visible to the naked eye and may miss internal or subtle defects [14]. Moreover, although visual inspection is the most convenient method for detecting damage on wind turbine blades, it is not an active detection system, as the turbine must be shut down during the inspection process. Acoustic emission is a method that utilizes mechanical vibrations generated by stress waves resulting from damage in composite materials, such as matrix microcracking, fibre-matrix debonding, localized delamination, fibre pull-out, and fibre breakage [15,16]. Advantages of acoustic emission include high sensitivity and rapid global detection using multiple sensors, which do not require disassembly from the material. However, its application is limited when detecting localized flaws in complex geometries of composite materials [17]. The detection methods mentioned above are either cost-prohibitive for widespread deployment in both onshore and offshore wind farms, or they possess limited detection capabilities, being effective primarily for readily visible damage or structures with simple geometries. The optical strain gauge is one of the most widely used active detection methods for wind turbine blades. When mechanical strain is applied to the composite fibre, it causes a change in the Fiber Bragg Grating (FBG) period. Since light signals propagate through optical fibers, the system functions effectively in both illuminated and dark environments. Changes in the Fiber Bragg Grating (FBG) period alter the reflected wavelength, which can then be captured and analyzed to identify the moment an impact occurs. Compared to conventional strain gauges, it offers significant long-range measurement capabilities [18], making it particularly suitable for large structures such as the IEA 15 MW wind turbine, which features a blade length of 117 meters. Additionally, optical strain gauges are wellsuited for harsh environmental conditions, especially for offshore operations [19]. Due to the working mechanism of the optical strain gauge, it can realize active monitoring of the impact on the wind turbine blade without shutdown the wind turbine. However, the higher initial cost of optical strain gauges can significantly increase the overall expense of wind turbine systems.

Therefore, based on the analysis of currently available wind turbine blade impact detection methods, there is an urgent need for a cost-effective active impact detection sensor with a flexible structure that can be applied to complex geometries. In 2012, Zhong Lin Wang's group introduced the triboelectric nanogenerator (TENG), which utilizes the triboelectric effect and electrostatic induction as its electrical generation mechanisms [20]. When two materials with different electron affinities come into contact, one becomes negatively charged while the other becomes positively charged. Upon separation, electrons from the negatively charged material transfer to the positively charged

one, generating an electrical current through electron flow [21]. Owing to its unique electrical generation mechanism, a TENG can function as both a novel energy harvester and a self-powered sensor [22]. As a sensor, it exhibits exceptional sensitivity to small mechanical inputs such as vibration, impact, and pressure [23].

In 2019, Garcia et al. introduced a flexible self-powered sensor based on TENG technology [24]. PVDF and PVP fibres were used as the triboelectric materials, with copper serving as the electrode. This self-powered sensor demonstrated excellent sensitivity to various impact energy levels, with a detection range from as low as 2 J up to 30 J. However, the sensor was relatively bulky and lacked sufficient flexibility to conform to complex external geometries. In 2024, Wu et al. introduced a fully flexible self-powered sensor that employed PTFE and FEP as the triboelectric materials [25]. Due to the inherent flexibility of both PTFE and FEP, the sensor could easily bend up to 180 degrees, demonstrating its capability to conform to complex external geometries, such as those found on wind turbine blades. This flexible self-powered sensor successfully detected small-scale kinetic energy sources, including sound vibrations, radial artery pulses, and human motion. The success of this sensor highlights that flexible design is an optimal solution for monitoring and detecting small-scale kinetic energy. In 2023, Mehamud et al. introduced an active alert system based on a self-powered sensor [26]. This alert system consists of a self-powered sensor, a power management unit, a measurement module (Arduino nano), and an alerting component. The self-powered sensor operates in a single-electrode mode and uses Aluminum and PTFE as the triboelectric materials [27]. An Arduino Nano is used as the measurement device. Once the input signal reaches a defined threshold, the buzzer and LED are activated. The use of the Arduino platform also offers the advantage of facilitating further data analysis. This study presents a concept that utilizes a selfpowered system and self-powered sensors to form an active alert system for detecting vibrations. However, for offshore wind turbines, a wired data processing approach is not ideal due to the long distance between the sensors and the onshore analysis station.

Herein, to address the limitations of current wind turbine blade impact detection methods, an active, self-powered impact detection sensor is proposed. This sensor features a flexible structure to accommodate various external geometries, along with a simple design and cost-effective fabrication. Owing to the unique working mechanism of the triboelectric nanogenerator, this sensor can perform two functions: first, it is primarily used to detect impact, and second, to monitor rainfall in the region where the wind turbine is located. Impact and rainfall can directly or indirectly damage wind turbine blades. This self-powered sensor provides a potential solution for active detection and early warning, enabling timely safety checks to prevent unexpected blade fractures and fatigue.

6.2 Experimental result

As shown in Figure 6.1(A), the single-electrode self-powered impact detection sensor features a simplified structure composed of three layers: the upper layer, a flexible electrode, and the bottom layer. The upper layer is fabricated from natural rubber, which offers exceptional resistance to humidity and corrosion, making it well-suited for offshore wind turbine farm environments. To enhance the sensor's performance, a silver-based conductive grease (CW7100, CircuitWorks, USA) is applied as electrode and other triboelectric nanomaterial. This grease provides high electrical and thermal conductivity while offering protection against moisture and corrosion, accounting not only for offshore humidity and salt exposure but also for temperature variations between day and night. The bottom layer is made of PDMS (Ecoflex 00-30, USA), a material known for its outstanding flexibility, allowing the sensor to conform easily to various curved surfaces on different parts of a wind turbine. Owing to the specific properties of the triboelectric materials used, this sensor offers dual functionality: its primary role is as an impact detection sensor, while it can also serve as a rain droplet detection sensor. Figure 6.1(B(i-iv)) illustrates the operational cycle of the self-powered sensor when functioning as an impact detection sensor. The initial state is shown in Figure 6.1(B(i)). When an object impacts the wind turbine blade, the kinetic energy is transmitted through the composite material to the sensor, causing vibrations at the contact surface of the self-powered sensor. This energy generates a transverse force on the carbon fibre board, inducing relative transverse movement between the natural rubber and the silver-based conductive grease. This interaction triggers the generation of an electrical signal, as illustrated in Figure 6.1(B(ii)). During this pressure, the negative charges on the surface of the natural rubber induce electron flow in the electrode layer via electrostatic induction. The resulting potential difference between the electrode and the ground wire drives an electron flow. As the natural rubber reaches its maximum transverse displacement, the relative transverse movement between the natural rubber and the silver-based conductive grease ceases, and the system reaches electrostatic equilibrium, as shown in Figure 6.1(B(iii)). At this stage, electrons flow from the natural rubber to the silver-based conductive grease. As the energy within the carbon fibre board dissipates, several small electrical signals are generated due to the gradual, linear reduction of internal energy rather than an abrupt release. These reduced vibrations cause the silver-based conductive grease to reattach to the natural rubber layer. During this process, an opposite-direction electron flow is generated. At this stage, electrons move from the silver-based conductive grease back to the natural rubber, that resulting in the generation of an electrical signal in the reverse direction, as illustrated in Figure 6.1(B(iv)). Figure 6.1(C(i-iv)) illustrates the operational cycle of the self-powered sensor when functioning as a rain droplet detection sensor. Previous studies results have found that when a water drop is falling from the sky, triboelectricity will be generated and contributes to the charged surface of water drop [28,29]. It is worth noting that the charge of a water droplet can be either positive or negative, depending on the material it interacts with. In this experimental setup, the water droplet contacts an Aluminum alloy needle, resulting in the droplet take a positive charge, as shown in Figure 6.1(C(i)). As the positively

charged water droplet contacts the natural rubber, as shown in Figure 6.1(C(ii)), an induce electron flow is generated between the electrode and the ground. In a short-circuit condition, electrons flow from the ground to the electrode to balance this potential difference, eventually reaching electrostatic equilibrium, as illustrated in Figure 6.1(C(iii)). Once the water droplet moves away from the surface of natural rubber, it will generate a opposite direction electron flow as shown in Figure 6.1(C(iv)). In conclusion, both functions of the self-powered sensor are based on the contact—separation mode.

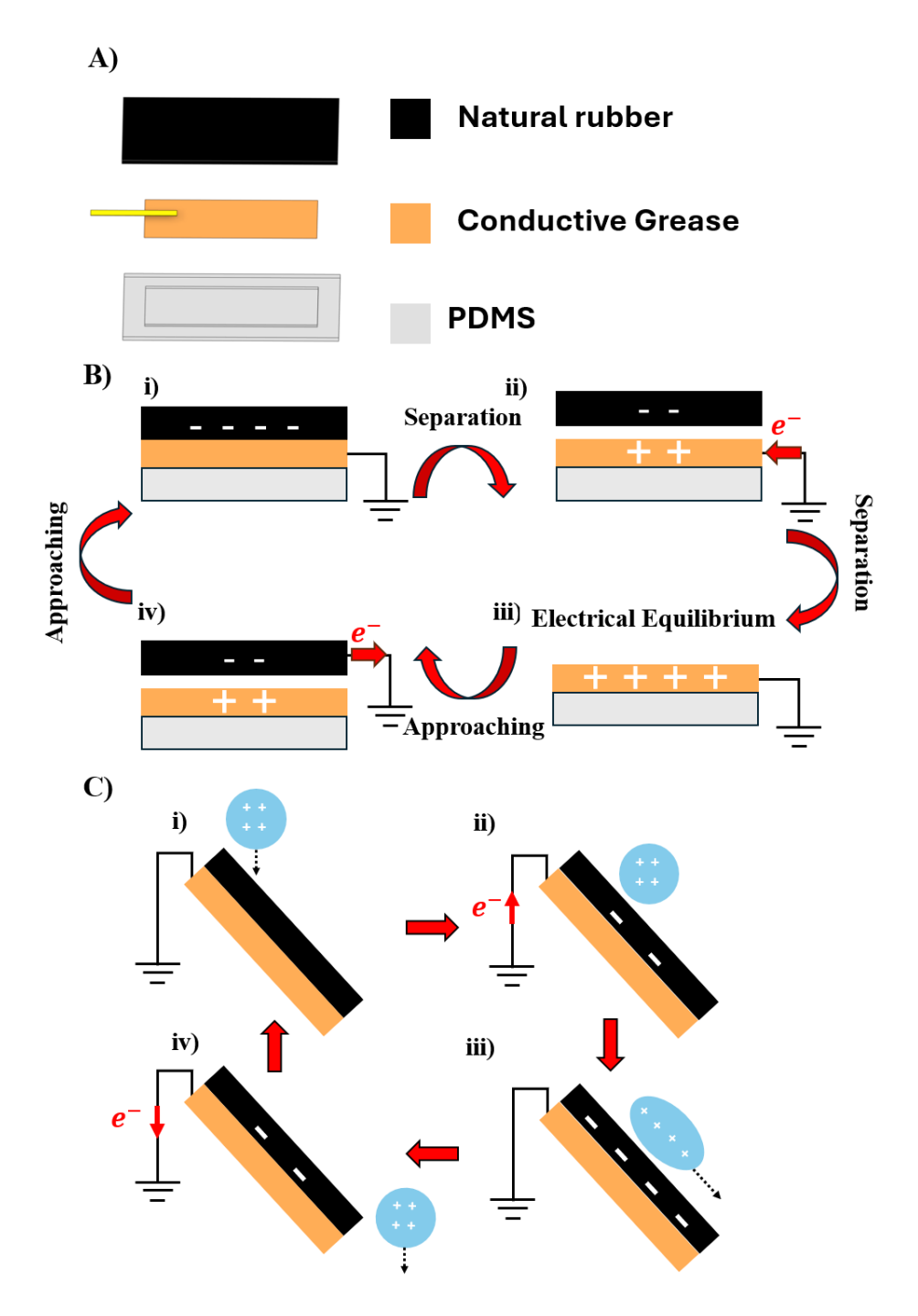


Figure 6.1 (A) Schematic of the self-powered single-electrode sensor. (B) Working mechanism of the sensor when operating as an impact detection device. (C) Working mechanism of the sensor when functioning as a water droplet detector.

6.2.1 Impact test

Impact testing was conducted using the Instron 9440 Drop Tower system, as shown in Figure 6.2(A(i)), with input impact energies ranging from 1.5 J to 3.5 J in 0.5 J increments. The carbon fibre board used to simulate the wind turbine blade measured 5 cm in width, 15 cm in length, and 2.5 mm in thickness, and was composed of five plies of carbon fibre sheets. The self-powered sensor was placed at one end of the carbon fibre board, while the oscilloscope probe was fixed to the side wall of drop tower system to monitor the generated electrical signals from sensor. The impact point was located at the opposite end of the carbon fibre board, as shown in Figure 6.2(A(ii)). The impact head of the Instron 9440 is made of soft nylon, as the purpose of this experiment is to investigate the relationship between increasing input impact energy and the resulting output electrical signal strength, rather than to study the mechanical properties of the carbon fibre board. According to Figure 6.2(C), the subfigures show the generated electrical signal waveforms under varying input impact energies, ranging from 1.5 J to 3.5 J. Each impact does not result in only a single impact. Instead, multiple vibrations occur after one impact. To analyse the experimental data, only the first peak of the electrical signal is used, because of it corresponds to the moment when the impact head contacts the carbon fibre board. Moreover, each input impact was tested three times to ensure the accuracy of the output signal. Based on the summary of experiment results of output electrical signal strength under different input impact energy as shown in Figure 6.2(B). The electrical signal strength exhibits a directly proportional relationship with the increasing input impact energy. The trend indicates a clear linear correlation between the output electrical signal strength and the applied input impact energy. According to subfigures in Figure 6.2(C), the positive portion of the generated electrical signals remains consistently around 0.05 V from 1.5 J to 3 J input impact energy. In comparison, the negative portion of the electrical signals shows a significant increase in magnitude as the input impact energy rises. Moreover, the output electrical signals corresponding to impact energies from 1.5 J to 3 J exhibit notable tolerance, demonstrating excellent potential for future applications. The subfigure of showing the 3.5 J impact result in Figure 6.2(C) illustrates the output waveform of the electrical signal under an input impact energy of 3.5 J. The positive and negative portions exhibit similar magnitudes. The generated electrical signal demonstrates significantly greater variability compared to the results obtained from 1.5 J to 3 J, resulting in a markedly larger tolerance.

In the summary, based on the impact testing results from the drop tower system, an impact energy of 3 J corresponds to an approximate puncture force of 5000 N. Based on the study by Zhou et al. (2025), the most common bird impact scenarios involve a bird mass of 10 kg such as falcons $(0.51\sim1.2 \text{ kg})$, golden eagles $(2\sim6.5 \text{ kg})$, and albatrosses $(8\sim9 \text{ kg})$ [30] with velocities ranging from 20 m/s to 40 m/s [31]. When converting this into momentum and estimated impact force, the resulting force is typically below 4 kN. This indicates that the self-powered sensor has sufficient capacity to detect bird impacts under real-world conditions.

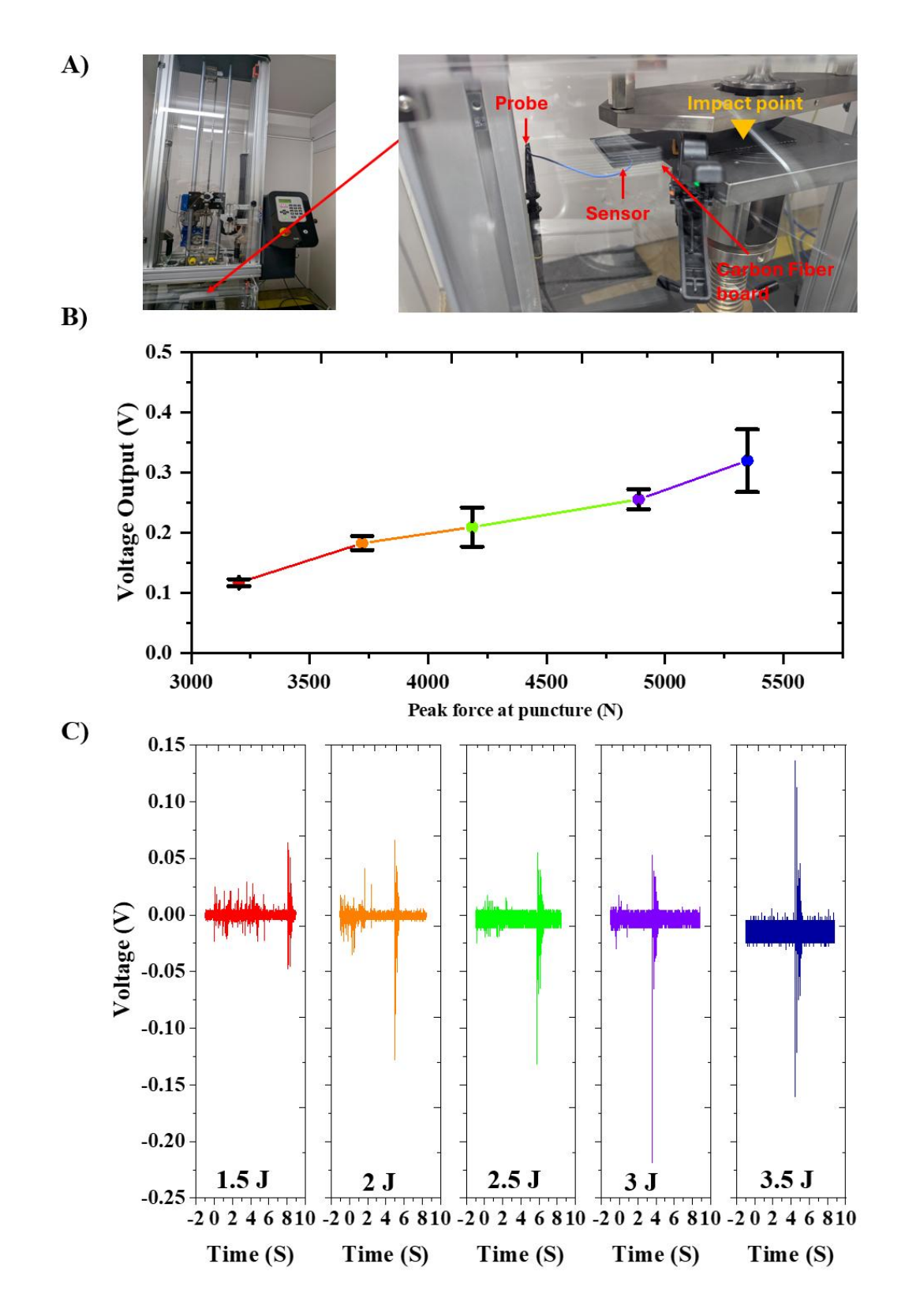


Figure 6.2 (A) Impact testing platform (Instron 9440 Drop Tower, USA) and experimental setup. (B) Relationship of trend curve between output signal strength and input impact energy, and (C) Waveform of output electrical signal strength under different impact energy levels.

6.2.2 Water droplet test

For the water droplet test, artificial seawater with a salinity of 35 ppt was used. The reason for using artificial seawater is that rainstorms are formed from atmospheric moisture, and in offshore wind turbine operating environments, the evaporated steam from seawater contains NaCl. As a result, rain in such conditions may carry salt content, making artificial seawater a more realistic for testing the self-powered sensor. To ensure continuous and stable droplet generation, a motor-driven syringe pump was employed. The droplet output rates were set to 1 mL/min, 3 mL/min, 5 mL/min, and 7 mL/min for experimental comparison. A 31 mm diameter syringe was used in conjunction with a fixed 0.8 mm diameter nozzle. This setup successfully achieved consistent droplet size and stable droplet formation throughout the experiment. A sensor holder with a 70-degree gradient was used to facilitate the smooth flow of water droplets off the sensor surface as shown in Figure 6.3(A). Based on the experiment results, the output signal strength of self-powered sensor under artificial seawater has significantly higher than the tap water. The strength of the generated electrical signals with artificial seawater reached approximately 1 V, compared to around 0.17 V with tap water at a droplet rate of 7 mL/min. The same phenomenon has also been observed at Zheng et al's report in 2024 [32]. This phenomenon is assumed to result from the complexity of the contents in tap water, such as suspended particles, organic compounds, and metal ions. These substances can adhere to the contact surface of the natural rubber, thereby affecting the electrical conductivity of the water and reducing the efficiency of electron transfer. Referring to Figure 6.3(B), the generated electrical signals under both artificial seawater and tap water show a notable linear increasing trend with the rising droplet rate. Based on the experimental results, the self-powered sensor demonstrates high sensitivity to variations in water droplet rate.

Based on the experiment results, the approximately rainfall can be estimated through equation (6.1).

$$Rainfall = \frac{water droplet \ rate \left(\frac{mL}{min}\right) *60 * \frac{10000}{area \ of \ sensor \ holder \ (cm^2)}}{1000}$$

$$(6.1)$$

In the Equation (6.1), the sensor holder is assumed to represent the surface of the wind turbine blade, on which the self-powered sensor is mounted. The area allocated for sensor placement is 28.6341 cm^2 . As is commonly known, 1 mm of rainfall is equivalent to 1 Liter (L) of water falling on a 1 square meter (m²) surface [33]. To relate the syringe pump droplet volume to actual rainfall intensity, the output water volume (mL) is converted to the equivalent amount of rainfall on a 1 m² area by multiple with $\frac{10000}{28.6341} = 349.17$. Then, divide the result by 1,000 to obtain the rainfall in millimetres (mm).

Table 6.1 Convert the measured water droplet rate into an equivalent daily rainfall value.

(mL/min)	(ml/h)	Volume of rain (ml) in 1	Volume of rain (L) in 1
		m²	m²
1	60	20954.02268	20.95402268
3	180	62862.06805	62.86206805
5	300	104770.1134	104.7701134
7	420	146678.1588	146.6781588

Based on the conversion results, this self-powered sensor is capable of detecting rainfall corresponding to intense rain (15–30 mm per hour) and torrential rain (more than 30 mm per hour) [34]. Rain droplets impact the surface of wind turbine blades, causing rain erosion on the surface of wind turbine blades that reduces aerodynamic efficiency. Consequently, this degradation leads to decreased energy output and higher maintenance expenses. The variation in rainfall levels accelerates blade wear, potentially shortening the turbine blade's operational lifespan to one-third of its intended design life [35]. Moreover, leading edge erosion (LEE) affects nearly all wind turbines, especially offshore ones. LEE reduces the annual energy production and lifetime profitability of wind turbines. Additionally, seawater aerosols exacerbate the severity of LEE, causing an average annual energy production drop of 1.8% due to moderate erosion levels, with the most affected turbines experiencing losses of up to 4.9% [36]. Moreover, it is worth noting that the sensor exhibits stable and repeatable signal generation under both artificial seawater and tap water, as shown in Figure 6.3(i) and (ii), respectively. This noteworthy and advanced property of the self-powered sensor enables it to provide accurate output signals at varying droplet rates, which is beneficial for further analysis in future applications through a remote data transmission system.

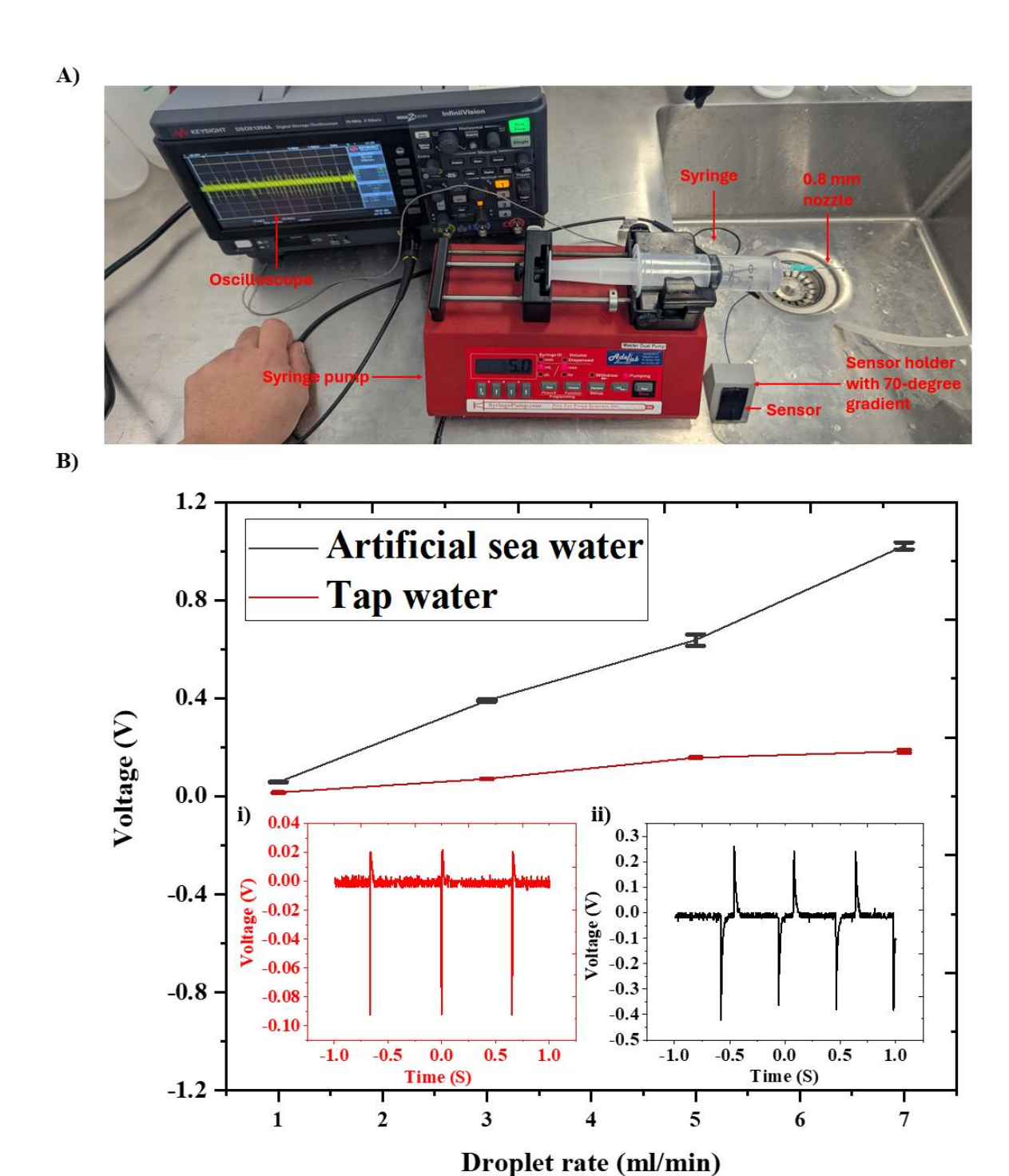


Figure 6.3 (A) Experimental setup for water droplet testing using an oscilloscope (Keysight DSOX1204A, USA) and a dual-syringe pump (Ade-lab, Australia); (B) comparison of the output electrical signal strength between artificial seawater and tap water, (i) typical output waveform of the self-powered sensor under tap water, (ii) typical output waveform of the self-powered sensor under artificial seawater. The waveform of the generated electrical signal was recorded at a water droplet rate of 5 mL/min.

6.2.3 Wireless data transmission system

The wireless data transmission module is the core component of the active impact detection system. In offshore operating environments, wired data transmission is inefficient and impractical. Maintaining and repairing transmission cables can also incur substantial costs in both labor and financial resources. The Bluetooth data transmission system comprises five main components. As shown in Figure 6.4(A), the black block represents the self-powered sensor. The sensor's output is connected to an RC circuit, which serves to filter unwanted noise during data captured. The Bluetooth module used in this system is the HC-05, which enables wireless data transmission. It is widely used with the Arduino platform due to its low cost and easy availability. An Arduino Nano functions as the central processing unit due to its compact size. It converts analogue signals into digital data for downstream transmission. An external power supply is used to power the wireless data transmission system for demonstration purposes. In future applications, this power source could be replaced with a solar panel or be directly integrated with the power supply of the offshore wind turbine. Figure 6.4(B) and Figure 6.4(C) illustrate the experimental setup for the wireless data transmission system for impact test (1.5 J) and water rainfall test (3 mL/min). For the impact test, a custom case was designed for the wireless data transmission system, allowing all components to be housed securely and fit within the drop tower setup. Figures 6.4(D) and 6.4(E) show the measurement results on the endpoint laptop, obtained through the designed wireless data transfer system during the impact test and the water rainfall test, respectively. According to Figure 6.4(D), the waveform obtained via Arduino shows a sloped profile during the measurement of impact energy from the drop tower, rather than a single sine wave. This result show similar trend with the waveform observed on the oscilloscope, as shown in Figure 6.2 (C). According to Figure 6.4(E), the waveform approximates the shape observed during the water rainfall test. Compared to the measurement results from the oscilloscope shown in Figures 6.3(B(i) and (ii)), it successfully captures three complete sine waves. However, due to the limited sampling rate of the Arduino and the data transfer rate of the HC-05 module, it cannot capture every detailed feature of the waveform as accurately as the oscilloscope. Replacing the HC-05 module with a Wi-Fi module could improve the sampling rate, wireless transfer speed, and communication distance.

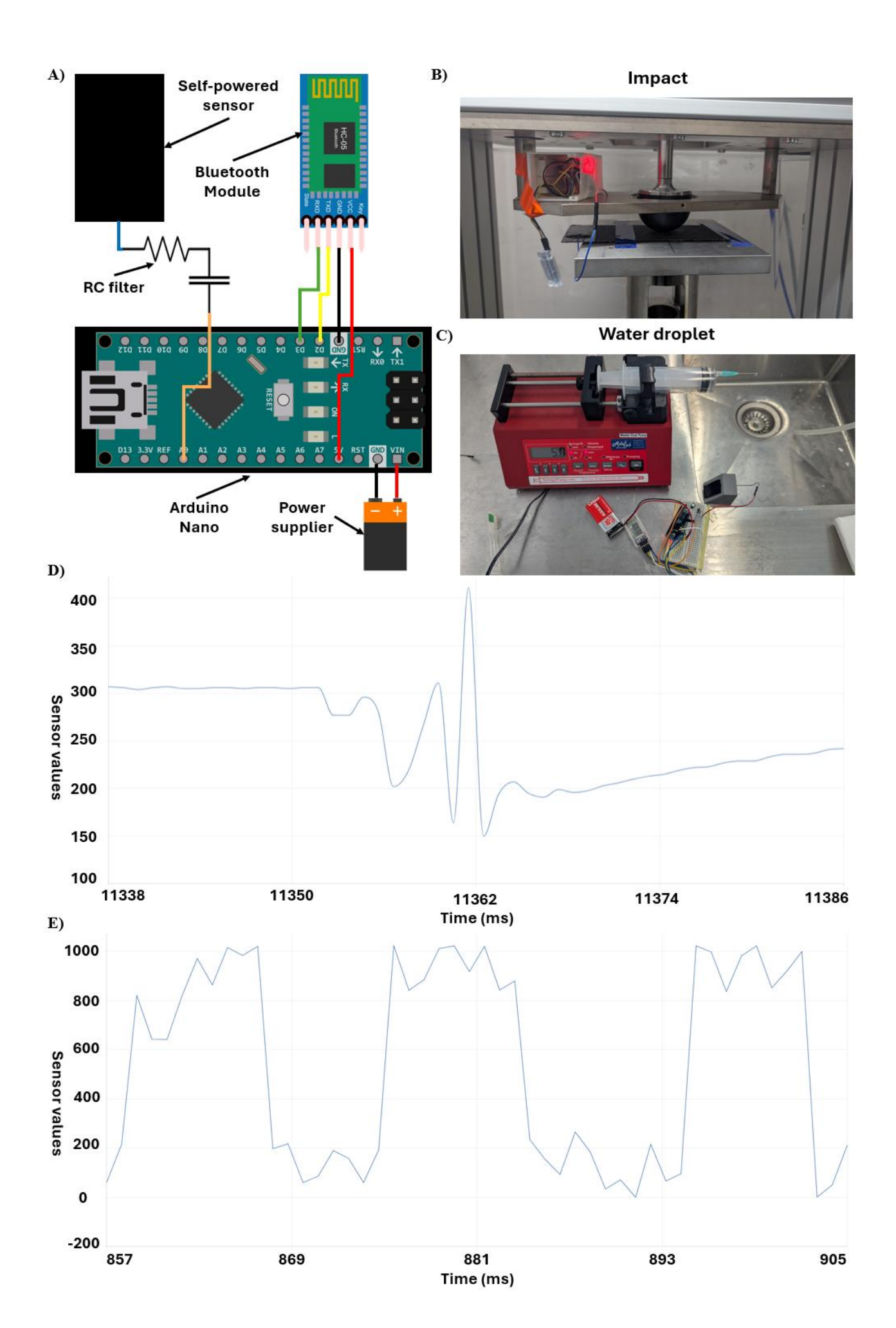


Figure 6.4 Schematic illustration: (A) Circuit diagram of the proposed active impact detection and wireless data transmission system; (B) Experimental setup for wireless data transmission during impact detection; (C) Experimental setup for wireless data transmission during the water rainfall test; (D) Waveform obtained from Arduino during impact test at 1.5 J; and (E) Waveform obtained from Arduino during the water rainfall test at a flow rate of 3 mL/min.

6.3 Demonstration

Figure 6.5(A) illustrates the experimental setup used for the vertical wind turbine demonstration. A vertical-axis wind turbine, provided by another research group at our university, served as the testing platform. The active impact detection system was housed in a 3D-printed enclosure, as shown in the zoomed-in section of Figure 6.5(A). The self-powered sensor was mounted at the tip of the wind turbine blade and connected to the wireless data transmission system via a wire that was secured along the top surface of the blade to minimize aerodynamic interference. Figure 6.5(B) presents the results of the wireless data transmission system. Due to limitations of the experimental platform, simulating actual bird impacts was not feasible. However, the sensor was still able to detect the vibration caused by wind pressure. The peaks in the captured waveform indicate instances when wind force acted on the sensor, causing contact between the natural rubber and the silver-based conductive grease. In comparison, the troughs represent periods during which no external force was applied to the sensor. In conclusion, the active impact detection system successfully demonstrated all the core functionalities as proposed. However, some tests could not be conducted at this stage due to the lack of an appropriate experimental platform.

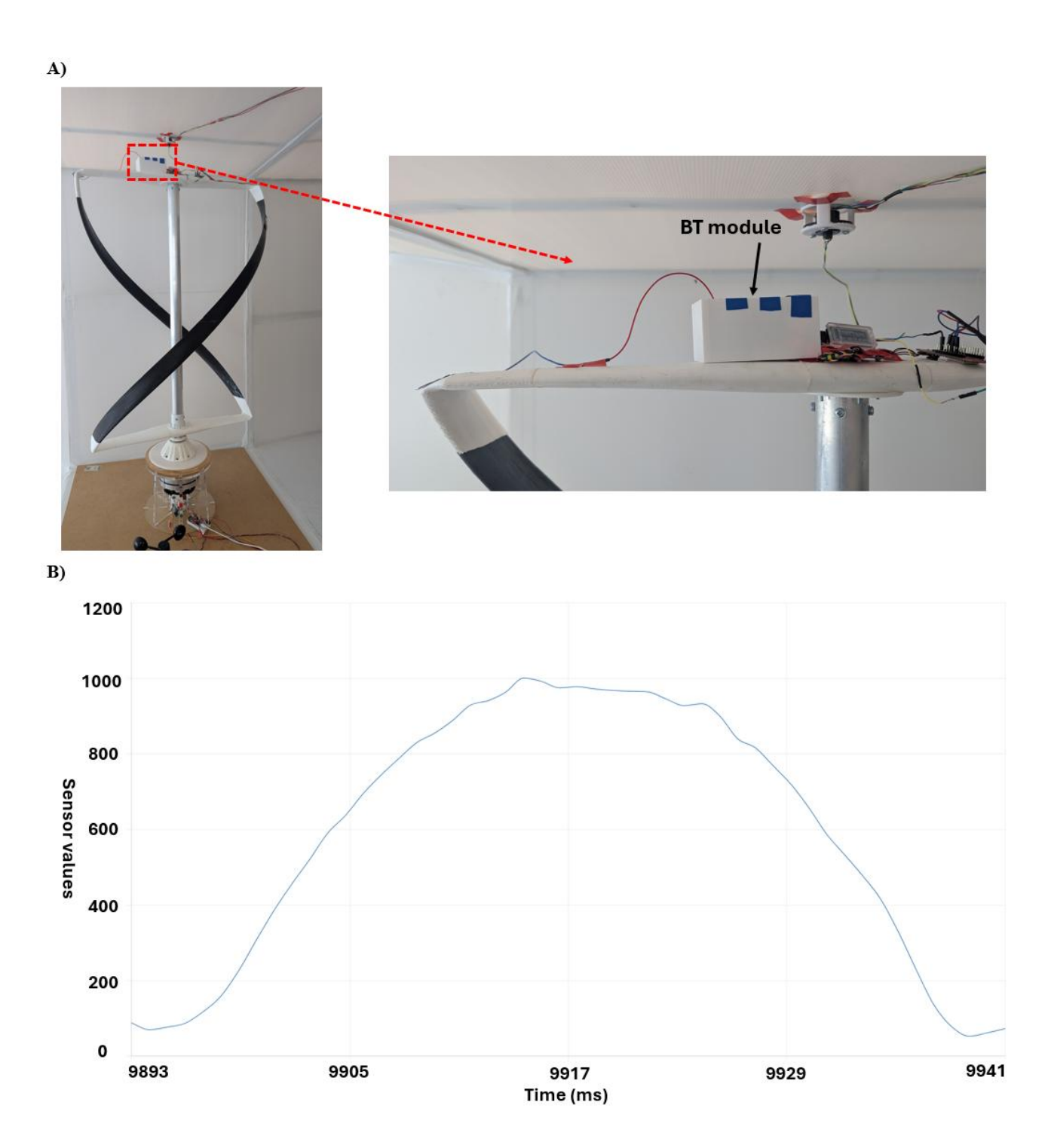


Figure 6.5 Demonstration on vertical wind turbine (A) Experimental setup demonstrating the active impact detection system and (B) Screen capture showing the sensor's generated electrical signal output.

6.4 Conclusion

Based on the experimental results, the proposed active impact detection sensor that based on triboelectric nanogenerator (TENG) technology has demonstrates effective performance and satisfy

its proposed functionalities. It shows strong potential as a novel active impact detection system, capable of providing early diagnosis and alerts for impact events, such as those caused by flying animals, which could otherwise lead to blade damage, power outages, and significant financial losses. The sensor can detect impact energies ranging from 1.5 J to 3.5 J. According to energy conversion calculations, 3.5 J corresponds to an approximate impact force of 5500 N, consistent with the typical maximum force generated by flying animals. Moreover, the self-powered sensor exhibits exceptionally stable output signals, ensuring high accuracy in detecting varying impact energies. This signal stability also facilitates future electrical signal analysis and seamless system integration. In addition to impact detection, the sensor demonstrates the capability to detect rainfall at wind turbine farms. Experimental results confirm its can effectively identify water droplet variations in both tap water and artificial seawater, mimic the environmental conditions of onshore and offshore wind farms. Furthermore, the integration of this self-powered sensor with a custom-developed wireless data transmission system has been successfully demonstrated on a vertical-axis wind turbine and validated through wind tunnel testing. The results confirm the system's ability to conduct real-time detection and wirelessly transmit data. Overall, this active impact detection sensor offers a promising solution for both onshore and offshore wind turbine farms, helping to prevent unexpected blade fractures and fatigue, thereby reducing the risk of power outages and minimizing maintenance costs.

6.5 Reference

- [1] Australian Government, Climate Active, Climate Active Carbon Neutral Standard (2023). https://www.dcceew.gov.au/climate-change/climate-active (accessed December 2, 2023).
- [2] Roland Schmehl, Airborne Wind Energy, (n.d.).
- [3] Y. Zhang, W. Shi, D. Li, X. Li, Y. Duan, A.S. Verma, A novel framework for modeling floating offshore wind turbines based on the vector form intrinsic finite element (VFIFE) method, Ocean Engineering 262 (2022) 112221. https://doi.org/10.1016/j.oceaneng.2022.112221.
- [4] H. Klinge Jacobsen, P. Hevia-Koch, C. Wolter, Nearshore and offshore wind development: costs and competitive advantage exemplified by nearshore wind in Denmark, Energy for Sustainable Development 50 (2019) 91–100. https://doi.org/10.1016/j.esd.2019.03.006.
- [5] Australian Government, Offshore wind in Australia, Department of Climate Change, Energy, the Environment and Water (2024).
- [6] Victoria Government, Offshore Wind Energy Victoria (OWEV), Victoria Government (2025).

- [7] A.S. Verma, N.P. Vedvik, P.U. Haselbach, Z. Gao, Z. Jiang, Comparison of numerical modelling techniques for impact investigation on a wind turbine blade, Compos Struct 209 (2019) 856–878. https://doi.org/10.1016/j.compstruct.2018.11.001.
- [8] Australian Government, Southern Ocean region off Victoria, declared offshore wind area, Department of Climate Change, Energy, the Environment and Water (2024).
- [9] G.V.P. Lapa, A. Gay Neto, G.R. Franzini, Effects of blade torsion on IEA 15MW turbine rotor operation, Renew Energy 219 (2023) 119546. https://doi.org/10.1016/j.renene.2023.119546.
- [10] A.S. Verma, S.G.P. Castro, Z. Jiang, J.J.E. Teuwen, Numerical investigation of rain droplet impact on offshore wind turbine blades under different rainfall conditions: a parametric study, Compos Struct 241 (2020) 112096. https://doi.org/10.1016/j.compstruct.2020.112096.
- [11] A.S. Verma, Z. Jiang, Z. Ren, Z. Gao, N.P. Vedvik, Effects of wind-wave misalignment on a wind turbine blade mating process: impact velocities, blade root damages and structural safety assessment, Journal of Marine Science and Application 19 (2020) 218–233. https://doi.org/10.1007/s11804-020-00141-7.
- [12] A.S. Verma, J. Yan, W. Hu, Z. Jiang, W. Shi, J.J.E. Teuwen, A review of impact loads on composite wind turbine blades: impact threats and classification, Renewable and Sustainable Energy Reviews 178 (2023) 113261. https://doi.org/10.1016/j.rser.2023.113261.
- [13] C. Yang, S. Ding, G. Zhou, Wind turbine blade damage detection based on acoustic signals, Sci Rep 15 (2025) 3930. https://doi.org/10.1038/s41598-025-88276-x.
- [14] J.C. Marín, A. Barroso, F. París, J. Cañas, Study of fatigue damage in wind turbine blades, Eng Fail Anal 16 (2009) 656–668. https://doi.org/10.1016/j.engfailanal.2008.02.005.
- [15] V. Arumugam, C.S. Kumar, C. Santulli, F. Sarasini, A.J. Stanley, A Global method for the identification of failure modes in fiberglass using acoustic emission, J Test Eval 39 (2011) 954–966. https://doi.org/10.1520/JTE103730.
- [16] S. Gholizadeh, Z. Leman, B.T.H.T. Baharudin, A review of the application of acoustic emission technique in engineering, Structural Engineering and Mechanics 54 (2015) 1075–1095. https://doi.org/10.12989/sem.2015.54.6.1075.
- [17] S. Gholizadeh, A review of non-destructive testing methods of composite materials, Procedia Structural Integrity 1 (2016) 50–57. https://doi.org/10.1016/j.prostr.2016.02.008.
- [18] BesTech, Fundamentals of Optical Strain Sensors: Working Principle and Applications, BesTech (n.d.).

- [19] HBK, Optical Strain Gauges: What You Need to Know, Hottinger Bruel (n.d.).
- [20] F.-R. Fan, Z.-Q. Tian, Z. Lin Wang, Flexible triboelectric generator, Nano Energy 1 (2012) 328–334. https://doi.org/10.1016/j.nanoen.2012.01.004.
- [21] S. Niu, Z.L. Wang, Theoretical systems of triboelectric nanogenerators, Nano Energy 14 (2015) 161–192. https://doi.org/10.1016/j.nanoen.2014.11.034.
- [22] Z.L. Wang, Triboelectric nanogenerators as new energy technology and self-powered sensors principles, problems and perspectives, Faraday Discuss 176 (2014) 447–458. https://doi.org/10.1039/C4FD00159A.
- [23] Q. Shi, H. Wang, H. Wu, C. Lee, Self-powered triboelectric nanogenerator buoy ball for applications ranging from environment monitoring to water wave energy farm, Nano Energy 40 (2017) 203–213. https://doi.org/10.1016/j.nanoen.2017.08.018.
- [24] C. Garcia, I. Trendafilova, J. Sanchez del Rio, Detection and measurement of impacts in composite structures using a self-powered triboelectric sensor, Nano Energy 56 (2019) 443–453. https://doi.org/10.1016/j.nanoen.2018.11.055.
- [25] L. Wu, J. Xue, J. Meng, B. Shi, W. Sun, E. Wang, M. Dong, X. Zheng, Y. Wu, Y. Li, Z. Li, Self-powered flexible sensor array for dynamic pressure monitoring, Adv Funct Mater 34 (2024) 2316712. https://doi.org/10.1002/adfm.202316712.
- [26] I. Mehamud, M. Björling, P. Marklund, Y. Shi, Small size and low-cost TENG-based self-powered vibration measuring and alerting system, Adv Electron Mater 9 (2023) 2300111. https://doi.org/10.1002/aelm.202300111.
- [27] I. Mehamud, P. Marklund, M. Björling, Y. Shi, Machine condition monitoring enabled by broad range vibration frequency detecting triboelectric nano-generator (TENG)-based vibration sensors, Nano Energy 98 (2022) 107292. https://doi.org/10.1016/j.nanoen.2022.107292.
- [28] T. Paillat, G. Touchard, Electrical charges and liquids motion, J Electrostat 67 (2009) 326–334. https://doi.org/10.1016/j.elstat.2009.01.038.
- [29] T. Takahashi, Measurement of electric charge of cloud droplets, drizzle, and raindrops, Reviews of Geophysics 11 (1973) 903–924. https://doi.org/10.1029/RG011i004p00903.
- [30] R. Zhou, B. Liang, Z. Yue, H. Yang, C. Zou, F. Zhang, S. Chen, High fidelity simulations of bird impact damages of a 5 MW wind turbine composite blade using SPH and damage models, Thin-Walled Structures 208 (2025) 112835. https://doi.org/10.1016/j.tws.2024.112835.

- [31] R. Zhou, B. Liang, Z. Yue, H. Yang, C. Zou, F. Zhang, S. Chen, High fidelity simulations of bird impact damages of a 5 MW wind turbine composite blade using SPH and damage models, Thin-Walled Structures 208 (2025) 112835. https://doi.org/10.1016/j.tws.2024.112835.
- [32] Y. Zheng, Y. Ni, Y. Zi, H. Cui, X. Li, Enhanced triboelectric nanogenerators in saline environments and their applications in the ocean, Nano Energy 126 (2024) 109636. https://doi.org/10.1016/j.nanoen.2024.109636.
- [33] Blue Mountain Co., Calculating Your Average Rainfall & Ideal Tank Size, Rainharvesting (n.d.).
- [34] PCDSPO, Rainfall Advisories, Classification and Measurement, Archive.Org (2015).
- [35] J.I. Bech, N.F.-J. Johansen, M.B. Madsen, Á. Hannesdóttir, C.B. Hasager, Experimental study on the effect of drop size in rain erosion test and on lifetime prediction of wind turbine blades, Renew Energy 197 (2022) 776–789. https://doi.org/10.1016/j.renene.2022.06.127.
- [36] H. Law, V. Koutsos, Leading edge erosion of wind turbines: effect of solid airborne particles and rain on operational wind farms, Wind Energy 23 (2020) 1955–1965. https://doi.org/10.1002/we.2540.

CHAPTER 7 CONCLUSIONS AND FUTURE PERSPECTIVES

7.1 Conclusions

In modern society, electrical energy is one of the most vital resources. The development and functioning of contemporary infrastructure increasingly rely on electricity due to the rapid electrification of traditional equipment and systems. This shift has led to a growing demand for electrical energy. Furthermore, environmental regulations, such as carbon neutrality strategies, are driving the transition toward renewable and clean energy sources to replace fossil fuels. These regulations are accelerating the adoption of renewable resources, such as solar, wind, and ocean energy, to reduce carbon emissions from conventional fuels like coal and diesel. Therefore, ocean wave energy has attracted significant attention due to its abundant presence in the natural environment, as the ocean covers approximately 71% of the Earth's surface. In addition, ocean wave motion is minimally influenced by external environmental factors. Therefore, based on the abovementioned benefits, harvesting ocean wave energy to meet electricity demand has become one of the most prominent research hotspots worldwide. Utilise the most innovative renewable energy generator triboelectric nanogenerator has become a highly popular research focus in recent years.

Chapter 3 introduces an ocean wave energy-driven TENG, named WD-TENG. This study investigates the effects of variations in both wave amplitude and wave frequency. The WD-TENG prototype was designed based on the contact-separation mode and fabricated cost-effectively using recyclable polylactic acid (PLA) and through 3D printing technologies. Two TENG units were installed at the bottom of the cylindrical outer structure and connected in series. The WD-TENG geometry was optimized, and the effects of wave frequency and amplitude were experimentally simulated to evaluate its performance under various ocean conditions, guided by computational fluid dynamics (CFD) simulations using the AQWA module of the ANSYS platform. Preliminary results show that, under the current design and experimental settings, the proposed WD-TENG successfully achieved a maximum output voltage of 133 V when the wave amplitude reached 11.5 cm at a frequency of 2.2 Hz, and a maximum output voltage of 333.67 V under a wave frequency of 7 Hz with 0 cm amplitude. Based on the experimental results, variations in wave frequency and wave amplitude significantly affect the output performance of WD-TENGs. In additional, WD-TENG can sustainably charge a 47 µF capacitor to 0.496 V in one minute. It also demonstrates excellent durability under eight hours of continuous operation and strong adaptability to different ocean wave frequencies and amplitudes. Experimental results indicate its potential to serve as an auxiliary power source in offshore conditions. Moreover, based on the simulation result of the minimal response frequency (approximately 1.9 Hz) and the experimental observation (3 Hz), the findings provide evidence that utilizing commercially available simulation software to predict the dynamics of ocean wave-driven TENGs is a feasible approach. The main contribution of this chapter is a systematic study of the effects of varying wave parameters, such as wave frequency and amplitude, on the

output performance of ocean wave energy harvesters. It also verifies the feasibility of using commercially available simulation software to predict the dynamics of ocean wave energy harvesters under actual ocean wave conditions.

Based on the experimental results presented in Chapter 3, variations in ocean wave amplitude significantly affect the output performance of WD-TENGs. However, systems used to simulate water waves are often expensive to build and maintain. Therefore, Chapter 4 proposes a wirelesscontrolled water wave generation system to replicate water wave motion for testing the hydrodynamics of WD-TENGs under laboratory conditions. Compared to conventional ground-based wave generation systems, the proposed system is cost-effective and requires only a water tank, resulting in low space requirements and operational costs. This wave generation system combines a modular design concept with advanced manufacturing techniques. A stepper motor and an Arduino are employed as the driving energy source and processor. A Bluetooth HC-05 module is used to enable remote control, enhancing the user operation experience. The system utilises motor parameters, such as rotational speed and number of travelled steps, to accurately control the generated wave frequency and amplitude. Based on experimental results, the proposed wave generation system can produce stable and repeatable waves with frequencies ranging from 1 Hz to 2 Hz and amplitudes between 1.5 cm and 7.1 cm under the current settings. Thanks to advanced manufacturing techniques, only minor modifications are needed to replace the system for differentsized water tanks or to achieve higher wave amplitudes by selecting a faster stepper motor in the future. The proposed wave generation system successfully provides an easily reproducible setup, suitable even for developing countries, which will accelerate the development of ocean wave energy-driven energy harvesting systems in the future. The major contribution of this chapter is the development of a cost-effective method to generate stable and repeatable water waves with a reasonable range of variation, which can be easily modified to suit different water tank dimensions.

Based on the research findings presented in Chapters 3 and 4, it has been observed that variations in wave amplitude significantly affect the energy harvesting efficiency of WD-TENGs. To enable more efficient placement of these TENGs, a detailed ocean wave spectrum of the coastline region is urgently needed. However, commonly used radar-based ocean data sensors struggle to monitor low-amplitude waves, as the measured amplitudes are often masked by environmental noise such as unexpected vibrations of the radar antenna caused by ocean wind. Herein, Chapter 5 introduces a hybrid self-powered wave sensing device (HSP-WS) consisting of a TENG and an EMH. The flexible single-electrode-mode TENG is employed as a self-powered sensor to detect variations in ocean wave amplitude. The EMH, in cooperation with the power management system, demonstrates the ability to power Bluetooth devices to enable remote signal transmission or can be directly used as a flashing indicator. Based on experimental results obtained using a previously published water wave generation system in Chapter 4, the HSP-WS demonstrated sufficient sensitivity to detect amplitude changes as small as 0.5 cm. Moreover, flexible TENG shows a linear relationship between

the strength of the output signal and the wave amplitude. Both the EMG and flexible TENG demonstrate durability for use as a device for low-amplitude wave spectrum measurement. HSP-WS provides the feasibility to fill the gap in the low-amplitude wave spectrum, leading to better utilization in ocean wave resources. The major contribution of this chapter is that the proposed self-powered sensor can detect wave amplitude changes as small as 5 mm. Thanks to the hybrid concept, the EMH provides a potential solution for powering the wireless data transmission system.

Based on the experimental results from Chapter 5, the flexible single-electrode TENG demonstrates notable sensitivity to small-scale motions. Considering that offshore wind turbine farms are becoming increasingly popular in Australia, there is currently no real-time system that effectively balances sensitivity and cost-efficiency for monitoring and detecting impacts from flying animals on wind turbine blades. Accidental impacts from flying animals pose a serious problem for wind turbines, as damage to the blades can reduce their lifespan and potentially cause unexpected fractures. Using flexible TENGs as self-powered sensors presents a promising alternative solution, offering both costeffectiveness and high sensitivity. Accordingly, in Chapter 6, an active impact detection system based on the flexible TENG has been proposed. Based on experimental results, this self-powered sensor successfully detects impact energies ranging from 1.5 J to 3.5 J. These energy levels are commonly generated by flying animals such as bats and birds. Furthermore, the sensor exhibits the capability to serve as a rain sensor, accurately detecting rainfall that maybe corrosive (due to high salinity) to wind turbine blade surfaces. Moreover, combined with the self-developed wireless data transfer system, this approach will significantly improve the convenience of data collection and better meet the demands of offshore operational conditions. The success of this active sensor system provides a promising active impact detection method for wind turbines. The major contribution of this chapter is the use of a self-powered sensor to detect bird impacts on wind turbine blades. Moreover, a wireless data transmission system has been proposed to support all necessary functions. However, the limited capture rate limits the level of detail recorded from the electrical signals generated by the self-powered sensor.

7.2 Future perspectives and discussion

This study thoroughly investigates the effects of ocean wave parameters on the output performance of ocean wave driven TENGs and provides several solutions and potential applications to evaluate and optimize the overall performance of ocean wave energy driven TENGs for widespread offshore energy harvesting. However, there are still some limitations that restrict the application of TENG technology in ocean wave energy harvesting and related offshore operational conditions. First of all, output power remains the major limitation of commercial TENG technology systems. Thanks to significant contributions from researchers worldwide, the instantaneous power of ocean wave—driven TENGs has reached up to 80.6 W/m³ [1], which is a promising achievement. However, this instantaneous power does not equate to the rated power, limiting practical applications. Therefore,

a specially designed energy storage system is essential for ocean wave driven TENGs. Currently, capacitors and supercapacitors are the most popular energy storage units due to their fast charge and discharge capabilities [2,3]. These properties enable TENGs to function as power suppliers for low-energy electronic devices such as thermometers, digital counters, and other ocean parameter sensors. However, capacitor-based energy storage systems typically require several minutes of charging before they can activate low-energy electronic devices. Fortunately, the hybrid concept of TENGs offers a solution to this slow charging issue. By integrating an electromagnetic harvester (EMH), the system can effectively compensate for the low current output of the TENG, while the TENG, in turn, compensates for the low voltage output of the EMH. Hybrid mode TENG greatly improves charging efficiency realise charging speed at 30 seconds which is a significant improvement compared to the single TENG unit [4]. On the other hand, capacitors or supercapacitors are not ideal for long-term energy storage because they require a continuous energy input. Otherwise, the stored energy will discharge into the load circuit. Therefore, for applications that demand longer storage durations, traditional batteries will be the best option. However, the energy required to charge a battery is significantly higher than that for a capacitor. Moreover, batteries require a DC voltage as the charging source. Therefore, the electrical energy generated by TENGs must first be rectified before charging. Luckily, a power management strategy called a voltage multiplier which was used in Chapter 5 of this thesis may be a good option for further development. This system can convert the AC output from TENGs into DC output while also enhancing the output energy level. Based on the experimental results, the voltage multiplier successfully boosted the TENG's 1.4 V output to power an LED requiring a minimum input of 2.5 V. Voltage multiplier promises a potential solution to boost output level of TENG to minimal requirement of charging battery. Alternatively, specifically designing lithium-ion batteries for TENG applications is another potential solution. For instance, Zi et al. designed and fabricated a lithium-ion battery for TENG applications, which is capable of theoretically providing a rated voltage of 3.8 V [5]. Developing a suitable energy storage system will greatly benefit the application of TENG technology in ocean environments and expand its feasibility for a wider range of uses.

Chapters 3 and 4 present a detailed study and analysis of how variations in wave parameters affect the output performance of a single ocean wave driven TENG under generated water waves. However, these results are limited to a single TENG unit. To fully understand the overall performance and scalability of ocean wave-driven TENGs, it is essential to investigate the behaviours of multiple TENG units connected in various configurations such as series, parallel (shunt), and series-parallel (series-shunt) in order to identify the optimal connection method for more efficient utilization of ocean wave energy. To enable testing of the TENG matrix, the currently used water channel for wave generation is too narrow. Therefore, a wider water channel will be required in future to study the effect of different connection method. Another important issue to address in the field of ocean wave energy driven TENG research is the standardisation of power density units and the scaling of testing wave parameter ranges. Currently, researchers use different units to express power density, such

as W/m² and W/m³. The unit W/m² represents the output power density per square meter of triboelectric material used, while W/m³ represents the output power density per cubic meter of the entire TENG device. Wave parameters also need to be standardised, including the ranges for wave frequency and wave amplitude. Uniform standardisation would make comparison between different study results easier and more meaningful in the future. Once the testing water wave parameters and power density units are standardised, it will be much easier to identify which external designs, internal structures, working modes, and combinations of triboelectric materials deliver optimised energy conversion efficiency under specific wave conditions. Once sufficient data from the developed TENG-based energy harvester is collected, Al tools and machine learning algorithms can be applied to study and optimize designs based on published devices. By inputting the required output performance and specific operating region, the design and configuration of TENG based energy harvester can then be automatically designed and configurated based on the previously analysed results. This will significantly increase the development efficiency for future studies.

Chapters 5 and 6 present two applications of TENG technology for offshore application. In Chapter 5, the hybrid mode self-powered ocean wave parameter sensor demonstrates the capability to power a low-energy Bluetooth module, enabling wireless data transfer for future offshore operations. For offshore wave energy generators and wind turbines, wired data transfer is inconvenient or even impossible due to the harsh marine conditions. Therefore, implementing a reliable wireless data transfer system is essential for effective offshore operation. In Chapter 6, a prototype wireless data transfer system is proposed, based on the Arduino platform and integrated with a low-energy Bluetooth module. It successfully realized wireless data transmission. However, due to the limitations of the Bluetooth module, the system supports only up to 1 Mbp/s for both upload and download speeds, which reduces the detail captured in the waveforms generated by the TENGs [6]. The newly released Arduino board, which integrates a Wi-Fi module, can serve as an alternative to the current prototype. It offers data transfer speeds up to 72 Mbps, enabling significantly higher data throughput within the same time frame. As a result, the monitored waveforms displayed on the endpoint laptop will contain much more detail compared to those transmitted via the Bluetooth module-based wireless system [7]. In addition, thanks to the rapid development of AI technology, advanced programming algorithms, and 5G connectivity, using AI to assist in data analysis is becoming increasingly feasible and reliable. Wave parameters detected by self-powered sensors can be wirelessly transmitted to an onshore station for further analysis, where analysts can apply AI or machine learning algorithms to process the captured wave data. This enables active prediction of future ocean conditions and enhances real-time environmental monitoring capabilities. The successful development of real-time data transfer would be a game changer for ocean spectrum mapping and would greatly enhance the overall utilization rate of ocean wave energy.

In 2024, Xi et al. introduced a wireless data transfer system powered by a hybrid-mode TENG. In their design, the EMH powered a wireless data transmission system based on an WIFI technology-

based Arduino processor. As the authors claim, the system achieved a maximum communication distance of 1.06 km under urban conditions [8]. Xi's design provided a potential application for ocean monitoring applications without battery. However, the generation frequency of EMHs must be minimum 60 Hz to achieve real-time data transmission. Based on previous publications and the current research progress, a power management system with an energy storage unit is required to enhance the output performance of EMHs and store the harvested energy in a battery for later use. This method provides a potential solution to ensures a relevant stable power supply for wireless data transmission system. Apart from that, the choice of power management strategy needs to be carefully considered, as it strongly depends on the dimensions of the TENG device. For sensing and detection purposes, a self-powered sensor system requires a compact size to minimize the threshold wave frequency and amplitude needed for response. Therefore, the internal space available for integrating the power management system and wireless data transmission module will be limited. Nevertheless, this issue would not be a concern if the power management system is specifically designed for a TENG-based ocean wave energy harvester. On the other hand, if the self-powered sensor is used to monitor large-scale variations in wave amplitude and frequency in far offshore regions, the weight and dimensions of the TENG device are no longer a concern, as offshore waves are large enough to easily overcome the minimum frequency and amplitude threshold requirements. Moreover, the robustness of the power management system and wireless data transmission system also needs to be carefully considered. If they require frequent maintenance, they are not suitable for offshore applications and are better suited for coastal applications. In addition, within the ocean operation environment, humidity and seawater corrosion show significant challenges for electronic components. More electronic components used in the power management and wireless data transmission systems, the higher the risk of system failure. This makes durability and reliability critical requirements for ocean applications. Therefore, a comprehensive test of the seawater corrosion resistance of the entire TENG device, including the power management system and wireless data transmission system, is necessary. The above mentioned challenges significantly affect the selection of a suitable power management system and wireless data transmission system, influencing their overall efficiency, longevity, and practicality under real-world ocean conditions.

In the summary, studying the overall energy conversion efficiency and power density of ocean wave energy driven TENG matrices is essential for future research, which requires standardized water wave testing conditions and uniform power density units. Additionally, a specially designed and fabricated lithium-ion battery energy storage system that integrated with rectification and voltage boosting circuits will be crucial for future TENG based ocean applications, because most Bluetooth or Wi-Fi based wireless data transmission systems require only approximately 3.3 V as input voltage, a specifically designed battery can help increase the charging speed and reduce the total time required for a full charge. On the other hand, commercially available lithium-ion batteries can be used for ocean wave energy generation. A fully charged battery can support several practical applications, such as providing emergency power for fishing vessels and rescue operations, as well

as enabling a continuous 24-hour power supply for sensors and wireless data transmission systems. This will enhance overall efficiency in both the fishery industry and offshore emergency rescue operations. On the other hand, with rapid advancements in electronics, communication technologies, and the upcoming 6G networks, there is an increasing need to develop low-energy, cost-effective wireless data transfer systems that also support long-range communication (more than 5 km). Moreover, omnidirectional wave testing for both ocean wave energy harvesters and self-powered sensors will be a major focus of future studies. This is because current wave generation systems, including large-scale ground-based setups, cannot fully replicate omnidirectional waves, which are the typical conditions in actual ocean environments.

7.3 Reference

- [1] W. Yuan, B. Zhang, C. Zhang, O. Yang, Y. Liu, L. He, L. Zhou, Z. Zhao, J. Wang, Z.L. Wang, Anaconda-shaped spiral multi-layered triboelectric nanogenerators with ultra-high space efficiency for wave energy harvesting, One Earth 5 (2022) 1055–1063. https://doi.org/10.1016/j.oneear.2022.08.013.
- [2] H. Wu, C. Shan, S. Fu, K. Li, J. Wang, S. Xu, G. Li, Q. Zhao, H. Guo, C. Hu, Efficient energy conversion mechanism and energy storage strategy for triboelectric nanogenerators, Nat Commun 15 (2024) 6558. https://doi.org/10.1038/s41467-024-50978-7.
- [3] M.V. Paranjape, P. Manchi, A. Kurakula, V.S. Kavarthapu, J.K. Lee, S.A. Graham, J.S. Yu, Generalized utilization of energy harvesting ability of TENG for concurrent energy storage and motion sensing application with effective external circuitry, Nano Energy 129 (2024) 109983. https://doi.org/10.1016/j.nanoen.2024.109983.
- [4] X. Sun, C. Shang, H. Ma, C. Li, L. Xue, Q. Xu, Z. Wei, W. Li, Y. Yalikun, Y.-C. Lai, Y. Yang, A tube-shaped solid–liquid-interfaced triboelectric–electromagnetic hybrid nanogenerator for efficient ocean wave energy harvesting, Nano Energy 100 (2022) 107540. https://doi.org/10.1016/j.nanoen.2022.107540.
- [5] Y. Zi, J. Wang, S. Wang, S. Li, Z. Wen, H. Guo, Z.L. Wang, Effective energy storage from a triboelectric nanogenerator, Nat Commun 7 (2016) 10987. https://doi.org/10.1038/ncomms10987.
- [6] Core Electronics, Bluetooth Module (HC-05), Core-Electronics (n.d.).
- [7] Arduino, Arduino Nano 33 IoT, Arduino Store. (n.d.).
- [8] Z. Xi, H. Yu, H. Du, H. Yang, Y. Wang, M. Guan, Z. Wang, H. Wang, T. Du, M. Xu, High performance magnetic mass-enhanced triboelectric-electromagnetic hybrid vibration energy harvester enabling totally self-powered long-distance wireless sensing, Adv Mater Technol 9 (2024) 2400451. https://doi.org/10.1002/admt.202400451.

APPENDICES

Supporting information for Chapter 3

Table S3.1. Main parameters of a WD-TENG in simulation

Draft / m	0.0255
Pontoon mass / Kg	1.9435E-4
lxx / Kg*m²	1.95707E-4
lyy / Kg*m²	7.633E-4
Izz / Kg*m²	7.633E-4

Set the working water depth of the WD-TENG as 2 m. The specific layout scheme and main parameters are shown in Figure S3.1 and Table S3.2.

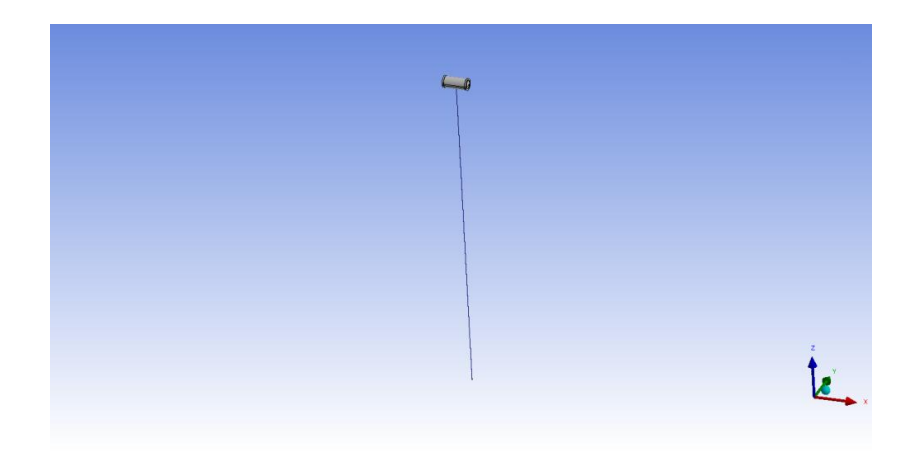


Figure S3.1 Mooring layout of a WD-TENG in an offshore working condition during the simulation

Table S3.2. A WD-TENG mooring system parameters

Anchor chain mass density	0.5 kg/m
Equivalent diameter	1E-6 m
Stiffness, EA	233 MN

The JONSWAP spectrum was used for wave spectrum. Table S3.3 lists the environmental parameters:

Table S3.3. The JONSWAP spectrum parameters

Wave Type	JONSWAP
Significant wave height	0.1/m
ak frequency	0.885/Hz
Gamma	1
Wind speed	1
Flow velocity	

The charge transferred Q_{sc} can be found:

$$Q_{sc} = I_{sc} * \Delta t \tag{S3.1}$$

where I_{sc} means short-circuit current, Δt means different of changing time.

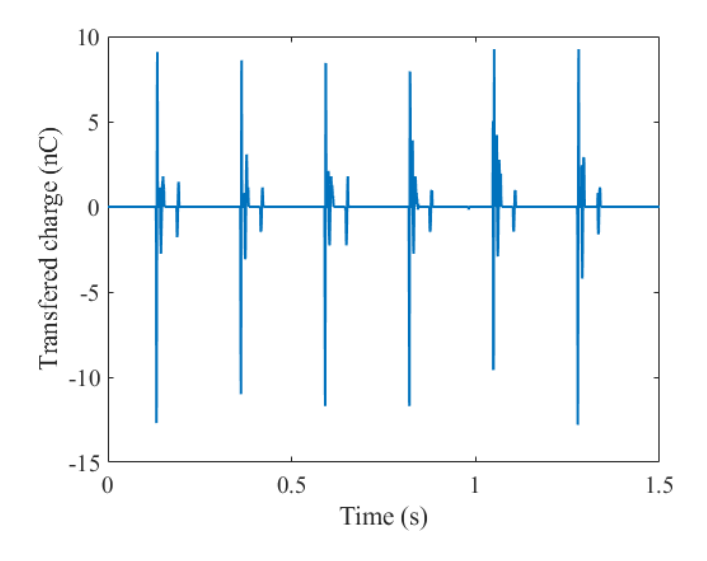


Figure S3.2 Transferred charged of the WD-TENG.

Figure S3.2 shows the plotting of the calculation result of the transferred charged, the means value be used as the transferred charged.

The frequency and the amplitude are the major parameters for the ocean waveform. The frequency of ocean waveform affects the period of the contact and separation cycle of the WD-TENG when it is placed in ocean. The relationship between frequency of ocean waveform and output of the WD-TENG is shown in Equation (S3.3).

$$Q_{SC} = \frac{A\sigma h}{\frac{d_1}{\varepsilon_1} + \frac{d_2}{\varepsilon_2} + h} \tag{S3.2}$$

$$I_{SC} = \frac{dQ_{SC}}{dt} = \frac{A\sigma\left(\frac{d_1}{\varepsilon_1} + \frac{d_2}{\varepsilon_2}\right)}{\left(\left(\frac{d_1}{\varepsilon_1} + \frac{d_2}{\varepsilon_2}\right) + h\right)^2} * \frac{dh}{dt} = \frac{A\sigma\left(\frac{d_1}{\varepsilon_1} + \frac{d_2}{\varepsilon_2}\right)}{\left(\left(\frac{d_1}{\varepsilon_1} + \frac{d_2}{\varepsilon_2}\right) + h\right)^2} * \frac{dh}{d\frac{1}{f}}$$
(S3.3)

where A is the contact area, d_1 and d_2 are the thickness of dielectric 1 and 2, respectively, ε_1 and ε_2 are the relative permittivity of dielectric 1 and dielectric 2, respectively. σ is the charge density, and h is the maximum displacement between triboelectric materials. All above parameters have been decided through the material properties and device designing.

From Fig. S3, assume the mass of the internal sliding module in the WD-TENG is m, the two horizontal component forces of the internal sliding module are $msin(\alpha)$ and $msin(\beta)$. Thus, the range of the degree of the slope should in a range (0 degree – 90 degrees). In this range, the sine value of the angle α increases with the increasing of the amplitudes. So, the relationship between two component forces is shown in Equation (S3.4).

$$msin(\alpha) < msin(\beta)$$
 (S3.4)

Based on the Newton's seconds law, Equation (3.5) can be transferred to Equation (S3.5).

$$mgsin(\alpha) = ma1 < mgsin(\beta) = ma2$$
 (S3.5)

where g is the constant of gravity of earth which is 9.81 m/s.

Simplify Equation (S3.5) to determine the relationship between the acceleration of both component forces to obtain Equation (S3.6).

$$gsin(\alpha) = a1 < gsin(\beta) = a2$$
 (S3.6)

Through Equation (S3.6), it shows that the acceleration of the internal sliding module increases with the increasing of the angle α .

$$V = a1t = gsin(\alpha)t \tag{S3.7}$$

where t is the time which is relevant to the frequency of ocean waves, and it is set to be a fixed value for the following testing in this study.

From Equations (S3.3) and (S3.7), increasing amplitude and frequency will increase of the velocity of the internal sliding module, which affect the output result of the WD-TENG. Effects of the output of the WD-TENG under different external frequencies and amplitudes will be evaluated here.

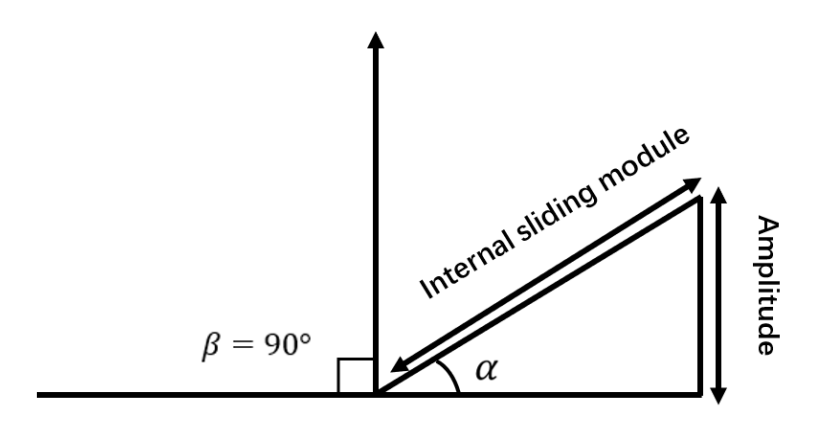


Figure S3.3 The proposed theory of the changing of amplitude. Where β is the maximum slope angle, which is 90 degrees, and α is the angle between slope and horizontal line which increases with the increasing of the amplitude.

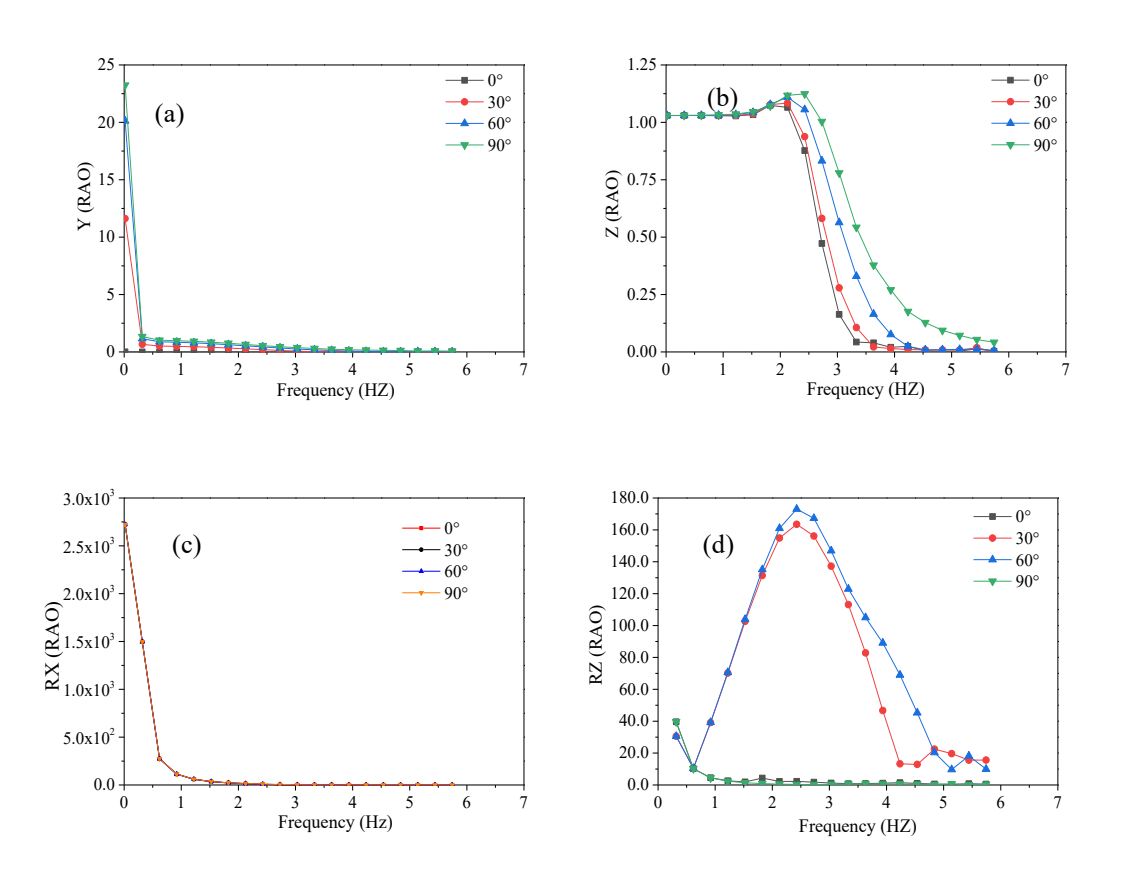


Figure S3.4 Response amplitude operators (RAOs) of the WD-TENG in (a) sway (Y), (b) heave (Z), (c) roll (RX) and (d) yaw (RZ) under CFD simulation.

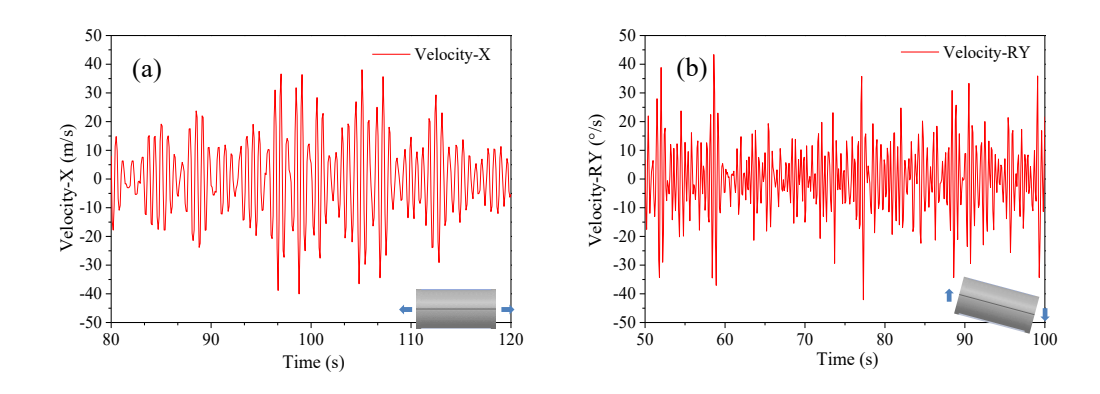


Figure S3.5 Time-history curves of WD-TENG velocity in (a) the X direction and in the RY direction under CFD simulation.

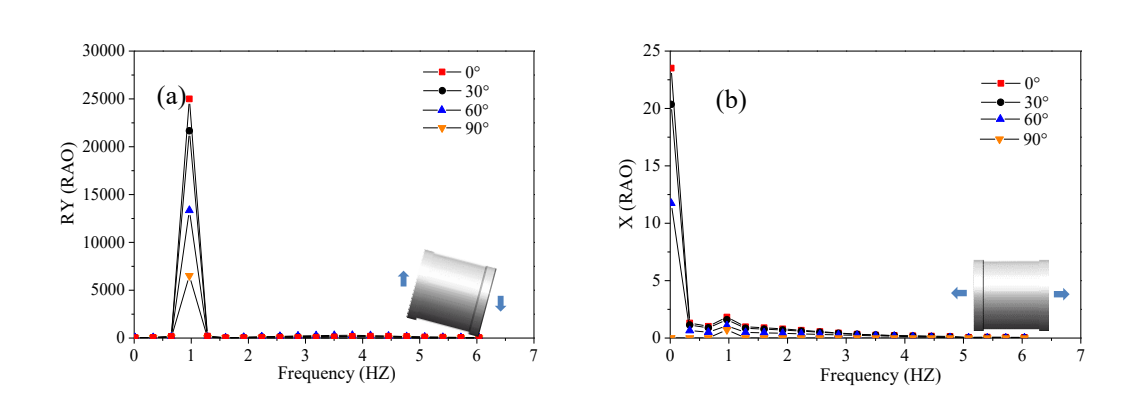


Figure S3.6 Response amplitude operators (RAOs) of the WD-TENG of Case 1 (Length: $0.5L_0$ and Diameter: $1.0D_0$) in (a) pitch and (b) surge of under CFD simulation.

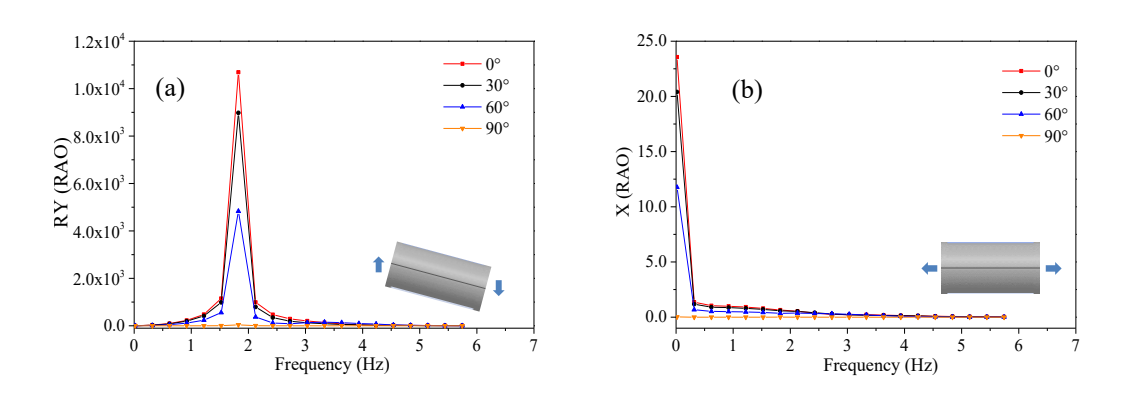
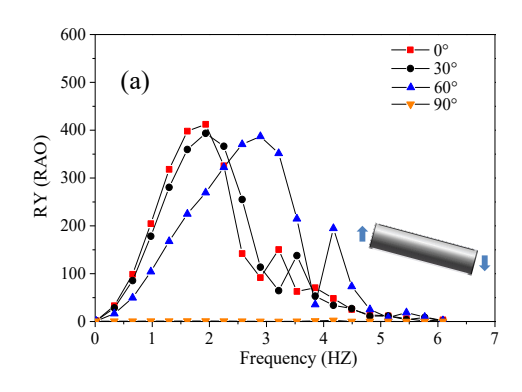


Figure S3.7 Response amplitude operators (RAOs) of the WD-TENG of Case 2 (Length: $1.0L_0$ and Diameter: $1.0D_0$) in (a) pitch and (b) surge of under CFD simulation.



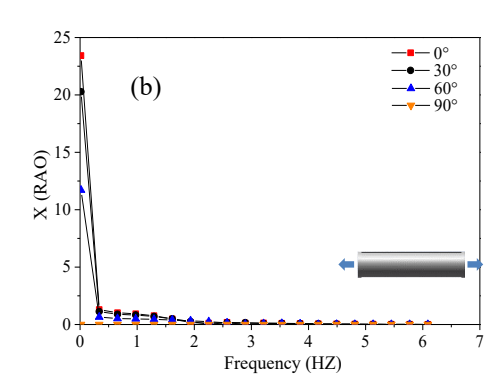
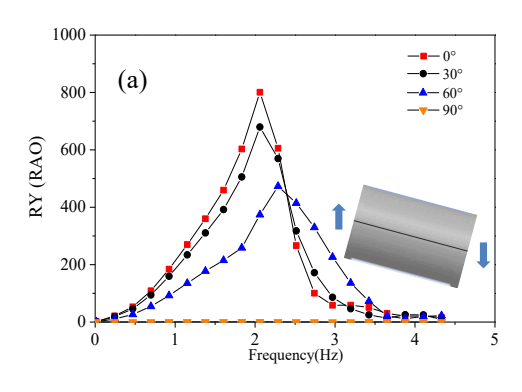


Figure S3.8 Response amplitude operators (RAOs) of the WD-TENG of Case 3 (Length: $2.0L_0$ and Diameter: $1.0D_0$) in (a) pitch and (b) surge of under CFD simulation.



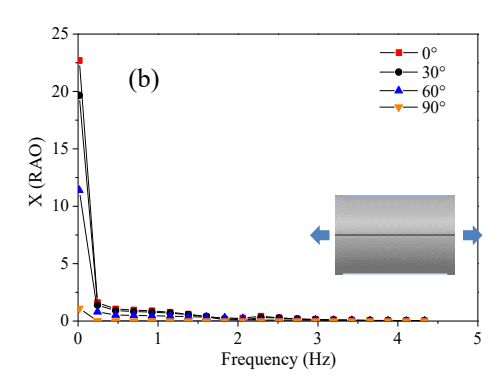


Figure S3.9 Response amplitude operators (RAOs) of the WD-TENG of Case 4 (Length: 2.0L₀ and Diameter 2.0D₀) in (a) pitch and (b) surge of under CFD simulation.

Figures S3.10-S3.13 show the time-history curves of displacement and structural response frequency spectra of the pitch and surge of Case 1-4 under the action of the wave in the 0° direction, respectively. The displacement frequency spectrum in the pitch and surge direction of the WD-TENG with the vertical coordinate representing the amplitude of the vibration response after the Fourier transform are shown in (c) and (d) of Figures S3.10-S3.13. Firstly, the vibration response of the surge is compared. The displacements are calculated with the centre of gravity of the WD-TENG as the reference point. In the surge direction of the WD-TENG, the characteristics of multi-frequency vibration and broadband vibration are obvious. According to (a) and (c) of Figures S3.10-S3.13, it can be seen that the vibration amplitude of Case 2 is the largest and the frequency domain that produces a large vibration response is the widest. The maximum and minimum displacement in the surge is 3.61 m and -3.66 m, respectively. Then the vibration response of pitch is compared. According to (b)(d) of Figures S3.10-S3.13, it can be seen that the pitch of WD-TENG of various sizes is broadband and multi-frequency vibration. Unlike the surge, it is difficult to specify the frequency corresponding to the peak vibration response of the pitch because the

pitch occurs over a wide range of frequency domains. However, the vibration amplitudes of Case 1 and Case 2 are the largest and more uniform, and the frequency domain of large vibration response is the widest. While the maximum and minimum displacement in the pitch (the RY direction) of Case 2 is 81.8° and -78.9°, respectively. In conclusion, in the calculated WD-Teng sizes, Case 2 can generate large vibration response amplitude over a wide range of frequency domains.

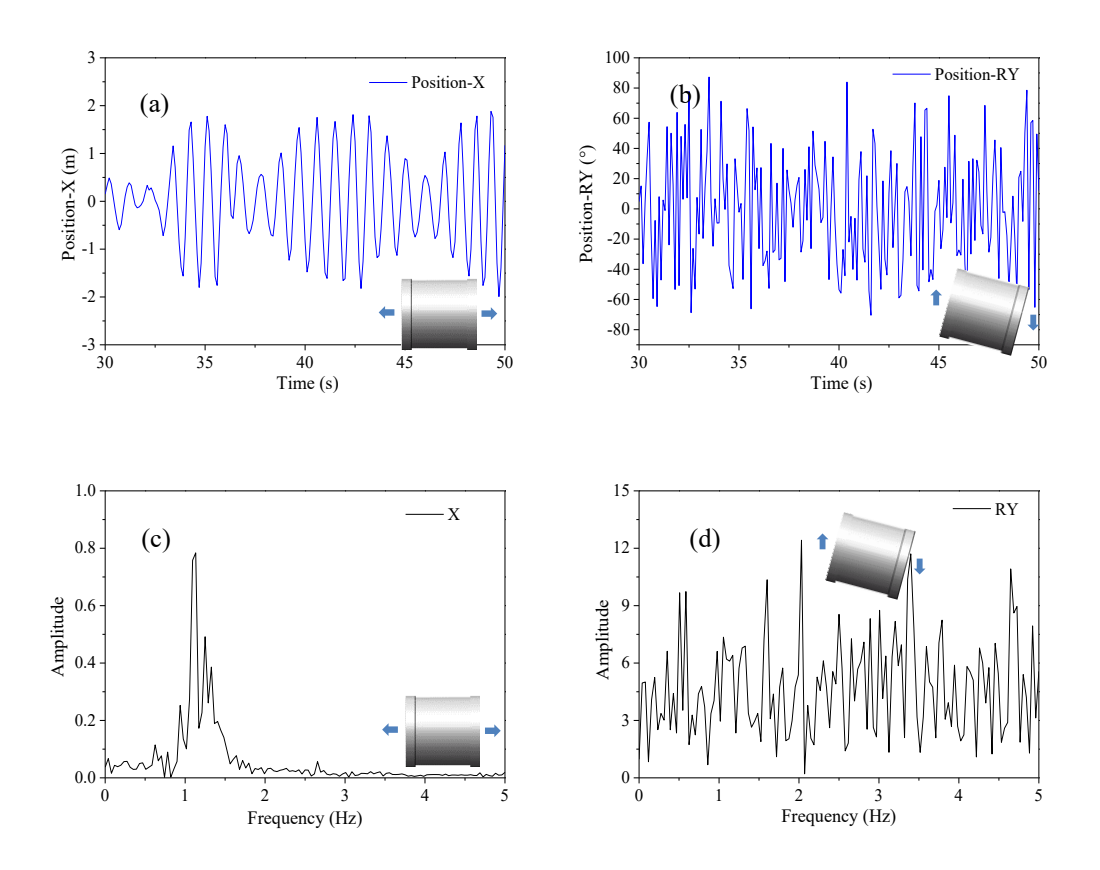
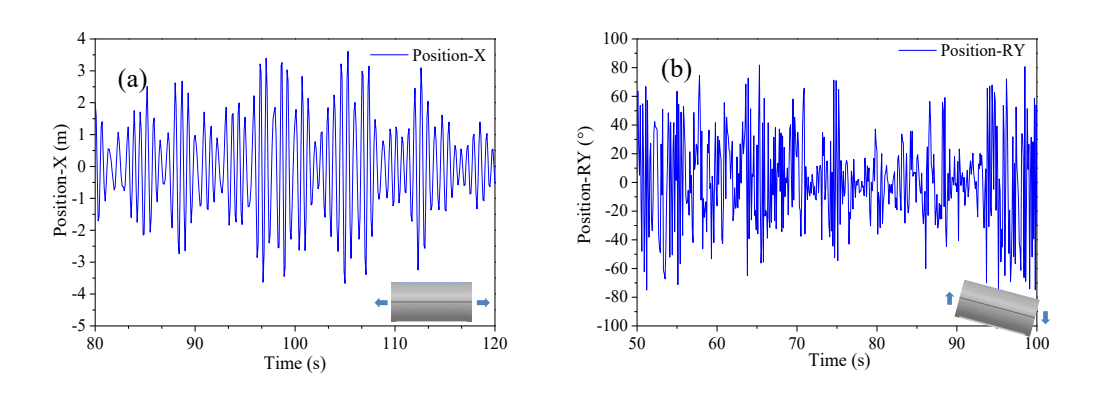


Figure S3.10 Case 1 WD-TENG (a) and (b) time-history curves of position and (c) and (d) structural response frequency spectra in (a) and (c) surge (the X direction) and (b) and (d) pitch (the RY direction).



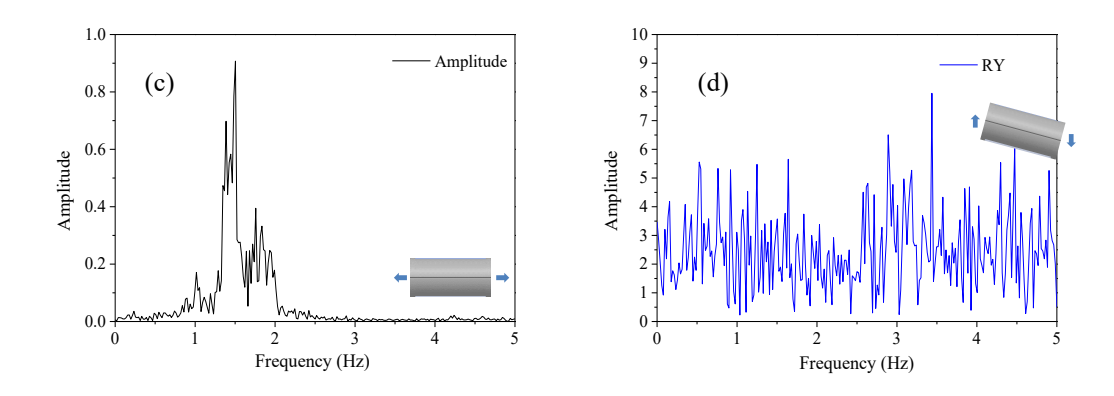


Figure S3.11 Case 2 WD-TENG (a) and (b) time-history curves of position and (c) and (d) structural response frequency spectra in (a) and (c) surge (the X direction) and (b) and (d) pitch (the RY direction).

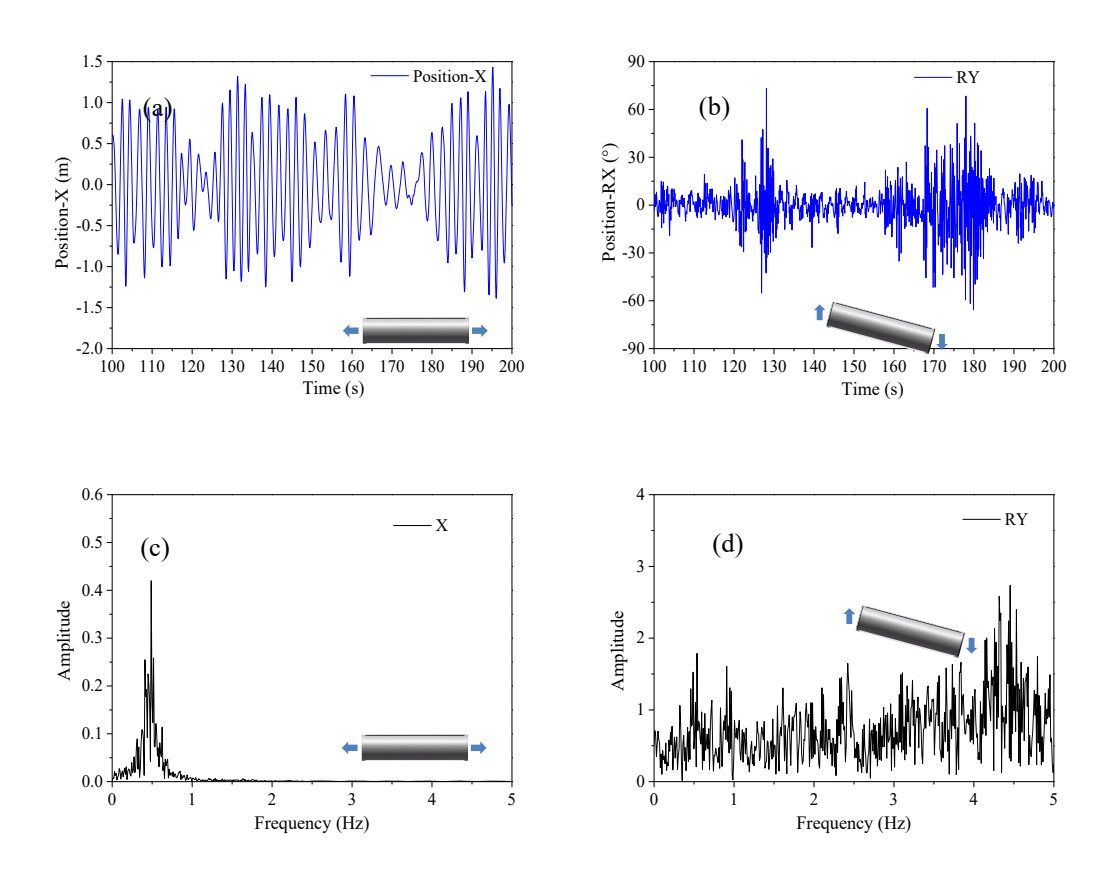


Figure S3.12 Case 3 WD-TENG (a) and (b) time-history curves of position and (c) and (d) structural response frequency spectra in (a) and (c) surge (the X direction) and (b) and (d) pitch (the RY direction).

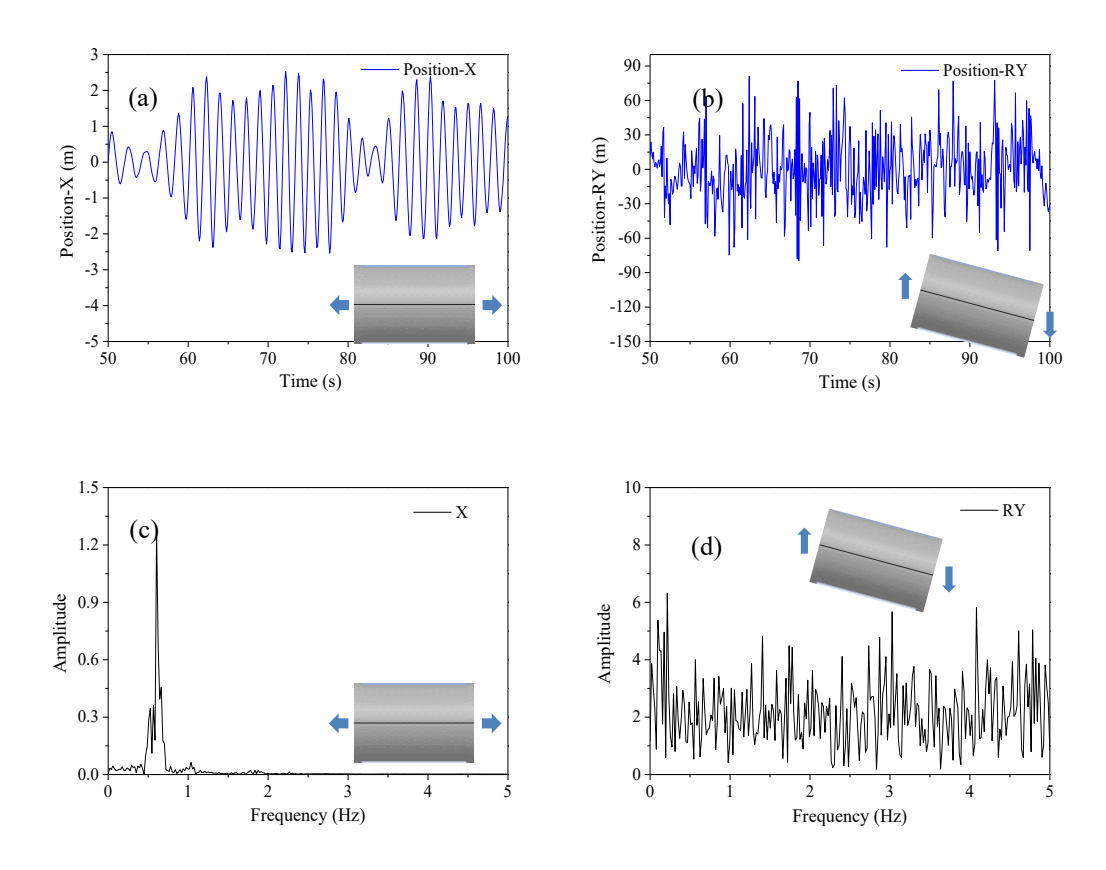
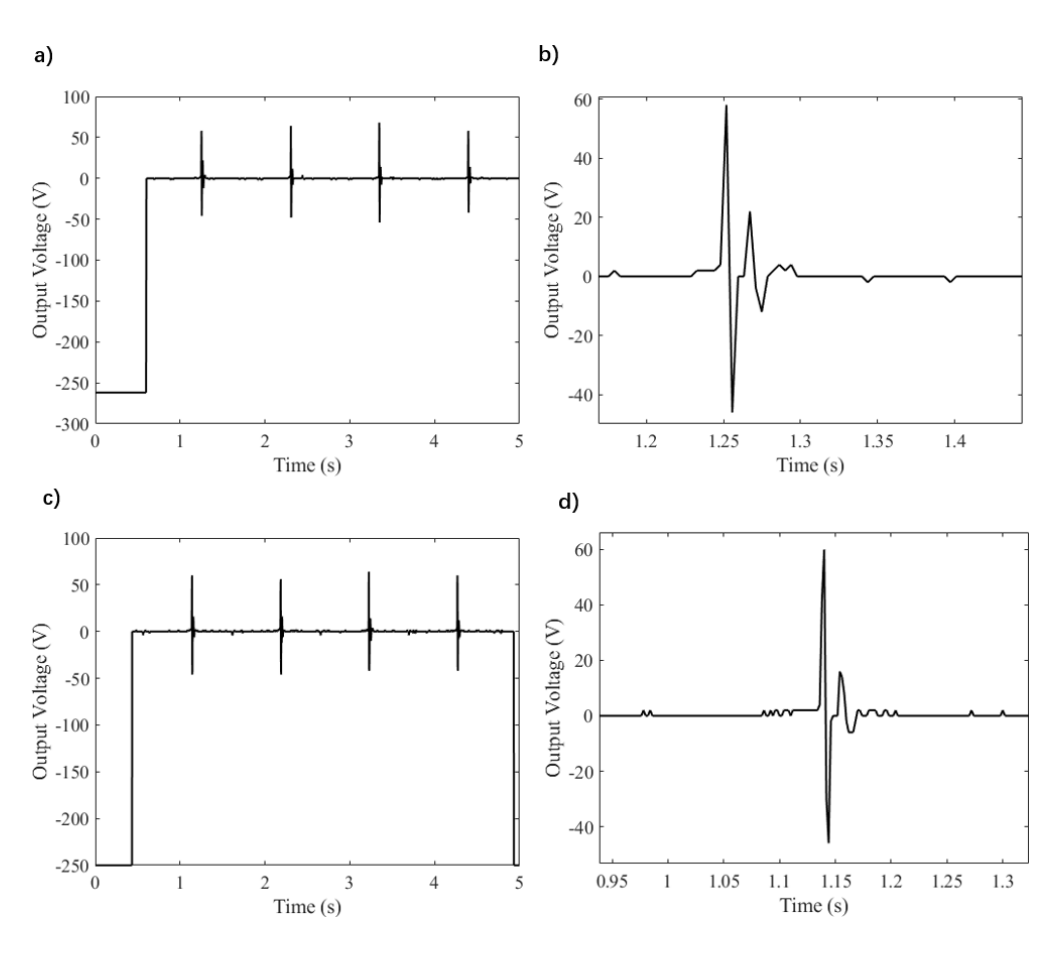


Figure S3.13 Case 4 WD-TENG (a) and (b) time-history curves of position and (c) and (d) structural response frequency spectra in (a) and (c) surge (the X direction) and (b) and (d) pitch (the RY direction).



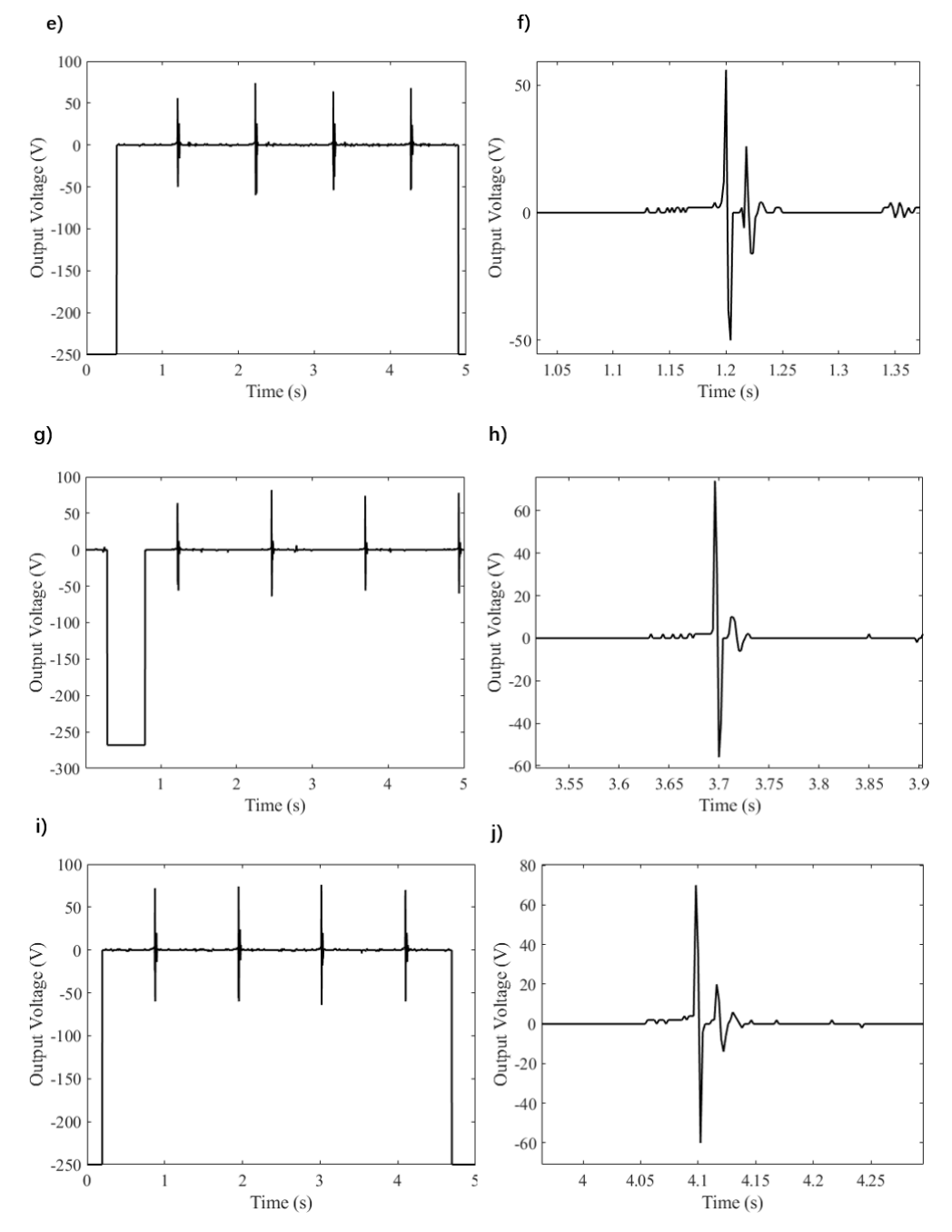
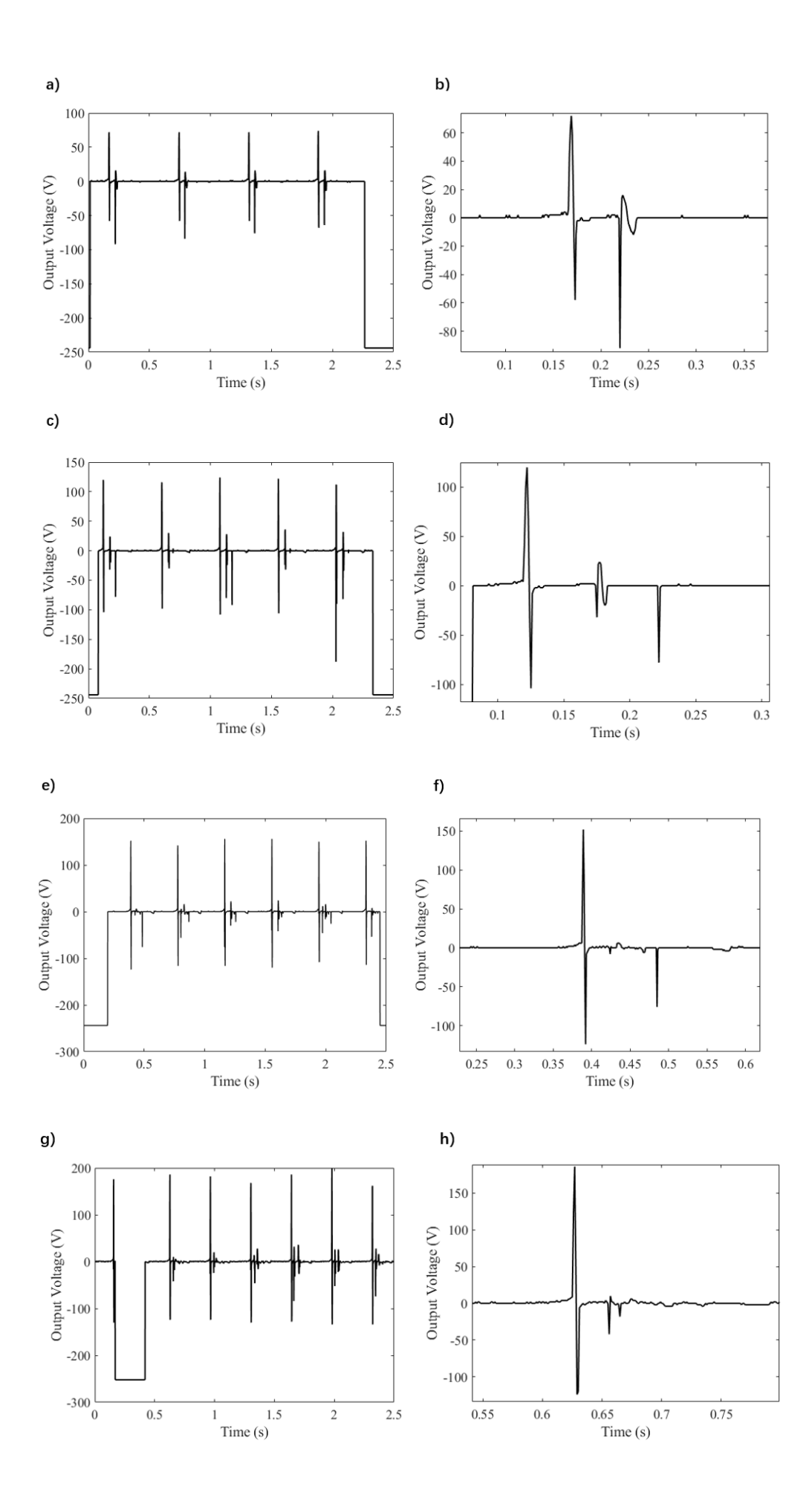


Figure S3.14 Waveform of the open-circuit voltage and detail waveform of WD-TENG under the different amplitudes (a) waveform of open-circuit voltage under 8.9 cm amplitude, (b) detail open-circuit voltage waveform under 8.9 cm amplitude, (c) waveform of open-circuit voltage under 9.5 cm amplitude, (d) detail open-circuit voltage waveform under 9.5 cm amplitude, (e) waveform of open-circuit voltage under 10.2 cm amplitude, (f) detail open-circuit voltage waveform under 10.2 cm amplitude, (g) waveform of open-circuit voltage under 10.9 cm amplitude, (h) detail open-circuit voltage waveform under 10.6 cm amplitude, (j) detail open-circuit voltage waveform under 11.6 cm amplitude. The operation frequency for different amplitudes testing is fixed at 2.2Hz.



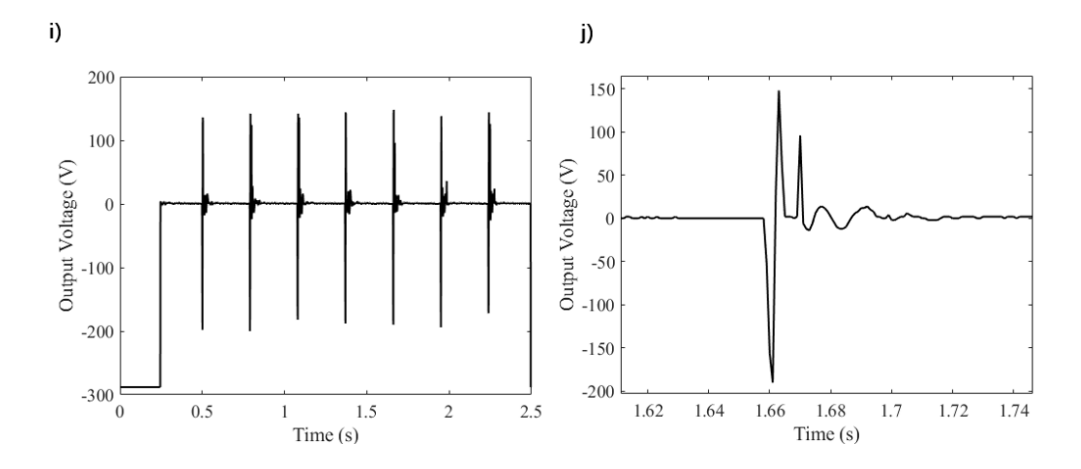


Figure S3.15 Waveform of the open-circuit voltage and detail waveform of WD-TENG under the different frequencies (a) waveform of open-circuit voltage under 3 Hz frequency, (b) detail open-circuit voltage waveform under 3 Hz frequency, (c) waveform of open-circuit voltage under 4 Hz frequency, (d) detail open-circuit voltage waveform under 4 Hz frequency, (e) waveform of open-circuit voltage under 5 Hz frequency, (f) detail open-circuit voltage waveform under 5 Hz frequency, (g) waveform of open-circuit voltage under 6 Hz frequency, (h) detail open-circuit voltage waveform under 6 Hz frequency, (i) waveform of open-circuit voltage under 7 Hz frequency, (j) detail open-circuit voltage waveform under 7 Hz frequency. The amplitude for different frequencies testing is fixed at 0 cm.

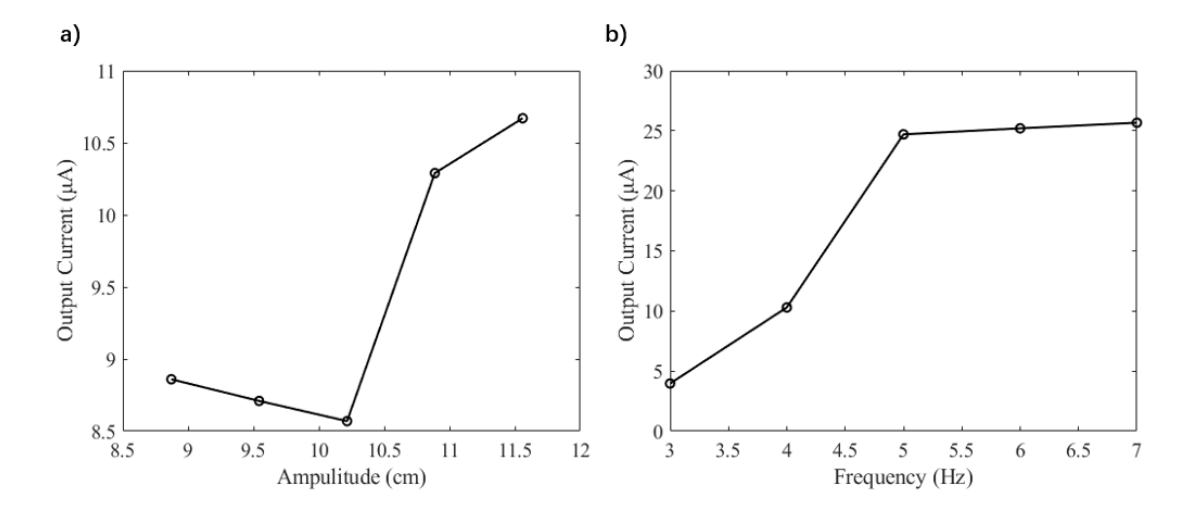


Figure S3.16 Short-circuit current of WD-TENG under different (a) amplitudes, and (b) frequencies. The frequency in (a) is 2.2 Hz, and the amplitude in (b) is fixed as 0. The load resistance is $5 \text{ M}\Omega$.

Supporting information for Chapter 4

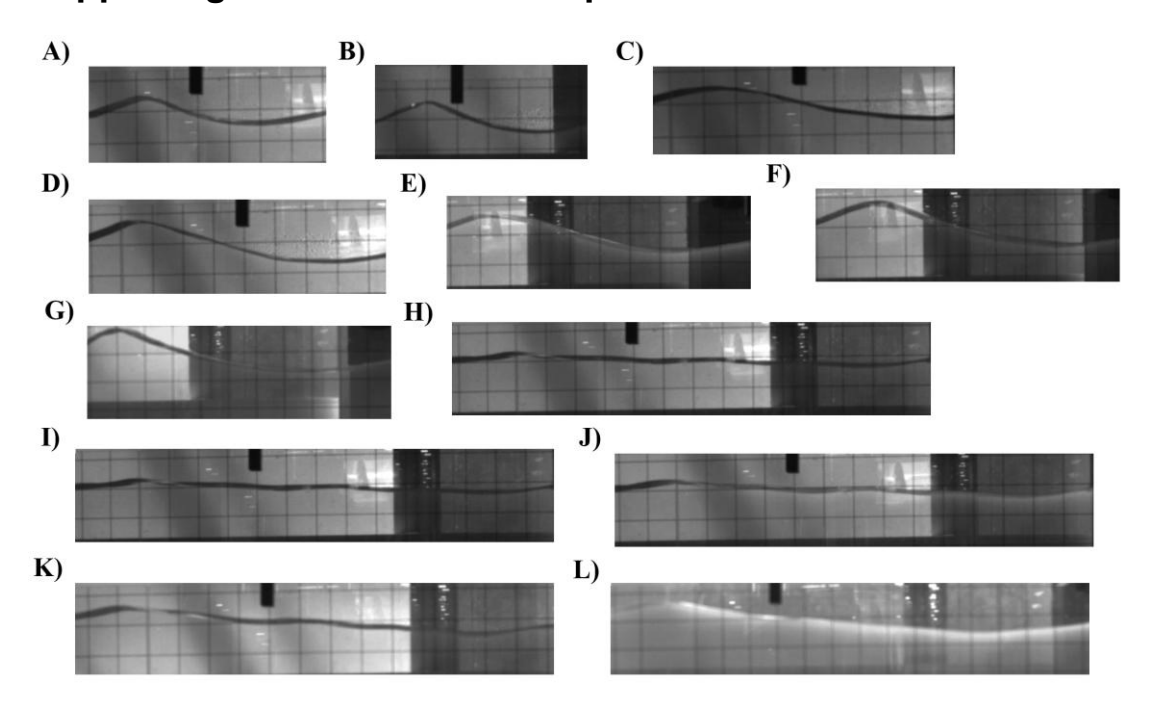


Figure S4.1 The wavelength of the generating wave is under 20 cm depth of water. A) 18.18 ° with 2 Hz, B) 21.51 ° with 2 Hz, C) 18.18 ° with 1.5 Hz, D) 21.51 ° with 1.5 Hz, E) 24.69 ° with 1.5 Hz, F) 27.72 ° with 1.5 Hz, G) 30.59 ° with 1.5 Hz, H) 18.18 ° with 1 Hz, I) 21.51 ° with 1 Hz, K) 24.69 ° with 1 Hz, J) 27.72 ° with 1 Hz, L) 30.59 ° with 1 Hz.

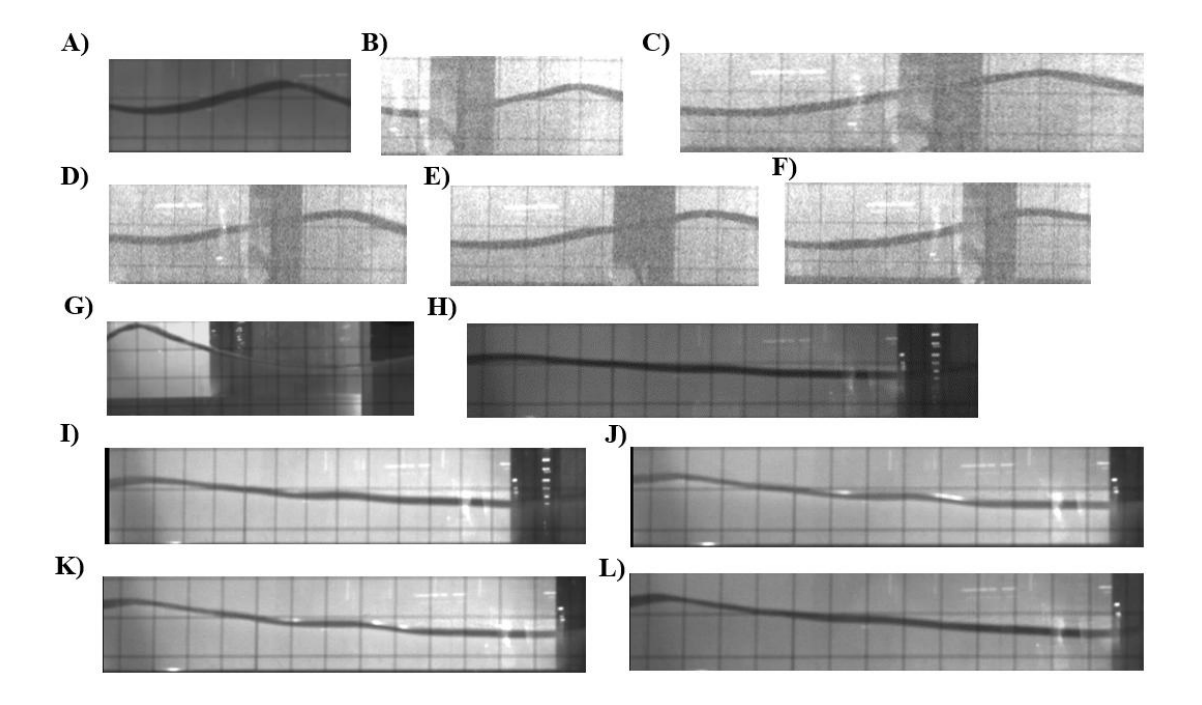


Figure S4.2 The wavelength of the generating wave is under 15 cm depth of water. A) 18.18 $^{\circ}$ with 2 Hz, B) 21.51 $^{\circ}$ with 2 Hz, C) 18.18 $^{\circ}$ with 1.5 Hz, D) 21.51 $^{\circ}$ with 1.5 Hz, E) 24.69 $^{\circ}$ with 1.5 Hz, F) 27.72 $^{\circ}$ with 1.5 Hz, G) 30.59 $^{\circ}$ with 1.5 Hz, H) 18.18 $^{\circ}$ with 1 Hz, I) 21.51 $^{\circ}$ with 1 Hz, K) 24.69 $^{\circ}$ with 1 Hz, J) 27.72 $^{\circ}$ with 1 Hz, L) 30.59 $^{\circ}$ with 1 Hz.

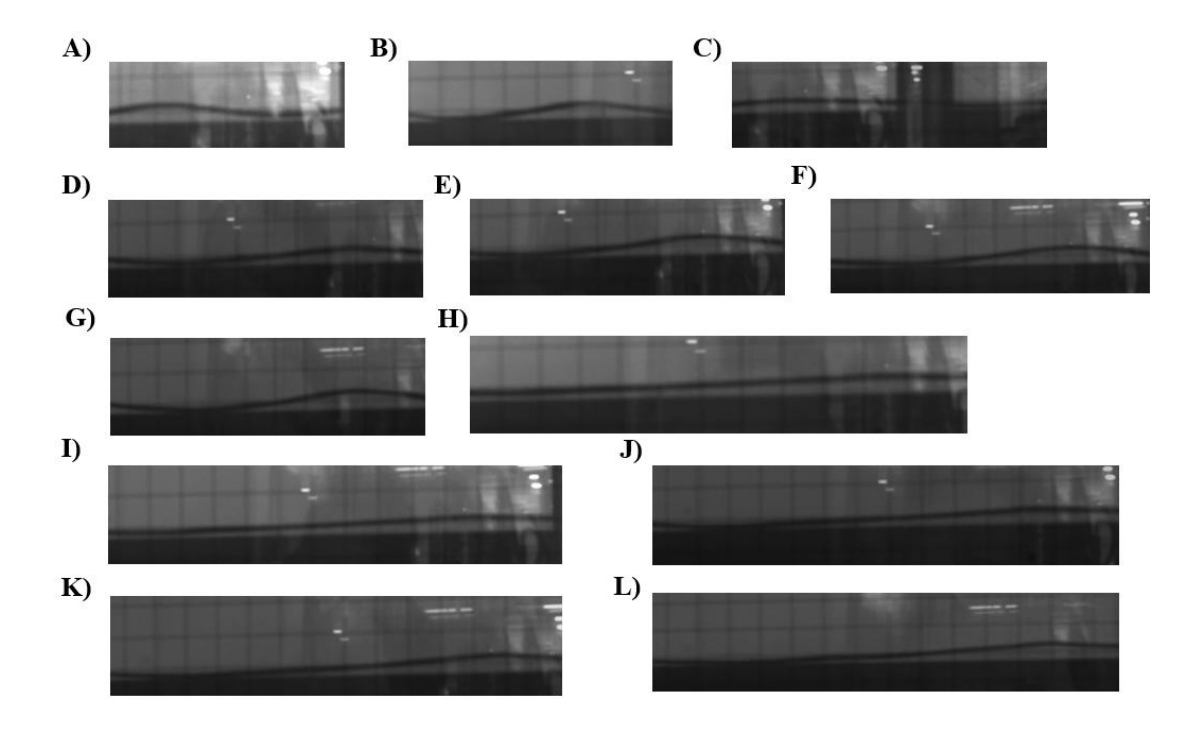


Figure S4.3 The wavelength of the generating wave is under 10 cm depth of water. A) 18.18 $^{\circ}$ with 2 Hz, B) 21.51 $^{\circ}$ with 2 Hz, C) 18.18 $^{\circ}$ with 1.5 Hz, D) 21.51 $^{\circ}$ with 1.5 Hz, E) 24.69 $^{\circ}$ with 1.5 Hz, F) 27.72 $^{\circ}$ with 1.5 Hz, G) 30.59 $^{\circ}$ with 1.5 Hz, H) 18.18 $^{\circ}$ with 1 Hz, I) 21.51 $^{\circ}$ with 1 Hz, K) 24.69 $^{\circ}$ with 1 Hz, J) 27.72 $^{\circ}$ with 1 Hz, L) 30.59 $^{\circ}$ with 1 Hz.

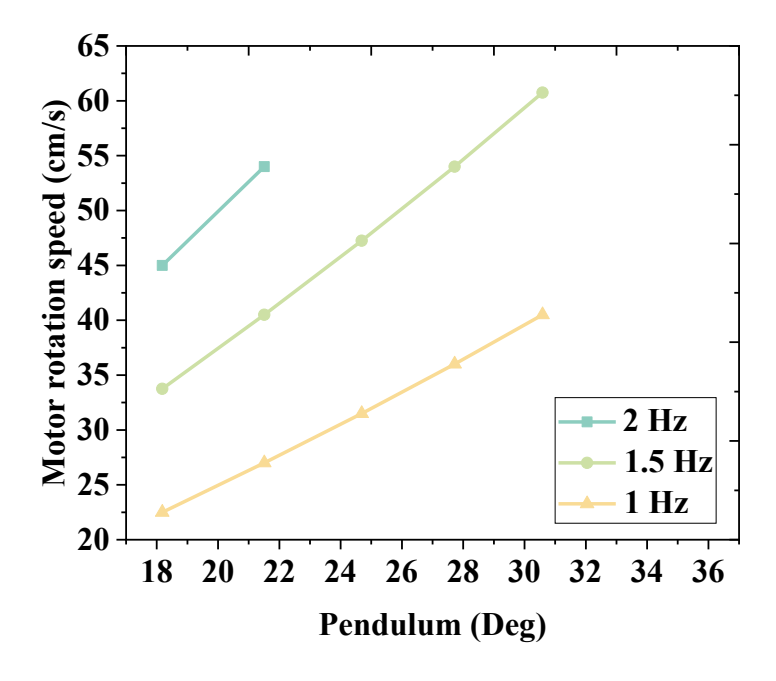


Figure S4.4 The relationship between different Paddle angles (θ) and motor rotation speeds (v). with 2 Hz, 1.5 Hz, and 1 Hz.

Note.1 Selection of step motor to achieve higher wave frequency and amplitude.

As shown in Table S4.1, the specifications of the two stepper motors have been compared: the motor currently in use (PD60-4-1076) and another motor (PD86-3-1180) used to achieve higher wave frequency and amplitude. Both motors belong to the same series, have similar connection pins, and are manufactured by the same company, Trinamic (Germany). Therefore, there is no need to change the wiring layout; simply swapping the stepper motor allows for higher wave frequencies and amplitudes, significantly increasing convenience. Based on programming and analysis of experimental results, the maximum frequency achievable by the PD60-4-1076 is 2 Hz at a pendulum angle of 21.51°, due to its maximum rotation speed being limited to 1200 rpm. In comparison, the PD86-3-1180, with a maximum rotation speed of 5000 rpm, can achieve a frequency at least four times higher, allowing wave frequencies to reach up to 8 Hz. The generated wave amplitude depends on the pendulum motion of the wave creation board. Using measurement data from a water depth of 20 cm and a frequency of 1.5 Hz, we derived a fitted equation (S4.1) to predict the generated wave amplitude at larger pendulum angles. The prediction results are shown in Table S4.2, where the wave amplitude can reach 25.39 cm at a pendulum angle of 49.77°. Additionally, based on experimental results and equation derivation, water depth has a more significant effect on wave amplitude compared to the pendulum angle. As shown in Figure 4 of the main text, the wave amplitude at a pendulum angle of 30.59° and a frequency of 1.5 Hz doubles when the water depth increases from 10 cm to 20 cm. Therefore, if the water depth reaches 30 cm, the maximum generated wave amplitude is approximately 50.78 cm.

Table S4.1 Comparison of step motor specifications to achieve higher wave frequency and amplitude.

	PD60-4-1076 (Current use) [S1]	PD-3-1180 (For higher frequency and wave amplitude) [S2]
Width (mm)	60	86
Height (mm)	60	86
Length (mm)	99	118
Weight (Kg)	1.4	2.8
Maximum rotation speed (rpm)	1200	5000
Price (AUD)	\$450.99	\$1280.75

Table S4.2 Comparison of the generated wave amplitude between the experiment and prediction under 20 cm water depth and 1.5 Hz frequency.

Experiment generated wave amplitude (cm)		Prediction generated wave amplitude (cm)	
18.18	4.2124	18.18	4.23
21.51	5.6466	21.51	5.58
24.69	6.2052	24.69	6.31
27.72	6.816	27.72	6.74
30.59	7.1314	30.59	7.15
		33.29	7.72
		35.84	8.59
		38.24	9.83
		40.49	11.47
		42.6	13.53
		44.57	15.98
		46.42	18.80
		48.15	21.95
		49.77	25.39

Reference

S4.1. Element 14. TRINAMIC / ANALOG DEVICES PD60-4-1076. https://au.element14.com/trinamic/pd60-4-1076/stepper-motor-driver-1-ph-2-8a/dp/2921448/ (accessed 22 April 2024).

S4.2. Element 14. TRINAMIC / ANALOG DEVICES PD86-3-1180-CANOPEN. https://au.element14.com/trinamic/pd86-3-1180-canopen/stepper-motor-2-ph-5-5a-7n-m/dp/2902251#(accessed 22 April 2024).

Supporting information for Chapter 5

Note S5.1 Analysis of the hydrogel property before and after freeze-drying.

Table S5.1 demonstrates the variation in hydrogel weight before and after freeze-drying. It clearly shows a significant change in weight after the freeze-drying process where 51 wt.% to 66 wt.% of moisture was lost during the drying process.

To assess the impact of rGO to the PVA-based hydrogels, four different samples were prepared, each with varying weight percentages of rGO (0 wt.%, 0.5 wt.%, 1.0 wt.%, and 1.5 wt.%) in the PVA-based hydrogels, respectively. The conductivity of each PVA-based hydrogel sample can be calculated using the measured data of resistivity from the digital multimeter readings. Four hydrogels were cut to a diameter of 25 mm and a thickness of 2 mm each. A freeze dryer was used to determine whether moisture influenced the conductivity of the PVA-based hydrogels. The conductivity values before freeze-drying are depicted in Figure S5.1 as the green bars. The conductivity of the hydrogel was measured after freeze drying and is shown in Figure S5.1 by the purple bars.

The red curved structures represent nano-crystalline domains, while the black cubes represent rGO within the hydrogel and the green lines that connect them represent the amorphous PVA chains as shown in Figure S5.2. In addition, the blue and the light blue background represent the different moisture ratio. Upon the removal of moisture from the hydrogel, a porous structure is formed [S1, S2]. It's important to note that air is not electrically conductive, so as the moisture content inside the hydrogel decreases, the internal impedance increases. In the context of this study, the PVA-based hydrogel is encased by the silicone rubber so that the moisture cannot evaporate, therefore maintaining good conductivity in the hydrogel. The rGO content did not contribute much to the conductivity in this study due to the low weight percentage. However, according to the experimental results from Lai et al. in 2022, once the volume of rGO increases, the conductivity is expected to rise under dried condition [S3].

Table S5.1. Weight changes of PVA-based hydrogels before and after freezing dry.

rGO weight ratio	Before (g)	After (g)	Total loss (%)
0%	1.678	0.569	66.1
0.5%	2.449	1.199	51.0
1%	2.856	1.327	53.5
1.5%	2.228	0.845	62.1

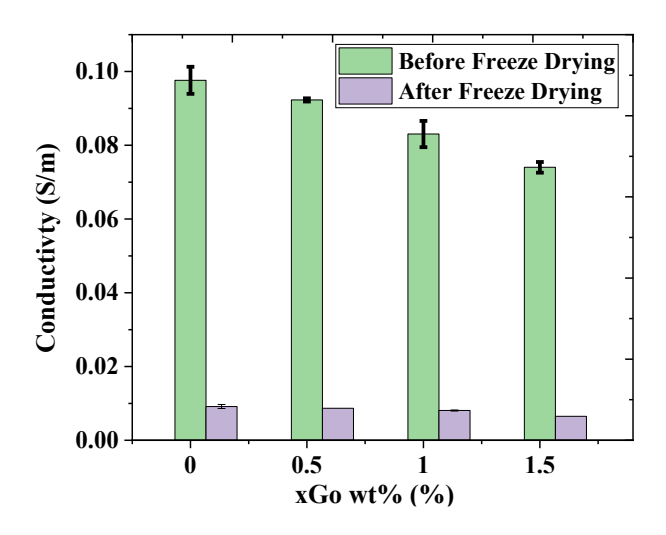


Figure S5.1 Comparison of the conductivity of PVA-based hydrogel before and after freeze-drying. At 0 wt.%, 0.5 wt.%, 1.0 wt.%, and 1.5 wt.% rGO.

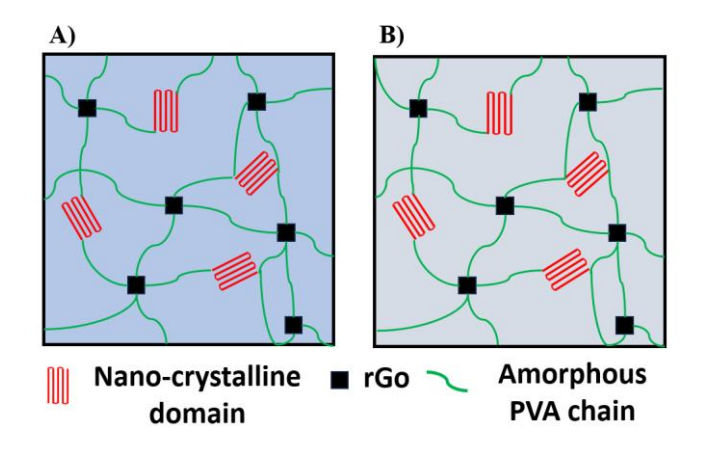


Figure S5.2 Schematic internal structures of PVA-based hydrogel before and after freeze-drying. (A) before and (B) after freeze-dried. The red curved structures represent nano-crystalline domains, while the black cubes represent rGO within the hydrogel and the green lines that connect them represent amorphous PVA chains. In addition, the blue and the light blue background represent the different moisture ratio.

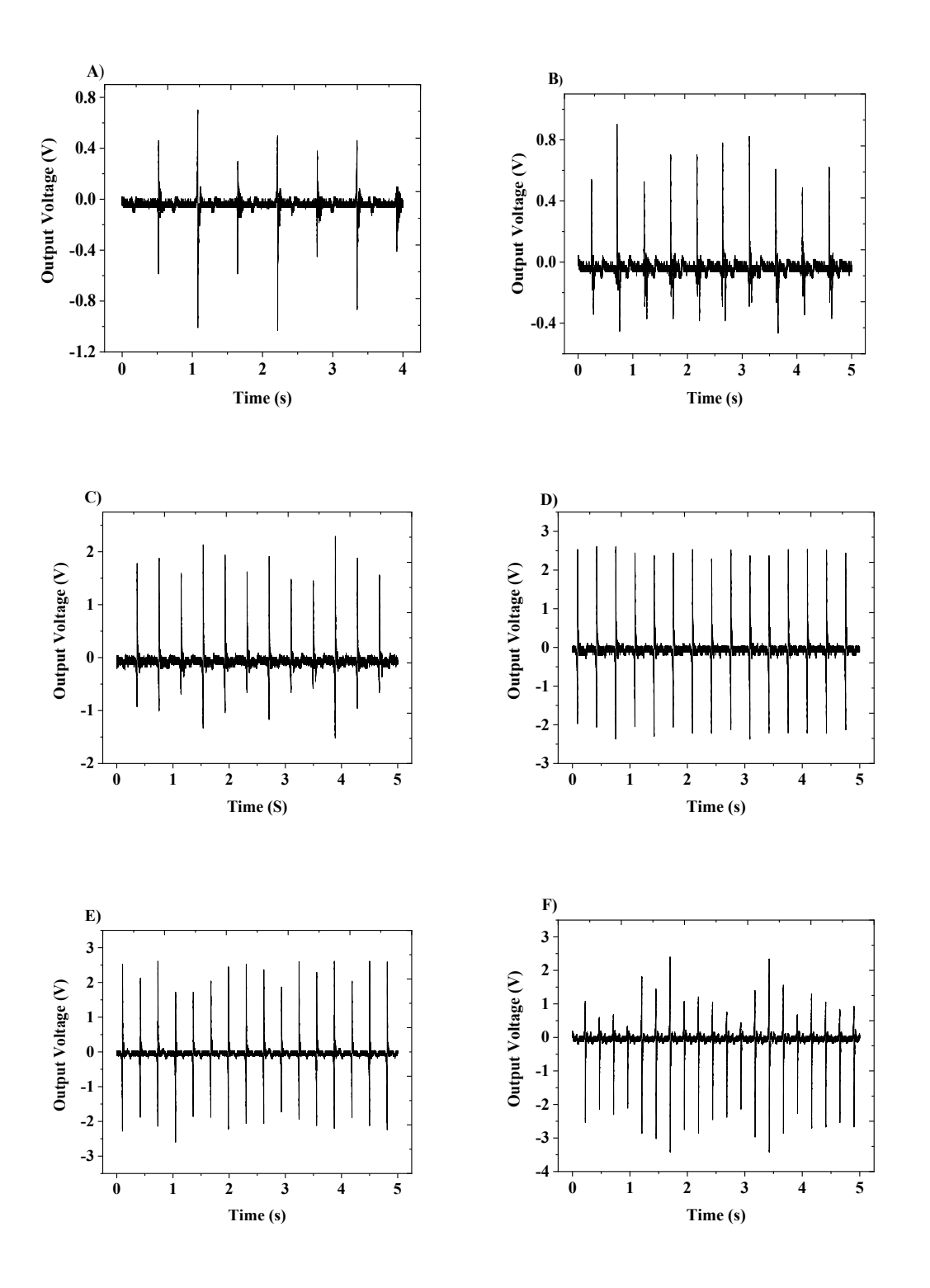


Figure S5.3 The output performance of CS-EMH analyses of different frequency under 6.6 cm amplitudes. (A) 1.5 Hz, (B) 2.0 Hz, (C) 2.5 Hz, (D) 3.0 Hz, (E) 3.5 Hz, and (F) 4.0 Hz.

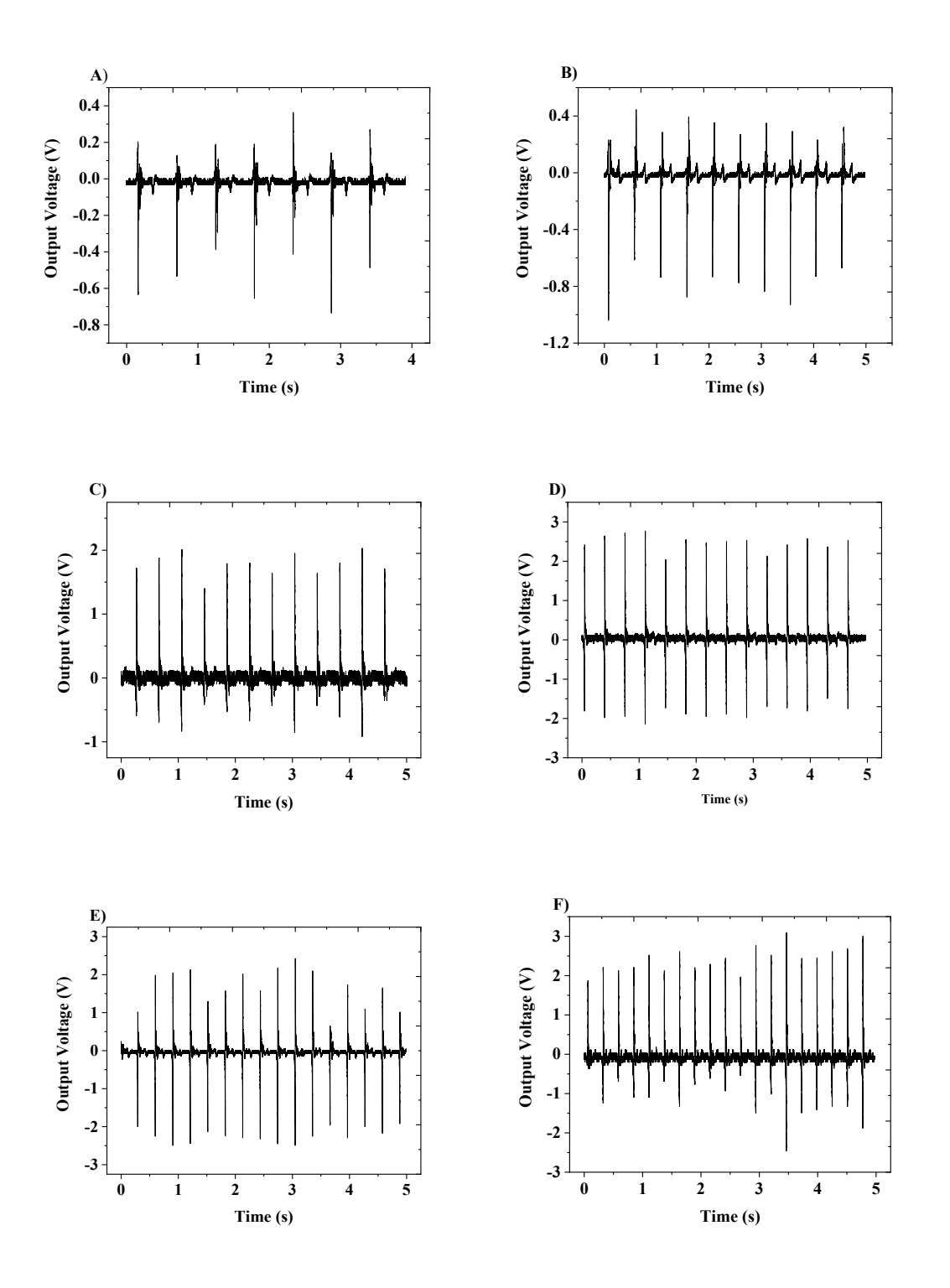


Figure S5.4 The output performance of CS-EMH analyses of different frequency under 7.1 cm amplitudes. (A) 1.5 Hz, (B) 2.0 Hz, (C) 2.5 Hz, (D) 3.0 Hz, (E) 3.5 Hz, and (F) 4.0 Hz.

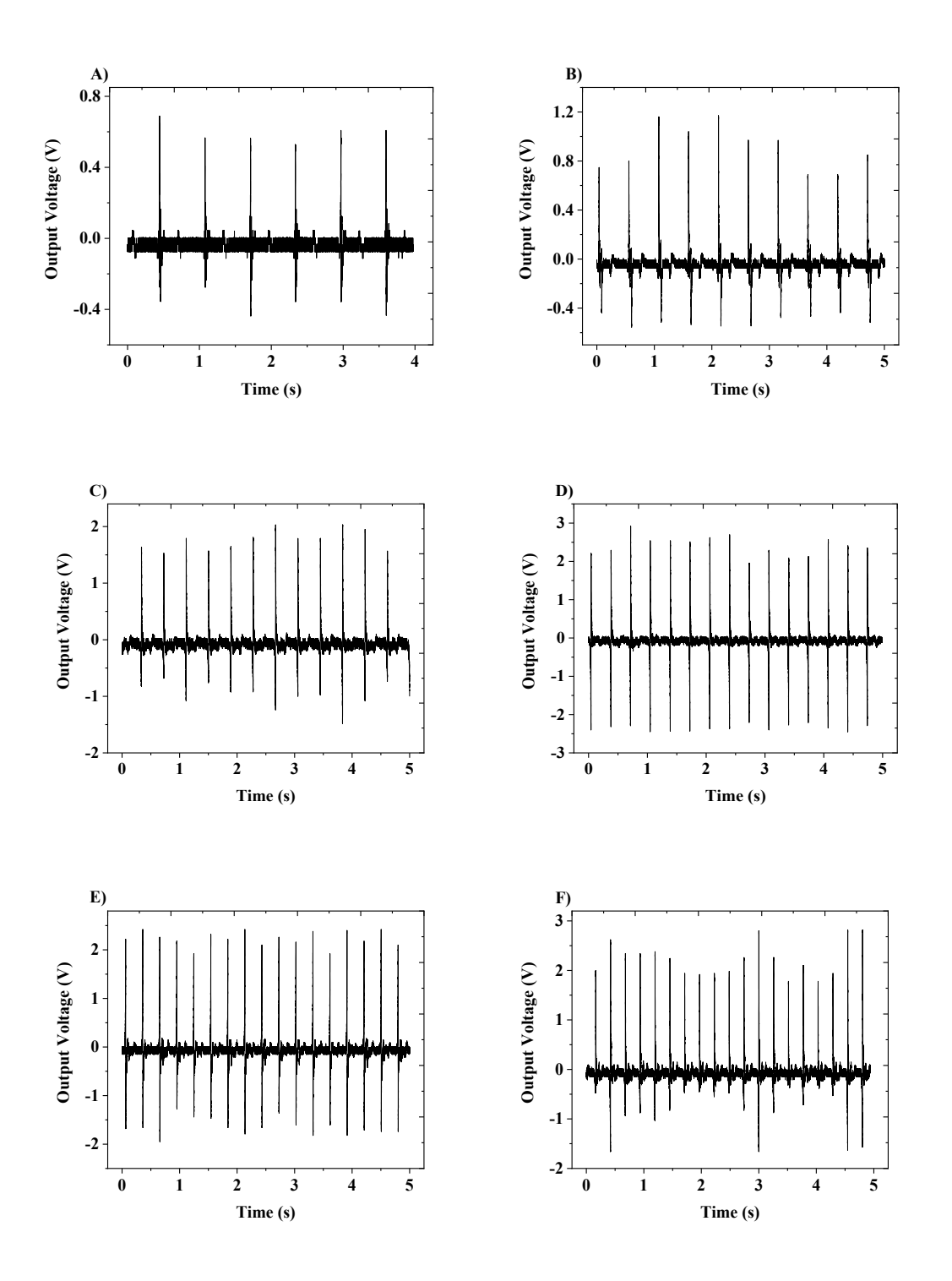


Figure S5.5 The output performance of CS-EMH analyses of different frequency under 7.6 cm amplitudes. (A) 1.5 Hz, (B) 2.0 Hz, (C) 2.5 Hz, (D) 3.0 Hz, (E) 3.5 Hz, and (F) 4.0 Hz.

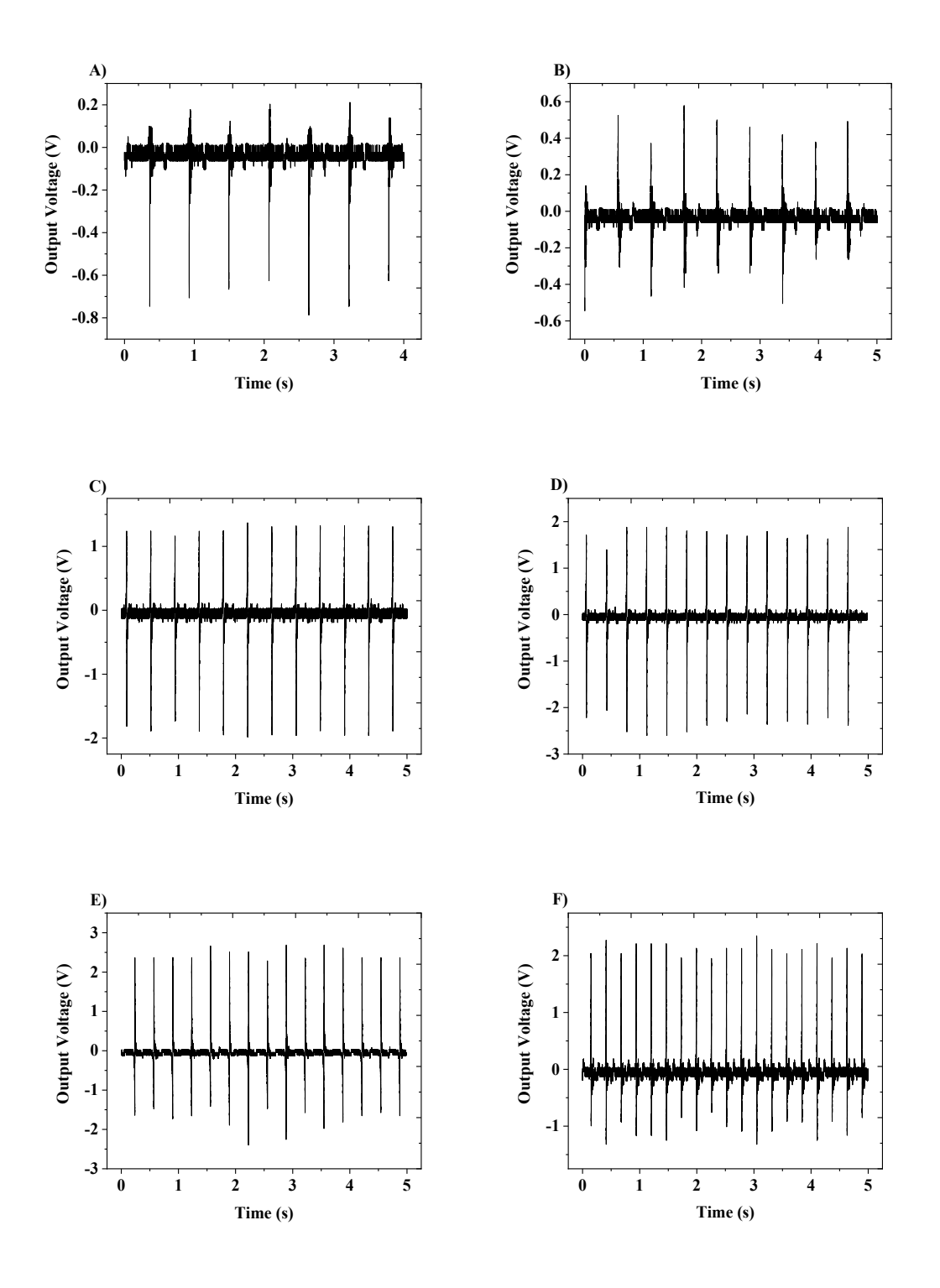


Figure S5.6 The output performance of CS-EMH analyses of different frequency under 8.1 cm amplitudes. (A) 1.5 Hz, (B) 2.0 Hz, (C) 2.5 Hz, (D) 3.0 Hz, (E) 3.5 Hz, and (F) 4.0 Hz.

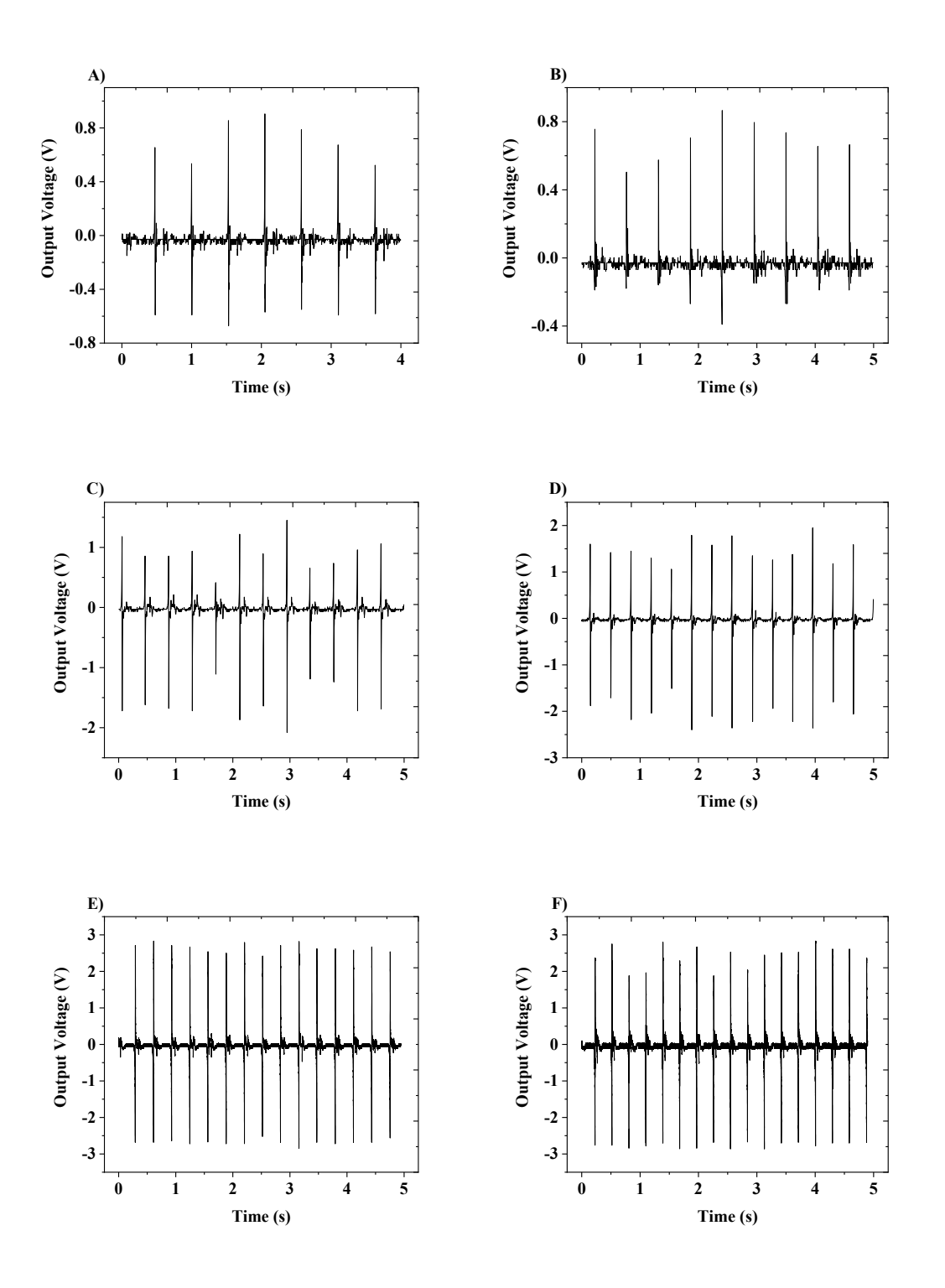


Figure S5.7 The output performance of CS-EMH analyses of different frequency under 8.6 cm amplitudes. (A) 1.5 Hz, (B) 2.0 Hz, (C) 2.5 Hz, (D) 3.0 Hz, (E) 3.5 Hz, and (F) 4.0 Hz.

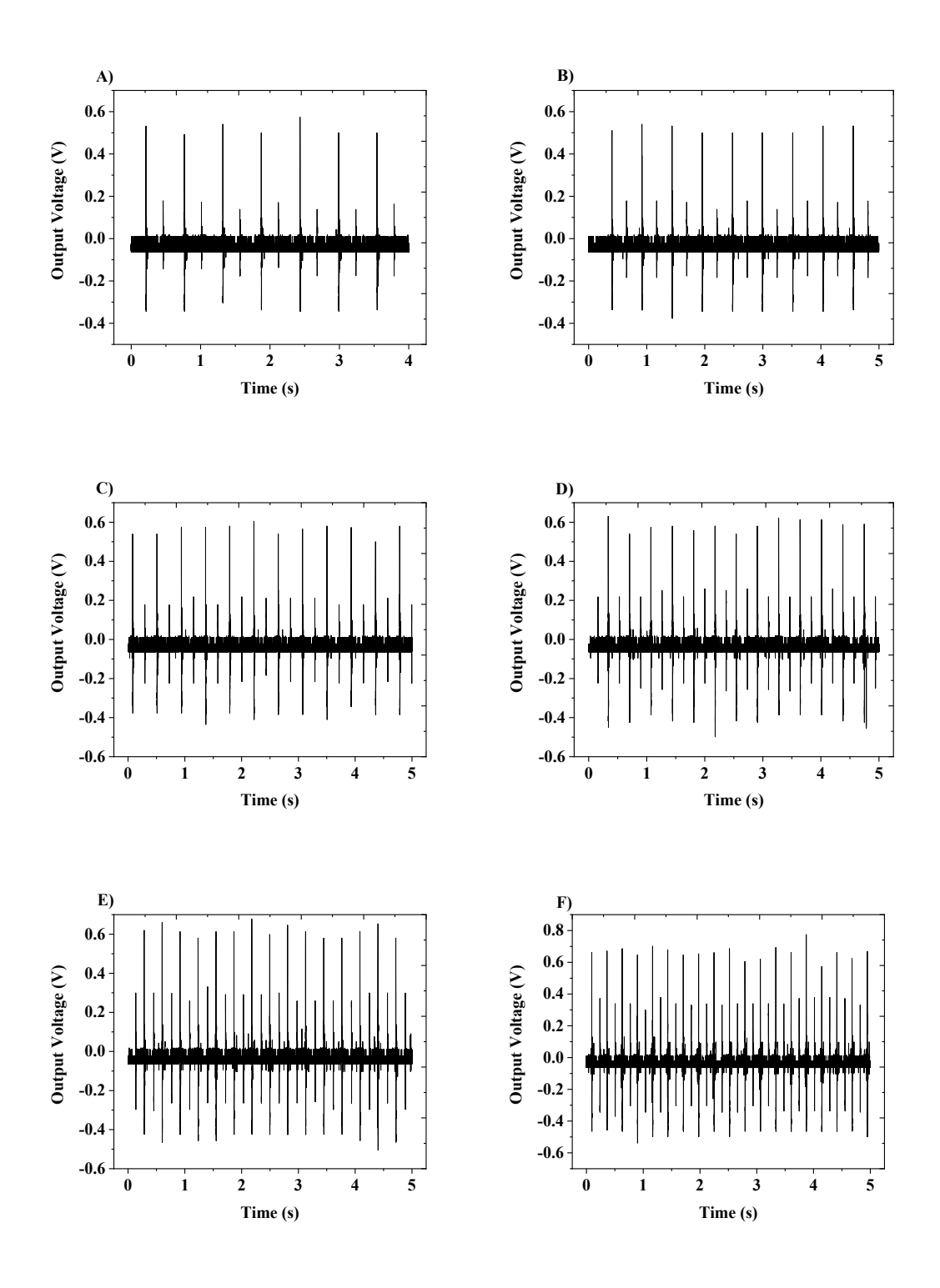


Figure S5.8 The output performance analyses of pure PVA-based hydrogel different frequency under 8.6 cm amplitudes. (A) 1.5 Hz, (B) 2.0 Hz, (C) 2.5 Hz, (D) 3.0 Hz, (E) 3.5 Hz, and (F) 4.0 Hz.

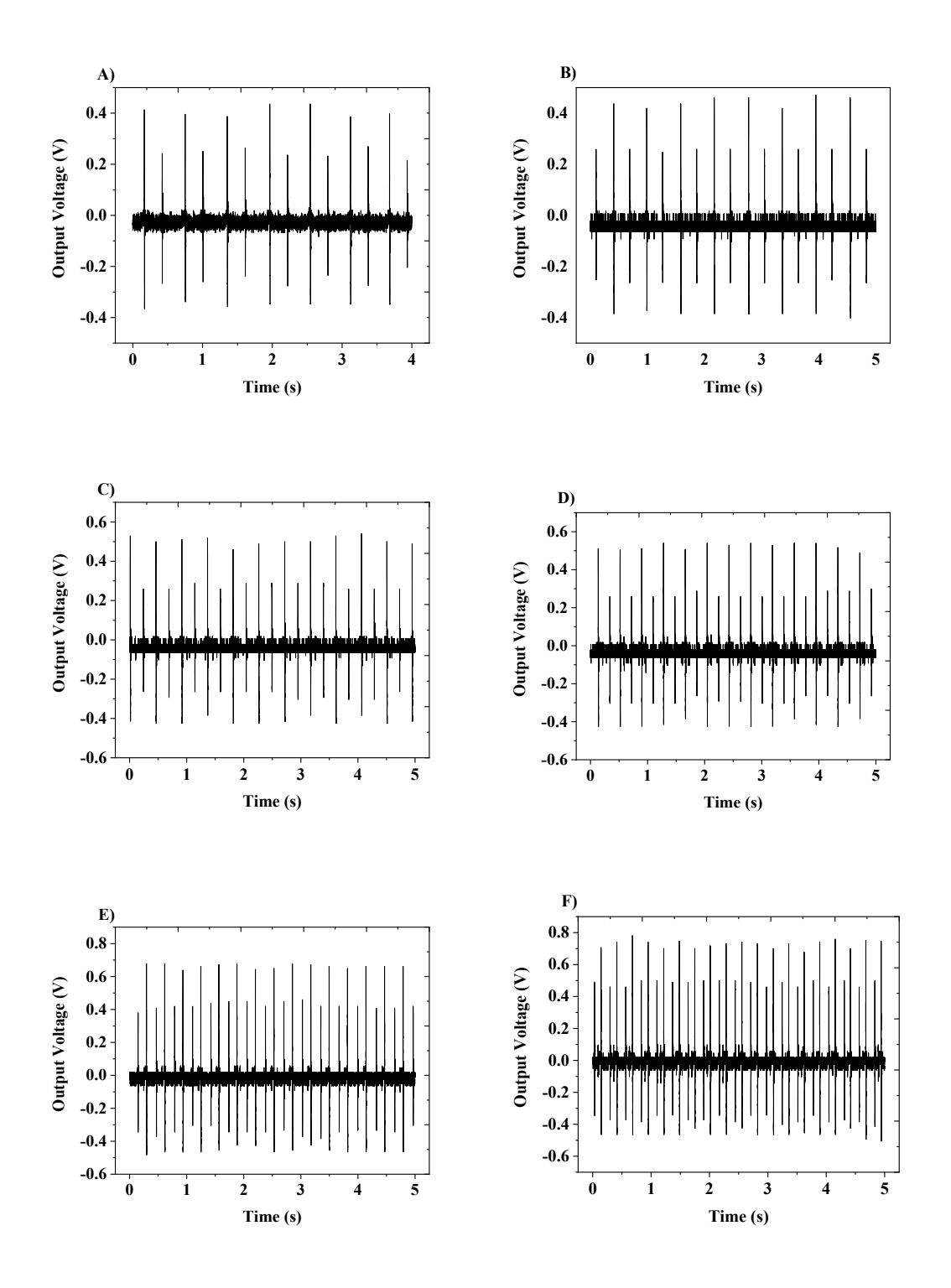


Figure S5.9 The output performance analyses of 0.5% rGO enhanced PVA-based hydrogel different frequency under 8.6cm amplitudes. (A) 1.5 Hz, (B) 2.0 Hz, (C) 2.5 Hz, (D) 3.0 Hz, (E) 3.5 Hz, and (F) 4.0 Hz.

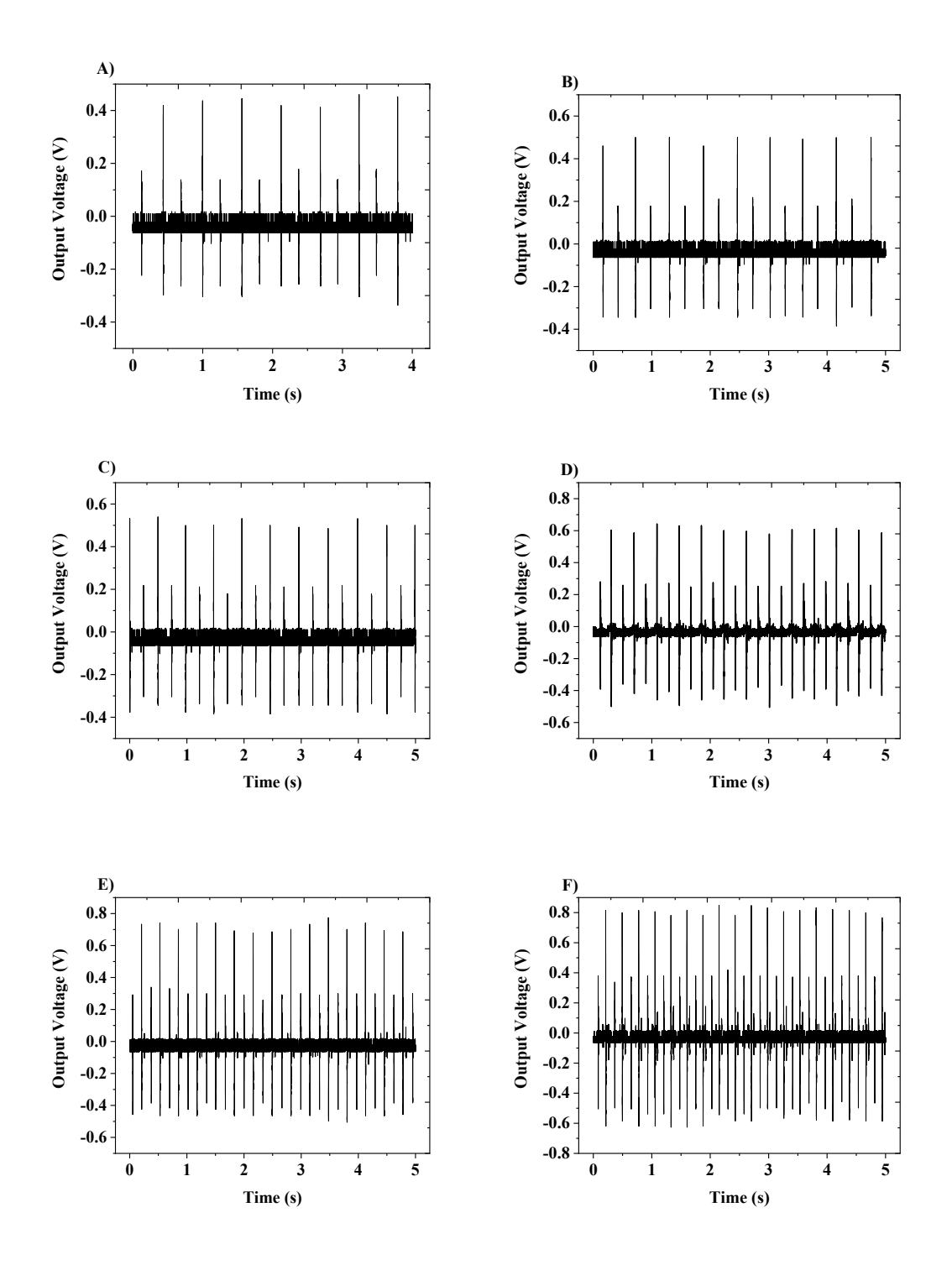


Figure S5.10 The output performance analyses of 1% rGO enhanced PVA-based hydrogel different frequency under 8.6 cm amplitudes. (A) 1.5 Hz, (B) 2.0 Hz, (C) 2.5 Hz, (D) 3.0 Hz, (E) 3.5 Hz, and (F) 4.0 Hz.

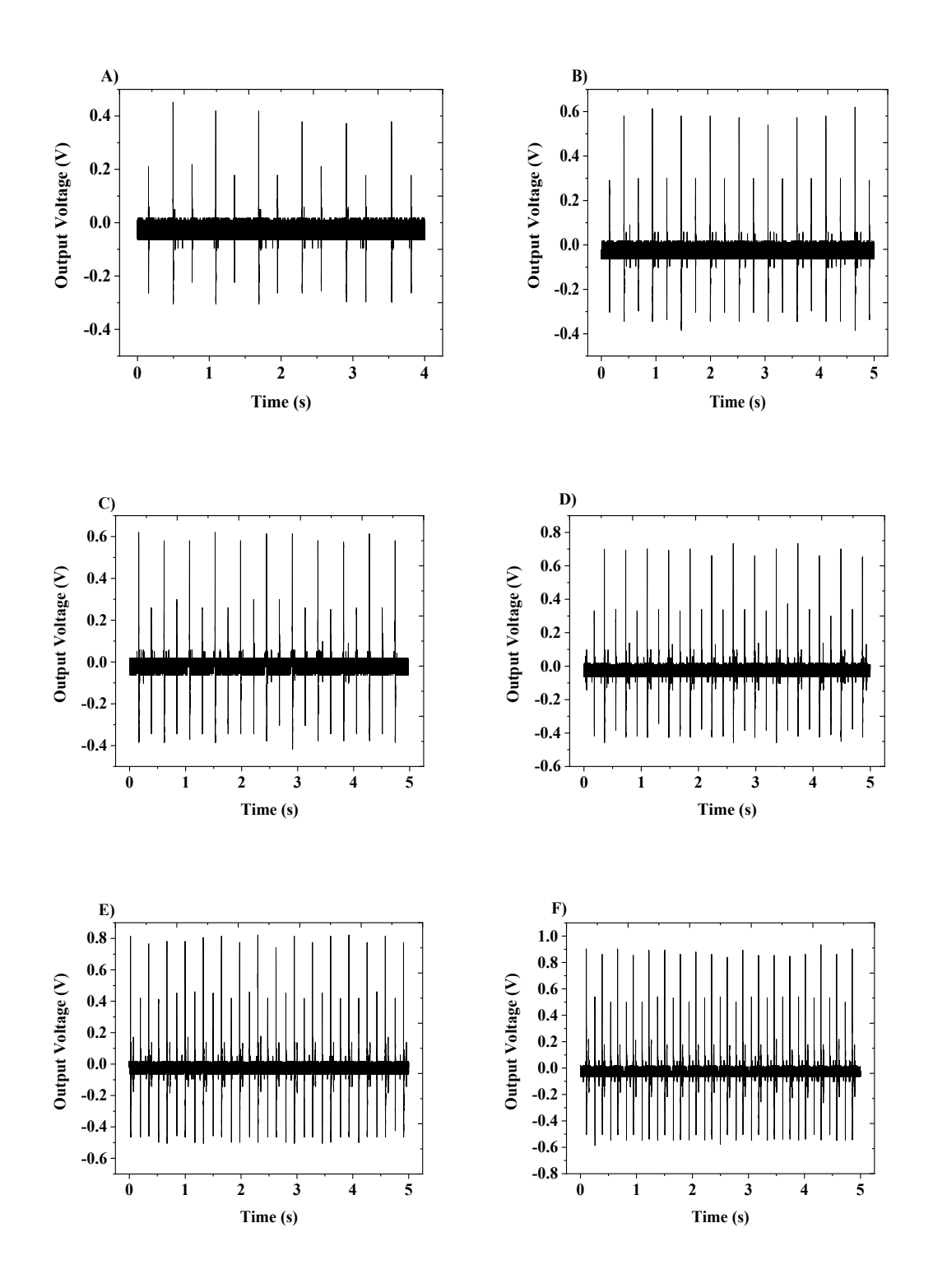


Figure S5.11 The output performance analyses of 1.5% rGO enhanced PVA-based hydrogel different frequency under 8.6cm amplitudes. (A) 1.5 Hz, (B) 2.0 Hz, (C) 2.5 Hz, (D) 3.0 Hz, (E) 3.5 Hz, and (F) 4.0 Hz.

Note S2. Analysis of the operation frequency for each amplitude.

The change in amplitude can be equated to the length variation of the bottom side of isosceles triangle. Since the length of platform shaft is fixed at 355 mm, the angle between two longer sides can be calculated. The results of angle θ calculations are presented in Table S5.2. Use the calculated values of angle θ at different amplitudes to calculate the approximate travelling time of spherical magnet under above 5 amplitudes as depicted in Equation (S5.1) through (S5.5).

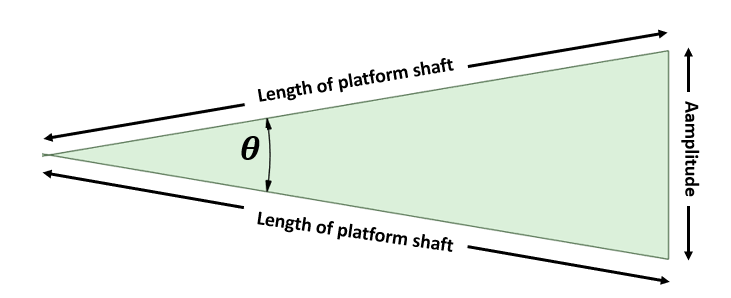


Figure S5.12. The geometric model for calculate the angle at different amplitudes.

Table S5.2. The angle θ at different amplitudes of testing platform.

Amplitude (cm)	Degree (°)
6.6	14.75
7.1	15.84
7.6	16.95
8.1	18.02
8.6	19.14

$$t_{travel\ 6.6cm} = \sqrt{\frac{14*(L-d)}{5gsin\theta}} = \sqrt{\frac{14*(0.102-0.025)}{5*9.81*\sin(14.75)}} = 0.2938 [s] = 3.40 [Hz]$$
 (S5.1)

$$t_{travel\ 7.1cm} = \sqrt{\frac{14*(L-d)}{5gsin\theta}} = \sqrt{\frac{14*(0.102-0.025)}{5*9.81*\sin(15.84)}} = 0.2837\ [s] = 3.52\ [Hz]$$
 (S5.2)

$$t_{travel\ 7.1cm} = \sqrt{\frac{14*(L-d)}{5gsin\theta}} = \sqrt{\frac{14*(0.102-0.025)}{5*9.81*\sin(16.95)}} = 0.2745\ [s] = 3.64\ [Hz]$$
 (S5.3)

$$t_{travel\ 7.1cm} = \sqrt{\frac{14*(L-d)}{5gsin\theta}} = \sqrt{\frac{14*(0.102-0.025)}{5*9.81*\sin(18.02)}} = 0.2665\ [s] = 3.75\ [Hz]$$
 (S5.4)

$$t_{travel\ 8.6cm} = \sqrt{\frac{14*(L-d)}{5gsin\theta}} = \sqrt{\frac{14*(0.102-0.025)}{5*9.81*\sin(19.14)}} = 0.2589\ [s] = 3.86\ [Hz]$$
 (S5.5)

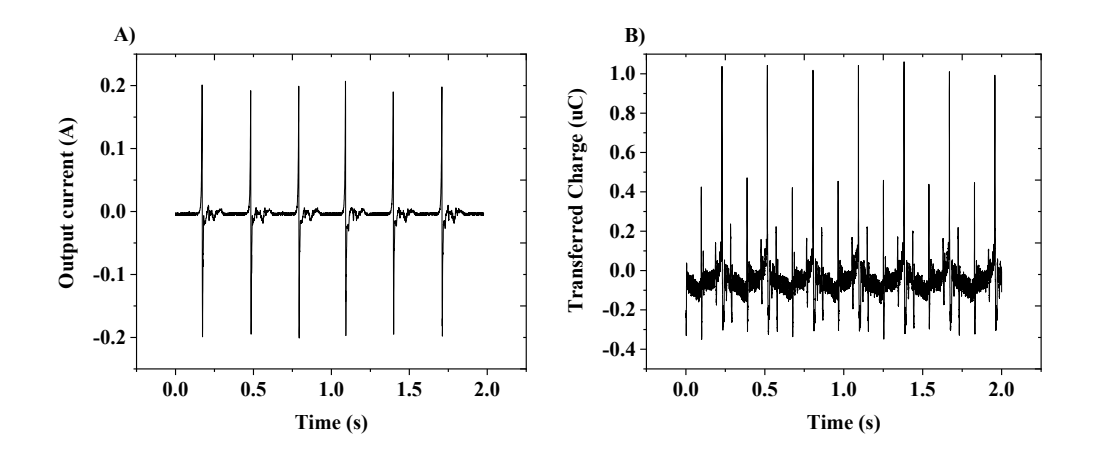


Figure S5.13 Supplemental output waveform of HSP-WS. (A) Typical waveform of the output current from the CS-EMG and (B) Maximum transferred charge.

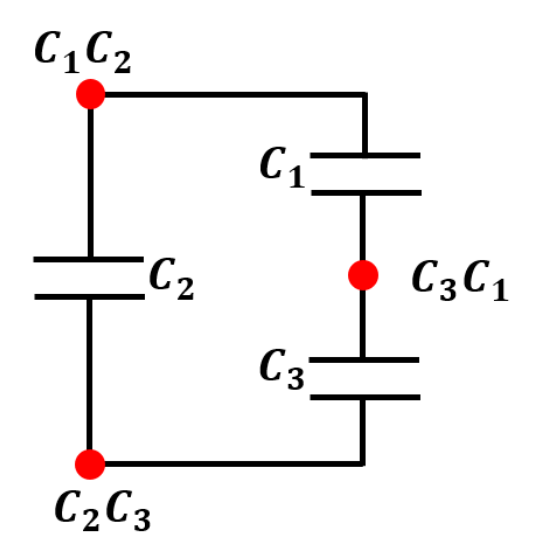


Figure S5.14 Equivalent circuit model of single-electrode TENG.

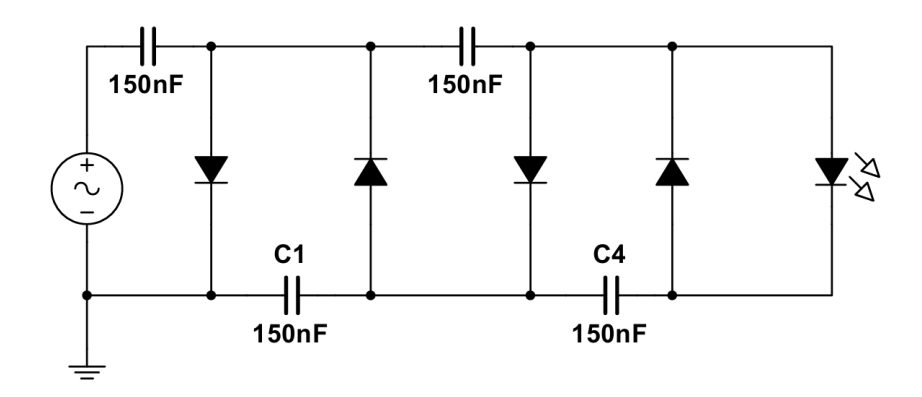


Figure S5.15 Power management system for CS-EMG.

Table S5.3. Power requirement for extra device

Name	Voltage	Current
EMG with power management circuit	3.8V	0.388A
Temperature sensor [S4]	3.3V – 2.7V	250 uA – 5uA
Low energy Bluetooth [S5]	3.6V – 1.7V	7.5mA – 5.4mA
Oxygen sensor [S6]	3.5V – 3.3V	0.10±0.05 mA

Reference

S5.1. Liu, Y., Liu, X., Duan, B., Yu, Z., Cheng, T., Yu, L., Liu, L., and Liu, K. (2021). Polymer-water interaction enabled intelligent moisture regulation in hydrogels. J. Phys. Chem. Lett 12, 2587–2592. 10.1021/acs.jpclett.1c00034.

S5.2. Xu, M., Qin, M., Zhang, X., Zhang, X., Li, J., Hu, Y., Chen, W., and Huang, D. (2020). Porous PVA/SA/HA hydrogels fabricated by dual-crosslinking method for bone tissue engineering. J. Biomater. Sci. Polym. Ed 31, 816–831. <u>10.1080/09205063.2020.1720155</u>.

S5.3. Lai, D., Chen, X., Wang, G., Xu, X., and Wang, Y. (2022). Arbitrarily reshaping and instantaneously self-healing graphene composite hydrogel with molecule polarization-enhanced ultrahigh electromagnetic interference shielding performance. Carbon 188, 513–522. 10.1016/j.carbon.2021.12.047.

S5.4. Phoenix sensors. WETS02 Wireless Temperature Transducer. https://phoenixsensors.com/products/wireless-temperature-transducer-wets02/

S5.5. Skylab. nRF52840 BLE5.0 Long Range Bluetooth Module. https://www.skylabmodule.com/product/nrf52840-ble5-0-long-range-bluetooth-module-skb501/

S5.6. Element 14. DFROBOT SEN0322.

https://au.element14.com/dfrobot/sen0322/i2c-oxygen-sensor-module-arduino/dp/3879708?CMP=KNC-GAU-GEN-SHOPPING-PLA-

PMAX&mckv=_dc%7Cpcrid%7C%7Cpkw%7C%7Cpmt%7C%7Cslid%7C%7Cproduct%7C387970 8%7Cpgrid%7C%7Cptaid%7C%7C&gad_source=1&gclid=CjwKCAjwhvi0BhA4EiwAX25ujzDGit0z nNe9al0E42yVHcftCLI73ir3QB0I3XmoWEqlxxwrSHL1URoCzd8QAvD_BwE#anchorTechnicalDOC S